HAROKOPIO UNIVERSITY

SCHOOL OF ENVIRONMENT, GEOGRAPHY & APPLIED ECONOMICS

DEPARTMENT OF GEOGRAPHY

Development of an integrated modeling system for simulating the air-ocean wave interactions

Doctoral Dissertation

Georgios Varlas

Athens, 2017

ΧΑΡΟΚΟΠΕΙΟ ΠΑΝΕΠΙΣΤΗΜΙΟ

ΣΧΟΛΗ ΠΕΡΙΒΑΛΛΟΝΤΟΣ, ΓΕΩΓΡΑΦΙΑΣ & ΕΦΑΡΜΟΣΜΕΝΩΝ ΟΙΚΟΝΟΜΙΚΩΝ

ΤΜΗΜΑ ΓΕΩΓΡΑΦΙΑΣ

Ανάπτυξη ενός ενοποιημένου συστήματος για την προσομοίωση των αλληλεπιδράσεων αέρα-θαλάσσιων κυμάτων

Διδακτορική Διατριβή

Γεώργιος Βάρλας

Αθήνα, 2017

HAROKOPIO UNIVERSITY

SCHOOL OF ENVIRONMENT, GEOGRAPHY & APPLIED ECONOMICS

DEPARTMENT OF GEOGRAPHY

The Doctoral Dissertation was examined by the following Committee:

P. Katsafados (Supervisor)

Associate Professor, Department of Geography, Harokopio University

A. Papadopoulos

Research Director, Institute of Marine Biological Resources and Inland Waters, Hellenic Center for Marine Research

G. Korres

Research Director, Institute of Oceanography, Hellenic Center for Marine Research

K. Pavlopoulos

Professor, Department of Geography, Harokopio University, Université Paris Sorbonne Abu Dhabi

E. Karymbalis

Associate Professor, Department of Geography, Harokopio University

E. Flocas

Associate Professor, Department of Physics, National and Kapodistrian University of Athens

V. Kotroni

Research Director, Institute for Environmental Research and Sustainable Development, National Observatory of Athens

Η έγκριση της διδακτορικής διατριβής από το τμήμα Γεωγραφίας του Χαροκοπείου Πανεπιστημίου δεν υποδηλώνει και αποδοχή των απόψεων του συγγραφέα.

Ο Γεώργιος Βάρλας δηλώνω υπεύθυνα ότι:

1) Είμαι ο κάτοχος των πνευματικών δικαιωμάτων της πρωτότυπης αυτής εργασίας και από όσο γνωρίζω η εργασία μου δε συκοφαντεί πρόσωπα, ούτε προσβάλει τα πνευματικά δικαιώματα τρίτων.

2) Αποδέχομαι ότι η ΒΚΠ μπορεί, χωρίς να αλλάξει το περιεχόμενο της εργασίας μου, να τη διαθέσει σε ηλεκτρονική μορφή μέσα από τη ψηφιακή Βιβλιοθήκη της, να την αντιγράψει σε οποιοδήποτε μέσο ή/και σε οποιοδήποτε μορφότυπο καθώς και να κρατά περισσότερα από ένα αντίγραφα για λόγους συντήρησης και ασφάλειας.

To my grandfather Georgios Varlas,

who was a great weather observer and inspirer.

Acknowledgements

This PhD dissertation has been carried out at the Geography Department of School of Environment, Geography and Applied Economics of Harokopio University of Athens.

I would like to thank my supervisor, Prof. Petros Katsafados for guiding and supporting me over the years. He has set an example of excellence as a researcher, mentor and instructor. Consequently, I would like to thank my advisory committee members. I am grateful to Dr. Anastasios Papadopoulos for his guidance, ideas and support on atmospheric modeling. I am thankful to Dr. Gerasimos Korres for our discussions as well as for his ideas, feedback and support on ocean wave modeling. I would like to thank the other members of examination committee, Prof. Elena Flocas, Dr. Vassiliki Kotroni, Prof. Kosmas Pavlopoulos and Prof. Efthymios Karymbalis for their consideration, ideas and support. I would also like to thank my friends and colleagues from the Atmosphere and Climate Dynamics Group (ACDG) of Harokopio University.

I am thankful to Dr. Arno Behrens for the kind provision of ocean wave model WAM and Dr. Øyvind Breivik for our constructive discussion during MyWave project meeting at Heraklio of Crete (May 2014). I am also grateful to Dr. Luigi Cavaleri, Dr. Jean Bidlot and Dr. Guy Caniaux for their useful ideas and advices. Moreover, I would like to thank Prof. Peter Webster for the immediate provision one of his academic article in Nature Journal.

The Italian National Institute for Environmental Protection and Research (ISPRA), the European Earth Observation Programme Copernicus, the National Data Buoy Center (NDBC) of United States and AVISO are gratefully acknowledged for the provision of buoy and satellite data. European Center for Medium-Range Weather Forecasts (ECMWF) is also acknowledged for the kind provision of the gridded analyses data and land surface observations. Additionally, the Greek Research and Technology Network (GRNET) is gratefully acknowledged for the access to the High Performance Computer (HPC) ARIS, where the simulations of this thesis have been performed. Intel Corporation is also acknowledged for the free provision of Fortran and C compilers.

I would especially like to thank my amazing family for the love, support, and constant encouragement I have gotten over the years. In particular, I would like to thank my fiancée Chryssa Chantzi. She is the salt of the earth, and I undoubtedly could not have done this without her.

This PhD thesis was funded by a 3-year PhD fellowship (2013-2016) from Hellenic Center for Marine Research (HCMR) and the EU-funded project MyWave (FP7-SPACE-2011-1/CP-FP, SPA.2011.1.5-03).

Table of Contents

Abstract

Nowadays, it has become clear that the fluid layer surrounding Earth should be considered as a single system both at short and longer spatiotemporal scales. This translates to simulating the atmosphere and the ocean as a single fully coupled system and constructing multi-scale, multi-model integrated systems. Air-sea interaction involving the exchange of momentum, mass and heat determines the Earth system equilibria and plays a crucial role in the state-of-the-science affecting human life and activities. First of all, this defines the development of cyclones which are associated with extreme winds, high waves and floods inflicting human casualties and economical damages in the affected areas. Additionally, as the global interest in renewable energy is growing, a refined simulation of air-sea interaction will contribute to better forecasts of wind and wave power production as well as provide early warnings about upcoming damages caused by extreme phenomena. Moreover, the improved wind and wave forecasts will better facilitate all human activities associated with the sea such as marine transportation, oil extraction, fishery, tourism and coastal constructions.

Nevertheless, the current knowledge on the complex mechanisms of air-sea interactions is still insufficient. Hence, this thesis envisages the implementation of a new two-way atmosphere-ocean wave fully coupled system with overarching aim to thoroughly unveil air-sea interactions focusing on the dynamical processes. The resulting system includes the Weather Research Forecasting (WRF) model as the atmospheric component and the Wave model (WAM) as the ocean wave component. WRF and WAM models have been coupled using the OASIS Model Coupling Toolkit (OASIS3-MCT) that enables the models to communicate and exchange the required information throughout the combined simulation. The latest version of system is appropriately implemented in order to support online coupling with Chemistry (WRF-Chem) and Hydrology (WRF-Hydro), offering the capability of simultaneous simulation of atmospheric, ocean wave, chemical and hydrological processes. Software aspects, data exchange and computational characteristics of the coupled system (CHAOS; Chemical Hydrological Atmospheric Ocean wave System) are elaborately discussed.

Two coupling modes have been applied to perform sensitivity tests. One-way coupling mode (only the ocean-wave component uses information produced by the atmospheric com-

ponent) and two-way coupling mode (both the atmospheric and ocean-wave components use information by each other). CHAOS simulations of various high-impact atmospheric and sea-state case studies over the Mediterranean Sea and under hurricane-force conditions (hurricane Sandy) over the Atlantic Ocean are analyzed. A remarkable finding is that ocean waves increase air-sea momentum and enthalpy transfer modifying the characteristics of atmospheric flow and ocean wave generation. Young wind-generated ocean waves are dominant on the modulation of momentum and enthalpy fluxes in the atmospheric surface layer. In two-way coupling mode, the space-time Charnock parameter variability decreases the medium to high-frequency gravity waves as the roughness length and the friction velocity are also increased. The roughness reduces for low-frequency waves forming a more slip sea surface under swell conditions. Two-way coupling improvements are more prominent for wave over open sea. In two-way coupling mode, atmosphere dynamically loses more momentum and energy by ocean waves but it thermodynamically gains more enthalpy. It is noteworthy that, two-way coupling balances lower the energy equilibrium attenuating atmospheric flow and, consequently ocean wave growth. This implies that two-way coupling simulates a more turbulent and thicker marine boundary layer (MABL) weakening the cyclonic systems as well. The energy imbalance delays the cyclone evolution and produces an average increase of the minimum central mean sea level pressure (MSLP). Two-way coupling simulates Mediterranean cyclones up to 2 hPa shallower than one-way coupling mode. The impact on the hurricane Sandy over the Atlantic Ocean is more intense with up to 5 hPa shallowing or 3 hPa deepening. The minimum central MSLP of the hurricanes is determined by complex nonlinear processes which can unveil heterogeneities of two-way coupling performance in shallowing or deepening the system. The troposphere also responds on the perturbations come from the sea surface fluxes. Differences in water vapor mixing ratio and relative humidity are detectable up to 7 km alongside with the wind speed, the vertical velocity and the temperature up to the tropopause.

CHAOS has been statistically assessed against buoys observations and satellite retrievals (Jason-1, 2, 3) over the sea as well as against land surface measurements. During extreme weather events, two-way coupling mode of CHAOS offers robust statistical improvements up to 10% and 24% for wind speed and significant wave height (SWH) over the sea, respectively, as well as up to 5% for wind speed, MSLP, temperature and precipitation over the land. Additionally, nesting techniques in CHAOS refine the simulation results with up to 9-10% improvements in forecast skill, due to better representation of high resolution interactions. Moreover, the

simulation of wind-induced wave breaking accompanied by sea spray production as well as of rain impact on waves offers improvements. It is noteworthy that the simulation of rain impact on waves offers up to 3.6% statistical improvements during hurricane-force conditions. Overall in a long-term operational approach (1 December 2013 - 1 December 2014), two-way coupling mode of CHAOS offers statistical improvements up to 3.7% and 6.3% for wind speed and SWH over the sea, respectively.

Keywords: Air-sea interaction, two-way coupling of atmosphere and ocean waves, CHAOS, surface momentum and enthalpy fluxes, rain impact on waves.

Περίληψη

Στις μέρες μας έχει καταστεί σαφές ότι η ατμόσφαιρα και ο ωκεανός θα πρέπει να θεωρούνται ως ενιαίο σύστημα τόσο σε μικρές όσο και σε μεγαλύτερες χωροχρονικές κλίμακες. Η θεώρηση αυτή απαιτεί την προσομοίωση της ατμόσφαιρας και του ωκεανού ως ενός ενιαίου, αμφίδρομου και πλήρως συζευγμένου συστήματος. Αυτό επιτυγχάνεται μέσω της δημιουργίας ολοκληρωμένων συστημάτων προσομοίωσης πολλών συζευγμένων μοντέλων και πολλαπλών μεταβλητών. Τα συζευγμένα συστήματα περιγράφουν πιο ρεαλιστικά τις αλληλεπιδράσεις ατμόσφαιρας-θάλασσας οι οποίες συνοδεύονται από ανταλλαγές ορμής, μάζας και θερμότητας. Οι ανταλλαγές αυτές καθορίζουν την ισορροπία ολόκληρου του Γήινου περιβαλλοντικού συστήματος και διαδραματίζουν σημαντικό ρόλο στις επιστήμες και τις ανθρώπινες δραστηριότητες. Είναι σημαντικό ότι οι αλληλεπιδράσεις αυτές καθορίζουν τη δημιουργία των κυκλώνων που συνοδεύονται από θυελλώδεις ανέμους, υψηλά κύματα και πλημμύρες προκαλώντας ανθρώπινα θύματα και οικονομικές ζημιές. Επίσης, καθώς το παγκόσμιο ενδιαφέρον για τις ανανεώσιμες πηγές ενέργειας αυξάνεται, η προσομοίωση της αλληλεπίδρασης ατμόσφαιρας-θάλασσας συμβάλλει στην καλύτερη πρόγνωση της παραγωγής αιολικής και κυματικής ενέργειας, καθώς και στην έγκαιρη προειδοποίηση για επερχόμενα ακραία καιρικά φαινόμενα που προκαλούν ζημιές στις εγκαταστάσεις. Επιπλέον, η βελτιστοποίηση στην πρόγνωση ατμοσφαιρικών και θαλάσσιων παραμέτρων όπως του ανέμου και του κύματος, συμβάλλει σε πολλές ανθρώπινες δραστηριότητες που σχετίζονται με τη θάλασσα, όπως οι θαλάσσιες μεταφορές, η εξόρυξη πετρελαίου, η αλιεία, ο τουρισμός και οι παραθαλάσσιες κατασκευές.

Οι γνώσεις σχετικά με τους πολύπλοκους μηχανισμούς των αλληλεπιδράσεων ατμόσφαιρας-θάλασσας εξακολουθούν μέχρι και σήμερα να είναι ανεπαρκείς. Ως εκ τούτου, η διατριβή αυτή έχει ως στόχο να συμβάλλει στην προσομοίωση, ανάλυση και τελικά την κατανόηση των αλληλεπιδράσεων ατμόσφαιρας-θάλασσας με επίκεντρο εκείνες μεταξύ ατμόσφαιρας και θαλάσσιων κυμάτων. Το εγχείρημα αυτό πραγματοποιείται μέσω της δημιουργίας ενός νέου αμφίδρομου πλήρως συζευγμένου συστήματος ατμόσφαιρας-θαλάσσιων κυμάτων. Το σύστημα προσομοιώσεων περιλαμβάνει το ατμοσφαιρικό μοντέλο Weather Forecast Research (WRF) και το κυματικό μοντέλο Wave Model (WAM). Τα μοντέλα WRF και WAM τρέχουν παράλληλα, επικοινωνούν και ανταλλάσσουν πληροφορία μέσω του συζευκτή (coupler) OASIS Model Coupling Toolkit (OASIS3-MCT). Η τελευταία έκδοση του συστήματος έχει διαμορφωθεί κατάλληλα προκειμένου να υποστηρίζεται η σύζευξη με το χημικό μοντέλο WRF-Chem και το

υδρολογικό μοντέλο WRF-Hydro, προσφέροντας τη δυνατότητα ταυτόχρονης προσομοίωσης ατμοσφαιρικών, ωκεάνιων, χημικών και υδρολογικών διαδικασιών. Οι δυσκολίες, ο σχεδιασμός, τα στάδια υλοποίησης και τα χαρακτηριστικά του νέου συζευγμένου συστήματος προσομοιώσεων (CHAOS; Σύστημα Προσομοίωσης Χημικών-Υδρολογικών-Ατμοσφαιρικών-Θαλάσσιων κυματικών διεργασιών) περιγράφονται αναλυτικά.

Με σκοπό την πραγματοποίηση πειραμάτων ευαισθησίας, δύο τρόποι σύζευξης διαμορφώθηκαν στο CHAOS, η μονόδρομη (μόνο το κυματικό μοντέλο χρησιμοποιεί πληροφορία από το ατμοσφαιρικό) και η αμφίδρομη (και τα δύο μοντέλα χρησιμοποιούν πληροφορία που παράγεται από το άλλο μοντέλο). Αρχικά το συζευγμένο σύστημα προσομοιώσεων CHAOS εφαρμόζεται στη μελέτη χαρακτηριστικών περιπτώσεων αλληλεπίδρασης ατμόσφαιρας-θαλάσσιων κυμάτων στην Μεσόγειο Θάλασσα και ακολούθως υπό ακραίες κυκλωνικές συνθήκες (τυφώνας Sandy 2012) στον Ατλαντικό Ωκεανό. Ένα αξιοσημείωτο εύρημα είναι ότι τα θαλάσσια κύματα αυξάνουν την ανταλλαγή ορμής και ενθαλπίας μεταξύ ατμόσφαιρας και θάλασσας, μεταβάλλοντας τα χαρακτηριστικά της ατμοσφαιρικής ροής και τη δημιουργία των κυμάτων. Τα νέα ανεμογενή κύματα κυριαρχούν στη διαμόρφωση των ροών ορμής και ενθαλπίας στο επιφανειακό στρώμα. Οι χωροχρονικά μεταβαλλόμενες τιμές της παραμέτρους Charnock εξασθενούν τον άνεμο και την ανεμογενή κυματογένεση, καθώς αυξάνουν το μήκος τραχύτητας και την ταχύτητα τριβής. Η τραχύτητα μειώνεται στα χαμηλής συχνότητας κύματα (swell waves) διαμορφώνοντας μια πιο ολισθηρή θαλάσσια επιφάνεια. Η επίδραση της αμφίδρομης σύζευξης είναι πιο έντονη στην ανοικτή θάλασσας. Τα κύματα δεσμεύουν ορμή και ενέργεια από την κατώτερη ατμόσφαιρα ενώ συμβάλλουν στη μεταφορά ενθαλπίας από τη θάλασσα στην ατμόσφαιρα. Προσομοιώνοντας με αμφίδρομη σύζευξη των μοντέλων, το ισοζύγιο της δυναμικής ενέργειας που χάνει η ατμόσφαιρα και της θερμικής ενέργειας που κερδίζει, καταλήγει σε μικρότερη στάθμη ισορροπίας και παράλληλη εξασθένηση της κυματογένεσης. Αυτό έχει ως αποτέλεσμα την προσομοίωση ενός παχύτερου και πιο τυρβώδους θαλάσσιου ατμοσφαιρικού οριακού στρώματος, το οποίο συντελεί στην εξασθένηση της ανάπτυξης των κυκλωνικών συστημάτων αυξάνοντας την ελάχιστη πίεση στο κέντρο τους. Η αμφίδρομη σύζευξη προσομοιώνει τους μεσογειακούς κυκλώνες πιο αβαθείς με διαφορές πίεσης (MSLP) στο κέντρο τους έως +2 hPa. Κατά τη διάρκεια του τυφώνα Sandy στον Ατλαντικό Ωκεανό οι διαφορές στην πίεση κυμαίνονται από -3 hPa έως +5 hPa. Αυτή η αβεβαιότητα για την πίεση οφείλεται στο γεγονός ότι η εκτίμηση της ελάχιστης πίεσης στους τυφώνες βασίζεται σε περίπλοκες μη γραμμικές διεργασίες, οι οποίες μπορούν να αποκαλύψουν ανομοιογένειες στην

επίδραση της αμφίδρομης σύζευξης στην εξέλιξη του συστήματος. Οι αλληλεπιδράσεις κατά μήκος της διεπιφάνειας αέρα-θάλασσας αντικατοπτρίζονται στην κατακόρυφη δομή της ατμόσφαιρας επηρεάζοντας τις δυναμικές και θερμοδυναμικές διεργασίες της. Διαφορές στην αναλογία μίγματος υδρατμών και στη σχετική υγρασία ανιχνεύονται έως τα 7 χλμ. Διαφορές στην ταχύτητα του ανέμου, την κατακόρυφη ταχύτητα ανύψωσης και τη θερμοκρασία ανιχνεύονται μέχρι την τροπόπαυση.

Το σύστημα CHAOS έχει στατιστικά αξιολογηθεί με βάση μετρήσεις από buoys και δορυφορικά δεδομένα (Jason-1, 2, 3) πάνω από τη θάλασσα και μετρήσεις επίγειων σταθμών πάνω από τη στεριά. Με την εφαρμογή της αμφίδρομης σύζευξης στο CHAOS επιτυγχάνονται στατιστικές βελτιώσεις πάνω από τη θάλασσα που φθάνουν το 10% για την εκτίμηση του ανεμολογικού πεδίου και το 24% για την εκτίμηση του σημαντικού ύψους κύματος κατά τη διάρκεια ακραίων καιρικών φαινομένων. Πάνω από τη στεριά οι στατιστικές βελτιώσεις στην εκτίμηση του ανέμου, της πίεσης (MSLP), τη θερμοκρασίας και του υετού φθάνουν το 5%. Επιπλέον, η εφαρμογή επάλληλων πλεγμάτων ολοκλήρωσης στο CHAOS βελτιώνουν τα αποτελέσματα των προσομοιώσεων έως 9-10%, καθώς περιγράφονται λεπτομερέστερα οι μικρότερης κλίμακας αλληλεπιδράσεις. Η προσομοίωση της θραύσης των κυμάτων λόγω ισχυρών ανέμων που συνοδεύεται από την παραγωγή θαλάσσιου σπρέι (sea spray) όπως και της επίδρασης της βροχής στα κύματα συμβάλλουν στους ορθότερους υπολογισμούς της ανταλλαγής μάζας μεταξύ ατμόσφαιρας και θάλασσας. Είναι αξιοσημείωτο ότι η προσομοίωση της επίδρασης της βροχής στα κύματα προσφέρει μέχρι και 3.6% στατιστικές βελτιώσεις κατά τη διάρκεια του τυφώνα Sandy. Συνολικά σε μια μακροπρόθεσμη επιχειρησιακή προσέγγιση (1 Δεκεμβρίου 2013 – 1 Δεκεμβρίου 2014), η αμφίδρομη σύζευξη στο CHAOS προσφέρει στατιστικές βελτιώσεις έως 3.7% στην εκτίμηση του ανεμολογικού πεδίου και έως 6.3% στην εκτίμηση του σημαντικού ύψους κύματος.

Λέξεις κλειδιά: Αλληλεπίδραση ατμόσφαιρας-θάλασσας, αμφίδρομη σύζευξη ατμόσφαιρας και θαλάσσιων κυμάτων, επιφανειακές ροές ορμής και ενθαλπίας, επίδραση της βροχής στο κύμα.

Table of Figures

List of Tables

Chapter 1

Introduction

1.1. Scope

This PhD thesis aims to investigate, analyze and explain the processes that take place between the atmosphere and the ocean waves through the implementation of an advanced simulation system. Atmosphere-ocean wave interaction is crucial for the development of cyclones and other extreme phenomena as well as climate change and human activities. In the context of this thesis, these mechanisms will be examined setting the ground for the main focus of the work, which is the design and implementation of a two-way atmosphere and ocean wave coupled system that produces a more physically-based representation of air-sea momentum, mass, enthalpy and moisture transfer (Varlas et al., 2017a). The coupled system facilitates the investigation of ocean waves impact on the dynamical and thermodynamic characteristics of the atmosphere in various spatiotemporal scales. Additionally, it enables the investigation of wave generation, wave age, wind-induced wave breaking accompanied by sea spray production as well as rain impact on waves as well as their feedbacks to the atmospheric properties.

1.2. Air-sea interaction

Earth's energy balance is determined by many interconnected physical factors as well as the human activity (von Schuckmann et al., 2016). Interaction plays an influential role in various aspects of life and determines the equilibria in the environment (Heimann and Reichstein, 2008). The Earth system is a typical example which involves a great amount of complex interactions that have been the subject of human curiosity for hundreds of years. Nowadays, it is considered to be consisted of five interconnected subsystems (Williams et al., 2012) as follows:

- the atmosphere – the body of air which surrounds the planet
- the hydrosphere – all the earth's water found in oceans, glaciers, streams, lakes, soil, groundwater, and in the air.
- the lithosphere – all inorganic material besides water and gasses
- the cryosphere – those portions of Earth's surface where water is in solid form
- the biosphere – all living organisms

Figure 1.1 illustrates the main physical and dynamical interactions between the above-mentioned subsystems. The linear and nonlinear interactions among the subsystems tend to generate physical and dynamical equilibria, configuring the climate and the weather (e.g. Knutti and Hegerl, 2008; van Nes et al., 2015).

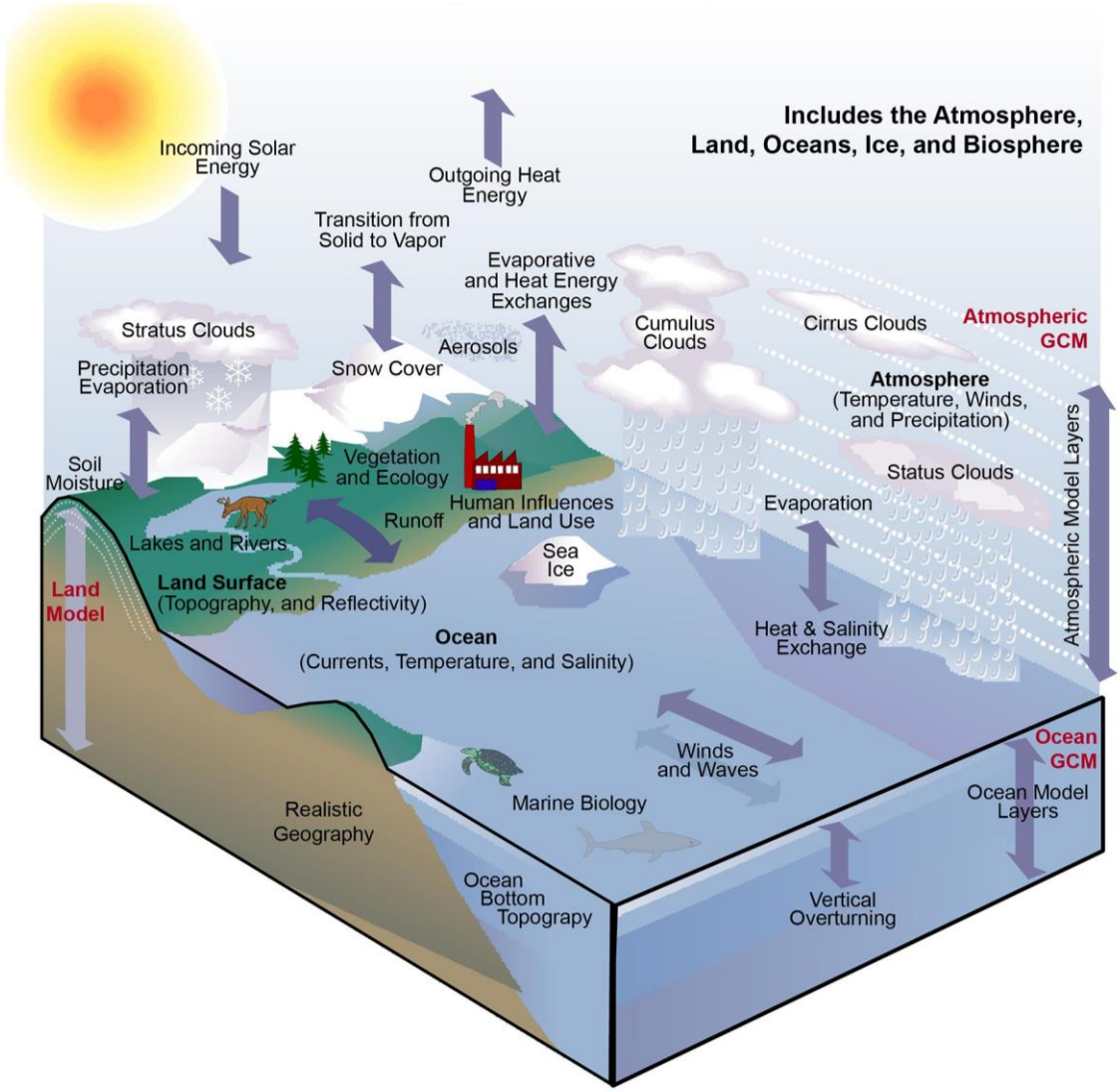

Figure 1.1: Schematic of the main interactions included in models of the Earth's climate system. GCM is an acronym for general circulation model. Adapted from Karl and Trenberth (2003).

Thinking that ocean covers approximately the 2/3 of the Earth's surface, the interaction between the atmosphere and the hydrosphere (air-sea interaction) is realized to has significant impact on various processes that couple the turbulent atmospheric and oceanic boundary layers across the interface. The dynamical and thermodynamic interactions among the lower-atmosphere, the ocean waves and the upper-ocean affect the momentum, energy and mass equilibria of Earth system. The interactions between oceans and the atmosphere can be categorized as follows:

- Dynamical – involving exchange of momentum and mass (water vapor, rain, sea spray)
- Thermodynamic – involving exchange of enthalpy (latent and sensible heat).

Air-sea interactions are complex because they include nonlinear relationships (Csanady, 2001; Warner et al., 2010). It is noteworthy that, dynamical and thermodynamic interactions are co-dependent, because the mass exchange is accompanied by latent heat transfer. Additionally, the dynamical interaction between atmosphere and waves determines sea surface aerodynamic roughness affecting momentum, enthalpy and moisture exchanges (Black et al., 2007; Drennan et al. 2007; French et al. 2007; Zhang et al., 2008; Andreas, 2011; Bell et al., 2012). Figure 1.2 depicts the main dynamical and thermodynamic interactions that are taking place between the air and the sea.

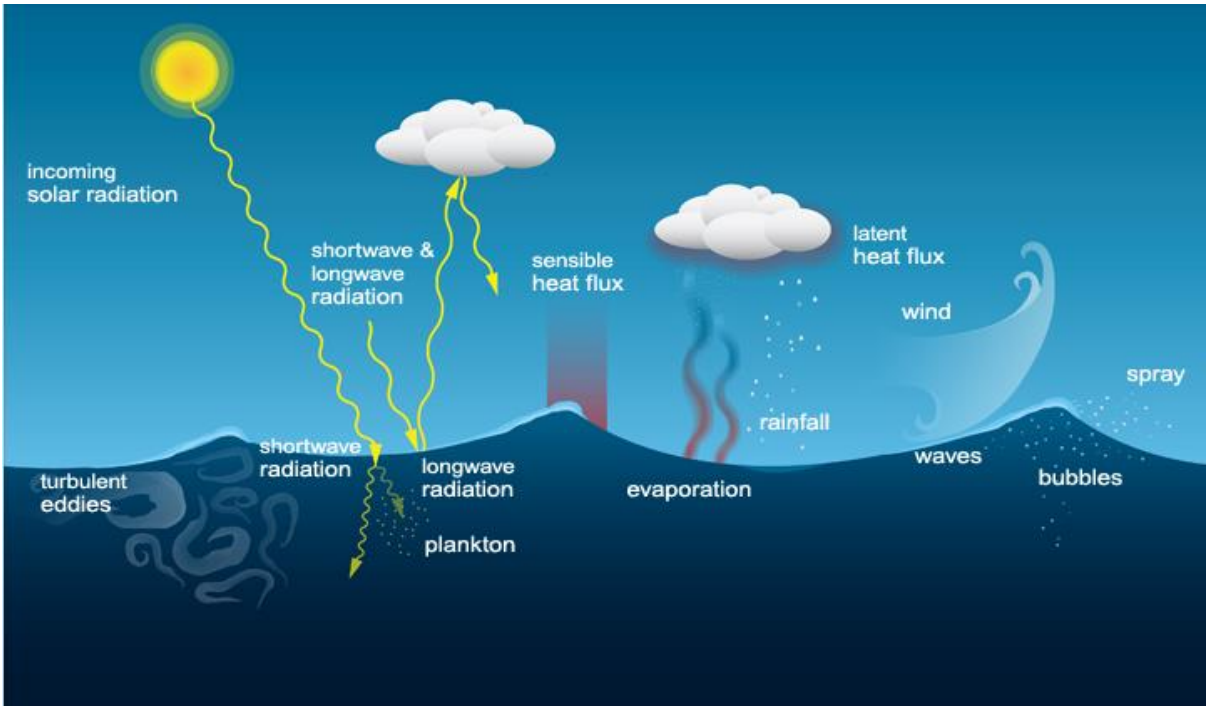

Figure 1.2: Schematic of the interactions in the atmosphere-ocean system. Illustration by Amy Caracappa-Qubeck, Woods Hole Oceanographic Institution.

The deeper understanding of air-sea interaction is of great importance for life on earth and human activities. First of all, these phenomena play a crucial role in the development of tropical cyclones which are associated with extreme winds, torrential rainfalls, high waves and damaging storm surges leading to extensive coastal flooding and, thus, inflicting human casualties and economical damages in the affected areas. Webster et al. (2005) observed a large increase in the number and proportion of intense tropical cyclones reaching categories 4 and 5 (Simpson and Saffir, 1974) from 1970 to 2004. This is mostly attributed to the sea surface temperature (SST) increase about 0.5°C over the Tropical Ocean. This aspect is increasingly important as many studies show that the number of the affected population is growing while predicting the continuation of this trend due to the increase of the population and climate change

(Figure 1.3) [e.g. Emanuel, 2005; Peduzzi et al., 2012]. In this context, Emanuel (2005) suggested that future warming may lead to an upward trend in tropical cyclone destructive potential and a substantial increase in tropical cyclone-related losses in the twenty-first century.

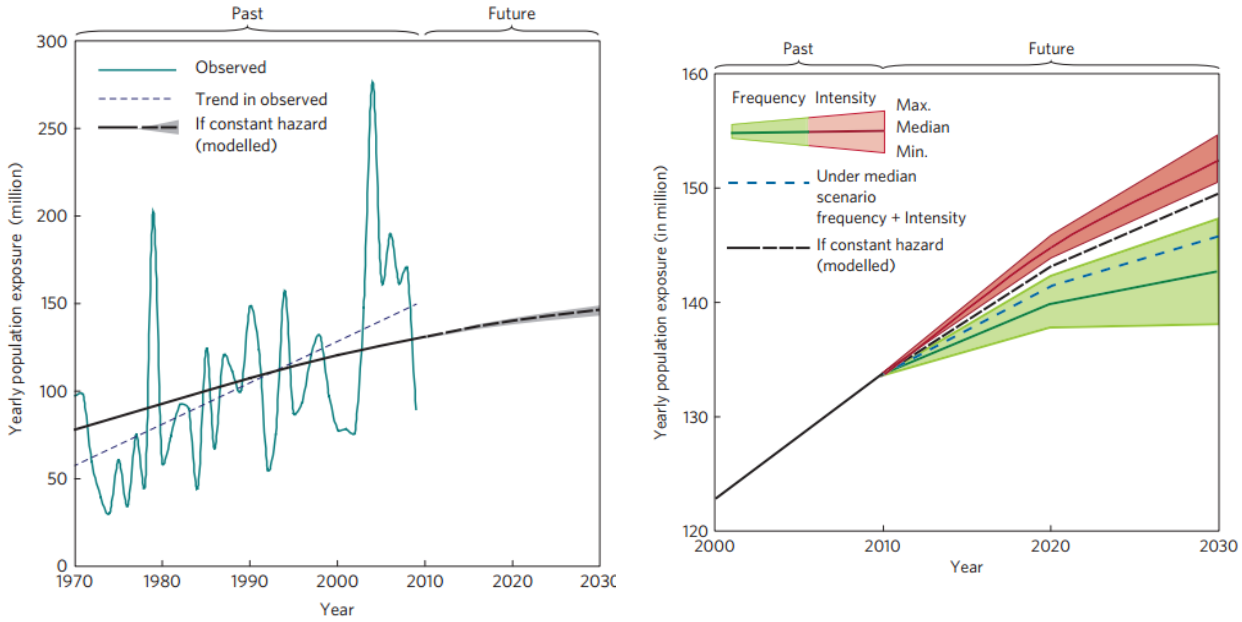

(a) (b)

Figure 1.3: (a) Change in tropical cyclone population yearly exposure with time. For the period 1970–2009 the exposure is provided for both observed and average trend (assuming constant hazard). The period 2010–2030 includes only the average trend under constant hazard, with uncertainty from population growth (−2.2 to 1.0%). (b) Scenarios until 2030. Influence of hazard on exposure for increase in intensity (red) and change (decrease) in frequency (green) and median scenario (dashed line in blue) [Peduzzi et al., 2012].

Additionally, as the global interest in renewable energy is growing, a refined simulation of air-sea interaction will contribute to improved design of offshore wind farms consist of floating wind turbines (Butterfield et al., 2005). This will also offer better wind and wave forecasts which are related to wind and wave power production (Kerbiriou et al., 2007; Bolanos et al., 2014; Christakos et al., 2016) as well as provide early warnings about upcoming damages caused by extreme phenomena (Sathe and Bierbooms, 2007; Christakos et al., 2014). Moreover, the improved wind and wave forecasts will better facilitate all human activities associated with the sea such as marine transportation (Tucker and Pitt, 2001), oil extraction, fishery, tourism and coastal constructions.

1.3. The role of Ocean Waves on Air-Sea Interaction

This thesis focuses on dynamical air-sea interactions which mainly involve the interactions between ocean waves and the lowest atmospheric layer. Near surface winds and medium to high-frequency gravity waves determine the sea surface roughness which affects the air-sea mo-

mentum exchange (Janssen, 1991; Donelan et al., 1993). High frequency wind-generated waves increase the sea surface roughness and extract energy and momentum from the atmosphere. The momentum exchange is the focal point of a number of recent studies highlighting the impact of ocean waves on the dynamical processes across the air-sea interface (Jenkins et al., 2012; Rutgersson et al., 2012; Katsafados et al., 2016; Wahle et al., 2017). The sea surface roughness also modulates the enthalpy (latent and sensible heat) and the moisture transfer between the atmosphere and the ocean determining their properties (Fairall et al., 2003; Bruneau and Toumi, 2016; Ricchi et al., 2016, 2017). Additionally, several studies have shown the relevance of the sea state dependent momentum transfer for the storm-surge modeling (Mastenbroek et al., 1993; Dietrich et al., 2011; Sikirić et al., 2013), the weather prediction (e.g. Doyle, 1995; Janssen et al., 2002; Davis et al., 2008; Gopalakrishnan et al., 2011; Cavalieri et al., 2012b; Chen et al., 2013; Torrisi et al., 2014; Zambon et al., 2014) and the atmospheric climate (Janssen and Viterbo, 1996; Andrews et al., 2012; Cavaleri et al., 2012a; Voldoire et al., 2013).

Air-sea enthalpy and moisture exchanges are dependent on air-sea properties such as sea surface roughness, wind speed, water vapor, currents, temperature, salinity etc. It is noteworthy that, atmosphere-wave interaction determines sea surface roughness and near surface wind speed modulating enthalpy and moisture transfer (Doyle, 1995; Bao et al., 2000; Fairall et al., 2003). The modification of momentum, enthalpy and moisture exchanges by sea surface roughness affects the marine atmospheric boundary layer (MABL) processes. Sullivan et al. (2008) showed that the waves support turbulence generation and change the mixing of MABL. Jenkins et al. (2012) observed that the waves act as roughness elements in MABL, affecting the turbulent flow and the vertical wind speed profile as well as inducing oscillatory motions in the atmospheric flow. Moreover, atmosphere-ocean wave interaction affects the mixing of heat and momentum in the upper ocean layers (Sullivan and Williams, 2010; D'Asaro et al., 2014; Breivik et al., 2015; Wu et al., 2015; Alari et al., 2016; Ličer et al., 2016; Staneva et al., 2016; Aijaz et al., 2017; Cai et al., 2017) and the ocean circulation (e.g. Burgers et al., 1995; Clementi et al., 2013; Turuncoglu et al., 2013; Fan and Griffies, 2014; Kim et al., 2014; Carniel et al., 2016).

Additionally, mass, momentum, enthalpy and moisture are transferred from the ocean to the atmosphere through sea spray droplets created by the bursting of sea bubbles and wave breaking (Deane and Stokes, 2002; Melville and Matusov, 2002; Andreas, 2004; Liu et al., 2011). Atmosphere-wave interaction determines wave breaking and the production of sea spray as well as its impact on the dynamical and thermodynamic processes of the atmosphere (Andreas

and Decosmo, 2002; Bao et al., 2011; Wu et al., 2015). Moon et al. (2004a, b, c) found that drag coefficient saturates in hurricane force wind conditions (above 33 m s^{-1}). At a wind speed of about 33 m s^{-1}, the drag coefficient starts levelling off, implying that the spray droplets begin to affect the dynamics of the atmospheric flow (Makin, 2005). Powell et al. (2003) speculated that increased foam coverage resulting from intensively breaking waves could progressively form a "slip" surface at the air-sea interface that leads to the reduction of the sea drag at wind speeds above 40 m s^{-1}. Moreover, during wave breaking, the "rain" of spray droplets back onto the sea surface creates a mass flux with a magnitude that has been shown to damp the short waves that sustain most of the atmospheric drag on the sea surface (Andreas, 2004). As a consequence, spray may play a key role in a negative feedback loop that limits air-sea momentum transfer and enhances the atmospheric flow.

Moreover, atmosphere-wave interaction involves the impact of rainfall on wave evolution and its feedback to the atmosphere. The variability in the sea-state by rainfall accounts for momentum exchange where a considerable amount of stress is imparted to the sea-surface (van Dorn, 1953; Malkus, 1962; Roll, 1965; Caldwell and Elliott, 1971). Rain falling on the ocean surface can change the atmosphere-ocean wave interaction processes in several ways. When raindrops strike the water surface, they generate ripples (Houk and Green, 1976; Poon et al., 1992) and calm down the surface gravity waves (Reynolds, 1900; Manton, 1973; Tsimplis and Thorpe, 1989; Tsimplis, 1992; Poon et al., 1992). Meanwhile, the rain can enhance the wind stress acting on the sea surface (van Dorn, 1953; Caldwell and Elliot, 1971, 1972).

For vertical or near vertical rainfall, the fluctuating sea surface forces are responsible for a non-negligible wave amplitude decay, particularly in the high frequency range (Le Mehaute and Khangaonkar, 1990; Cavaleri et al., 2015). In the case of high winds, the rain horizontal velocity component is large and the corresponding stress on the sea surface is nearly in phase with sea surface slope. Then instead of causing decay, the rain adds its effect to the wind and enhances the growth of high frequency waves. Cavaleri et al. (2015) proposed that rain attenuates high-frequency waves decreasing sea surface roughness and white-capping as well as increasing the wind speed. Yang et al. (1997) observed that damping or enhancement of the surface roughness by rain is shown at various wavenumber bands and depends on both wind and rain conditions. Additionally, Peirson et al. (2013) observed that the attenuation of gravity waves presents a systematic finite-amplitude effect above a mean steepness of 0.10.

Kumar et al. (2009) following Kitaigorodskii (1973) and Houk and Green (1976) added a rain-induced roughness length to the roughness length produced by wind blowing over sea-surface. Kumar et al. (2009) observed that damping at low wind speed occurs when horizontal momentum produced by rain is negligible compared with the vertical momentum. As also referred by Cavaleri et al. (2015), Kumar et al. (2009) showed that young waves are very sensitive to change in external force such as the raindrop striking. On the other hand, mature waves are not much affected by rain of low intensity and short duration irrespective of wind speed magnitudes which exist over the sea-surface.

1.4. Approaches on Simulation of Air-Sea Interaction

The lack of consistent skill in uncoupled forecasting systems may be partially attributed to inadequate surface and boundary layer formulations and the lack of full coupling to a dynamic ocean (Chen et al., 2007). It is, thus, essential to develop appropriate multi-model, multi-scale advanced prediction systems that simulate the atmospheric, wave and oceanic processes in a cross-talking way.

First, large-scale atmosphere-ocean coupled systems developed targeting to simulate the major climatic interactions (Battisti, 1988; Philander et al., 1992; Webster et al., 1999; Soden and Held, 2006; Roberts and Battisti, 2011). Due to the small spatial and temporal interaction scales between atmosphere and ocean, the direct and sufficient response between the coupled models is a substantial factor (Warner et al., 2010). In this context, a number of centers and institutes worldwide developed operational atmosphere-ocean coupled systems managing to resolve higher spatiotemporal scales. In the middle 1990s, the Naval Research Laboratory (NRL) of United States developed the 3-dimensional Coupled Ocean/Atmosphere Mesoscale Prediction System (COAMPS) specialized in tropical cyclones (Hodur, 1997). In 1998, the European Centre for Medium-Range Weather Forecasts (ECMWF) was the pioneer in the implementation of atmosphere-ocean wave coupled systems. The coupled system consisted of the ocean wave model of ECMWF (ECMWF WAM or ECWAM) and the Integrated Forecasting System (IFS), the operational global atmospheric model of ECMWF (Janssen et al., 2002).

In the following years, a number of atmosphere-ocean coupled systems were developed in order to unveil the air-sea interactions at even higher spatiotemporal scales. Powers and Stoelinga (2000) implemented a coupled air-sea numerical model and tested its performance

during an event of frontal passage over a lake in North America. Bao et al. (2000) implemented an atmosphere-wave-ocean coupled system to better represent surface momentum and heat fluxes as well as the contribution of sea spray under hurricane-force winds. In 2001, the Geophysical Fluid Dynamics Laboratory (GFDL) of United States developed an operational atmosphere-ocean coupled system to support tropical cyclone predictions (Bender et al., 2007). Lionello et al. (2003) developed the Model of Interacting Atmosphere and Ocean (MIAO) to resolve the atmosphere-wave-ocean interaction processes over the Mediterranean Sea. Later, the Coupled Boundary Layer Air-Sea Transfer (CBLAST)-Hurricane program at United States aimed to analyze the internal mechanisms of tropical cyclones at 1 km spatial resolution implementing an atmosphere-wave-ocean coupled system (Chen et al., 2007). In 2007, the National Center for Environmental Prediction (NCEP) of United States in collaboration with GFDL carried out the development of the Hurricane Weather Research Forecasting (HWRF) system in support of operational forecasting of tropical cyclones for all the tropical ocean basins (Gopalakrishnan et al., 2010). HWRF is an ongoing updated atmosphere-ocean modeling system involving new capabilities (Kim et al., 2014). In 2010, the United States Geological Survey (USGS) introduced the Coupled Ocean Atmosphere Wave Sediment Transport (COAWST) modeling system to better identify the dynamical processes affecting the coastlines (Warner et al., 2010). Later, Jenkins et al. (2012) implemented a modeling system involving the Weather Research Forecasting (WRF) model and the Wave model (WAM) coupled by MCEL coupler in order to study the impact of waves on the MABL over the North Sea and Norwegian Sea area. Chen et al. (2013) proposed a new directional wind-wave coupling method using the wave-stress vector from two-dimensional wave spectra, which improves the simulation of the evolution and the structure of hurricanes. At the same period, Voldoire et al. (2013) proposed the Earth system model (CNRM-CM5), running operationally at Meteo-France and involving several models to simulate atmosphere-land-ocean interactions.

Workstation Eta WAM (WEW) system is a two-way fully coupled atmosphere-ocean wave system, designed to explicitly resolve air-sea interactions supporting research and operational activities over the Mediterranean Sea (Katsafados et al., 2014, 2015a, 2015b, 2016a, 2016b, 2017; Varlas et al., 2014, 2015). The atmosphere-ocean wave interaction analysis with WEW was the initial research navigator of this thesis. The system was built in the Multiple Program Multiple Data (MPMD) environment where the atmospheric and the ocean wave components are handled as parallel tasks on different processors (Katsafados et al., 2016a). Interac-

tions considered in WEW were mainly driven by the momentum exchanges within the ocean wind-wave system and included the effects of the resolved wave spectrum on the drag coefficient and its feedback on the momentum flux. WEW offered a more realistic representation of the aerodynamic drag over rough sea surfaces. The performance of the system was tested in a high-impact atmospheric and sea-state case study of an explosive cyclogenesis in the Mediterranean Sea (Varlas et al., 2014; 2015). Despite the underestimation of both wind speed and significant wave height, WEW offered an overall improvement of RMSE up to 11% in respect to the uncoupled simulation.

1.5. Open issues

The current approaches in the literature have offered improvements in the research of air-sea interaction and especially in air-ocean wave interaction mechanisms (e.g. Csanady, 2001; Jones and Toba, 2001; Janssen, 2004; Liss and Duce, 2005; Lau and Waliser, 2011; Dobson et al., 2012). However, there is the necessity for a better understanding of the interaction mechanisms across air-sea interface related to momentum, heat and sea spray fluxes mainly under extreme weather conditions (Makin and Kudryavtsev, 1999; Kudryavtsev et al., 1999; Lionello et al., 2003; Andreas, 2004; Chen et al., 2007; Soloviev et al., 2014). Moreover, there are still many open scientific issues to investigate and complex nonlinear interactions to explore such as the understudied effect of rain on wind wave generation and dissipation (Cavaleri et al., 2015).

First, it is commonly accepted that short gravity-capillary waves play the most important role in the momentum loss from air flow (e.g. Janssen, 1989, 1991; Kudryavtsev and Makin, 2002; Jenkins et al., 2012). In general, current studies using wave-induced stress, wave steepness and wave age in air-sea momentum exchange parameterizations indicate that the surface aerodynamic roughness increases during rapidly-developing and short-fetch conditions (e.g. Taylor and Yelland, 2001; Janssen, 2004; Liu et al., 2011; Jenkins et al., 2012; Katsafados et al., 2016a, 2017). In this context, a fundamental challenge is to quantify the impact of wave frequency and wave age on the near surface atmosphere and its feedbacks on wave generation. However, the interaction between waves and currents can modify wave generation and sea surface roughness. A source of uncertainty, thus, is the description of the interactions between the waves and the oceanic boundary layer (Chen et al., 2007; Breivik et al., 2015).

Additionally, there are still open questions regarding the impact of sea surface roughness on momentum exchange as well on as sensible and latent heat fluxes, which affect the atmospheric conditions up to high heights, especially during sea-driven atmospheric phenomena such as cyclones. A disadvantage of current approaches is the use of observational data fitting methods in order to implement the air-sea parameterizations in the atmospheric models. The relations, thus, between atmospheric and ocean wave parameters are lacking universality mainly under extreme wind and sea state conditions (Donelan et al., 2004; Soloviev et al., 2014).

Another issue is the wave breaking and the estimation of sea spray production as well as its impact on the dynamical and thermodynamic processes in the atmospheric surface layer (Andreas and Decosmo, 2002; Bao et al., 2011; Wu et al., 2015). Breaking waves include a number of processes across the air-sea interface including the horizontal stress exerted by the wind, the energy dissipation of surface waves, the vertical mixing in the upper ocean, the exchange of heat and gases and the generation of sea spray by wave crests breaking as well as by bursting bubbles (Zhao and Toba, 2001). Wave breaking is a highly nonlinear process and its quantitative estimation is very difficult both experimentally and theoretically especially under hurricane-force conditions. There are several studies proposing that sea spray generated by intensive wave breaking saturates and even reduces aerodynamic drag at high wind speeds (Kudryavtsev and Makin, 2001; Powell et al., 2003; Donelan et al., 2004; Makin, 2005; Kudryavtsev, 2006; Jarosz et al., 2007; Liu et al., 2012; Holthuijsen et al., 2012; Kudryavtsev et al., 2012; Liu et al., 2012; Sahlée et al., 2012; Soloviev et al., 2014; Andreas et al., 2015; Potter et al., 2015; Wu et al., 2015). Additionally, breaking waves are likely to modify the total energy flux into surface waves and the viscous dissipation inside the wave boundary layer. Nevertheless, it is difficult to quantify these effects since our knowledge of breaking wave processes, such as statistical distribution of breaking waves and energy and momentum flux into individual breaking waves, is poor with uncertainties of factor of 10 or larger (Hara and Belcher, 2004). Hence, there is a need for a better understanding of the factors that control the wave breaking and sea spray production mechanisms as well as their impact on atmospheric and oceanic boundary layers.

Additionally, the impact of rain on wave evolution and its feedback to the atmosphere is still an open issue. While the underlying physics of air-sea interaction processes have been the subject of investigation for the last few decades, less attention has actually been paid to studying the impact of descending raindrops in alteration of sea surface roughness and thereby modifying the oceanic wave features over a region of concern. Quantitatively, a significant percent-

age of shear stress at ocean surface is provided by the impact of descending rain-drops. Poon et al. (1992) quantified the ratio of rain-induced stress and wind stress at sea surface to be in the order of about 7 to 25% based on an experimental study in a circulating wind-wave tank. However, the rain-wave interactions are highly dependent on intensity and duration of rainfall and on raindrops diameter and terminal velocity. There are also many unprecedented factors affecting the rain-wave-atmosphere interactions such as the white-capping decrease, the angle of raindrop incidence with the sea surface and the blowing away of raindrops by extreme winds (Cavaleri et al., 2015). Hence, the physics of dynamical rain-wave interaction is determined by nonlinear momentum and mass exchanges, making the implementation of a universal parameterization that resolves all interaction mechanisms considerable research issue.

1.6. Research goals

This PhD thesis aims to enhance the dynamical representation of the air-sea interaction, implementing a new two-way atmosphere-ocean wave modeling system (Varlas et al., 2017a). The research goals of this thesis are the following:

- As discussed above, there are open questions regarding the impact of sea surface roughness on air-sea momentum, enthalpy and moisture exchange and, consequently, on atmospheric conditions and ocean wave growth. In this context, a fundamental research goal of the thesis is the design and implementation of a two-way coupled atmosphere-ocean wave modeling system in order to simultaneously simulate the atmosphere-wave interactions approaching the impact of sea surface roughness on air-sea transfer processes. This is finally achieved by integrating suitable dynamical air-sea parameterizations and making sensitivity tests during extreme weather events. The impacts of sea state conditions on the dynamical characteristics of the MABL are also resolved through numerical experiments.

- It is essential to investigate atmosphere-ocean wave interaction under various spatiotemporal scales. As mentioned previously, the relations between atmospheric and ocean wave parameters are lacking universality mainly under extreme wind conditions. Furthermore, atmosphere-wave interaction is more intense during young wave growth. The second research goal is, thus, to resolve higher frequencies in the wind-wave spectrum by employing nesting capability in the two-way coupled system. On the other hand, the impact of atmosphere-ocean wave interaction in operational mode is approached through a set of long-term simulations.

- The role of medium to high-frequency waves and their breaking accompanied by sea spray production on the development of extreme weather phenomena is a critical research issue. Hence, the third research goal of this thesis is the investigation of the rapidly-developed high-frequency waves and the analysis of their breaking mechanisms. This is achieved by exploring the dynamical effect of sea spray on the atmospheric flow and the wave growth as well as on the thermodynamic structure of well-organized cyclonic systems such as hurricanes.

- Despite the fact that, a percentage of shear stress at ocean surface is provided by the impact of descending raindrops, the rain-wave interactions are not included in ocean wave generation and the atmospheric surface layer processes. Obviously, this is an important open research issue characterized by complex nonlinear physical and dynamical interactions. Thus, the impact of rain to wave evolution and its feedback to the atmospheric conditions mainly under extreme weather conditions is the fourth research goal of the thesis.

1.7. Thesis Outline

The main focus of this thesis is to expand the current knowledge and research in dynamical air-sea interaction in the context of numerical modeling as well as suggest optimizations to the simulation techniques of this complex topic. The next chapters are, thus, structured as follows:

- In the **second chapter**, the theory of atmosphere-ocean wave interactions is presented. That chapter focuses on the theoretical background of the problem which the modeling and the analyses of atmosphere-ocean wave interactions are based on. The physical processes and the dynamical mechanisms which determine the atmospheric surface layer and the ocean wave generation are discussed. The modeling of air-sea surface momentum, enthalpy and moisture transfer is also described.

- In the **third chapter**, the modeling tools of the new two-way fully coupled Chemical Hydrological Atmospheric Ocean wave System (CHAOS), used to simulate and analyze the atmosphere-ocean wave interactions, are presented. The main characteristics of the atmospheric model WRF, the ocean wave model WAM and the coupler OASIS3-MCT are reported.

- The **fourth chapter** is dedicated to the core of this thesis, the development of the new two-way fully coupled Chemical Hydrological Atmospheric Ocean wave System (CHAOS). The model coupling efforts, the difficulties, the techniques, the changes in source code of the

models involved and the final development and configuration of the system are analyzed. Additionally, the statistical evaluation methodology of the new system is described.

- In the **fifth chapter**, the new coupled system is assessed in order to simulate atmosphere-ocean wave interactions. Sensitivity tests on extreme weather events and long-term performance employing one-way and two-way coupling modes are presented. Atmosphere-ocean wave interactions and their feedbacks to the atmosphere and the ocean wave growth are analyzed. A physical interpretation of the results is also described. Additionally, the results are statistically evaluated.
- In th**e sixth chapter,** the utility of nesting techniques in two-way coupling mode to resolve the atmosphere-ocean wave interactions in finer spatiotemporal scales is investigated. Additionally, two simulations employing and not employing nesting techniques are statistically assessed.
- In the **seventh chapter**, sensitivity tests on an extreme hurricane event and analysis of the atmosphere-ocean wave interactions under hurricane-force winds and high sea state are presented. Wind-induced wave breaking accompanied by sea spray production, wave age based parameterizations and rainfall impact on wave generation as well as their feedbacks to the atmospheric and wave conditions are also investigated. Additionally, the results are statistically evaluated and discussed.
- The **eighth chapter** is the last chapter, where the conclusions of the thesis are summarized. The answers of the research questions, various further analyses, the final conclusions and the future plans with respect to the simulation and analysis of the atmosphere-ocean wave interactions are discussed.

Chapter 2

Theoretical Background on Modeling of Atmosphere – Ocean Wave Interactions

2.1. Atmospheric Surface Boundary Layer

The atmospheric surface boundary layer (or surface layer) constitutes the lower turbulent region of PBL in the troposphere -approximately the lowest 10% of the total depth of PBL- wherein the turbulent fluxes vary less than 10% of their magnitude (Stull 1988). As this is an interfacial layer between the Earth's surface and the overlying atmosphere, it controls the land-atmosphere and sea-atmosphere momentum and energy exchange processes (Jiménez et al., 2012; Hari Prasad et al., 2015). Meteorological variables experience a sharp variation with height within this layer that exhibits the most significant exchanges of momentum, heat, and moisture (Arya, 1988). Consequently, the accurate formulation of surface layer state is crucial to provide an adequate atmospheric evolution by numerical models.

The Monin-Obukhov similarity theory (Obukhov, 1946; Monin and Obukhov, 1954) is a framework used widely to compute the surface turbulent fluxes (Beljaars and Holtslag, 1991). The theory also provides information about the profiles within the surface layer that are used to diagnose meteorological variables at their typical observational height such as the wind at 10 meters. A limitation, however, is that the calculation of both the fluxes and the profiles need to be determined empirically. Thus, there is a number of studies suggesting reworks of the Monin-Obukhov similarity theory.

Jiménez et al. (2012) have introduced some modifications to the classic Monin-Obukhov similarity theory mainly concerning the estimation of similarity functions for momentum and heat. This revision of Monin-Obukhov similarity theory has been embraced by the research community because of the solutions it suggests to some of the limitations of the traditional theory. The Weather Research Forecasting model (WRF) involves this revised approach of Monin-Obukhov similarity theory. Because WRF model is one of the coupled models of the new system proposed by this thesis, this revised approach will be presented below.

The sea surface momentum flux or kinematic stress (τ), the sensible heat flux (H), the latent heat flux (LH) and the enthalpy flux (E) are parameterized as follows:

$$\tau = \rho_a {u_*}^2 = \rho_a C_d (U - U_s)^2 = \rho_a C_d U^2 \qquad (2.1)$$

$$H = -\rho_a c_p u_* \theta_* = -\rho_a c_p C_h U(\theta_a - \theta_s) \qquad (2.2)$$

$$LH = L_v \rho_a u_* q_* = L_v \rho_a C_q U (q_s - q_a) \quad (2.3)$$

$$E = H + LH = \rho_a U \left[c_p C_h (\theta_s - \theta_a) + L_v C_q (q_s - q_a) \right] \quad (2.4)$$

where ρ_a is the air density of the surface layer, u_* is the friction velocity, U_s is the sea surface current velocity and U is the wind speed at the lower level enhanced by a convective velocity following Beljaars (1995) and a sub-grid velocity following Mahrt and Sun (1995). As proposed by Oost and Oost (2004) $U_s = 0$ in a coordinate system moving with the sea surface current. Additionally, θ_* and q_* are the temperature and moisture scales respectively and c_p is the specific heat capacity at constant pressure; L_v is the latent heat of vaporization; θ_a and θ_s are the air and sea surface potential temperature, respectively; q_s is the interfacial value of the water vapor mixing ratio (Fairall et al., 1996), q_a is the specific humidity in the surface layer and $\mathrm{C_d}$, $\mathrm{C_h}$ and $\mathrm{C_q}$ are the dimensionless bulk transfer coefficients for momentum, sensible heat and moisture (Stull, 1988). As discussed by Green and Zhang (2013), when the interfacial air-sea transfer is considered alone, neglecting sea spray flux, the bulk transfer coefficient for enthalpy C_k is approximately equal to C_h and C_q. Thus, enthalpy flux can be parameterized as follows:

$$E \simeq \rho_a C_k U \left[c_p (\theta_s - \theta_a) + L_v (q_s - q_a) \right] \quad (2.5)$$

where $C_k \simeq C_q \simeq C_h$.

The dimensionless wind shear and potential temperature gradient in surface layer are usually expressed as (e.g., Arya, 1988):

$$\frac{\kappa z}{u_*} \frac{\partial u_a}{\partial z} = \varphi_m \left(\frac{z}{L} \right) \quad (2.6)$$

$$\frac{\kappa z}{\theta_*} \frac{\partial \theta}{\partial z} = \varphi_h \left(\frac{z}{L} \right) \quad (2.7)$$

where z is a height level, θ is the air potential temperature, u_a is the wind speed at level z, L is the Obukhov length (Obukhov, 1946) and κ is the von Kármán constant. Moreover, φ_m (with $\varphi_m(0) = 1$) and φ_h are the basic universal similarity functions for momentum and sensible heat respectively which relate the constant fluxes

$$\tau = \tau_0 = \rho_a {u_*}^2 \quad (2.8)$$

$$H = H_0 = -\rho_a c_p u_* \theta_* \quad (2.9)$$

to the mean gradients $\partial u_a/\partial z$ and $\partial\theta/\partial z$ in the surface layer. In equations (2.6) and (2.7), c_p is the specific heat capacity at constant pressure. The friction velocity u_* is the velocity scale and θ_* is the temperature scale defined along with the equations (2.8) and (2.9) as follows:

$$u_* = \sqrt{\frac{\tau_0}{\rho_a}} \quad (2.10)$$

$$\theta_* = -\frac{H_0}{\rho_a c_p u_*} \quad (2.11)$$

The term z/L is the Monin-Obukhov stability parameter which is defined as:

$$\frac{z}{L} = \kappa \frac{g}{\theta_a} z \frac{\theta_*}{{u_*}^2} \quad (2.12)$$

where g is the acceleration of gravity and θ_a the air potential temperature at level z.

Integrating the equations (2.6) and (2.7) with respect to height z, leads to

$$u_a = \frac{u_*}{\kappa}\left[\ln\left(\frac{z}{z_0}\right) - \psi_m\left(\frac{z}{L}\right) + \psi_m\left(\frac{z_0}{L}\right)\right] \quad (2.13)$$

$$\theta_a - \theta_g = \frac{\theta_*}{\kappa}\left[\ln\left(\frac{z}{z_{0t}}\right) - \psi_h\left(\frac{z}{L}\right) + \psi_h\left(\frac{z_0}{L}\right)\right] \quad (2.14)$$

where z_0 is the roughness length (i.e. the height at which the wind speed theoretically becomes zero), z_{0t} is the thermal roughness length, θ_g is the ground surface potential temperature and $\psi_{m,h}$ are the integrated similarity functions for momentum and heat that are defined as follows (Panofsky, 1963):

$$\psi_{m,h}\left(\frac{z}{L}\right) \equiv \int_0^{z/L} \left[1 - \varphi_{m,h}(\zeta)\right]\frac{d\zeta}{\zeta} \quad (2.15)$$

Finally, the bulk transfer coefficients for momentum, sensible heat and moisture over the sea are defined as (see more details at Fairall et al. (2003) and Jiménez et al. (2012) and references there in):

$$C_d = \left\{\frac{\kappa}{\left[\ln\left(\frac{z+z_0}{z_0}\right) - \psi_m\left(\frac{z+z_0}{L}\right) + \psi_m\left(\frac{z_0}{L}\right)\right]}\right\}^2 \quad (2.16)$$

$$C_h = \frac{\kappa\sqrt{C_d}}{\left[\ln\left(\frac{z+z_{0t}}{z_{0t}}\right) - \psi_h\left(\frac{z+z_0}{L}\right) + \psi_h\left(\frac{z_0}{L}\right)\right]} \quad (2.17)$$

$$C_q = \frac{\kappa\sqrt{C_d}}{\left[\ln\left(\frac{z+z_{0q}}{z_{0q}}\right) - \psi_h\left(\frac{z}{L}\right) + \psi_h\left(\frac{z_0}{L}\right)\right]} \quad (2.18)$$

where z_{0q} is the humidity transfer roughness length. According to Coupled Ocean-Atmosphere Response Experiment (COARE) algorithm, version 3.0 (Fairall et al., 2003), z_{0t} and z_{0q} are defined as:

$$z_{0t} = z_{0q} = \min(1.1\times10^{-4}, 5.5\times10^{-5}R_r^{-0.6}) \quad (2.19)$$

where R_r is the Reynolds number:

$$R_r = \frac{u_* z_0}{v_t} = \frac{u_* z_0}{(1.32 + 0.009T)\times10^{-5}} \quad (2.20)$$

where v_t is the kinematic viscosity of air, dependent on temperature T in °C.

The bulk transfer coefficients are affected by the stability of surface layer and the roughness length. In general, the integrated similarity functions are calculated through empirical approaches for different stability conditions using the Richardson number. Especially for the lowest part of MABL, the roughness length over the oceanic surface is strongly dependent on sea state.

Observational evidence indicates that the surface drag over the ocean is a positive function of the wind speed (Jones and Toba, 2001). Using non-dimensional arguments, Charnock (1955) postulated that, neglecting molecular motions, roughness length z_c is proportional to the square of the friction velocity (u_*), the variable that represents the intensity of the atmospheric turbulent mixing of momentum associated with surface friction (Jiménez and Dudhia, 2014). Nevertheless, total roughness length z_0 over ocean is calculated by Charnock (1955) equation adding a term for viscous sublayer z_v near the sea surface ($z < z_0$), where the molecular motions are important in a smooth flow as follows (e.g. Businger, 1973; Smith, 1988; Pielke, 2002):

$$z_0 = z_c + z_v = \frac{au_*^2}{g} + \frac{0.11v}{u_*} \quad (2.21)$$

For the first term of the equation, the factor a is an empirical constant known as the Charnock parameter. The Charnock parameter indicates the sea state impact on the lowest part of the surface layer. Subsequent field experiments have reported a range of values for the parameter (Kitaigorodskii and Volkov, 1965; Garrat, 1977; Wu, 1982; Geernaert et al., 1986). Wu (1982) proposed an often-used constant value for Charnock equal to 0.0185. Most recent empirical evidence suggests a dependence of the Charnock parameter on the wind speed (Fairall et al., 2003; Edson et al., 2013), or even on the sea state (Donelan, 1990; Janssen, 1991; Smith et al., 1992; Taylor and Yelland, 2001; Oost et al., 2002; Drennan et al., 2003; 2005; Fairall et al., 2003; Liu et al., 2011; Katsafados et al., 2017). For the second term of equation (2.21), $v = 1.5\times10^{-5}\,\frac{m^2}{s}$ is a representative value of the kinematic viscosity of air for temperature equal to 20°C. It is noteworthy that this term becomes significant when u_* decreases and the atmospheric flow can be assumed as smooth.

In this context, the near surface wind speed (often at 10 meters) can be diagnostically calculated according to:

$$u_{10m} = u_a \frac{\ln\left(\frac{10+z_0}{z_0}\right) - \psi_m\left(\frac{10+z_0}{L}\right) + \psi_m\left(\frac{z_0}{L}\right)}{\ln\left(\frac{z+z_0}{z_0}\right) - \psi_m\left(\frac{z+z_0}{L}\right) + \psi_m\left(\frac{z_0}{L}\right)} \qquad (2.22)$$

The near surface wind plays the most significant role in wind-generated waves growth on the free ocean surface. The wind-generated waves or wind waves are examples of gravity waves on ocean surface and the most important waves in the spectrum of waves at sea (Sorensen, 2005).

2.2. Development of Wind-Generated Waves

One of the most important dynamical air-sea interactions is the surface wind wave generation which adjusts aerodynamic drag in surface layer (Stewart, 1974; Janssen, 2004). Surface layer is governed by high complexity nonlinear physical mechanisms which are resolved by empirical parameterizations based on the roughness length. However, a more sophisticated approach for the impact of sea state on aerodynamic drag (examined using roughness length) will be discussed, starting with the growth processes of surface wind waves.

Wind blowing over the surface of a water body will transfer energy to the water in the form of a surface current and by generating waves on the water surface (Sorensen, 2005). The fundamental question is; how does the horizontal wind initiate the formation of waves on an

initially flat water surface? This process is best explained by a resonance model proposed by Phillips (1957, 1960). There are turbulent eddies in the wind field that exert a fluctuating pressure on the water surface. Pressure fluctuations vary in magnitude and frequency and they move forward at a range of speeds. They also cause water surface undulations to develop and grow (Figure 2.1). The key to their growth is that a resonant interaction occurs between the forward moving pressure fluctuations and the free waves that propagate at the same speed as the pressure fluctuations.

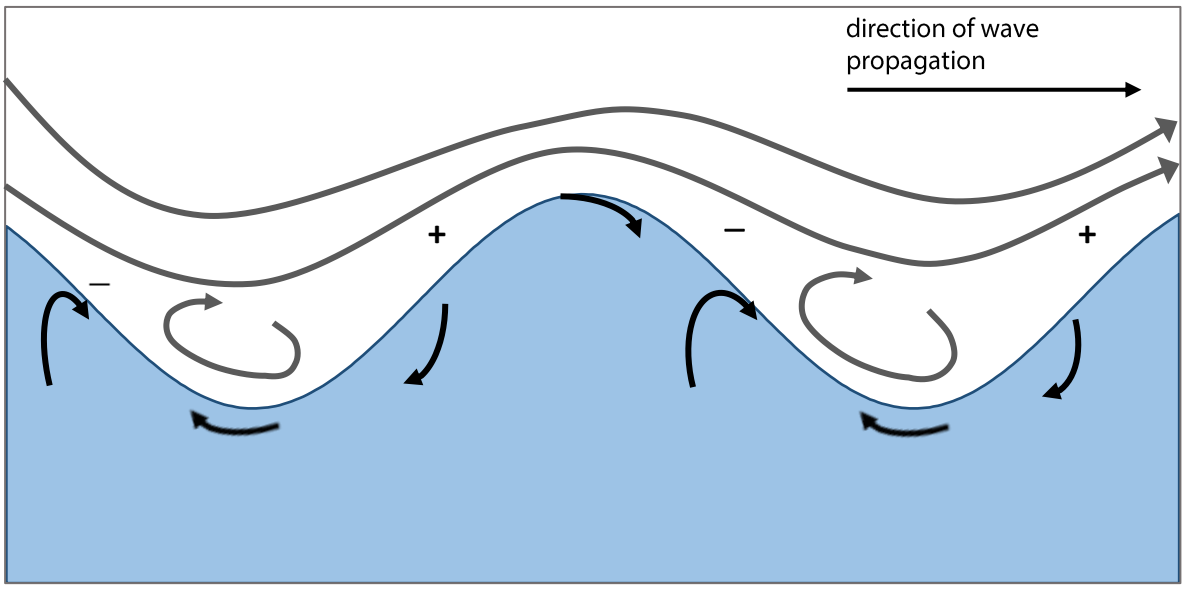

Figure 2.1: This diagram shows the generation process of wind-waves, it shows how the flow of air causes differential pressures that steepen the waves. Positive and negative areas of pressure are shown by the plus and minus symbols. The curved arrows represent the flow of air and fluid. This is known as the Jeffrey's 'sheltering' model of wave generation.

Although the Phillips model explains the initiation of wave motion, it is insufficient to explain the continued growth of the waves. This growth is best explained by a shear flow model proposed by Miles (1957). As the wind blows over a forward moving wave a complex air flow pattern develops over the wave. This involves a secondary air circulation that is set up around an axis that is parallel to the wave crest, by the wind velocity profile acting over a moving wave surface profile (Figure 2.2). Below a point on the velocity profile where the wind velocity equals the wave celerity, air flow is reversed relative to the forward moving wave profile. Above this point air flow is in the direction of the wave motion. This results in a relative flow circulation in a vertical plane above the wave surface that causes a pressure distribution on the surface that is out of phase with the surface displacement. The result is a momentum transfer to the wave that selectively amplifies the steeper waves (Sorensen, 2005).

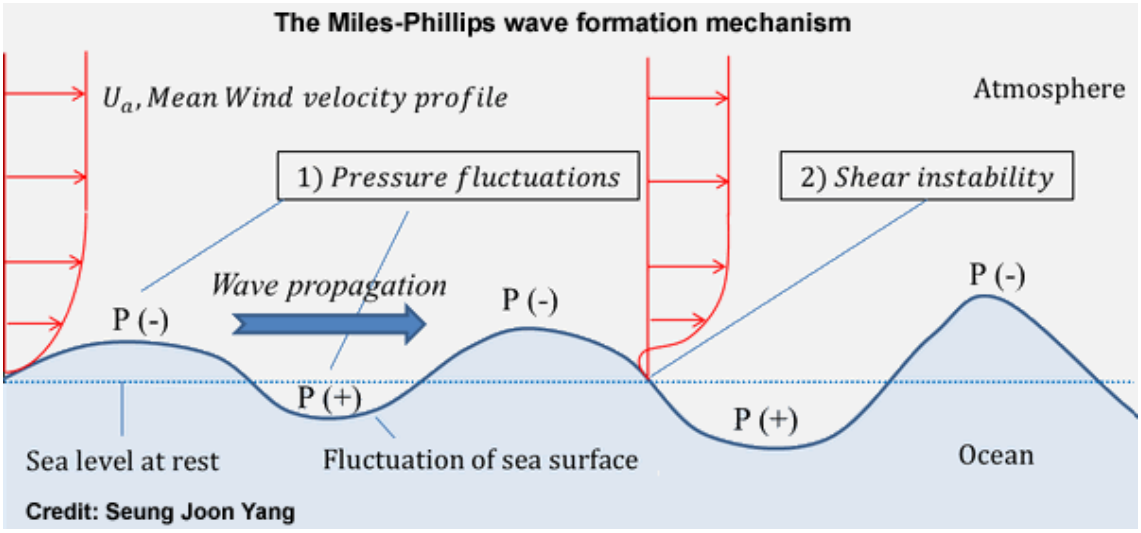

Figure 2.2: Similar to Figure 2.1 with additional wind profile and shear instability illustration (Seung Joon Yang).

Numerical solution of the air flow momentum balance over growing surface waves have been presented in a series of studies by Janssen et al. (1984), Janssen (1989) and Janssen (1991). The main conclusion was that the growth rate of the waves generated by wind depends on the ratio of friction velocity and phase speed and on a number of additional factors, such as the atmospheric density stratification, wind gustiness and wave age (Janssen and Komen, 1985; Voorrips et al., 1995). It is known that stratification effects observed in fetch-limited wave growth can be partly accounted for by scaling with u_* (which is consistent with theoretical results). The following paragraphs focus on the dependence of wave growth on wave age, and the related dependence of the aerodynamic drag on the sea state (IFS Documentation, 2013). The wave age z_a is defined as follows:

$$z_a = \frac{c_p}{u_*} \qquad (2.23)$$

where c_p is the wave phase velocity at the peak of the wave spectrum. The equations for the calculation of c_p and u_* will be presented in next paragraphs.

The wave phase velocity is the speed at which a particular phase of the wave propagates, for example, the speed of propagation of the wave crest (e.g. Stewart, 2008). The wave phase velocity at the peak of the wave spectrum is defined as follows:

$$c_p = \sqrt{\frac{g\lambda_p}{2\pi} tanh\left(\frac{2\pi h}{\lambda_p}\right)} \qquad (2.24)$$

where λ_p is the wavelength at the peak of the spectrum, g is the acceleration of gravity and h is the water depth. The wave phase velocity is different for shallow and deep water approximations. Shallow water approximation is valid if the water depth is much less than the wave length ($h < \lambda/11$). Deep-water approximation is valid if the water depth is much greater than the wave length ($h > \lambda/4$). The wave phase velocity at the peak of the spectrum for deep water approach is defined as follows:

$$c_p = \sqrt{\frac{g\lambda_p}{2\pi}} = \frac{g}{2\pi f_p} \qquad (2.25)$$

where f_p is the peak frequency of the wave spectrum. For shallow water approximation, the water depth h is significant and thus, the wave phase velocity at the peak of the spectrum is defined according to the following equation:

$$c_p = \sqrt{gh} \qquad (2.26)$$

In deep water, the wave phase velocity depends on wave length or wave frequency. Longer waves travel faster. Thus, deep-water waves are dispersive. In shallow water, the phase speed is independent of the wave; it depends only on the depth of the water. Shallow-water waves are non-dispersive. Nevertheless, various empirical formulas are used in order to calculate the wave phase velocity at the peak of the spectrum in the case of intermediate water approximation ($\lambda/11 < h < \lambda/4$) or when there are both shallow and deep waters during a calculation.

A realistic parameterization of the interaction between wind and wave was given by Janssen (1991), a summary of which is given below. The basic assumption of Janssen (1989, 1991) indicates that even for young wind waves, the wind profile has a logarithmic shape, though with a roughness length that depends on the wave-induced stress. As shown by Miles (1957), the growth rate of gravity waves due to wind then only depends on two parameters, namely

$$x = \left(\frac{u_*}{c}\right) \max(cos(\theta - \varphi), 0) \text{ and } \Omega_m = \frac{g\kappa^2 z_0}{{u_*}^2} \qquad (2.27)$$

where x denotes the wave-induced velocity, u_* the friction velocity, c the phase speed of the waves, φ the wind direction, θ the direction in which the waves propagate and κ the von Kármán constant. The so-called profile parameter Ω_m characterizes the state of the mean air flow through its dependence on the roughness length z_0. Thus, through Ω_m the growth rate depends on the roughness of the air flow, which, in its turn, depends on the sea state. A simple parame-

terization of the growth rate of the waves follows from a fit of numerical results presented in Janssen (1991). One finds

$$\frac{\gamma}{\omega} = \epsilon\beta x^2 \qquad (2.28)$$

where γ is the growth rate, ω the angular frequency, ϵ the air–water density ratio and β the so-called Miles' parameter. In terms of the dimensionless critical height $\mu = kz_c$ [with k the wavenumber and z_c the critical height defined by $U_0(\mathrm{z} = \mathrm{z}_c)$ = c] the Mile's parameter becomes as extended to any water depth h.

$$\beta = \frac{\beta_m}{\kappa^2}\tan(kh)\,\mu\ln^4(\mu), \qquad \mu \leq 1 \qquad (2.29)$$

where β_m is a constant. In terms of wave and wind quantities μ is given as

$$\mu = \left(\frac{u_*}{\kappa c}\right)^2 \tanh(kh)\,\Omega_m \exp\left(\frac{\kappa}{\hat{x}}\right), \qquad \hat{x} = \left(\frac{u_*}{c} + w_a\right)\cos(\theta - \varphi) \qquad (2.30)$$

where $w_a = 0.008$ is the wave age tuning parameter.

The stress of air flow over sea waves depends on sea state and from a consideration of the momentum balance of air it is found that the kinematic stress is given as (Janssen, 1991)

$$\tau = \rho_\alpha {u_*}^2 = {u_*}^2 = \left(\frac{\kappa\, U\, z_{\mathrm{obs}}}{\ln\frac{z_{\mathrm{obs}}}{z_0}}\right)^2 \qquad (2.31)$$

For the air density $\rho_\alpha = 1$ is assumed because it is much smaller than the water density $\rho_w$as $\rho_\alpha \ll \rho_w$ or $\varepsilon \ll 1$. The friction velocity is defined as

$$u_* = \frac{\kappa\, U(z_{\mathrm{obs}})}{\ln\frac{z_{\mathrm{obs}}}{z_0}} \qquad (2.32)$$

and the roughness length neglecting viscous stress is calculated as

$$z_0 = \frac{0.01\,\tau}{g\sqrt{1-y}}, \qquad y = \frac{\tau_w}{\tau} \qquad (2.33)$$

Here z_{obs} is the mean height above the waves and τ_w is the stress induced by gravity waves (wave stress)

$$\tau_w = \frac{g}{\epsilon}\int S_{in} k \mathrm{d}\omega\, \mathrm{d}\theta \qquad (2.34)$$

where $S_{in} = \gamma N$ is the term of wind input with N the action density spectrum (see more at Section 3.2).

The frequency integral extends to infinity, but in its evaluation only an f^{-5} tail of gravity waves is included and the higher level of capillary waves is treated as a background small-scale

roughness (for more details refer to IFS Documentation, 2013). In general, it is noteworthy that the wave stress points in the wind direction as it is mainly determined by the high-frequency waves which respond quickly to changes in the wind direction. Equation (2.33) shows that the roughness length using a non-dimensional approach, neglecting the impact of the molecular motions in viscous sublayer on aerodynamic roughness, is given by the Charnock (1955) relation, as in equation (2.21):

$$z_0 = \frac{a\tau}{g} = \frac{au_*^2}{g} \qquad (2.35)$$

2.3. Parameterizations of Atmosphere-Ocean Wave interactions

As already discussed, in nature, the atmospheric processes in surface layer are inseparable from ocean wave mechanisms. The near surface atmospheric flow determines the generation of wind-waves while ocean waves change the aerodynamic roughness. Hence, the encapsulation of ocean waves in surface layer advances the description of dynamical air-sea interaction. In this context, this section is dedicated to an overview of the theoretical background behind some of the most advanced parameterization schemes introducing sea state information in surface layer.

As already mentioned, using non-dimensional arguments, Charnock (1955) postulated that, neglecting molecular motions, roughness length z_c is proportional to the square of the friction velocity (u_*), the variable that represents the intensity of the atmospheric turbulent mixing of momentum associated with surface friction. Charnock's parameter had a constant value, often expressed as Charnock coefficient. An advanced description of a not constant dimensionless Charnock parameter α was suggested by Janssen (1991). Charnock parameter depends on the sea state through the wave-induced stress since

$$\alpha = a_J = \frac{0.01}{\sqrt{1 - \frac{\tau_w}{\tau}}} \qquad (2.36)$$

Evidently, whenever τ_w becomes of the order of the total stress in the surface layer (this happens, for example, for young wind sea) a considerable enhancement of the Charnock parameter is found, resulting in an efficient momentum transfer from air to water.

Besides Janssen's description of Charnock parameter, there are alternative sea state formulations described in literature employing other wave properties such as wave age, significant wave height and wave steepness. Smith et al. (1992) introduced an empirical sea surface aerodynamic roughness parameterization using wave age, as follows:

$$\alpha = a_S = \frac{0.48}{z_a} \qquad (2.37)$$

On the other hand, Donelan et al. (1990) sought a different approach, using a more general wave age dependence. Instead of (2.35) the roughness length is described as

$$z_0 = H_S A_1 \left(\frac{1}{z_a}\right)^{B_1} \qquad (2.38)$$

where $H_S = 4\sqrt{\langle \eta^2 \rangle}$ is the significant wave height with $\langle \eta^2 \rangle$ the wave variance and A_1, B_1 are constants. Drennan et al. (2003, 2005) proposed empirical values $A_1 = 3.35$ and $B_1 = 3.4$ which were found to describe the physical mechanisms adequately. Due to high sensitivity of wave age to the variability of friction velocity, Taylor and Yelland (2001) suggested an alternative scaling, independent from wave age, for dimensionless roughness based on wave steepness:

$$z_0 = 1200 H_S \left(\frac{H_S}{\lambda_p}\right)^{4.5} \qquad (2.39)$$

where the H_S/λ_p represents the wave steepness with λ_p the wavelength at the peak of the wave spectrum:

$$\lambda_p = \frac{2\pi {c_p}^2}{g} \qquad (2.40)$$

This representation manages to be free of spurious correlation with friction velocity and is used for deep water approximation. Liu et al. (2011) obtained a parameterization of sea surface aerodynamic roughness applicable to both low to moderate and high winds by combining the Scientific Committee on Oceanic Research (SCOR) relation (Jones and Toba, 2001) with the resistance law of Makin (2005). The parameterization of sea surface aerodynamic roughness is dependent on wave age and wind-induced wave breaking accompanied by sea spray production as shown below:

$$\alpha = a_L = \begin{cases} \left(0.085 {z_a}^{3/2}\right)^{1-(1/b)} [0.03 z_a \exp(-0.14 z_a)]^{1/b}, & \sim 0.35 < z_a < 35 \\ 17.60^{1-(1/b)}\, 0.008^{1/b}, & z_a \geq 35 \end{cases} \qquad (2.41)$$

where b is the correction parameter indicating the influence of wave breaking and sea spray on the logarithmic wind profile with

$$b = \min\left(1, \frac{a_{cr}}{\kappa u_*}\right) \quad (2.42)$$

and $a_{cr} = 0.64\ m\ s^{-1}$ is the critical value of terminal fall velocity of sea spray droplets (Makin, 2005).

Additionally, Kumar et al. (2009) added a rain-induced roughness length to the roughness length produced by wind blowing over sea-surface. According to Kitaigorodskii (1973) and Houk and Green (1976), surface roughness length due to rain can be expressed in the following form:

$$Z_r = 0.03\sigma_w \quad (2.43)$$

where, σ_w is standard deviation of mean water level obtained through experiments in determining characteristic surface waves created by raindrops striking the sea surface. Expansion for σ_w can be written in the form:

$$\sigma_w = \beta_r \times \frac{KD}{g v_w} \quad (2.44)$$

Where, β_r ~ 0.01 is a non-dimensional constant, D the drop diameter, v_w is the kinematic viscosity of water, and K the rain kinetic energy flux. The rain kinetic energy flux can be related to rain intensity I and terminal velocity of rain drop V_r as:

$$K = \frac{IV_r^2}{2} \quad (2.45)$$

Hence, the surface roughness connecting rain intensity, terminal velocity of raindrop and drop diameter from equations (2.43), (2.44) and (2.45) can be written in the form:

$$Z_r = \frac{1.5 \times 10^{-4} I V_r^2 D}{g v_w} \quad (2.46)$$

The total roughness length adding the above term along with the equations (2.21) is expressed as follows:

$$z_0 = \frac{a u_*^2}{g} + \frac{0.11 v_a}{u_*} + Z_r \quad (2.47)$$

including the impact of surface waves, smooth surface and rain on the roughness length of surface layer.

Chapter 3

Components of the New Atmosphere – Ocean Wave Coupled System

As already discussed, due to the complexity of the interactions across the air-sea interface, there is a need for a better understanding and simulation of the factors that contribute to air-sea interaction mechanisms (Lionello et al., 2003; Chen et al., 2007; Katsafados et al., 2016a). Indeed, forecasts exhibit reduced skill especially in cases of high-impact metocean events. This fact may be partly attributed to the limited work on fully coupled atmosphere-ocean wave simulation systems. Consequently, the development of a two-way fully coupled modeling system between atmosphere and ocean waves is essential for the analysis of dynamical air-sea interaction, thus, contributing to the evolution of numerical weather prediction models (Varlas et al., 2017a).

In this chapter the components of the two-way atmosphere-ocean wave coupled system, proposed by this thesis, will be presented. The coupled system consists of three components (Figure 3.1):

- The Advanced Weather Research Forecasting model (WRF-ARW) coupled to Chemistry (WRF-Chem) and Hydrology (WRF-Hydro) as atmospheric component which will be referred as WRF.
- The Ocean Wave Model WAM.
- The OASIS3-MCT coupler.

The choice of WRF and WAM modeling systems as atmospheric and ocean wave components of the coupled system respectively, was based on their advanced capabilities (e.g. Korres et al., 2011; Christakos et al., 2014, 2016). More specifically, the atmospheric component WRF is a widely used next-generation mesoscale numerical weather prediction (NWP) model with high scalability (e.g. Michalakes et al., 2008; Koesterke et al., 2009) designed with software architecture allowing for computational parallelism and system extensibility. WRF is suitable for a broad spectrum of applications across scales ranging from meters to thousands of kilometers having a variety of choices for physics and dynamics. This research is based on version 3.8 (for WRF version 3 see Skamarock et al., 2008). Advanced packages of atmospheric chemistry and hydrology can be also embedded in WRF model. WRF-Chem (version 3.8) can be used in order to resolve chemical processes such as the aerosols physics. Moreover, WRF-Hydro model (version 3.0) is a modern hydrological model with the capability to resolve soil and hydrological processes (Gochis et al., 2015). The ocean wave component is based on the updated version 4.5.4 of the WAM model (WAMDI, 1988; Komen et al., 1994). WAM has also parallel

software architecture and offers many choices in order to resolve the ocean wave spectrum. The coupling of WRF and WAM models is implemented using OASIS3-MCT coupler version 3.0 (Valcke et al., 2015) along with Message Passive Interface (MPI) routines. OASIS3-MCT 3.0, which will be referred as OASIS3-MCT, is "the-state-of-the-art" of couplers with advanced capabilities in weather and climate modeling characterized by flexibility, portability and scalability (Valcke, 2015). The name of the proposed fully coupled system is CHAOS, a synthesis of some letters of Chemical Hydrological Atmospheric Ocean wave System.

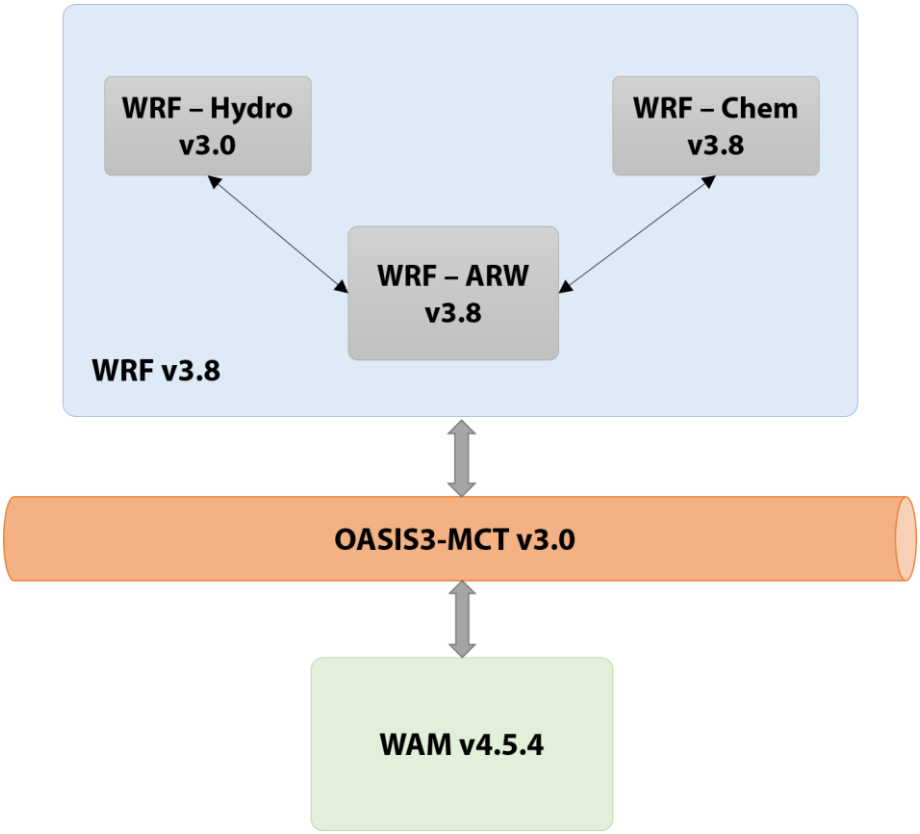

Figure 3.1: The components of the two-way fully coupled system WRF / OASIS3-MCT / WAM (CHAOS).

3.1. The Weather Research and Forecasting Model WRF

The Weather Research and Forecasting (WRF) model is a numerical weather prediction (NWP) and atmospheric simulation system designed for both research and operational applications (Skamarock et al., 2008). WRF is supported as a common tool for the university/research and operational communities to promote closer ties between them and to address the needs of both. WRF reflects flexible, "state-of-the-art", portable code that is efficient in computing environments ranging from massively-parallel supercomputers to laptops. Its modular, single-source code can be configured for both research and operational applications. Its spectrum of

physics and dynamics options reflects the experience and input of the broad scientific community.

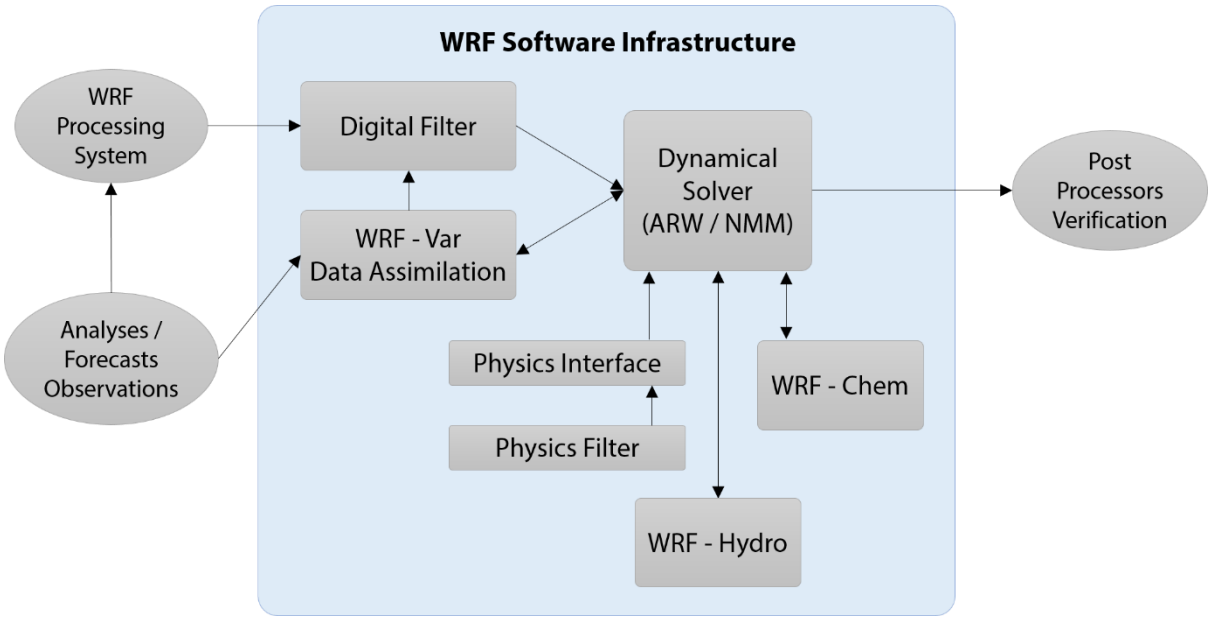

Figure 3.2: WRF system components diagram (based on the original diagram, Skamarock et al., 2008).

The principal components of the WRF system are depicted in Figure 3.2. The WRF Software Framework (WSF) provides the infrastructure that accommodates the dynamics solvers, physics packages that interface with the solvers, programs for initialization, WRF-Var, WRF-Chem and WRF-Hydro. There are two dynamics solvers in the WSF: the Advanced Research WRF (ARW) solver and the Non-hydrostatic Mesoscale Model (NMM) solver. WRF-Var variational data assimilation system can ingest a host of observation types in pursuit of optimal initial conditions, while WRF-Chem provides a capability for air chemistry modeling (Grell et al., 2005). Additionally, WRF is coupled (offline or online) with the hydrological model WRF-Hydro to resolve soil and hydrological processes (Gochis et al., 2015).

WRF is maintained and supported as a community model to facilitate wide use internationally, for research, operations and teaching. It is suitable for a broad span of applications across scales ranging from large-eddy to global simulations. Such applications include real-time NWP, data assimilation development and studies, parameterized-physics research, regional climate simulations, air quality modeling, atmosphere-ocean coupling, and idealized simulations. The number of registered WRF users exceeds 6000, and WRF is in operational and research use around the world.

The ARW solver is a subset of the WRF modeling system that encompasses physics schemes, numerics/dynamics options, initialization routines, and the data assimilation package (WRF-Var). Physics packages are largely shared by both the ARW and NMM solvers, although specific compatibility varies with the schemes considered. The majority of WRF components, such as WRF-Var, WRF-Chem and WRF-Hydro, mainly operate with the ARW solver. The major characteristics of the ARW system (Version 3) are presented in Table 3.1.

Table 3.1: Major Characteristics of WRF-ARW System version 3

ARW Solver	
Equations	Fully compressible, Euler non-hydrostatic with a run-time hydrostatic option available. Conservative for scalar variables.
Prognostic Variables	Velocity components u and v in Cartesian coordinate, vertical velocity w, perturbation potential temperature, perturbation geopotential, and perturbation surface pressure of dry air. Optionally, turbulent kinetic energy and any number of scalars such as water vapor mixing ratio, rain/snow mixing ratio, cloud water/ice mixing ratio, and chemical species and tracers.
Vertical Coordinate	Terrain-following, dry hydrostatic-pressure with vertical grid stretching permitted. Top of the model is a constant pressure surface.
Horizontal Grid	Arakawa C-grid staggering
Time Integration	Time-split integration using a 2nd- or 3rd-order Runge-Kutta scheme with smaller time step for acoustic and gravity-wave modes Variable time step capability
Spatial Discretization	2nd- to 6th-order advection options in horizontal and vertical
Turbulent Mixing and Model Filters	Sub-grid scale turbulence formulation in both coordinate and physical space. Divergence damping, external-mode filtering, vertically implicit acoustic step off-centering. Explicit filter option.
Initial Conditions	Three dimensional for real-data, and one-, two- and three-dimensional for idealized data. Digital filtering initialization (DFI) capability available (real-data cases).
Lateral Boundary Conditions	Periodic, open, symmetric, and specified options available. • Top Boundary Conditions: Gravity wave absorbing (diffusion, Rayleigh damping, or implicit Rayleigh damping for vertical velocity). Constant pressure level at top boundary along a material surface. Rigid lid option.
Bottom Boundary Conditions	Physical or free-slip
Earth's Rotation	Full Coriolis terms included
Mapping to Sphere	Four map projections are supported for real-data simulation: polar stereographic, Lambert conformal, Mercator, and latitude-longitude (allowing rotated pole). Curvature terms included.
Nesting	One-way interactive, two-way interactive, and moving nests. Multiple levels and integer ratios.
Nudging	Grid (analysis) and observation nudging capabilities available
Global Grid	Global simulation capability using polar Fourier filter and periodic east-west conditions

Model Physics	
Microphysics	Schemes ranging from simplified physics suitable for idealized studies to sophisticated mixed-phase physics suitable for process studies and NWP
Cumulus Parameterizations	Adjustment and mass-flux schemes for mesoscale modeling
Surface Physics	Multi-layer land surface models ranging from a simple thermal model to full vegetation and soil moisture models, including snow cover and sea ice
Planetary Boundary Layer Physics	Turbulent kinetic energy prediction or non-local K schemes
Atmospheric Radiation Physics	Longwave and shortwave schemes with multiple spectral bands and a simple shortwave scheme suitable for climate and weather applications. Cloud effects and surface fluxes are included

WRF-Chem	
Coupling Mode	Online (or "inline") model, in which the model is consistent with all conservative transport done by the meteorology model.
Dry deposition	Coupled with the soil/vegetation scheme
Aqueous Phase Chemistry	Coupled to some of the microphysics and aerosol schemes
Biogenic Emissions Options	- No biogenic emissions - Online calculation of biogenic emissions - Online modification of user specified biogenic emissions (e.g., EPA Biogenic Emissions Inventory System (BEIS)).
Anthropogenic Emissions Options	- No anthropogenic emissions - User-specified anthropogenic emissions.
Gas-phase Chemical Reaction Calculations	- RADM2 chemical mechanism - CBM-Z mechanism - Additional options through the use of the Kinetic Pre-Processor (KPP).
Photolysis Schemes	- Madronich scheme coupled with hydrometeors, aerosols, and convective parameterizations; - Fast-J Photolysis scheme coupled with hydrometeors, aerosols, and convective parameterizations - FTUV scheme coupled with hydrometeors, aerosols, and convective parameterizations.
Aerosol Schemes	- The Modal Aerosol Dynamics Model for Europe (MADE/SORGAM); - Model for Simulating Aerosol Interactions and Chemistry (MOSAIC) - The GOCART aerosol model (experimental)

WRF-Hydro	
Parallelization	The code has also been parallelized for distributed memory, parallel computing applications
Coupling Mode	Online or offline coupling with WRF-ARW. Additionally, it is offline coupled with other models through meteorological forcing data
Online Coupling Method	The online coupling between WRF-ARW and WRF-Hydro is based on a coupler including MPI subroutines
Land Soil Models options	Noah, Noah-MP, CLM, NASA LIS
Routing	Surface overland flow routing, channel routing, subsurface routing, lake/reservoir routing

Prominent Capabilities	Fully coupled land surface hydrology-regional atmospheric modeling capability for use in hydrometeorological and hydroclimatological research and applications

WRF Software Framework	
Maintainability	Highly modular, single-source code
Decomposition	Two-level domain decomposition for parallel and shared-memory generality
Portability	- Portable across a range of available computing platforms. - Efficient execution on a range of computing platforms (distributed and shared memory, vector and scalar types). - Support for accelerators (e.g., GPUs).
Versatility	- Support for multiple dynamics solvers and physics modules. - Separation of scientific codes from parallelization and other architecture-specific issues.
Input / Output API	Application Program Interface enabling various external packages to be installed with WRF, thus allowing WRF to easily support various data formats.
Interoperability	Use of Earth System Modeling Framework (ESMF) and interoperable as an ESMF component.
Model coupling API	Model coupling API enabling WRF to be coupled with other models such as ocean, and land models using ESMF, OASIS, MCT, or MCEL.

3.1.1. Vertical Coordinate and Variables

The WRF-ARW model uses a semi-staggered Arakawa C grid (Skamarock et al., 2008) on which the wind grid points are not the same as the mass grid points (Figure 3.3). Additionally, this grid is non-rectangular as the number of points on x axis is not constant with respect to y axis.

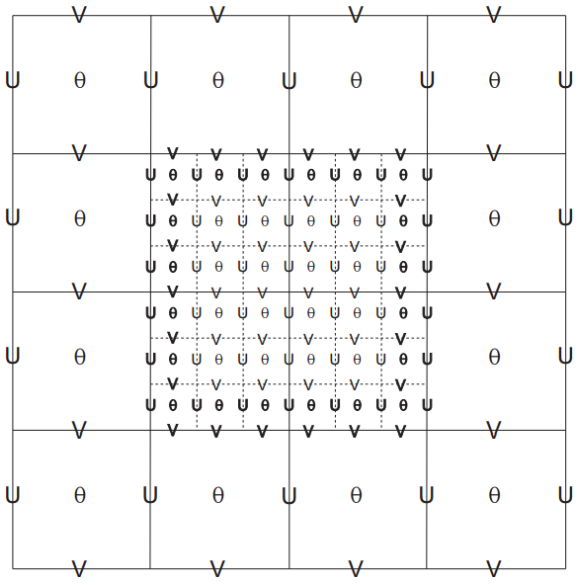

Figure 3.3: Arakawa-C grid staggering for a portion of a parent domain and an embedded nest domain with a 3:1 grid size ratio. The solid lines denote coarse grid cell boundaries, and the dashed lines are the boundaries for each fine grid cell. The horizontal components of velocity ($\boldsymbol{U}$ and $\boldsymbol{V}$) are defined along the normal cell face, and the thermodynamic variables ($\boldsymbol{\theta}$) are defined at the center of the grid cell (each square). The bold typeface variables along the interface between the coarse and the fine grid define the locations where the specified lateral boundaries for the nest are in effect (Skamarock et al., 2008).

The WRF-ARW equations are formulated using a terrain-following hydrostatic-pressure vertical coordinate denoted by η and defined as:

$$\eta = (p_h - p_{ht})/\mu \quad \text{where } \mu = p_{hs} - p_{ht} \qquad (3.1)$$

where

p_h the hydrostatic component of the pressure,

p_{hs} the pressure value along the surface boundary,

p_{ht} the pressure value along the top boundary.

The coordinate definition (3.1), proposed by Laprise (1992), is the traditional σ coordinate used in many hydrostatic atmospheric models. η varies from a value of 1 at the surface to 0 at the upper boundary of the model domain (Figure 3.4). This vertical coordinate is also called a mass vertical coordinate.

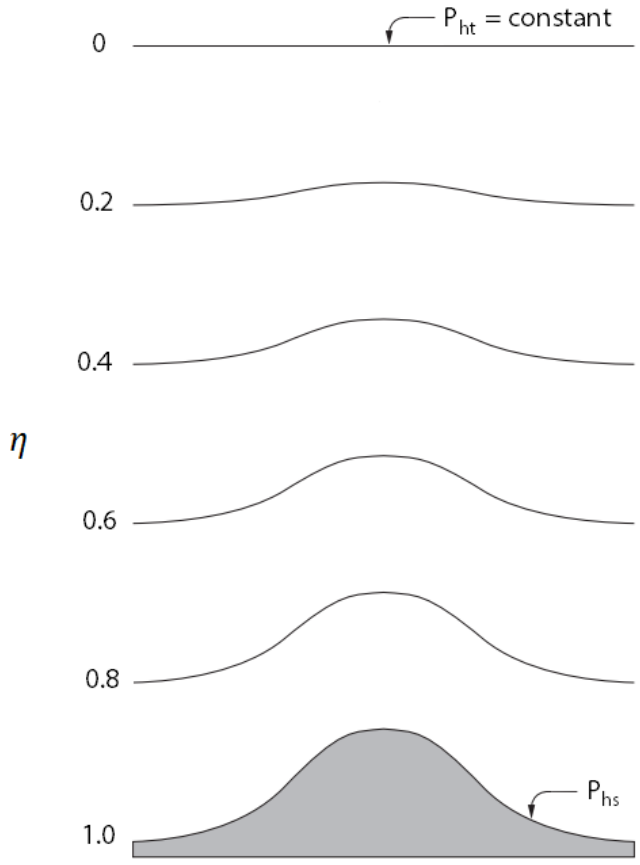

Figure 3.4: ARW vertical coordinate η

Since $\mu(x, y)$ represents the mass per unit area within the column in the model domain at point (x, y), the appropriate flux form variables are:

$$\vec{V} = \mu\vec{v} = (U, V, W), \quad \Omega = \mu\dot{\eta}, \quad \Theta = \mu\theta \tag{3.2}$$

where

$\vec{v} = (u, v, w)$ the covariant velocities in the two horizontal and vertical directions,

$\omega = \dot{\eta}$ the contravariant vertical velocity,

θ the potential temperature.

3.1.2. Flux-Form Euler Equations

Using the variables defined above, the flux-form Euler equations which represent the conservation of mass (continuity), and balance of momentum and energy can be written as:

$$\partial_t U + \left(\vec{\nabla} \cdot \vec{V}u\right) - \partial_x\left(p\varphi_\eta\right) + \partial_\eta(p\varphi_x) = F_U \tag{3.3}$$

$$\partial_t V + \left(\vec{\nabla} \cdot \vec{V}v\right) - \partial_y\left(p\varphi_\eta\right) + \partial_\eta\left(p\varphi_y\right) = F_V \tag{3.4}$$

$$\partial_t W + \left(\vec{\nabla} \cdot \vec{V}w\right) - g\left(\partial_\eta p - \mu\right) = F_W \tag{3.5}$$

$$\partial_t \Theta + \left(\vec{\nabla} \cdot \vec{V}\theta\right) = F_\Theta \tag{3.6}$$

$$\partial_t \mu + \left(\vec{\nabla} \cdot \vec{V}\right) = 0 \tag{3.7}$$

$$\partial_t \varphi + \mu^{-1}\left[\left(\vec{\nabla} \cdot \vec{V}\varphi\right) - gW\right] = 0 \tag{3.8}$$

along with the diagnostic relation for the inverse density:

$$\partial_\eta \varphi = -\alpha\mu \tag{3.9}$$

and the equation of state:

$$p = p_0\left(\frac{R_d\theta}{p_0 a}\right)^\gamma \tag{3.10}$$

where

$\varphi = gz$ the geopotential,

p the pressure,

$\alpha = 1/\rho$ the specific volume, or the inverse density.

In (3.3) - (3.10), the subscripts x, y and η denote differentiation

$$\vec{\nabla} \cdot \vec{V}a = \partial_x(Ua) + \partial_y(Va) + \partial_\eta(\Omega\alpha) \tag{3.11}$$

and

$$\vec{V} \cdot \vec{\nabla}a = U\partial_x a + V\partial_y a + \Omega\partial_\eta\alpha \tag{3.12}$$

where

a represents a generic variable,

$\gamma = c_p/c_v = 1.4$ the ratio of the heat capacities for dry air

R_d the gas constant for dry air

p_0 is a reference pressure (typically 10^5 Pascals) and

F_U, F_V, F_W and F_Θ represent forcing terms arising from model physics, turbulent mixing, spherical projections, and the earth's rotation.

The prognostic equations (3.3) – (3.8) are cast in conservative form except for (3.8) which is the material derivative of the definition of the geopotential. Equation (3.8) could be cast in flux form however, there is no advantage in doing so since $\mu\varphi$ is not a conserved quantity. Another option would be to use a prognostic pressure equation in place of (3.8) [Laprise, 1992], but pressure is not a conserved variable while a pressure equation cannot be used together with the conservation equation for Θ (3.6) as they are linearly dependent. Additionally, prognostic pressure equations have the disadvantage of possessing a mass divergence term multiplied by a large coefficient (proportional to the sound speed) which makes spatial and temporal discretization problematic. It should be noted that the relation for the hydrostatic balance (3.9) does not represent a constraint on the solution, rather it is a diagnostic relation that formally is part of the coordinate definition. In the hydrostatic counterpart to the non-hydrostatic equations, (3.9) replaces the vertical momentum equation (3.5) and it becomes a constraint on the solution.

In order to formulate the moist Euler equations, the coupling of dry air mass to the prognostic variables and the conservation equation for dry air (3.7) are retained, as opposed to coupling the variables to the full (moist) air mass and hence introducing source terms in the mass conservation equation (3.7). Additionally, the coordinate is defined with respect to the dry-air mass. Based on these principles, the vertical coordinate can be written as:

$$\eta = \frac{p_{dh} - p_{dht}}{\mu_d} \qquad (3.13)$$

where

μ_d the mass of the dry air in the column,

p_{dh} the hydrostatic pressure of the dry atmosphere,

p_{dht} the hydrostatic pressure at the top of the dry atmosphere.

The coupled variables are defined as:

$$\vec{V} = \mu_d \vec{v}, \quad \Omega = \mu_d \dot{\eta}, \quad \Theta = \mu_d \theta \tag{3.14}$$

Based on these definitions, the moist Euler equations can be written as:

$$\partial_t U + \left(\vec{\nabla} \cdot \vec{V} u\right) + \mu_d a \partial_x p + \frac{a}{a_d} \partial_\eta p \partial_x \varphi = F_U \tag{3.15}$$

$$\partial_t V + \left(\vec{\nabla} \cdot \vec{V} v\right) + \mu_d a \partial_y p + \frac{a}{a_d} \partial_\eta p \partial_y \varphi = F_V \tag{3.16}$$

$$\partial_t W + \left(\vec{\nabla} \cdot \vec{V} w\right) - g\left(\frac{a}{a_d} \partial_\eta p - \mu_d\right) = F_W \tag{3.17}$$

$$\partial_t \Theta + \left(\vec{\nabla} \cdot \vec{V} \theta\right) = F_\Theta \tag{3.18}$$

$$\partial_t \mu_d + \left(\vec{\nabla} \cdot \vec{V}\right) = 0 \tag{3.19}$$

$$\partial_t \varphi + \mu^{-1}\left[\left(\vec{\nabla} \cdot \vec{V} \varphi\right) - gW\right] = 0 \tag{3.20}$$

$$\partial_t Q_m + \left(\vec{\nabla} \cdot \vec{V} q_m\right) = F_{Q_m} \tag{3.21}$$

with the diagnostic equation for the dry inverse density:

$$\partial_\eta \varphi = -a_d \mu_d \tag{3.22}$$

and the diagnostic relation for the full pressure (vapor plus dry air):

$$p = p_0 \left(\frac{R_d \theta_m}{p_0 a_d}\right)^\gamma \tag{3.23}$$

where

$a_d = 1/\rho_d$ the inverse density of the dry air,

$a = a_d(1 + q_v + q_c + q_r + q_i + \cdots)^{-1}$ the inverse density taking into account the full parcel density,

q_* the mixing ratios (mass per mass of dry air) for water vapor, cloud, rain, ice, etc.,

$\theta_m = \theta\left(1 + \frac{R_v}{R_d} q_v\right) \approx \theta(1 + 1.61 q_v)$

$Q_m = \mu_d q_m, \quad q_m = q_v, q_c, q_i, \ldots.$

3.2. The Ocean Wave Model (WAM)

The global ocean wave prediction model called WAM was the first 3rd-generation wave model and it was conceived by the Wave Model Development and Implementation group (WAMDI, 1988). The WAM solves the wave transport equation explicitly without any presumptions on the shape of the wave spectrum (Gunther et al., 1992). It represents the physics of the wave evolution in accordance with our knowledge today for the full set of degrees of freedom of a 2d wave spectrum. In general, the model runs for any given regional or global grid with a pre-

scribed topographic dataset. The grid resolution can be arbitrary in space and time. The propagation can be done on a latitudinal-longitudinal or on a Cartesian grid. The model outputs the significant wave height, mean wave direction and frequency, the swell wave height and mean direction, wind stress fields corrected by including the wave induces stress and the drag coefficient at each grid point at chosen output times, and also the 2d wave spectrum at chosen grid points and output times.

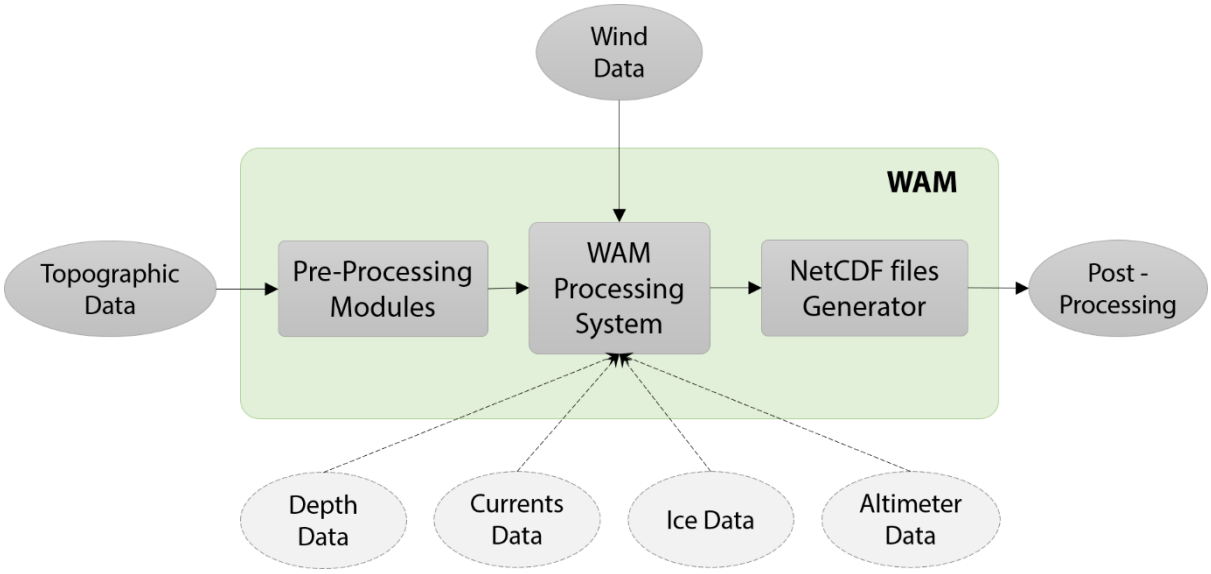

Figure 3.5: WAM system components.

Within the last approximately thirty years, the WAM wave prediction model has become a standard tool for operational wave prediction as well as for research and engineering application. The model is widely distributed and used at about 150 institutions. The code distribution has created a large user community with a wide range of applications for the model. The availability of high-speed computers and the increasing demands for wave prediction products have led to this large user community of the model code. Quality of wave analysis and forecast continuously improved, mainly due to a much better quality of the forcing wind fields. Only minor changes have been introduced into the model itself. This is a clear indication, that the approach taken approximately thirty years ago by the WAMDI (1988) group has been very successful.

Nowadays, WAM Cycle 4.5 (version 4.5.4) is an update of the WAM Cycle 4 wave model, which is described in Gunther et al. (1992) and Komen et al. (1994). The basic physics and numerics are kept in this new release. The source function integration scheme made by Hersbach and Janssen (1999) and the revised wave model dissipation source function of Bidlot et al. (2007) and Janssen (2008) are incorporated in this version. The other main improvements introduced

in WAM version 4.5.4 are technical improvements which take into account the new possibilities of Fortran 90 and parallel programming. Detailed descriptions of its dynamics, physics and technical characteristics can be found in several studies (e.g. WAMDI, 1988; IFS Documentation, 2013; Komen et al., 1994). Figure 3.5 and Table 3.2 describe WAM version 4.5.4 system components, the input data (wind, bathymetry etc), the output data (NetCDF capability) and the modeling capabilities (deep or shallow water approximation, cold or hot start etc).

It is noteworthy that, the WAM model is used at the European Centre for Medium-Range Weather Forecasts (ECMWF) as the operational wave model. It is tightly coupled to the local Integrated Forecasting System (IFS Documentation 2013). The theoretical basis of the model established at the ECMWF by Janssen (1989, 1991) is described below.

Table 3.2: Major Features of WAM System version 4.5.4

WAM	
Water approximation	Shallow or deep water approximation
Initialization	Cold or hot start capability
Topographic data	Choice of static or updated bathymetry
Wind input data	Winds at 10 meters above sea surface or surface stresses or friction velocities
Propagation	Cartesian or spherical propagation
Nesting	Nesting capability calculating the boundary spectra for a fine grid model run
Shallow water capabilities	Depth refraction and depth induced wave breaking capabilities
Sea-ice	Sea-ice update option
Currents	Currents update and current refraction capability
Data assimilation	Option for assimilation of altimeter data
Time interpolation	Time interpolation of winds, currents, water depth, and ice fields or no time interpolation
Output	Model output at regular intervals or by list. Printer and/or file output of individually selected parameters. Output variables. Output sites for spectra
NetCDF	Creation of NetCDF output files for easier post-processing

3.2.1. Basic Transport Equation

Let x_1 and x_2 be the spatial coordinates, k_1 and k_2 the wave coordinates and let

$$\mathrm{z} = (x_1, x_2\,, k_1, k_2\,) \qquad (3.24)$$

be their combined four-dimensional vector. The most elegant formulation of the "energy" balance equation is in terms of the action density spectrum N which is the energy spectrum divided by the so-called intrinsic frequency σ. The action density plays the same role as the particle density in quantum mechanics. Hence there is an analogy between wave groups and particles, because wave groups with action N have energy σN and momentum kN. Thus, the most fundamental form of the transport equation for the action density spectrum $N(\mathrm{k},\mathrm{x},t)$ without the source term can be written in the flux form

$$\frac{\partial}{\partial t}N + \frac{\partial}{\partial z_i}(\dot{z}_i N) = 0 \qquad (3.25)$$

where $\dot{\mathrm{z}}$ denotes the propagation velocity of a wave group in the four-dimensional phase space of x and k. This equation holds for any field $\dot{\mathrm{z}}$, and also for velocity fields which are not divergence-free in four-dimensional phase space. In the special case when x and k represent a canonical vector pair – this is the case, for example, when they are the usual Cartesian coordinates – the propagation equations for a wave group (also known as the Hamilton–Jacobi propagation equations) are:

$$\dot{x}_i = \frac{\partial}{\partial k_i}\Omega \qquad (3.26)$$

$$\dot{k}_i = -\frac{\partial}{\partial x_i}\Omega \qquad (3.27)$$

where Ω denotes the dispersion relation

$$\omega = \Omega(\mathrm{k},\mathrm{x},t) = \sigma + \mathrm{k}\cdot\mathrm{U} \qquad (3.28)$$

with σ the so-called intrinsic frequency

$$\sigma = \sqrt{gk\tanh kh} \qquad (3.29)$$

where the depth $h(\mathrm{x},t)$ and the current $\mathrm{U}(\mathrm{x},t)$ may be slowly-varying functions of x and t. The Hamilton-Jacobi equations have some interesting consequences. First of all, (3.26) just introduces the group speed $\partial\Omega/\partial k_i$ while (3.27) expresses conservation of the number of wave crests. Secondly, the transport equation for the action density may be expressed in the advection form

$$\frac{\mathrm{d}}{\mathrm{d}t}N = \frac{\partial N}{\partial t} + \dot{z}_i\frac{\partial}{\partial z_i}N = 0 \qquad (3.30)$$

because, due to (3.26) and (3.27), the field $\dot{\mathrm{z}}$ for a continuous ensemble of wave groups is divergence-free in four-dimensional phase space so:

$$\dot{z}_i \frac{\partial}{\partial z_i} = 0 \qquad (3.31)$$

Thus, along a path in four-dimensional phase space defined by the Hamilton–Jacobi equations (3.26) and (3.27), the action density N is conserved. This property only holds for canonical coordinates for which the flow divergence vanishes (Liouville's theorem – first applied to wave spectra by Dorrestein [1960]). Thirdly, the analogy between Hamilton's formalism of particles with Hamiltonian H and wave groups obeying the Hamilton–Jacobi equations should be pointed out. Indeed, wave groups may be regarded as particles and the Hamiltonian H and angular frequency Ω play similar roles. Because of this similarity Ω is expected to be conserved as well (under the restriction that Ω does not depend on time). This can be verified by direct calculation of the rate of change of Ω following the path of a wave group in phase space

$$\frac{\mathrm{d}}{\mathrm{d}t}\Omega = \dot{z}_i \frac{\partial}{\partial z_i}\Omega = \dot{x}_i \frac{\partial}{\partial x_i}\Omega + \dot{k}_i \frac{\partial}{\partial k_i}\Omega = 0 \qquad (3.32)$$

The vanishing of $\mathrm{d}\Omega/\mathrm{d}t$ follows at once upon using the HamiltonJacobi equations (3.26) and (3.27). Note that the restriction of no time dependence of Ω is essential for the validity of (3.32), just as the Hamiltonian H is only conserved when it does not depend on time t. The property (3.32) will play an important role in the description of refraction.

Moving on to the spherical coordinates, when one transforms from one set of coordinates to another there is no guarantee that the flow remains divergence-free. However, noting that (2.2) holds for any rectangular coordinate system, the generalization of the standard Cartesian geometry transport equation to spherical geometry is straightforward (Groves and Melcer [1961]; WAMDI Group [1988]). To that end let us consider the spectral action density $\widehat{N}(\omega, \theta, \varphi, \lambda, t)$ with respect to angular frequency ω and direction θ (measured clockwise relative to true north) as a function of latitude φ and longitude λ. The reason for the choice of frequency as the independent variable is that for a fixed topography and current the frequency Ω is conserved when following a wave group; therefore, the transport equation is simplified. In general, the conservation equation for $\widehat{N}$ -the action balance equation- thus reads

$$\frac{\partial}{\partial t}\widehat{N} + \frac{\partial}{\partial \varphi}\left(\dot{\varphi}\widehat{N}\right) + \frac{\partial}{\partial \lambda}\left(\dot{\lambda}\widehat{N}\right) + \frac{\partial}{\partial \omega}\left(\dot{\omega}\widehat{N}\right) + \frac{\partial}{\partial \theta}\left(\dot{\theta}\widehat{N}\right) = 0 \qquad (3.33)$$

and since $\dot{\omega} = \partial\Omega/\partial t$ the term involving the derivative with respect to ω drops out in the case of time-independent current and bottom. The action density $\widehat{N}$ is related to the normal spectral

density N with respect to a local Cartesian frame (x, y) through $\widehat{N}\mathrm{d}\omega\mathrm{d}\theta\mathrm{d}\varphi\mathrm{d}\lambda = N\mathrm{d}\omega\mathrm{d}\theta\mathrm{d}x\mathrm{d}y$, or

$$\widehat{N} = NR^2\cos\varphi \tag{3.34}$$

where R is the radius of the earth. Substitution of (3.34) into (3.33) yields

$$\frac{\partial}{\partial t}N + (\cos\varphi)^{-1}\frac{\partial}{\partial\varphi}(\dot{\varphi}\cos\varphi N) + \frac{\partial}{\partial\lambda}(\dot{\lambda}N) + \frac{\partial}{\partial\omega}(\dot{\omega}N) + \frac{\partial}{\partial\theta}(\dot{\theta}N) = 0 \tag{3.35}$$

If c_g the magnitude of the group velocity

$$\dot{\varphi} = \left(c_g\cos\theta - \mathrm{U}|_{\mathrm{north}}\right)R^{-1} \tag{3.36}$$

$$\dot{\lambda} = \left(c_g\sin\theta - \mathrm{U}|_{\mathrm{east}}\right)(R\cos\varphi)^{-1} \tag{3.37}$$

$$\dot{\theta} = c_g\sin\theta\tan\varphi\,R^{-1} + \left(\dot{\mathrm{k}}\times\mathrm{k}\right)k^{-2} \tag{3.38}$$

$$\dot{\omega} = \frac{\partial\Omega}{\partial t} \tag{3.39}$$

represent the rates of change of the position and propagation direction of a wave packet. Equation (3.35) is the basic transport equation used in the numerical wave prediction model. The remainder of this section is devoted to a discussion of some of the properties of this equation. There are some peculiarities presented for the infinite depth case in the absence of currents as well as the special cases of shoaling and refraction due to bottom topography and currents.

3.2.2. Properties of the Basic Transport Equation

- **Great circle propagation on the globe**

Equations (3.36) - (3.39) imply that in spherical coordinates the flow is not divergence-free. Considering the case of no depth refraction and no explicit time dependence, the divergence of the flow becomes:

$$\frac{\partial}{\partial\varphi}\dot{\varphi} + \frac{\partial}{\partial\lambda}\dot{\lambda} + \frac{\partial}{\partial\omega}\dot{\omega} + \frac{\partial}{\partial\theta}\dot{\theta} = c_g\cos\theta\tan\frac{\varphi}{R} \neq 0 \tag{3.40}$$

This expression is non-zero because the wave direction, measured with respect to true north, changes while the wave group propagates over the globe along a great circle. Consequently, wave groups propagate along a great circle. This type of refraction is therefore entirely apparent and only related to the choice of coordinate system.

▪ Shoaling

Moving on to the finite depth effects in the absence of currents by considering some simple topographies, in case of wave shoaling where the wave propagation is parallel to the direction of the depth, gradient depth refraction does not contribute to the rate of change of wave direction $\dot{\theta}$ because, with (3.29), $\dot{\mathrm{k}}\times\mathrm{k}=0$. Additionally, the wave direction θ is considered equal to zero so that the longitude is constant ($\dot{\lambda}=0$) and $\dot{\theta}=0$. For time-independent topography (hence $\partial\Omega/\partial t=0$) the transport equation becomes

$$\frac{\partial}{\partial t}N+(\cos\varphi)^{-1}\frac{\partial}{\partial\varphi}(\dot{\varphi}\cos\varphi N)=0 \qquad (3.41)$$

where

$$\dot{\varphi}=\frac{c_g\cos\theta}{R}=\frac{c_g}{R} \qquad (3.42)$$

and the group speed only depends on latitude φ. Restricting the attention to steady waves the conservation of the action density flux in the latitude direction is

$$\frac{c_g\cos\varphi}{R}N=\mathrm{const} \qquad (3.43)$$

If, in addition, it is assumed that the variation of depth with latitude occurs on a much shorter scale than the variation of $\cos\varphi$ the latter term may be taken constant for present purposes. It is then found that the action density is inversely proportional to the group speed c_g so

$$N\sim\frac{1}{c_g} \qquad (3.44)$$

and if the depth is decreasing for increasing latitude, conservation of flux requires an increase of the action density as the group speed decreases for decreasing depth. This phenomenon, which occurs in coastal areas, is called shoaling. Its most dramatic consequences may be seen when tidal waves, generated by earthquakes, approach the coast resulting in tsunamis. It should be emphasized though, that in the final stages of a tsunami the kinetic description of waves, as presented here, breaks down because of strong nonlinearity.

▪ Refraction

The second example of finite depth effects that examined is refraction. It is again assumed that there are no currents and a time-independent topography. In the steady state the action balance equation becomes:

$$(\cos\varphi)^{-1}\frac{\partial}{\partial\varphi}\left(\frac{c_g}{R}\cos\theta\cos\varphi\,N\right)+\frac{\partial}{\partial\lambda}\left(\frac{c_g\sin\theta}{R\cos\varphi}N\right)+\frac{\partial}{\partial\theta}\left(\dot{\theta}_0 N\right)=0 \qquad (3.45)$$

where

$$\dot{\theta}_0=\left(\sin\theta\frac{\partial}{\partial\varphi}\Omega-\frac{\cos\theta}{\cos\varphi}\frac{\partial}{\partial\lambda}\Omega\right)(kR)^{-1} \qquad (3.46)$$

In principle, (3.45) can be solved by means of the method of characteristics. The details of this are not given, but the role of the $\dot{\theta}_0$ term for the simple case of waves propagating along the shore is pointed out. Consider, therefore, waves propagating in a northerly direction (hence $\theta=0$) parallel to the coast. Suppose that the depth only depends on longitude such that it decreases towards the shore. Since $\partial\Omega/\partial\lambda<0$, the rate of change of wave direction is then positive as:

$$\dot{\theta}_0=-\frac{1}{k\,R\cos\varphi}\frac{\partial}{\partial\lambda}\Omega>0 \qquad (3.47)$$

Therefore, waves which are propagating initially parallel to the coast will turn towards the coast. This illustrates that, in general, wave rays will bend towards shallower water resulting in, for example, focusing phenomena and caustics. In this way a sea mountain plays a similar role for gravity waves as a lens for light waves.

▪ Action balance equation in spherical coordinates

A global, third generation wave model solves the action balance equation in spherical coordinates. By combining previous results of this section, the action balance equation becomes:

$$\frac{\partial}{\partial t}N+(\cos\varphi)^{-1}\frac{\partial}{\partial\varphi}(\dot{\varphi}\cos\varphi N)+\frac{\partial}{\partial\lambda}\left(\dot{\lambda}N\right)+\frac{\partial}{\partial\omega}(\dot{\omega}N)+\frac{\partial}{\partial\theta}\left(\dot{\theta}N\right)=S \qquad (3.48)$$

where

$$\dot{\varphi}=\left(c_g\cos\theta-\mathrm{U}|_{\mathrm{north}}\right)R^{-1} \qquad (3.49)$$

$$\dot{\lambda}=\left(c_g\sin\theta-\mathrm{U}|_{\mathrm{east}}\right)(R\cos\varphi)^{-1} \qquad (3.50)$$

$$\dot{\theta}=c_g\sin\theta\tan\varphi\,R^{-1}+\dot{\theta}_{\mathrm{D}} \qquad (3.51)$$

$$\dot{\omega}=\frac{\partial\Omega}{\partial t} \qquad (3.52)$$

$$\dot{\theta}_{\mathrm{D}}=\left(\sin\theta\frac{\partial}{\partial\varphi}\Omega-\frac{\cos\theta}{\cos\varphi}\frac{\partial}{\partial\lambda}\Omega\right)(kR)^{-1} \qquad (3.53)$$

and Ω is the dispersion relation given in (3.28). The parameterization of the source term S is given by:

$$S = S_{in} + S_{nl} + S_{ds} + S_{bot} \quad (3.54)$$

These terms represent the physics of wind input (S_{in}), wave-wave interactions (S_{nl}), dissipation due to white-capping (S_{ds}), and bottom friction (S_{bot}).

3.3. OASIS3-MCT Coupler

The exchange of information between large software packages running on parallel computers requires efficient management of the communications between them. Consequently, a coupler which distributes the tasks to the thousands of processors is crucial for the execution of the computations and the organization of the communication between the models (Boumediene and Valcke, 2015). OASIS3-MCT coupler is "the-state-of-the-art" of couplers with advanced capabilities in weather and climate modeling. In 1991, Centre Européen de Recherche et de Formation Avancée en Calcul Scientifique (CERFACS) started the development of a software interface to couple existing ocean and atmosphere numerical General Circulation Models (Valcke et al., 2015). The first objective was to couple the ocean General Circulation Model OPA developed by the Laboratoire d'Oceanographie Dynamique et de Climatologie (LODYC) to two different atmospheric General Circulation Models, ARPEGE and LMDz developed by Meteo-France and the Laboratoire de Meteorologie Dynamique (LMD), respectively (Valcke et al., 2013).

The initial period of investigation led to the conclusion that the technical coupling between the oceanic and atmospheric models should take the form of an external coupler, i.e., a coupling library linked to the components, exchanging the coupling data with a separate application performing the regridding of the coupling fields. This approach ensured a minimal level of changes to the existing codes while focusing on modularity and portability. As the coupling was, at this stage, involving only a relatively small number of 2-D coupling fields at the air-sea interface, efficiency was not considered a major criterion.

Today, different versions of OASIS coupler with advanced capabilities are used by about 45 modeling groups all around the world on different computing platforms (Valcke et al., 2013; Valcke et al., 2015). OASIS sustained development is ensured by a collaboration between CERFACS and the Centre National de la Recherche Scientifique (CNRS). The latest version of OASIS, OASIS3-MCT, is interfaced with MCT, the Model Coupling Toolkit2 (Jacob et al., 2005; Larson et al., 2005), developed by the Argonne National Laboratory in the USA and allows a completely parallel exchange of fields and interpolation. MCT implements fully parallel regrid-

ding, as a parallel matrix vector multiplication, and parallel distributed exchanges of the coupling fields, based on pre-computed regridding weights and addresses. Its design philosophy, based on flexibility and minimal invasiveness, is close to the OASIS approach. MCT has proven parallel performance and is, most notably, the underlying coupling software used in National Center for Atmospheric Research Community Earth System Model (NCAR CESM).

OASIS3-MCT is a portable set of Fortran 77, Fortran 90 and C routines. Low-intrusiveness, portability and flexibility are OASIS3-MCT key design concepts. After compilation, OASIS3-MCT is a coupling library to be linked to the component models supporting the interpolation and the exchange of the coupling fields. OASIS3-MCT supports coupling of 2D logically rectangular fields but 3D fields and 1D fields expressed on unstructured grids are also supported using one-dimensional degeneration of the structures. All transformations, including regridding, are performed in parallel on the set of source or target component processes and all coupling exchanges are now executed in parallel directly between the component processes via Message Passing Interface (MPI). OASIS3-MCT also supports file I/O using NetCDF.

The latest version, OASIS3-MCT 3.0, which is employed for the purposes of this thesis, supports coupling exchanges between components deployed in much more diverse configurations than before. It is of course possible to implement coupling exchanges between two components corresponding to two different executables running concurrently on separate sets of tasks, as in the previous versions, but also between two components running concurrently on separate sets of tasks within one same executable, or between different sub-components defined on separate or overlapping sets of tasks within one executable. Additionally, the coupler offers the option to have some or all tasks of a component not participating to the coupling exchanges.

In order to create an interface between a model and OASIS3-MCT, the first stage is to link the libraries of the coupler (psmile, scrip, mct) to the model using the routines specific to each step of the coupling. Figure 3.6 shows a high level illustration of the coupling between two models with OASIS3-MCT.

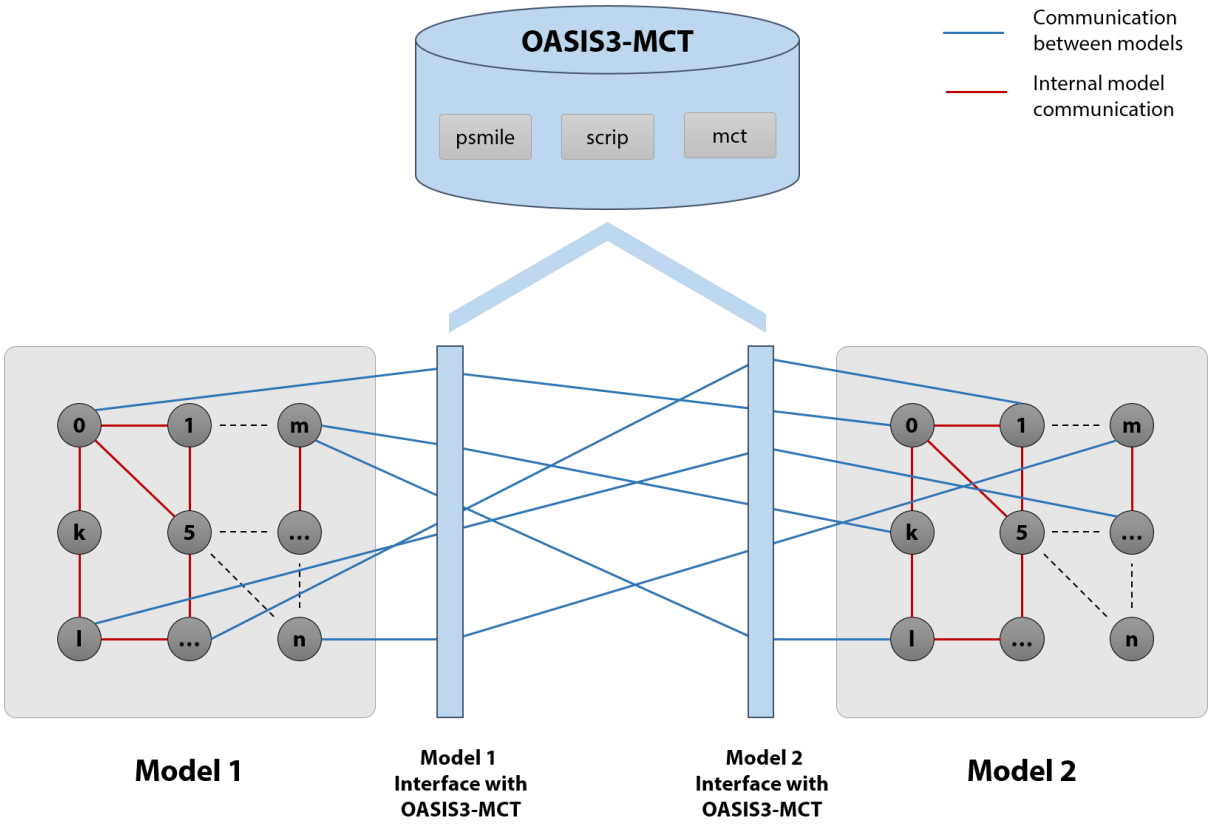

Figure 3.6: Illustration of a coupling system consisted of 2 models through OASIS3-MCT (reconstruction of the original [Boumediene and Valcke, 2015]).

Afterwards, in order for each component (model) to be able to interact with the rest of the coupled system, a number of OASIS3-MCT calls must be implemented in the code of the component:

1. **Initialization**: During this stage, the coupling environment is initialized, creating a local communicator which links the processes participating in the coupling.
2. **Definition of the files containing the longitudes, latitudes and the mask of the grid**: There is the option to choose between generating the grid data files during run time using OASIS3-MCT routines and using data created beforehand by the user.
3. **Definition of the partitioning**: The coupling fields sent or received by a model are usually scattered to the different processes of the model. Using OASIS3-MCT, all processes that exchange coupling data have to declare their local partition in a global grid indexing space. The user has the option to use any of the 5 available partitioning methods: Serial (no partition), Apple partition, Box partition, Orange partition, Points partition.

4. **Definition of coupling fields**: Each model process must declare the fields sent or received during the simulation.
5. **End of the definition phase**: Establishment of the communication schemes between the model processes and generation of the necessary output files (regridding, masks etc.) from the previous steps is performed at this stage, as well as an overall synchronization between all the processes before starting the data exchange.
6. **Data exchange**: In the temporal loop of the model, each process sends and/or receives its share of the coupled fields.
7. **Finalization**: All processes must call the specific routine to ensure a normal termination of the coupling.

Chapter 4

Development Stages of the New Atmosphere – Ocean Wave Coupled System

4.1. Design and Implementation of the System

4.1.1. Design of the system

WRF and WAM models utilize different domain projections, integration time step, grid geometry, and cell size. Therefore, in order to enable the two models to operate in two-way coupled mode, major effort has been undertaken in order to homogenize, synchronize and handle the data exchange between the atmospheric and the ocean wave components of the system.

The implementation of the coupled system CHAOS was essentially consisted of three parts as shown in Figure 4.1. In more detail:

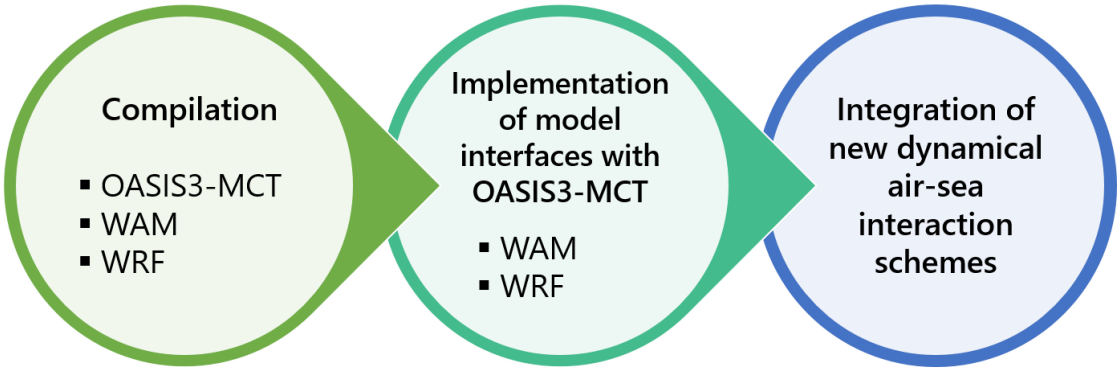

Figure 4.1: The workflow for the implementation of the two-way fully coupled system WRF / OASIS3-MCT / WAM (CHAOS)

1. **Compilation of OASIS3-MCT, WRF and WAM**

The first step was the compilation of OASIS3-MCT coupler which produces the respective libraries and object files. Afterwards, WRF and WAM models were compiled including the libraries and object files of OASIS3-MCT.

2. **Implementation of the interfaces between WAM and OASIS3-MCT as well as WRF and OASIS3-MCT**

The next stage of the coupling was the development of the WAM-OASIS3-MCT interface which enables WAM to exchange information with OASIS3-MCT. The details of this implementation stages are presented in the Appendix.

WRF receives the Charnock parameter, the wave age, the significant wave height, the phase velocity at the peak of wave spectrum, the friction velocity and the roughness length calculated by WAM. On the other hand, WAM receives the U and V components of wind at 10 meters produced by WRF. Figure 4.2 illustrates the information exchanges taking place through OASIS3-MCT.

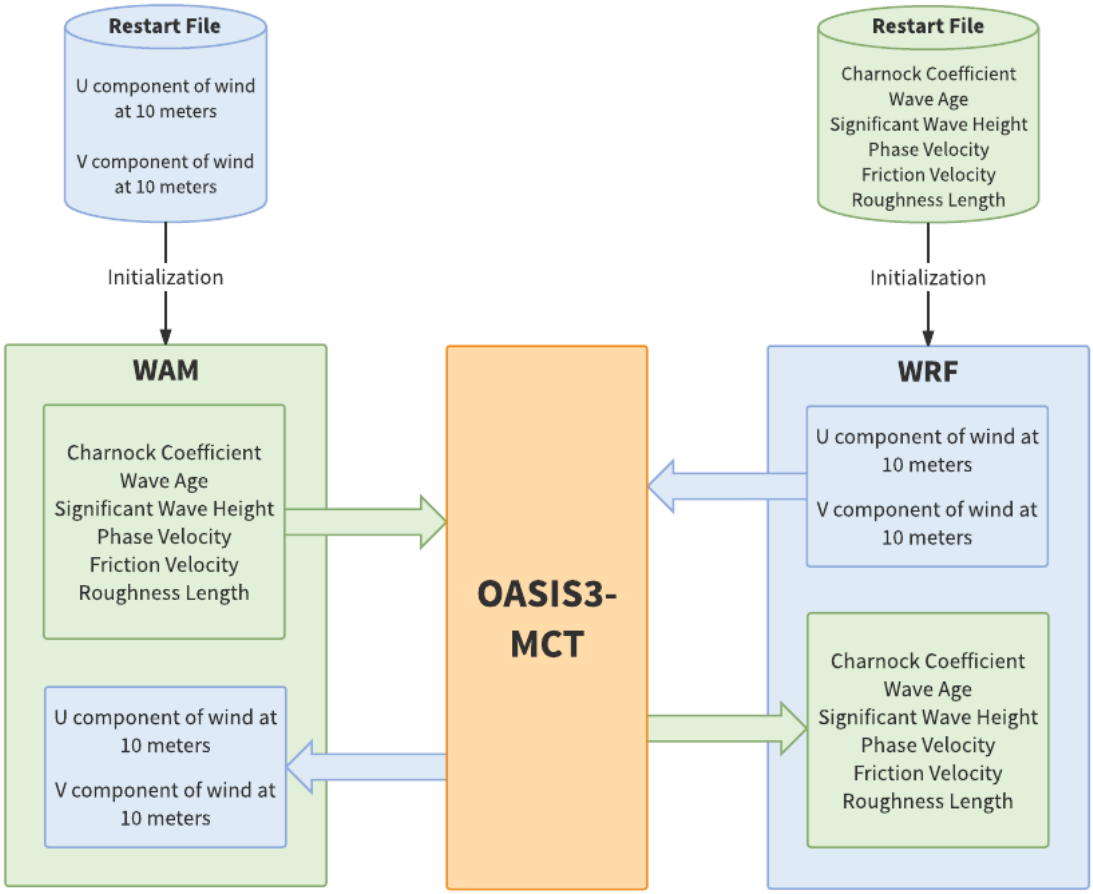

Figure 4.2: Illustration of the fields exchanged between WRF and WAM in CHAOS.

4.1.2. Integration of air-ocean wave parameterization schemes in CHAOS surface layer

In Section 2.3 the theoretical background of a modified surface layer including some of the most advanced parameterizations schemes of dynamical air-sea interaction used by numerical models was discussed. At this stage of the implementation, the parameterization schemes were embedded into CHAOS to refine the simulation and analysis of the air-sea interaction. In the following paragraphs, the implementation stages of the most important parameterization schemes which are used in this thesis will be presented. In particular, the parameterizations

schemes proposed by Donelan (1990), Drennan et al. (2003, 2005), and Taylor and Yelland (2001) will not presented, although CHAOS incorporates them. During the initial assessment, these schemes exhibited the worst performance among the others and, thus, they are not further investigated.

The parameterization schemes are introduced in WRF, in order to estimate the roughness length (z_0) based on equation (2.21)

$$z_0 = \frac{a u_*^2}{g} + \frac{0.11 v_a}{u_*}$$

using the sea state information calculated by WAM. It should be noted that, even though CHAOS supports the exchange of roughness length z_0 and friction velocity u_* calculated by WAM to WRF, the coupling configuration using Charnock parameter a is preferable. The calculation of roughness length z_0 and friction velocity u_* in WRF includes more realistic representation of the physical mechanisms of viscous sublayer and atmospheric stability which are not resolved in the respective calculation in WAM. The details of the integration of each approach are presented below employing WRF friction velocity u_* and calculating Charnock parameter a using the sea state information retrieved by WAM.

- **Janssen's Scheme (1991)**

The description of the dimensionless Charnock parameter α suggested by Janssen (1991) is not constant and depends on the sea state through the wave-induced stress (τ_w) and the total stress (τ) over the air-sea interface:

$$\alpha = a_J = \frac{0.01}{\sqrt{1 - \frac{\tau_w}{\tau}}}$$

The Charnock parameter α was not being calculated in WAM and, thus, the above calculation was incorporated into WAM. The resulting Charrnock parameter α is sent to WRF as part of the coupling process.

- **Smith's Scheme (1992)**

Smith et al. (1992) suggested an alternative, empirical formulation for the Charnock parameter using wave age (z_a):

$$\alpha = a_S = \frac{0.48}{z_a}$$

As the calculation wave age is not part of the original WAM configuration, it is introduced using the formulations described in Section 2.3 [equations (2.23), (2.25)].

- **Liu's Scheme (2011)**

Liu et al. (2011) proposed a parameterization of sea surface roughness dependent on wave age and wind-induced wave breaking accompanied by sea spray production, yielding a modified formula for the Charnock parameter:

$$\alpha = a_L = \begin{cases} \left(0.085{z_a}^{3/2}\right)^{1-(1/b)}[0.03z_a \exp(-0.14z_a)]^{1/b}, & \sim 0.35 < z_a < 35 \\ 17.60^{1-(1/b)}\ 0.008^{1/b}, & z_a \geq 35 \end{cases}$$

where the correction parameter b is calculated as

$$b = \min\left(1, \frac{0.64}{0.4\ u_*}\right)$$

- **Rain-Wave Interaction Scheme (Kumar et al., 2009)**

Kumar et al. (2009) added a rain-induced factor to the roughness length produced by wind blowing over sea surface. The surface roughness connecting rain intensity, terminal velocity of raindrop and drop diameter from equations (2.43), (2.44) and (2.45) is calculated by:

$$Z_r = \frac{1.5\times10^{-4} I {V_r}^2 D}{g v_w}$$

The total roughness length in WRF adding the above term along with the equations (2.21) is expressed as:

$$z_0 = \frac{a u_*^2}{g} + \frac{0.11 v_a}{u_*} + Z_r$$

including the impact of surface waves, smooth surface and rain on the aerodynamic roughness of surface layer. The term $a u_*^2/g$ is calculated using any of the abovementioned parameterizations. In the current version of CHAOS precipitation rate calculated by the atmospheric component is used as rain intensity I while predefined values are used for terminal velocity of raindrop V_r and raindrop diameter D. The precipitation rate is different for shallow and deep convection as well as for stratiform conditions. For deep and shallow convection, terminal velocity of raindrop and raindrop diameter are set equal to 5 m s^{-1} and 1 mm respectively whereas for stratiform precipitation the corresponding values are $V_r = 3\ \mathrm{m\ s^{-1}}$ and $D = 0.5\ \mathrm{mm}$ (Salles and Creutin, 2003; Tokay et al., 2008; Niu et al., 2010). The kinematic viscosity of water

was set equal to 1.051×10^{-6} which corresponds to a mean water temperature equal to 20 K as proposed by Partanen et al. (2014) using the parameterization of Sharqawy et al. (2010) with constant water salinity of 35 g kg^{-1}. An overview of the computations in CHAOS's surface layer parameterization schemes described above is illustrated in Figure 4.3.

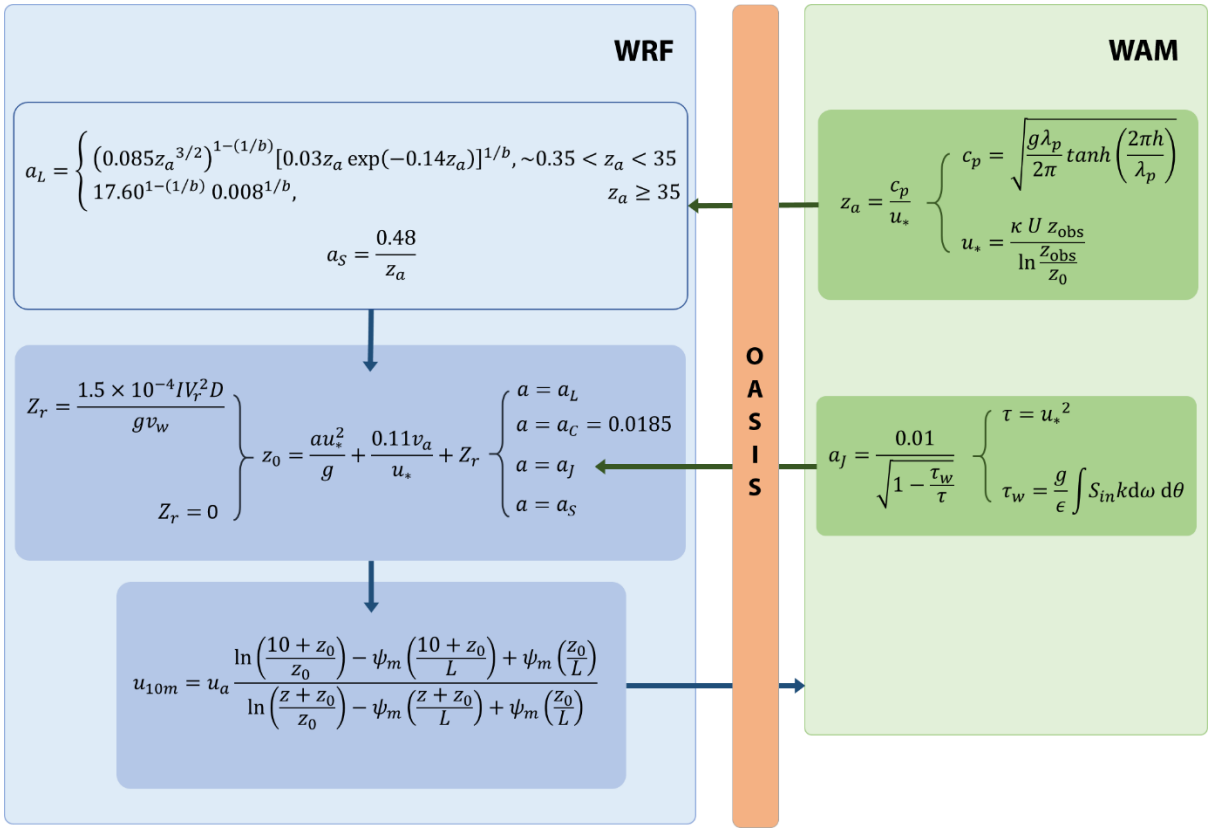

Figure 4.3: Illustration of equations resolved in CHAOS to represent dynamical air-sea interaction.

4.2. Configuration over the Mediterranean and Black Sea

CHAOS has been configured on a domain covering the Mediterranean Sea and the Black Sea in order to carry out the sensitivity tests under extreme wind and sea state conditions (Figure 4.4). The atmospheric component has a horizontal resolution of 10km x 10km with 488x242 C-grid points, time step of 60sec (1 min) and 38 vertical levels stretching from surface to 50 mb. Gridded analysis data from the European Centre for Medium-Range Weather Forecasts (ECMWF) in horizontal resolution of 0.5°x0.5° and time increment of 6 hours were used for the creation of initial and boundary conditions of the atmospheric component. Moreover, ECMWF Sea Surface Temperature (SST) analyses were used for SST update every 6 hours during the simulations. The

Global Multi-resolution Terrain Elevation Data (30-arc-sec USGS GMTED 2010; Danielson and Gesch, 2011), the vegetation data MODIS FPAR (Myneni et al., 2002) and the land-use data 21-class IGBP MODIS (Friedl et al., 2011) were used as static input data in the preprocessing stage of WRF model.

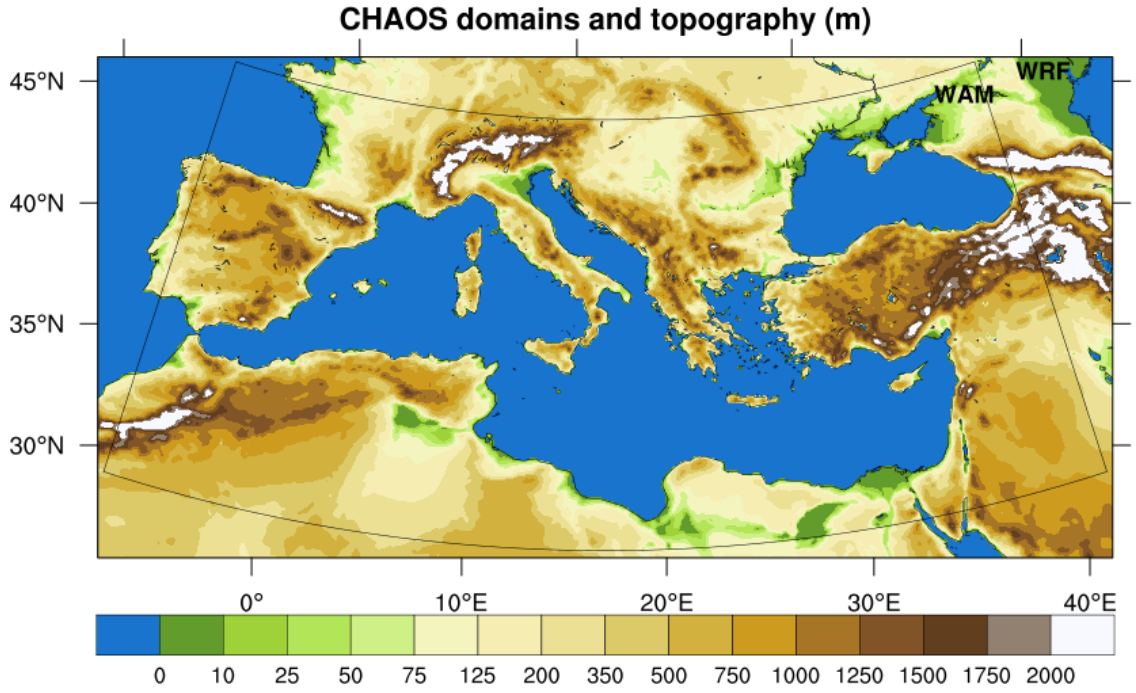

Figure 4.4: Domain configurations of WRF and WAM (black line) models of CHAOS and topography (m) distribution used by WRF are depicted.

The grid of the wave model for the Mediterranean and Black seas covers the geographical area 8° W - 42° E and 29° N - 48° N as shown in Figure 4.4 (black line) using a resolution of 0.1°x0.1° with 501x191 regular lat-lon points. WAM has propagation time step of 75 sec and source time step 600 sec (10 min). Moreover, WAM uses 24 directional bins (15° directional resolution) and 25 frequency bins (ranging from 0.042 to 0.411 Hz) to represent the wave spectra distribution. The initialization of WAM was based on the "hot start" approach in order to use realistic initial wave spectrum. The initial wave spectrum was computed by a preprocessing CHAOS simulation for a time period of one day before the initial time of each case study. The initialization of WAM is based on the "hot start" approach in order to obtain a realistic initial wave spectrum. The initial wave spectrum has been computed based on a prior CHAOS simulation (initialized with "cold start") of a one-day time period. The bathymetric map has been constructed from Etopo1 data (Amante and Eakins, 2009; 1 min Gridded Global Relief Data) using bi-linear interpolation and some degree of smoothing (Figure 4.5). Local corrections have been

introduced in shallow areas of Mediterranean and Black Sea basins. Additionally, a shallow water approximation with depth refraction and depth induced wave breaking (Battjes and Janssen, 1978) was employed due to the complex bathymetry of the Mediterranean and Black Seas. The shallow water approximation includes the wave energy loss due to bottom friction and percolation and it is preferred for high resolution simulations (e.g. Monbaliu et al., 2000; Korres et al., 2011). Furthermore, as proposed by Katsafados et al. (2016), the Gibraltar, the Dardanelles and the Bosporus straits are considered to be closed boundaries; thus, no wave energy is advected through these channels.

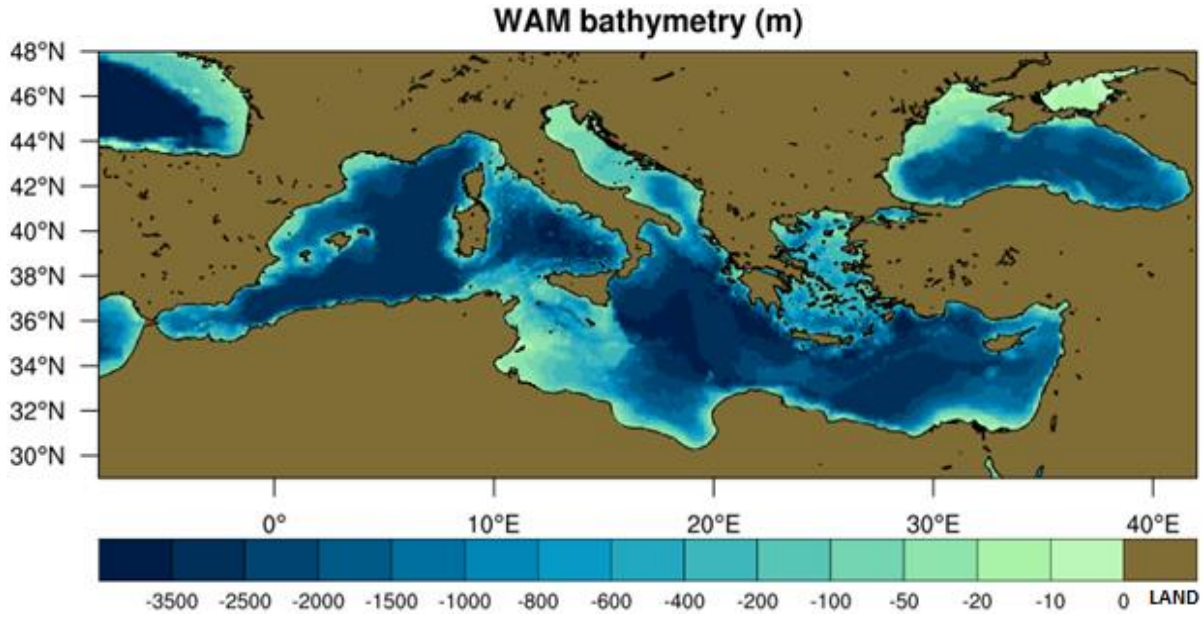

Figure 4.5: Bathymetry (m) distribution used by WAM model is illustrated. The bathymetric map has been constructed from Etopo1 data (Amante and Eakins, 2009; 1 min Gridded Global Relief Data (Etopo1); National Geophysical Data Center, NOAA – National Oceanic and Atmospheric Administration)

As far as the parameterizations of atmospheric mechanisms are concerned, the default schemes were retained for the majority of options in the configuration of CHAOS. These schemes are widely used and well known for offering very realistic representation of atmospheric processes. In this thesis CHAOS run as a standalone atmosphere-ocean wave coupled system without its additional options for simulating atmospheric chemistry and hydrology as well. The revised Monin-Obukhov scheme (Jimenez et al., 2012) is employed to simulate the processes in the surface layer, involving a number of modifications to encapsulate sea state information. The surface layer scheme is the major focus of this thesis as, among other atmospheric processes, it resolves the dynamical exchange of the air-sea momentum and heat fluxes. It is noteworthy that the dynamical air-sea interaction schemes described in Section 2.3 were integrated into that parameterization scheme for the atmospheric processes over water.

For the simulation of Planetary Boundary Layer (PBL) processes the Yonsei University scheme (Hong et al., 2006; YSU) is used. The ground processes are simulated using the unified land surface model (Tewari et al., 2004; Unified NOAH). In order to resolve the long-wave and short-wave radiation processes the RRTM (Mlawer et al., 1997) and the Dudhia (1989) schemes are employed, respectively. In order to simulate the microphysics, the more sophisticated Thompson scheme (Thompson et al., 2008) was preferred rather than the default WRF Single-moment 3-class scheme (Hong et al., 2004; WSM 3-class). Moreover, the Kain-Fritsch scheme (Kain, 2004) is employed so as to represent the convective processes.

The different projections of the two components yield a mismatch between the two domains. Thus, a constant Charnock parameter $a_{const} = 0.0185$ was implemented for the sea grid points of the atmospheric domain (near its western boundary), which were outside the WAM model domain. A smoothing filter was also applied over the transition zone in order to eliminate artificial-generated waves. Moreover, the initial input sea state parameters in WRF were calculated by the preprocessing 1-day WAM simulation for getting more realistic initial sea state conditions. Each component of CHAOS maintained its own time step. Thus, the coupling procedure exchanges data on the source time step of WAM model, every 600 sec. As the time step of the atmospheric model was 60 sec, the exchange took place every 10 time steps of the atmospheric model. Every hour, CHAOS stored its unified outputs (including atmospheric and ocean wave fields) on both the native semi-staggered Arakawa C and spherical latitude-longitude grids. Moreover, the MPI topology of the system was configured according to scalability tests (Figure 4.6). Out of the configurations depicted, the one using 75 and 5 CPUs for atmospheric and ocean wave components respectively was found to be the most efficient. CHAOS presents very good performance with respect to the execution time, due to the limited time overhead compared to standalone WRF simulations. For convenience, the coupling parameterization schemes and parameters can be adjusted using namelist files, without recompilation of CHAOS. The configuration of the system and the main parameterization schemes used are summarized in Table 4.1.

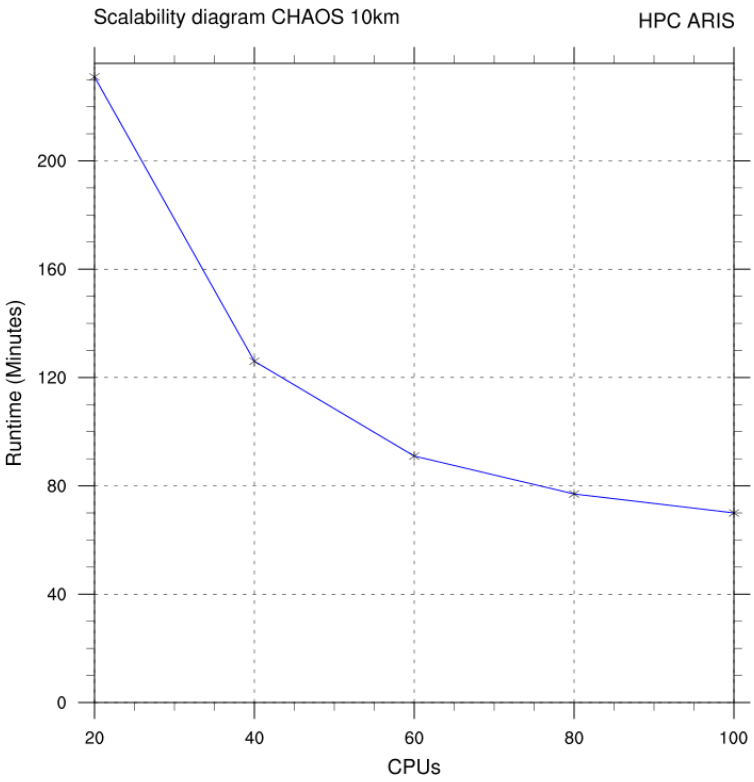

Figure 4.6: CHAOS scalability on High Performance Computer (HPC) ARIS. The test simulations were performed for the case study 4-11 January, 2012 (7 days).

Table 4.1: Configuration of CHAOS

CHAOS	Atmospheric Component	Ocean Wave Component
Model	WRF-ARW, WRF-Chem V3.8 and WRF-Hydro V3.0	WAM Version 4.5.4
Coupler	OASIS3-MCT Version 3.0	
Integration Domain	Mediterranean Sea, Europe, Black Sea	
Grid	Arakawa semi-staggered C-grid	Spherical latitude-longitude grid
Horizontal grid Increment	10km x 10km	0.1^{o}x0.1^{o}
Spectral resolution	–	24 directional bins (15^{o} directional resolution), 25 frequency bins (ranging from 0.042 to 0.411 Hz)
Vertical coordinate	Terrain-following hydrostatic pressure η coordinate	–
Vertical levels	38	–
Time steps	60 s	Propagation time step: 75 s Source time step: 600 s
Initial & boundary Conditions	ECMWF, 0.5^{o}x0.5^{o} 17 isobaric levels 6h update of boundary conditions	Hot start
SST	ECMWF SST update every 6 hours	–
Exchange rate	600 s	
Surface layer	Revised Monin-Obukhov	–

PBL	YSU	–
Microphysics	Thompson	–
Cumulus	Kain-Fritsch	–
Land surface	Unified NOAH	–
Radiation	RRTM and Dudhia schemes	–
Chemistry options	Disabled	–
Coupled to WRF-Hydro	Disabled	–
Topography	30-arc-second USGS GMTED2010	–
Vegetation	MODIS FPAR	–
Land-use	21-class IGBP MODIS	–
Bathymetry	–	ETOPO1
Water approximation	–	Shallow water approximation with depth refraction and wave breaking due to depth change near shore
MPI topology	75 CPUs	5 CPUs

Finally, two configuration modes have been applied to perform the simulations:

- Two-way coupling (CPL_JANSSEN or CPL): Both the atmospheric and ocean-wave component use information produced by employing Janssen's parameterization scheme for the estimation of Charnock parameter as described in Section 4.1.2.
- One-way coupling (control, CTRL): Only the ocean-wave component uses information produced by the atmospheric component. The Charnock parameter in the atmospheric component remains constant and equal to 0.0185 throughout the simulation (Section 4.1.2). The results of this simulation mode are going to be used as a reference for the sensitivity tests and the statistical evaluation of the two-way coupling mode.

4.3. Evaluation Methodology

In order to evaluate the results of CHAOS and test the system for its consistency and performance, a statistical software tool was developed. The performance of the two-way coupling mode (CPL) is statistically evaluated over the sea and land against its performance in the one-way coupling mode (CTRL). The meteorological variables considered in the evaluation are: the near surface wind speed, the significant wave height, the near surface temperature, the mean sea level pressure (MSLP) and the accumulated precipitation. The evaluation is based on the point-to-point comparison with remote sensed and in situ observations for characteristic cases

of atmospheric and sea state development significance. The performance of CHAOS for the selected cases will be assessed using the network of 48 available buoys in the Mediterranean Sea as reference (excluding buoys of Gibraltar Strait) as depicted in Figure 4.7.

The system is also evaluated against remote sensed data retrieved from satellites Jason 1, Jason 2 and Jason 3 (Figure 4.8). Additionally, the sensitivity of the system will be assessed over the land at the positions of almost 1000 surface meteorological stations across Europe, Middle East and Northern Africa (Figure 4.9).

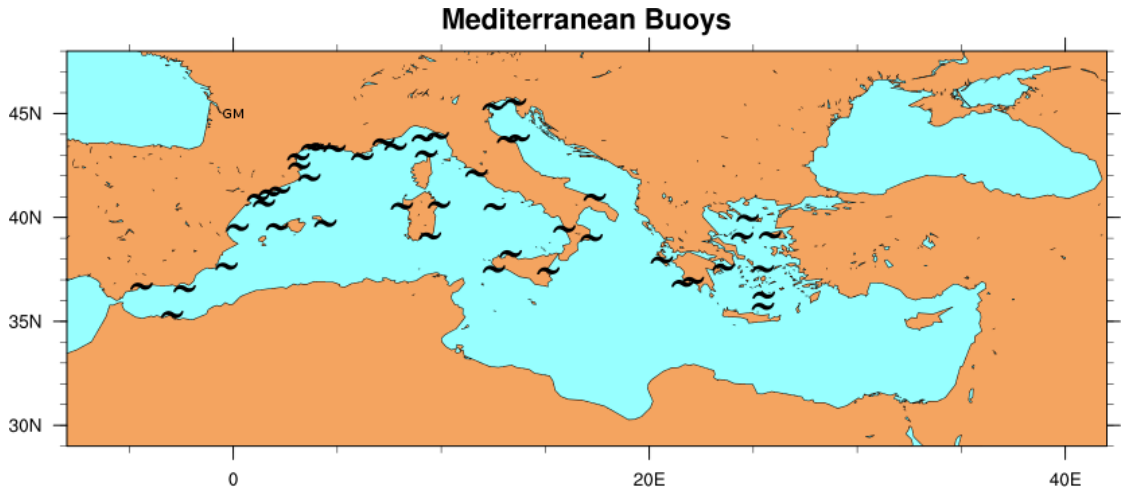

Figure 4.7: Spatial distribution of Mediterranean buoys applied for the evaluation of the system. Data were made available from ISPRA for MyWave project Subtask 3.3.2 and from MyOcean/MyOcean2/Copernicus projects (ftp://medinsitu.hcmr.gr/)

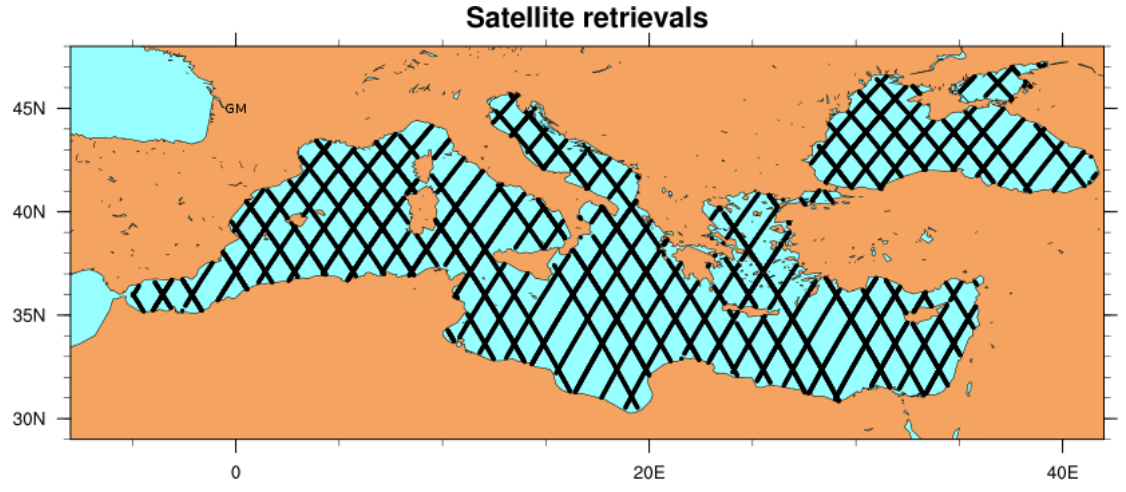

Figure 4.8: Trajectories of satellite retrievals used for the evaluation of the system. The altimeter data were produced and distributed by Aviso (http://www.aviso.altimetry.fr/), as part of the Ssalto ground processing segment.

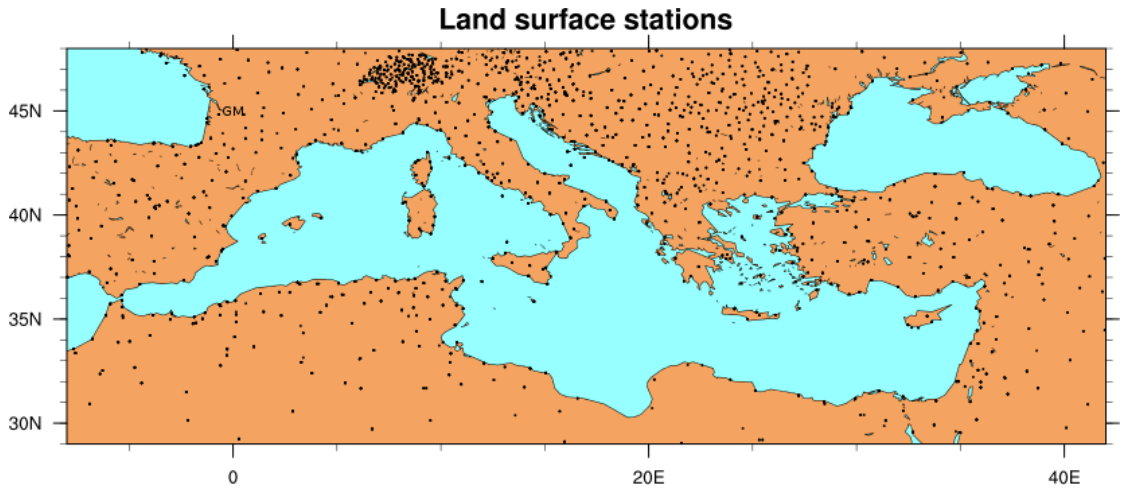

Figure 4.9: Spatial distribution of the land surface stations applied for the evaluation of the system. Data source: ECMWF-GTS network.

The data processing and the statistical evaluation are based on the NCAR Command Language (NCL, 2016). The software developed (on NCL) includes modules for the post-processing of the system outputs in NetCDF format and a new statistical package. In the decoding procedure, the NetCDF data are initially converted to intermediate ASCII format which are then employed for the estimation of statistical indices for both continuous and discrete variables. The use of intermediate ASCII files enables efficient evaluation while at the same time simplifies debugging. The software has been developed in a modular and effective way; it is flexible and easy to configure under various environments and platforms. During the final stage of the process, the scores are visualized in form of spatial maps, X-Y plots, scatter plots, and Taylor diagrams (Taylor, 2001).

Taylor diagrams have been employed to visualize the overall performance of CHAOS. Taylor diagrams (Taylor, 2001) provide a way of graphically summarizing how closely a pattern (or a set of patterns) matches observations. The similarity between two patterns is quantified in terms of their correlation, their centered root mean square difference (or error) and the amplitude of their variations (represented by their standard deviations). The standard deviation (STD) of the simulated pattern is proportional to the radial distance from the origin. Additionally, the centered root mean square (RMS) difference between the simulated and observed patterns is proportional to the distance to the point on the x-axis identified as "observed". In this thesis, the Pearson correlation coefficients, the normalized STD and the normalized RMS differences are illustrated on Taylor diagrams. For the normalization of the values produced by the simulations, the STD and the RMS differences of the observational data were used.

The evaluation methodology is based on the point-to-point hourly comparison between model-generated variables and the observations (Papadopoulos and Katsafados, 2009). The gridded outputs are interpolated at each buoy location using the nearest-neighbor interpolation scheme, taking care of whether the nearest source point is a sea masked grid point. This way, thousands of pairs of model outputs and observations were produced for both the one-way and two-way coupling modes. The evaluation procedure is based on the estimation of traditional verification scores such as the standard mean error (bias), and the root mean square error (RMSE) for continuous predictants (wind speed and the significant wave height). Also, mean value (mean), standard deviation (STD) and Scatter Index (SI) are also calculated for both model and observed values. Supplementary scores are also the Pearson correlation coefficient and the coefficient of determination (R^2). The formulas of the evaluation indices for N measurements, where M_i and O_i are the model-estimated and the observed values respectively (Wilks, 2011), are shown below:

$$MeanObs = \frac{\sum_{i=1}^{N} O_i}{N} \quad (4.1)$$

$$MeanMod = \frac{\sum_{i=1}^{N} M_i}{N} \quad (4.2)$$

$$STDObs = \sqrt{\frac{\sum_{i=1}^{N} (O_i - \overline{O})^2}{N}} \quad (4.3)$$

$$STDMod = \sqrt{\frac{\sum_{i=1}^{N} (M_i - \overline{M})^2}{N}} \quad (4.4)$$

$$Bias = \frac{\sum_{i=1}^{N} (M_i - O_i)}{N} \quad (4.5)$$

$$RMSE = \sqrt{\frac{\sum_{i=1}^{N} (M_i - O_i)^2}{N}} \quad (4.6)$$

$$Pearson = \frac{\sum_{i=1}^{N}(O_i - \overline{O})(M_i - \overline{M})}{\sqrt{\sum_{i=1}^{N}(O_i - \overline{O})^2}\sqrt{\sum_{i=1}^{N}(M_i - \overline{M})^2}} \quad (4.7)$$

$$R^2 = 1 - \frac{\sum_{i=1}^{N}(M_i - O_i)^2}{\sqrt{\sum_{i=1}^{N}(O_i - \overline{O})^2}} \quad (4.8)$$

$$SI = \frac{\sqrt{\frac{\sum_{i=1}^{N}(M_i - O_i)^2}{N}}}{\frac{\sum_{i=1}^{N}O_i}{N}} = \frac{RMSE}{MeanObs} \quad (4.9)$$

The software also includes an advanced quality control package in order to filter erroneous measurements, based on checking the physical range of each parameter being verified, the allowable rate of change in time and the stationarity. An overall evaluation of the system was also performed over the land against a number of land surface observations obtained from the GTS network (Figure 4.9). The extracted scores are the standard mean error (Bias) and the root mean square error (RMSE) for the basic continuous predictants (wind speed, temperature and mean sea level pressure). The verification scores used for the discrete variable (accumulated precipitation) are based on the contingency table approach (Wilks, 2011). As shown in Table 4.2, the contingency table is a two-dimensional matrix where each element counts the number of occurrences in which the observations and the model forecasts exceeded or failed to reach a certain threshold for a given forecast period.

Table 4.2: Contingency table.

Event Forecast	Event Observed		
	Yes	**No**	**Marginal Total**
Yes	A	B	A+B
No	C	D	C+D
Marginal Total	A+C	B+D	A+B+C+D=N

The table elements are defined as:

A : model forecast and observation exceeded the threshold;

B : model forecast exceeded the threshold but observation not;

C : model forecast did not reach the threshold but observation exceeded it;

D : model forecast and observation did not reach the threshold.

N : total number of observations being verified

Considering the above elements, the forecast skill can be measured by evaluating the bias score (BIAS) and the equitable threat score (ETS), using pairs of 6-hour simulated and measured precipitation values and 6 predefined precipitation thresholds (0.5, 2, 4, 8, 16, and 24 mm). Thus, the bias score is defined as

$$BIAS = \frac{A+B}{A+C} \qquad (4.10)$$

while the ET score defined as

$$ETS = \frac{A-E}{A+B+C-E} \qquad (4.11)$$

and E is defined by

$$E = \frac{F \times O}{N} = \frac{(A+B)\times(A+C)}{N} \qquad (4.12)$$

The introduction of the *E* term (Mesinger, 1996) is an enhancement to the normal threat score (as defined in Wilks, 2011); since it reduces it by excluding the number of randomly forecast "hits". To measure the magnitude of the difference between model forecast and observed precipitation the root mean square error (RMSE) was also calculated as follows (Colle et al., 2000; Mass et al., 2002):

$$RMSE = \sqrt{\frac{\sum_{i=1}^{N}(MP_i - OP_i)^2}{N}} \qquad (4.13)$$

where MP_i and OP_i are the model-estimated and the observed precipitation, respectively, and the N is the total number of observations at a specific location reaching or exceeding a certain threshold amount.

Combining these statistical criteria, a comprehensive evaluation of system performance is attempted. Computing the bias and the equitable threat scores, a measurement of the model accuracy on the frequency of occurrences at or above a certain precipitation threshold amount can be revealed (Papadopoulos et al., 2005). Consequently, at given thresholds, the bias score may yield a systematic overestimation (when BIAS > 1) or underestimation (when BIAS < 1), and

the ET score may present poor forecasts (when ETS ≈ 0) or perfect forecasts (when ETS = 1). For example, a greater ETS will represent a significant model improvement only if it is accompanied by a BIAS value close to 1 and a low RMSE.

Chapter 5

Sensitivity Tests on the Modeling of Atmosphere – Ocean Wave Interactions

Upon completion of the development phase of the coupled system, CHAOS can be applied to resolve the atmosphere-ocean wave interactions. For this purpose, four extreme weather and sea state events were selected. For this purpose, four extreme weather and sea state events were selected. Additionally, continuous simulations over a period of one year were executed in order to examine the overall long-term performance of the system. At this stage, the focus of the study is on the Mediterranean and the Black Sea. The main case study examined is the following:

- **Case Study A: 4-8 March 2015**

The results and research findings of the main case study are also investigated in case studies:

- **Case Study B: 21-25 March 2016**
- **Case Study C: 9-13 December 2010**
- **Case Study D: 4-11 January 2012**

The impact of atmosphere-ocean wave interaction in operational mode is approached through a set of long-term simulations:

- **Long-term Study: 1 December 2013 – 30 November 2014**

The above case studies will be first analyzed in terms of the synoptic conditions. Afterwards, the results of CHAOS simulations will be presented, both in two-way and one-way coupling mode. To conclude, the performance of CHAOS will be statistically evaluated using the methodology described in Section 4.3. The outputs from the two simulation modes (see Section 4.2), one-way coupling (CTRL) and two-way coupling using the Janssen parameterization (CPL), have been statistically evaluated based on the point-to-point hourly comparison between model-generated variables and the available Mediterranean buoys measurements. Moreover, the results have been statistically evaluated against satellite retrievals and land surface measurements. A summary of the most important statistical scores is available in Tables Table 5.1-Table 5.4 at the end of the Chapter.

5.1. Case Study A: 4-8 March, 2015

5.1.1. Synoptic Analysis

The impact of the two-way coupling on atmosphere and waves is assessed in an extreme weather event that occurred over the central Mediterranean Sea in March 2015. The case study of 4-8 March 2015 has been selected due to the severity of the prevailing atmospheric and sea state conditions. Figure 5.1 (a-b) shows that during 5-6 March 2015, a barometric low accompanied by increased pressure gradients and fronts was generated over Italy. The barometric system was supported by the upper-level atmospheric conditions. Figure 5.1 (c-d) presents a cut-off upper-level trough which gradually penetrated in the core of the barometric low over the Ligurian and the Tyrrhenian Seas. The cold upper-level air entrainment in combination with the positive vorticity advection increased the instability of the cyclone driving to its deepening and intensification. The cyclonic system provoked gale-force winds and high sea state conditions more prominent over the central Mediterranean Sea.

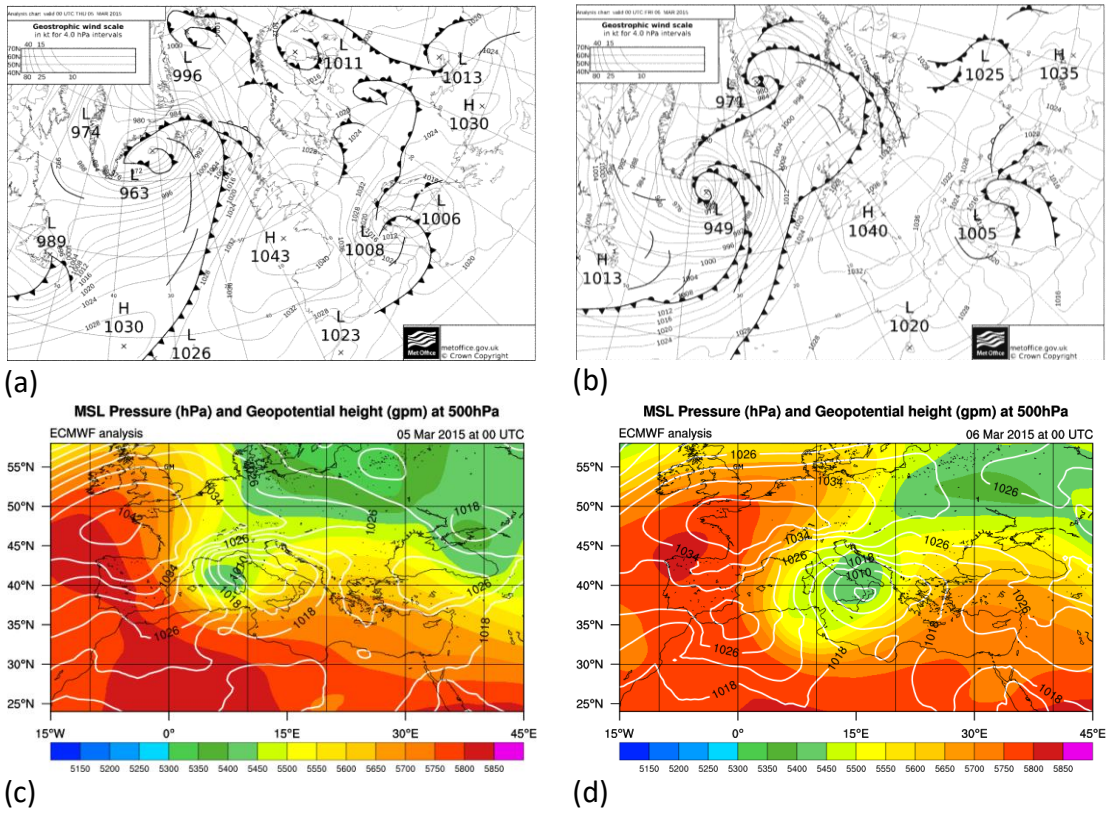

Figure 5.1: Surface pressure analysis map (hPa) for (a) 5 March at 00:00 UTC and (b) 6 March at 00:00 UTC, 2015. The maps derived from UK Met office surface analyses archive. Mean Sea Level Pressure (contours in hPa) and geopotential height at 500 hPa (colored shaded in gpm) for (c) 5 March at 00:00 UTC and (d) 6 March at 00:00 UTC, 2015. Data are based on ECMWF operational analyses.

5.1.2. Simulation Results and Statistical Evaluation

The performance of the two-way coupled simulation is compared against the one-way coupling mode that run for the same period. Figure 5.2 (a-d) presents the horizontal distributions of the wind speed at 10 m and the significant wave height (SWH) obtained from the two experiments during the development phase of the cyclone, on 5 March 2015 at 15:00 UTC. Compared against one-way coupling mode, CPL experiment decreases wind speed and SWH approximately up to 12% and 20% respectively (Figure 5.2e and f). This is attributed to the rougher sea surface in two-way coupling mode, which attenuates the atmospheric flow and, consequently, the wind-generated waves (Janssen, 2004).

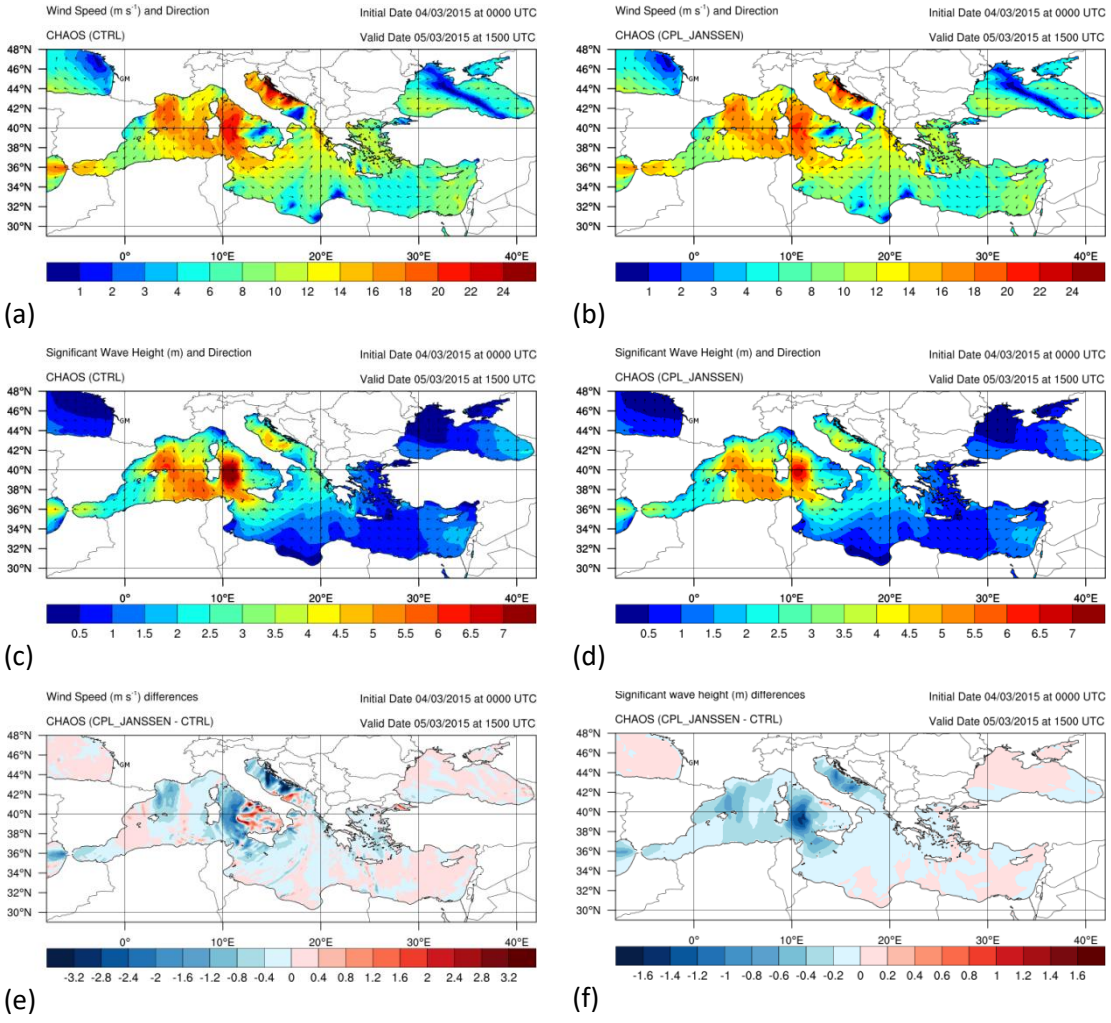

Figure 5.2: Horizontal distribution of wind speed (m s-1) and direction by (a) CTRL and (b) CPL experiments. Horizontal distribution of significant wave height (m) and direction by (c) CTRL and (d) CPL experiments. Horizontal distribution of (e) wind speed (m s-1) and (f) significant wave height (m) differences between CPL and CTRL experiments. Figures (a-f) refer to 5 March 2015 at 15:00 UTC.

The maximum negative differences are collocated with the wind speed and SWH maxima over Tyrrhenian and Adriatic Seas. Other studies, including those of Jenkins et al. (2012), Veiga and Queiroz (2015) and Wahle et al. (2017), indicate that the sea surface roughness apparently increases over areas where waves are rapidly-generated with low wave ages. Wave age is equal to C_p/u_* ratio, where C_p is the wave phase speed at the peak spectral frequency. Janssen (2004) proposed that wave stress is determined by the medium to high-frequency gravity waves. These waves are usually characterized by inverse wave age ranging from 0.1 to 1 (or wave age from 10 to 1). As depicted in Figure 5.3 (a-d), Tyrrhenian and Adriatic Seas are covered by younger, wind-generated waves which are characterized by higher Charnock values, higher friction velocities and, consequently, increased roughness length. The dependence of sea surface roughness on the inverse wave age observed in the simulation results is consistent with previous theoretical and experimental studies (Smith, 1988; Janssen, 1991; Donelan et al., 1993; Oost et al., 2002; Drennan et al., 2003).

A few spots of wind speed rise (Figure 5.2e) may be attributed to the existence of old waves (swell) which result to decrease of the sea surface roughness (Figure 5.3e). The modified sea surface roughness can also alter the track of the cyclone and causes local wind speed differences. Indeed, Figure 5.3f shows that CPL results in slightly higher MSLP minimum and a shift of the center of the low pressure system approximately 50 km eastward compared to CTRL run. This shift causes local wind speed differences. Despite the higher sea surface roughness, CPL simulates a more rapid eastward movement of the cyclone This may be attributed to the fact that the air-sea interaction processes are nonlinear and the final track of the system is dependent on its thermodynamic equilibrium. Simulations of a hurricane by Lee and Chen (2012) resulted analogous unexpected behavior for the system track. Nevertheless, CPL delays the eastward movement of the cyclone compared with CTRL at some different times. This uncertain behavior indicates that such shift may be attributed to the fact that the atmosphere-ocean wave interaction processes are nonlinear and the final shift of the system is influenced by the variations of the upper-level controlling dynamical and thermodynamic factors. Additionally, the temporary increase in the wind speed, as simulated by the CPL experiment, is not accompanied by a synchronized increase of the SWH because the winds are still too weak to generate new waves. Therefore, the weaker mean sea state enforces the negative differences over the areas with increased winds. One of the advantages of the newly developed two-way coupled system can be demonstrated by the large values of Charnock parameter and roughness length

over south Aegean Sea, despite the fact that the friction velocity is still characterized by low-moderate values (~0.5 m s^{-1}). This situation is associated with the presence of young waves that increase Charnock parameter and, consequently, roughness length; a coherence that cannot be resolved in the atmospheric model of the CTRL experiment.

Attention should be also paid in Charnock parameter and roughness length which are increased over south Aegean Sea despite the fact that friction velocity is characterized by low-moderate values (~0.5 m s^{-1}). This may be associated with the presence of young waves that increase Charnock parameter and, consequently, roughness length.

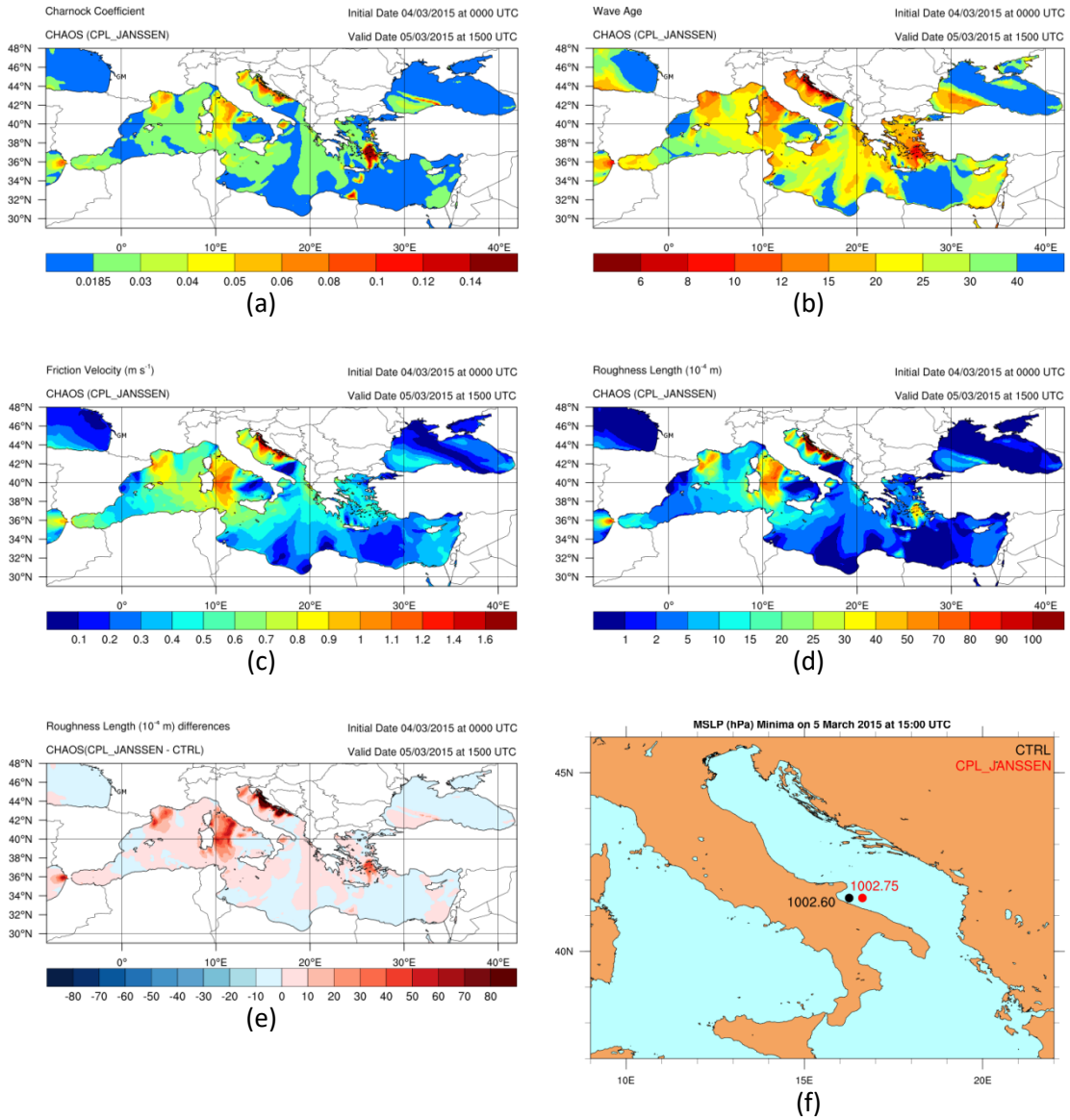

Figure 5.3: Horizontal distribution of CPL (a) Charnock parameter, (b) wave age, (c) friction velocity (m s^{-1}), (d) roughness length (10^{-4} m), (e) roughness length (10^{-4} m) differences between CPL and CTRL experiments. (f) MSLP (hPa) minima for CTRL (black dot) and CPL (red dot) experiments. Figures (a-f) refer to 5 March 2015 at 15:00 UTC.

The young ocean waves modulate the momentum and enthalpy fluxes at the air-sea interface (Doyle, 1995; Doyle et al., 2002). Figure 5.4 (a-b) demonstrates the spatial agreement of

the surface fluxes with the sea surface roughness parameters. The mechanism that adjusts the surface fluxes is initiated from the wind momentum which is transferred to the sea surface and generates the wind induced waves while sensible and latent heat are then released from the sea to the atmospheric surface layer. Figure 5.4 (c-d) shows that, CPL experiment increases the surface momentum and enthalpy fluxes over rougher areas where young waves are generated. The surface fluxes alteration confirms previous studies for tropical and extratropical cyclones over the United States (e.g. Bao et al., 2000; Desjardins et al., 2000). Nevertheless, the finer resolution of CHAOS experiments supports to a more detailed representation of spatiotemporal surface fluxes variability over the closed Mediterranean Sea characterized by complex shores. Additionally, areas of slightly reduced surface fluxes appear in the CPL compared to CTRL experiment which is attributed to the decrease of the sea surface roughness over areas with old waves and to the displacement of the barometric low, as it was mentioned before.

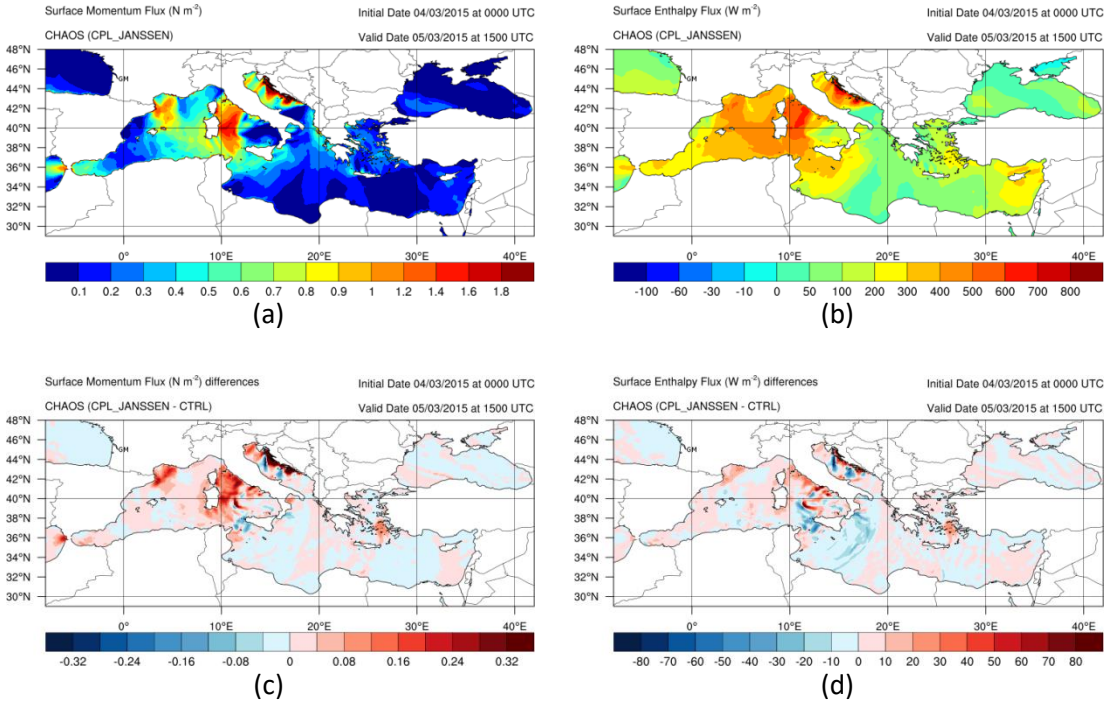

Figure 5.4: Horizontal distribution (a) surface momentum flux (N m^{-2}) and (b) surface enthalpy flux (W m^{-2}). Horizontal distribution of surface (c) momentum flux (N m^{-2}) and (d) enthalpy flux (W m^{-2}) differences between CPL and CTRL experiments. Figures (a-d) refer to 5 March 2015 at 15:00 UTC.

Figure 5.5 (a-b) illustrates the dependence of the roughness length and the Charnock parameter to the friction velocity for the Mediterranean and Black Seas during the period 4-8 March 2015. In general, CPL increases roughness length, Charnock parameter and friction velocity. Roughness length is increased in calm conditions due to the molecular motions which are dominant during the initial development of the viscous sublayer (Smith, 1988). For friction velocities up to 0.1 m s^{-1} roughness length is decreased while sea surface is transitioning from an

aerodynamically smooth to an aerodynamically rougher condition, as also reported by Katsafados et al. (2016a). In CPL experiment, Charnock parameter is diagnostically calculated by WAM and is not constant as in CTRL experiment (0.0185). This reveals the potential of the CPL simulation to determine roughness length for rougher sea state regimes. Indeed, Charnock reaches its peak for friction velocities approximately equal to 0.4 m s^{-1} which in turn causes a local peak of the roughness length. This may be attributed to the development of the young waves, which increase the sea surface roughness without a consequential increase of friction velocity, as also observed for 5 March at 15:00 UTC (Figure 5.3). In fully developed conditions, Charnock parameter tends to become saturated and this is an indication that the sea surface roughness is not characterized by constant increase rate offering a slight positive forcing to the flow under high wind conditions. Although this mechanism is described in Donelan et al. (2004), WAM model does not resolve processes such as flow separation or wave breaking under high wind conditions. The behavior of Charnock parameter at high friction velocities may be attributed to the rapidly-developed waves which are unable to carry the full stress (Bidlot, 2012).

Figure 5.5 (c-e) demonstrates the dependence of surface momentum, enthalpy and moisture fluxes to the wind speed at 10 m height. CPL increases the surface momentum flux from the atmosphere to the waves up to 100% for wind speed exceeding 5 m s^{-1}. This indicates the momentum flux response to the simulated rougher sea surface conditions. This regime causes momentum loss in the form of kinetic energy from the MABL to the waves. On the other hand, CPL increases the surface enthalpy and moisture fluxes from the sea surface to the atmosphere up to 30% for wind speed exceeding 15 m s^{-1}, feeding with excess of thermal energy and moisture the MABL. Figure 5.5f shows that the CPL simulation is characterized by higher ratio C_k/C_d (for these coefficients see more in Section 2.1), between the dimensionless bulk transfer coefficients for enthalpy (C_k) and momentum (C_d or drag coefficient), under calm conditions and, in general, lower ratio C_k/C_d for wind speeds exceeding 5 m s^{-1}. These ratio values are comparable with measurements obtained in hurricane conditions (Black et al., 2007; Drennan et al. 2007; French et al. 2007; Zhang et al., 2008; Andreas, 2011; Bell et al., 2012).

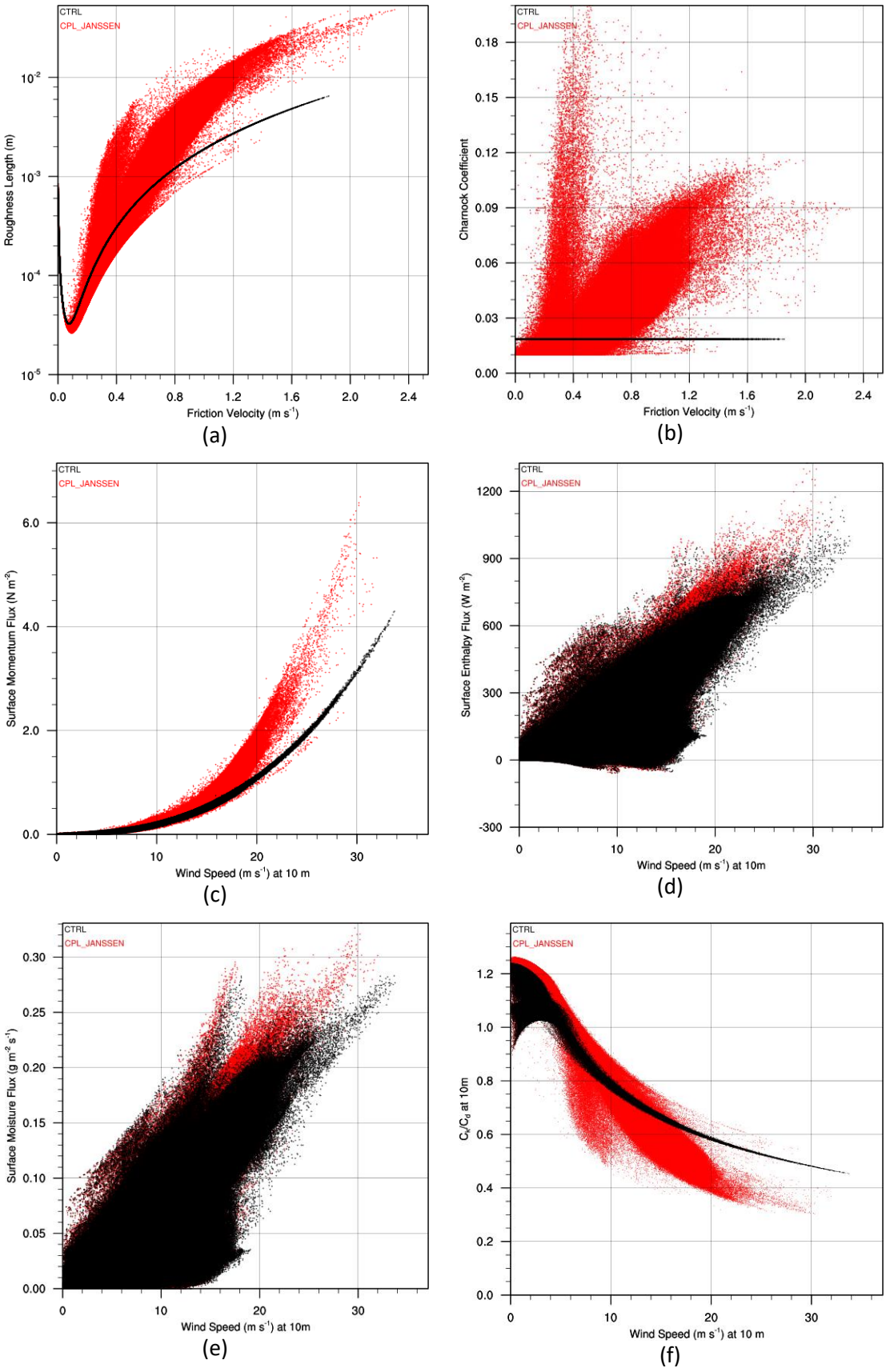

Figure 5.5: (a) Roughness length (m) and (b) Charnock parameter dependence on the friction velocity (m s^{-1}). The black line stands for the constant Charnock (0.0185) in CPL simulation. Surface (c) momentum flux (N m^{-2}), (d) enthalpy flux (W m^{-2}) and (e) moisture flux (g m^{-2} s^{-1}) dependence on the wind speed (m s^{-1}) at 10 m. (f) Dependence of ratio between the dimensionless bulk transfer coefficients for enthalpy (C_k) and momentum (C_d) to the wind speed (m s^{-1}) at 10 m. Figures (a-f) refer to the time period from 4 March at 00:00 UTC to 8 March at 00:00 UTC, 2015. CTRL and CPL results are shown in black and red colors, respectively.

The decrease of the ratio in moderate and high wind speeds by CPL indicates that the energy loss due to sea surface stress exceeds any enthalpy gain. Emanuel (1995) proposed that the structure and the intensity of hurricanes are dependent on this ratio. Despite the fact that our case study refers to a mid-latitude cyclone in the Mediterranean Sea, this ratio was used to get a perspective insight into the energy balance of the cyclonic system. Thus, CPL is expected to simulate a weaker-shallower barometric system characterized by lower energy content due to the competition between the wave-induced stress and the surface heat fluxes. In this context, Doyle (1995) showed that the roughness effects of ocean waves can decrease the mean kinetic energy up to 3-8% throughout the middle and upper-troposphere.

Indeed, Figure 5.6 (a-b) depicts a shallower (up to 1 hPa) barometric low over Italy on 5 March 2015, at 15:00 UTC. Such systematic trend is also evidenced for the whole simulation period with local maxima up to 2 hPa. Similar results have been also drawn by Wahle et al. (2017). However, Doyle (2002) in a case study of a tropical cyclone found its MSLP response in the range of 8 hPa deeper to 3 hPa shallower. This is an indication that the intrinsic air-sea processes are dominated by complex nonlinear interactions making difficult to draw distinct and pronounced conclusions. Figure 5.6 (a-c) shows that the two-way coupling affects the precipitation pattern as well. Indeed, the spatial distribution of the precipitation is modified due to the system displacement and the overall amount of precipitation is also reduced by 5% in CPL simulation. Despite the fact of the near surface atmospheric response, the air-sea momentum and energy exchange affects the MABL and the lower-to-mid troposphere as well. Figure 5.6 (d-e) shows that the enhanced sea surface roughness as it was simulated by CPL affects MABL height over the area of the cyclone. This is aligned with previous results found in literature (Sullivan et al., 2008; Lee and Chen, 2012; Rutgersson et al., 2012). As proposed by Katsafados et al. (2016a), the increased sea surface roughness develops a more turbulent and deeper MABL shallowing the cyclone. In this context, CPL deepens MABL over sea surface roughness peaks simulating weaker cyclone as confirmed by the findings for MSLP. The upper-level trough is also affected due to its dependence of geopotential height on the MSLP and it is accompanied with a decrease of temperature at 500 hPa over the areas where the geopotential height increases (Figure 5.6f, g and h). Thus, the sea surface roughness seems to produce a shallower cyclonic structure in a deeper and more turbulent MABL. The issue that arises at this point is to determine the vertical scale over which the sea surface roughness affects the troposphere.

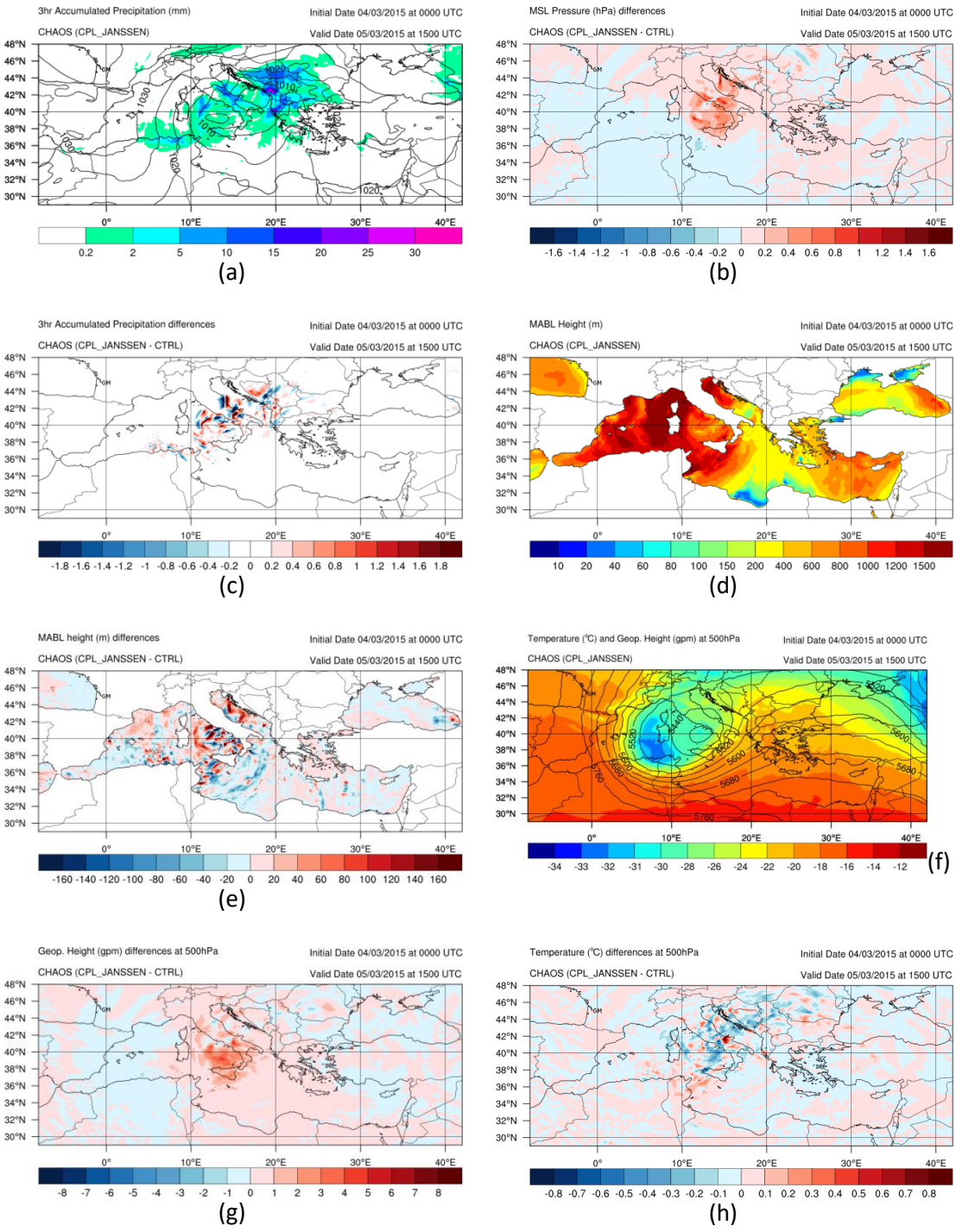

Figure 5.6: Horizontal distribution of (a) 3-hour accumulated precipitation (mm) and MSLP (hpa), (b) MSLP (hPa) and (c) 3-hour accumulated precipitation (mm) differences between CPL and CTRL experiments, (d) MABL height (m), (e) MABL height (m) differences between CPL and CTRL experiments, (f) temperature (°C) and geopotential height (gpm) at 500 hPa, (g) geopotential height (gpm) at 500 hPa and (h) temperature (°C) at 500 hPa differences between CPL and CTRL experiments. Figs. (a-h) refer to 5 March 2015 at 15:00 UTC.

Figure 5.7 shows that the vertical response of the temperature, horizontal and vertical wind speed, humidity and water vapor mixing ratio is enclosed over the cyclonic system and it is not spread to remote areas or over land. In general, the thermodynamic characteristics of the cyclone are mainly affected at the stage of development and they are horizontally and vertically propagated with the evolution of the system. In that manner, CPL increases the relative humidi-

ty and the water vapor mixing ratio up to 7 km while the responses on the wind speed, the vertical velocity and the temperature can be detected up to the tropopause.

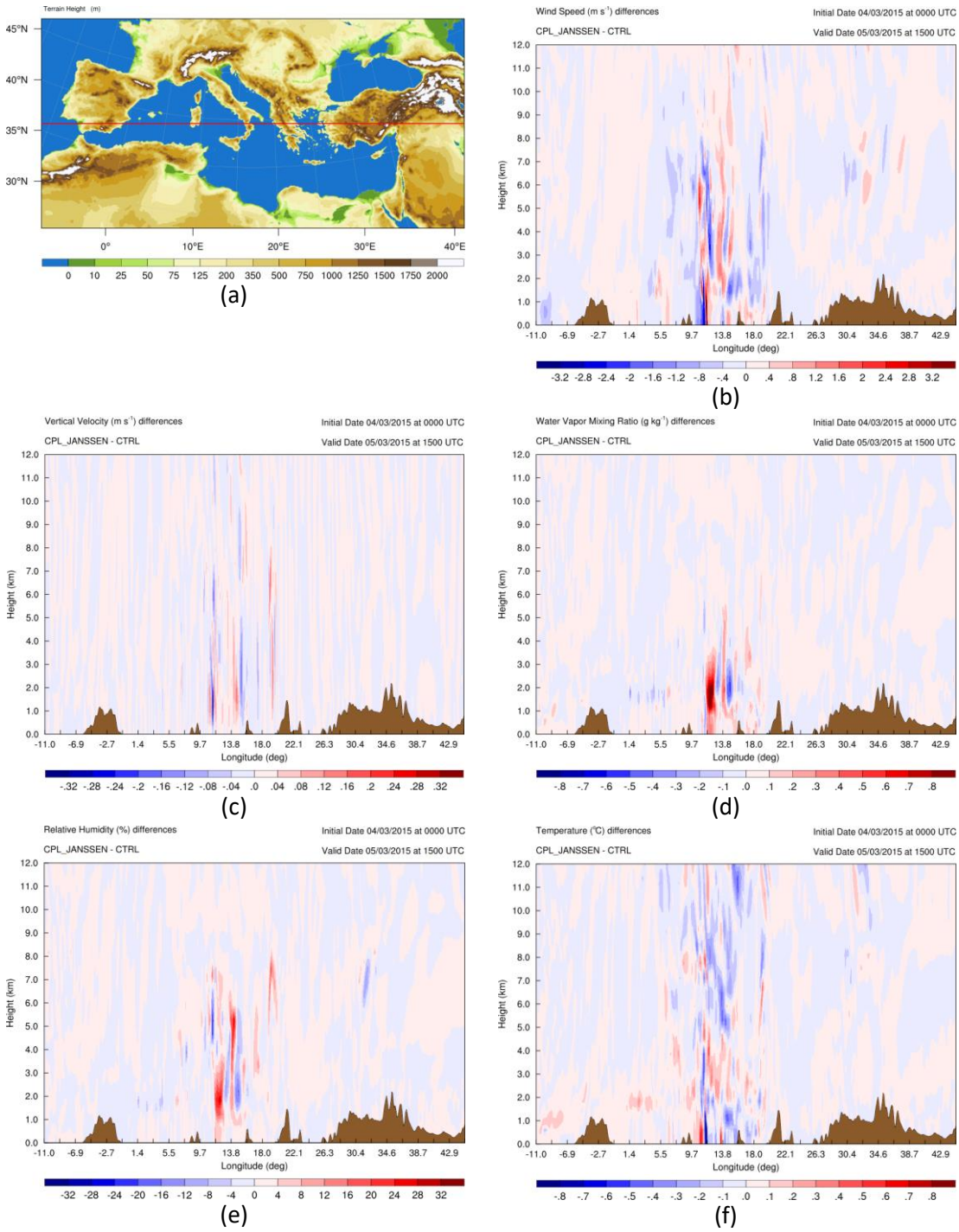

Figure 5.7: (a) Terrain height (m). Vertical cross section area is illustrated by red line. Vertical cross section of (b) wind speed (m s^{-1}), (c) vertical velocity (m s^{-1}), (d) water vapor mixing ratio (g kg^{-1}), (e) relative humidity (%) and (f) temperature (°C) differences between CPL and CTRL experiments. Figures (a-f) refer to 5 March 2015 at 15:00 UTC.

The modification of humidity amount and vertical advection could lead in variations of cloud density. Additionally, the vertical extension of the cyclone and possibly its overshooting top could be affected in the two-way coupled simulations as a feedback caused by the variations of updrafts. However, such feedback mechanisms are characterized by increased hetero-

geneity as they are mainly modulated by complex and nonlinear processes. It is, thus, difficult to draw pronounced conclusions regarding any systematic effect of the sea surface roughness on the vertical atmospheric structure.

Compared against buoys observations both experiments overestimate wind speed (Figure 5.8a). This is owed to the fact that WRF model tends to overestimate the near surface wind speed (Shimada and Ohsawa, 2011; Jimenez et al., 2012), more prominent for low intensities. This is mainly attributed to the surface layer scheme and the estimation of wind speed at the lower level of the atmospheric model in PBL. CPL improves the root mean square error (RMSE) more than 3% and decreases the bias error about 9%. The results are characterized by high confidence level (>95%). Additionally, CPL improves the correlation coefficient (Pearson), the scatter index (SI) and the coefficient of determination (R^2) up to 5%. The overall improvement in the wind speed field appears to have a strong impact on the SWH estimations due to the attenuation of wind-generated waves. This is in agreement with previous findings in the literature (Doyle et al., 2002; Katsafados et al., 2016a; Wahle et al., 2017). Particularly, CPL (with respect to the CTRL experiment) shows reduced bias error (~32%) and RMSE (~6%) and less but still distinctive improvements in the STD, R^2 and SI (Figure 5.8b). Figure 5.8 (c-d) indicates that two-way coupling offers further improvement to the results against remotely sensed data. Indeed, for CPL, the relative improvement versus the CTRL experiment for the wind speed (e.g., 5% reduction in the RMSE and 20% in the bias error) is higher than the respective improvement found when the verification performed against the buoy observations. For SWH, the relative improvements are even larger, 20% reduction in the RMSE and 60% reduction in the bias error. A reasonable explanation for such a boost in performance is that remotely sensed data encapsulate offshore areas where CPL resolves rougher sea state conditions and consequently more prominent wind and wave differences than at the near shore buoys. Moreover, the satellite retrievals incorporate the average spatial distribution of the wind speed and the SWH as the simulations do instead of the buoy point measurements. Figure 5.8e illustrates an overall Taylor diagram (see more in Section 4.3 and at Taylor, 2001) for wind speed and SWH against buoys observations and satellite retrievals. The diagram shows that CPL run is characterized by lower STD and RMSE as well as by slightly better correlation compared with CTRL run. Thus, two-way coupling offers statistical improvements over the sea as it was also reported by the relevant literature (e.g. Lionello et al., 2003; Renault et al., 2012; Katsafados et al., 2016a; Wahle et al., 2017).

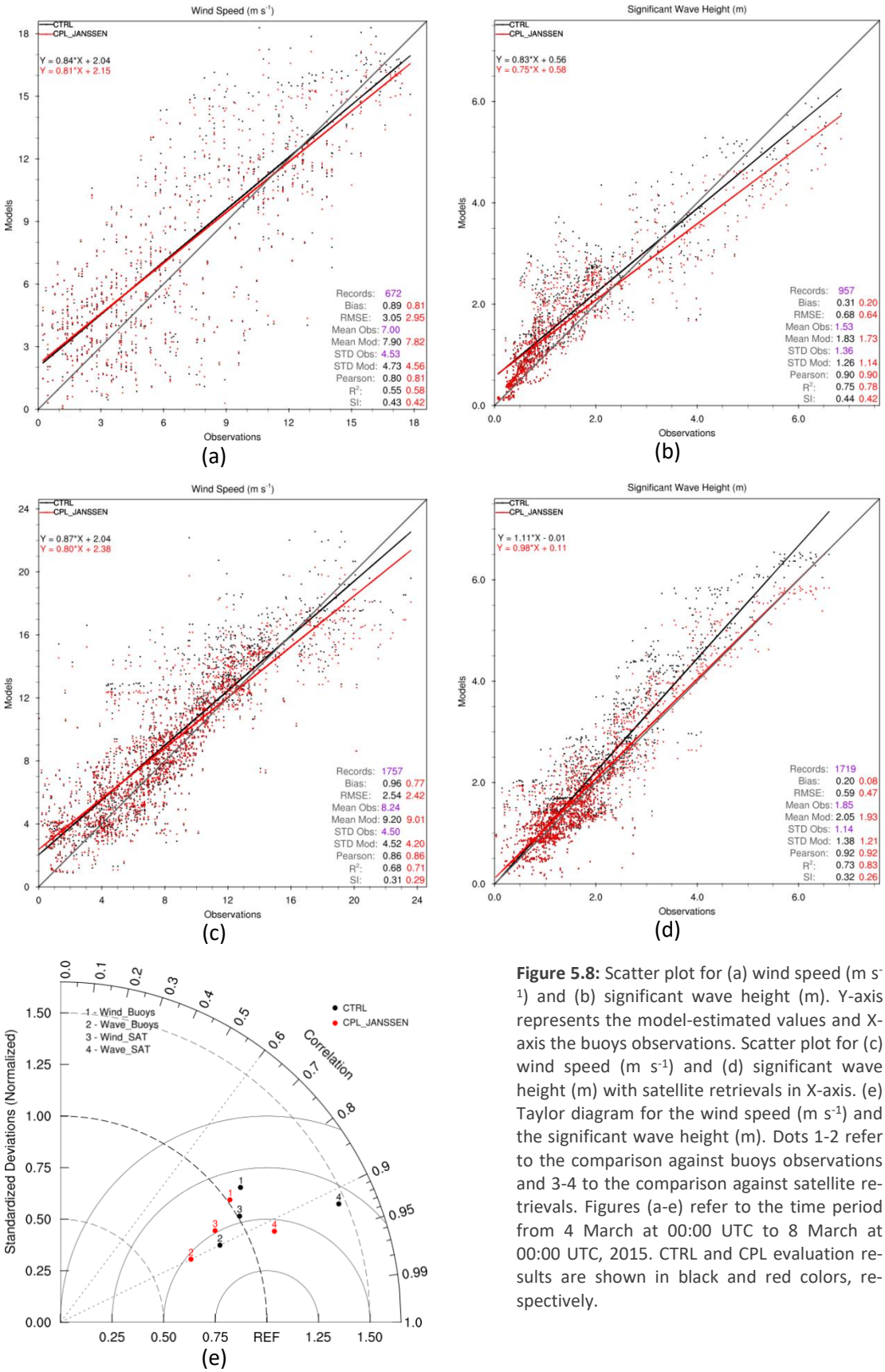

Figure 5.8: Scatter plot for (a) wind speed (m s^{-1}) and (b) significant wave height (m). Y-axis represents the model-estimated values and X-axis the buoys observations. Scatter plot for (c) wind speed (m s^{-1}) and (d) significant wave height (m) with satellite retrievals in X-axis. (e) Taylor diagram for the wind speed (m s^{-1}) and the significant wave height (m). Dots 1-2 refer to the comparison against buoys observations and 3-4 to the comparison against satellite retrievals. Figures (a-e) refer to the time period from 4 March at 00:00 UTC to 8 March at 00:00 UTC, 2015. CTRL and CPL evaluation results are shown in black and red colors, respectively.

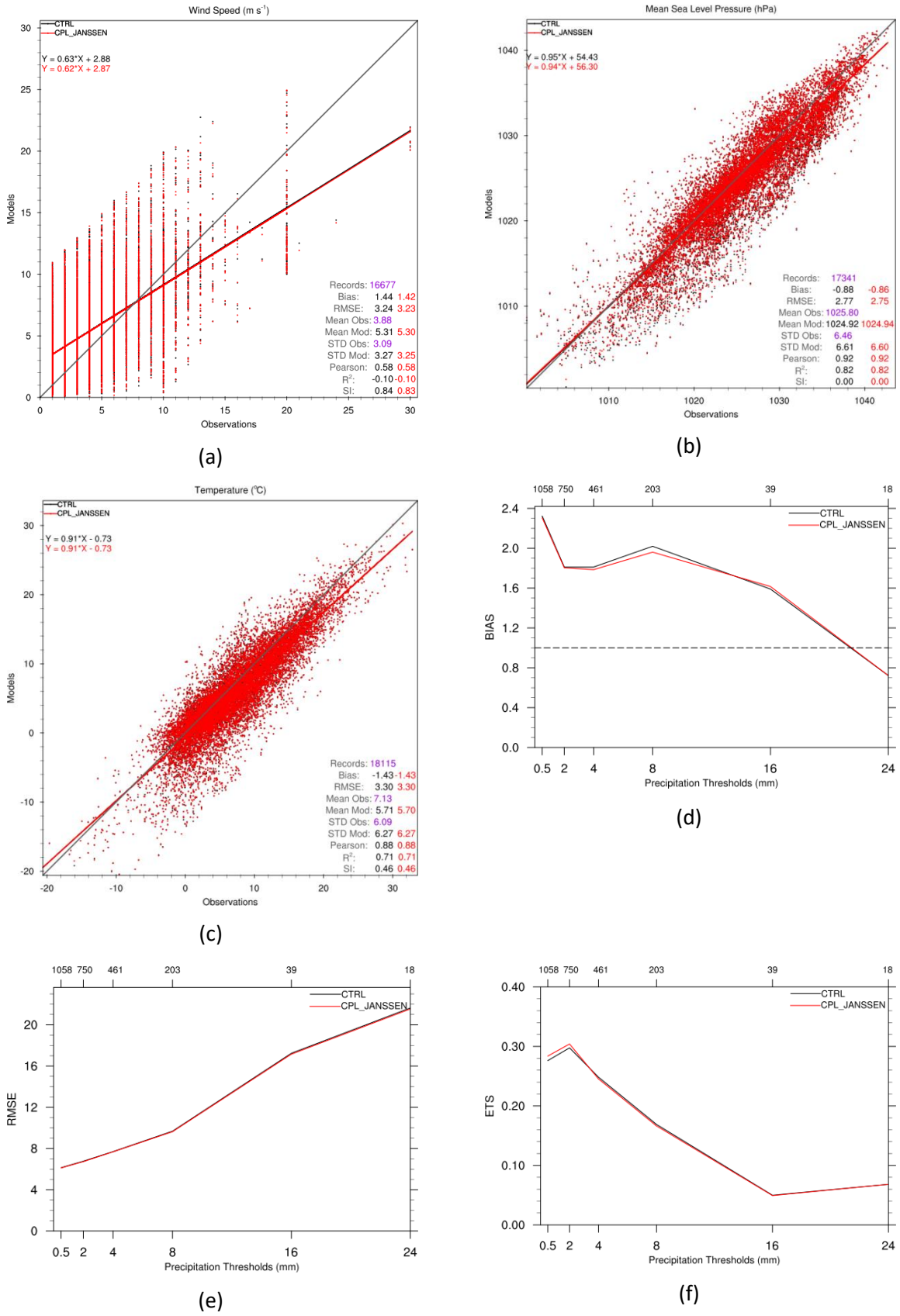

Figure 5.9: Scatter plot for (a) wind speed (m s^{-1}), (b) MSLP (hPa) and (c) temperature (°C) over the land. Y-axis represents the model-estimated values and X-axis the buoys observations. (d) BIAS (e) RMSE and (f) ETS for specific 6-hour precipitation (mm) thresholds. The numbers above each tick mark denote the sample for the corresponding threshold value. Figures (a-f) refer to the time period from 4 March at 00:00 UTC to 8 March at 00:00 UTC, 2015. CTRL and CPL evaluation results are shown in black and red colors, respectively.

This thesis aims to resolve air-ocean wave interactions improving the forecast skill over the sea conserving it over the land. It is noteworthy that two-way coupling not only conserve the performance over the land but it offers improvements. Both simulations overestimate wind speed and underestimate temperature and MSLP. The statistical scores reflect the intrinsic forecast skill of WRF and they are in agreement with previous studies regarding WRF model performance (e.g. Katsafados et al., 2011; Shimada and Ohsawa, 2011). Despite the fact that, CPL improves RMSE up to 1% for wind speed, MSLP, temperature and precipitation (Figure 5.9a-c). Two-way coupling decreases the overestimation of 6-hour accumulated precipitation in medium thresholds while preserving RMSE and even slightly improving ETS in low thresholds (Figure 5.9d-f).

It is noteworthy that there is a lack of references in literature for the two-way coupling statistical improvements over the land. The improvements over the land resulted by two-way coupling mode of CHAOS may be attributed to the impact of ocean waves on the tropospheric processes which determine the evolution, the intensity and the trajectory of the cyclonic system. The impact of two-way coupling over the sea is characterized by teleconnection effects on atmospheric flow and stability up to middle to upper-tropospheric levels, modifying the dynamical and thermodynamic mechanisms of PBL and cloud microphysics even over the land.

5.2. Additional Case Studies

5.2.1. Case Study B: 21-25 March, 2016

On 21 March, 2016, a deep barometric low system was formed over Italian Peninsula. The system was accompanied with cold and warm fronts and passed gradually over Italy and Greece (Figure 5.10a, b). The system was supported by an extended trough moving south from central Europe (Figure 5.10a, b) causing gale force winds, high waves and torrential rainfall at many areas. It is noteworthy that this system affected the entire Mediterranean Sea and spread over a wide part of the Black Sea.

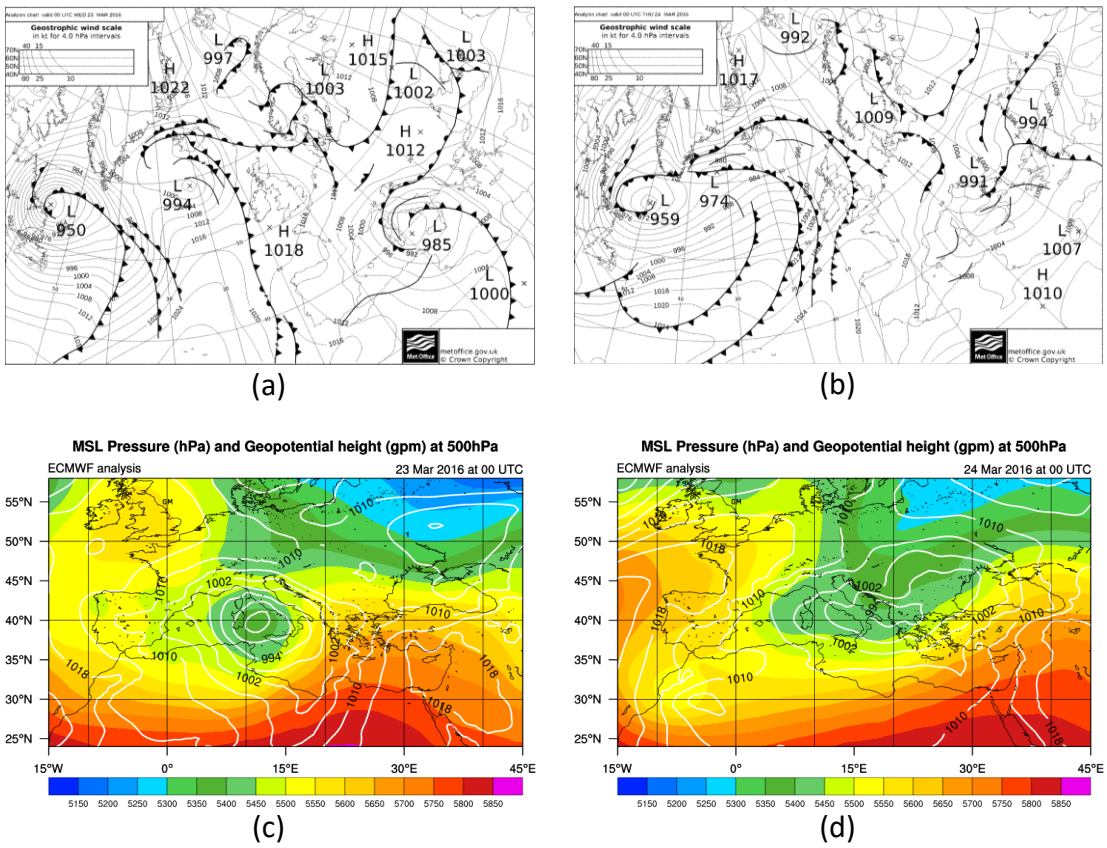

Figure 5.10: Surface pressure analysis map (hPa) for (a) 23 March at 00:00 UTC and (b) 24 March at 00:00 UTC, 2016. The maps derived from UK Met office surface analyses archive. Mean Sea Level Pressure (contours in hPa) and geopotential height at 500 hPa (colored shaded in gpm) for (c) 23 March at 00:00 UTC and (d) 24 March at 00:00 UTC, 2016. Data are based on ECMWF operational analyses.

This case is characterized by rapid intensification of wind and wave fields mainly over the central Mediterranean Sea and the Aegean Sea. Figure 5.11 (a-d) shows that CPL experiment generally decreases wind speed and SWH with differences exceeding 1 m s^{-1} and 0.5 m, respectively. The impact of two-way coupling is more prominent over local maxima as in the previous case study. As illustrated in Figure 5.11 (e-f), CPL increases Charnock parameter and momentum transfer from the atmosphere to the sea over the areas where young waves are dominated. CPL builds a deeper MABL over these areas, as definitely observed over the Aegean Sea (Figure 5.11g, h). Additionally, two-way coupling affects the dynamical and thermodynamic structure of the troposphere, as in the previous case study.

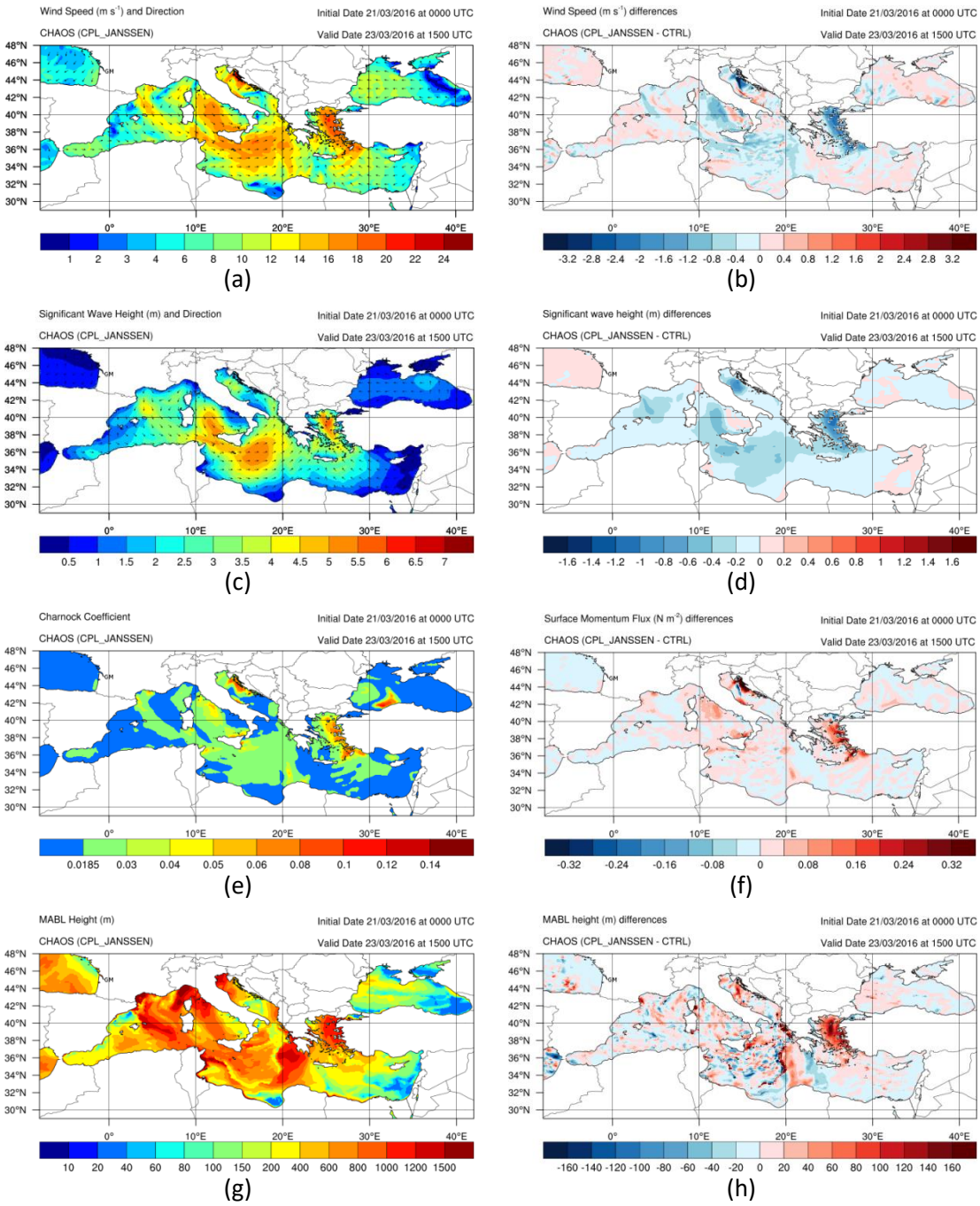

Figure 5.11: Horizontal distribution of (a) CPL wind speed (m s^{-1}) and direction, (b) wind speed (m s^{-1}) differences between CPL and CTRL, (c) CPL significant wave height (m) and direction, (d) significant wave height (m) differences between CPL and CTRL, (e) CPL Charnock parameter, (f) surface momentum flux (N m^{-2}) differences between CPL and CTRL, (g) CPL MABL height (m) and (h) MABL height (m) differences between CPL and CTRL. Figures (a-h) refer to 23 March 2016 at 15:00 UTC.

An in depth analysis reveals a rather heterogeneous distribution of the statistical scores among the buoys. Indeed, some buoys records confirmed noticeable improvements for the entire statistical scores. For instance, substantial RMSE reduction (30%) of the SWH is evidenced by the buoy 61196 records at Balearic Sea (Figure 5.12a, c). On the other hand, the forecast skill is decreased at buoy 61198 over Gibraltar Sea. Both coupling modes reveal underestimation of wind speed and SWH (Figure 5.12b, d). This is attributed to the inefficiency of the system to

represent the atmospheric and wave conditions near the coastline under narrow fetch conditions. Nevertheless, two-way coupling even at these conditions offers small improvements.

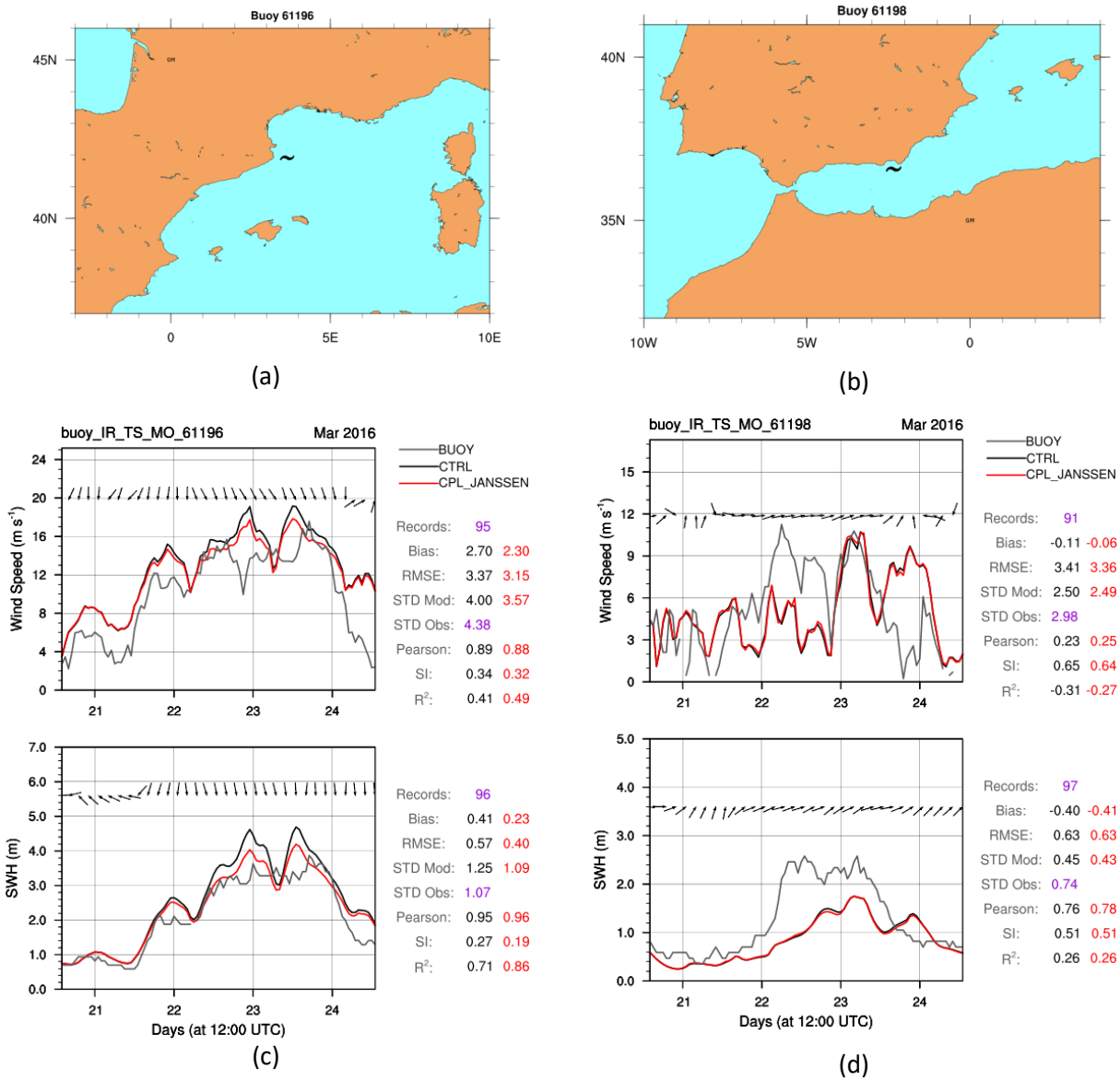

Figure 5.12: Location of Mediterranean buoys (a) 61196 and (b) 61198. Time series of wind speed (m s^{-1}) and SWH (m) based on the observations of Mediterranean buoy (c) 61196 and (d) 61198 (gray), CTRL (black) and CPL (red) simulations. The black arrows represent wind and SWH directions, measured by the buoy. On the right, the results of statistical evaluation through the calculation of statistical indices are illustrated. Time period from 21 March at 00:00 UTC to 25 March at 00:00 UTC, 2016.

Overall, Figure 5.13a shows that the two-way coupled simulation (with respect to the one-way coupled simulation) reduces the RMSE (~3%) and the bias error, improving the R^2 (~15%) and the SI (~4%) against buoys observations. On the other hand, CTRL yields slightly better correlation coefficient than the two-way coupling mode. As far as SWH is concerned, CPL reduces the RMSE (~12%) and improves the SI (~11%), as shown in Figure 5.13b. Moreover, CPL reduces bias error while the correlation coefficient is equal for both simulations. The results are characterized by high confidence level (>95%).

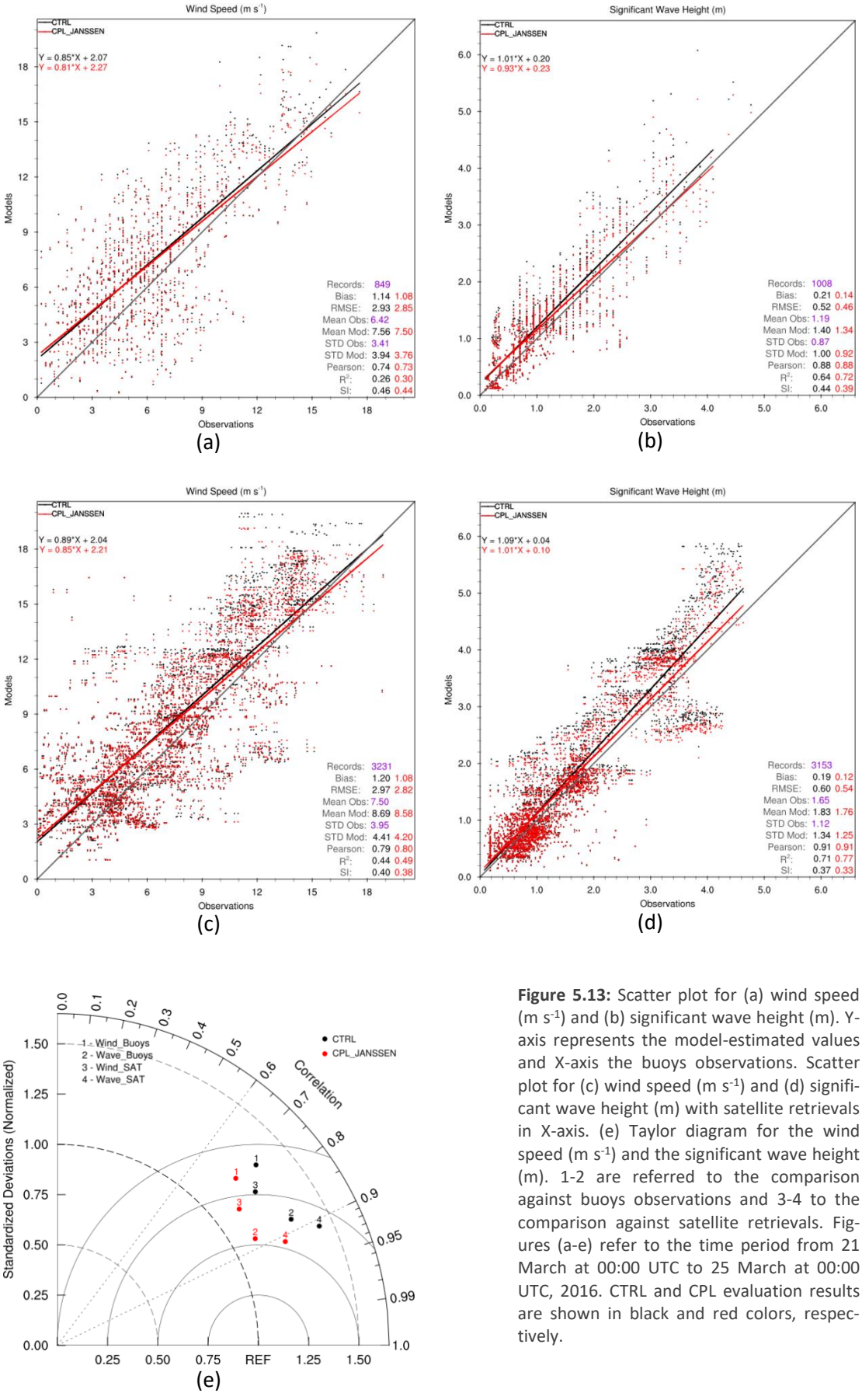

Figure 5.13: Scatter plot for (a) wind speed (m s^{-1}) and (b) significant wave height (m). Y-axis represents the model-estimated values and X-axis the buoys observations. Scatter plot for (c) wind speed (m s^{-1}) and (d) significant wave height (m) with satellite retrievals in X-axis. (e) Taylor diagram for the wind speed (m s^{-1}) and the significant wave height (m). 1-2 are referred to the comparison against buoys observations and 3-4 to the comparison against satellite retrievals. Figures (a-e) refer to the time period from 21 March at 00:00 UTC to 25 March at 00:00 UTC, 2016. CTRL and CPL evaluation results are shown in black and red colors, respectively.

Compared against satellite retrievals, the two-way coupled simulation offers reduction of approximately 5% to RMSE, decreasing bias error. Additionally, it improves the SI (~2.5%), the R^2 (~11%) and the Pearson coefficient (~1%) [Figure 5.13c]. The SWH is overestimated by both simulations (Figure 5.13d). Nevertheless, the two-way coupled simulation is characterized by lower bias error. Moreover, CPL reduces RMSE (10%) improving R^2 (~8%) and SI (~11%). It is also increases the correlation as it is shown in the Taylor diagram (Figure 5.13e).

5.2.2. Case Study C: 4-11 January, 2012

The weather incident of 4-11 January, 2012, has been selected due to the severity of the prevailed atmospheric conditions characterized by an explosive cyclogenesis in Ligurian Sea (Varlas et al., 2014; 2015). In more details, on 5 January 2012 a barometric low formed over the cyclogenetic area of the Ligurian Sea.

It was mainly triggered by a widespread upper-level trough extending from Central Europe to the Mediterranean Sea (Figure 5.14a). The upper-level trough rapidly intensified the system and supported its southeastern movement (Figure 5.14b). Figure 5.14 (c-d) shows that the system moved on 6 January towards the Eastern Mediterranean Sea, where the pressure dropped more than $24\times sin\varphi/sin60^{\circ}$ hPa in 24 h, classifying the event as explosive cyclogenesis (Sanders and Gyakum, 1980). During 6 and 7 January, the strong pressure gradient provoked gale force winds and significant storm surge over a vast area including Central Mediterranean Sea, Aegean Sea and Black Sea. It is noteworthy that the buoys at the Ligurian and Balearic Seas recorded wind speeds exceeding 20 m s^{-1} and significant wave height over 5 m.

In general, CPL experiment decreases wind speed and SWH mainly over the areas of maxima, as also observed in the previous case studies (Figure 5.15a-d). This reduction of wind speed and SWH is attributed to young wave generation since two-way coupling includes the effects of the resolved wave spectrum on the drag coefficient and its feedback on the momentum flux (Janssen, 1991). Figure 5.15 (e-h) demonstrates that such a feedback affects cyclogenesis, shallowing the surface barometric low (~1 hPa) and the upper-level trough (~ 4-7 gpm).

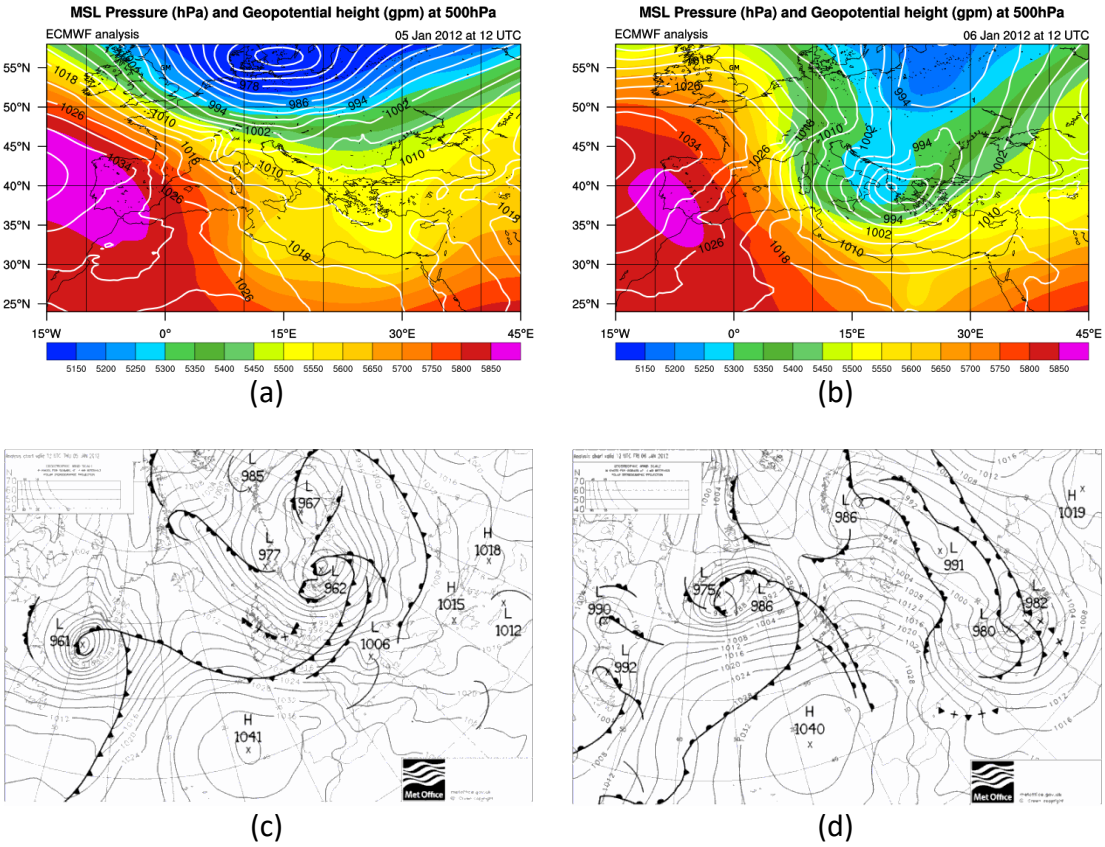

Figure 5.14: Mean Sea Level Pressure (contours in hPa) and geopotential height at 500 hPa (colored shaded in gpm) for (a) 5 January at 12:00 UTC and (b) 6 January at 12:00 UTC, 2012. Data are based on ECMWF operational analyses. Surface pressure analysis map (hPa) for (c) 5 January at 12:00 UTC and (d) 6 January at 12:00 UTC, 2012. The maps derived from UK Met office surface analyses archive.

As far as the comparison against buoys observations is concerned, Figure 5.16a shows that CPL (with respect to the CTRL experiment) reduces the RMSE (~3%) improving the R^2 (~6%) and the SI (~4%). Additionally, CPL reduces the bias error. Correlation coefficient Pearson is almost equal for both simulations. Moreover, CPL improves the statistical indices up to 6% for SWH (Figure 5.16b) presenting a slight underestimation as opposed to the overestimation of CTRL. This difference gets more significant as the wave height increases. This may be attributed to the dependence of two-way coupling impact on wind and wave intensity. Compared against satellite retrievals, CPL offers reduces the RMSE (2%) and the bias error. Additionally, it improves SI (~3%) and R^2 (~3%) while maintaining the Pearson coefficient (Figure 5.16c). The SWH is overestimated by CTRL run and underestimated by CPL run (Figure 5.16d). Furthermore, CPL reduces RMSE (~5%) and improves SI (~6%). The results are characterized by high confidence level (>95%). Summarizing, Taylor diagram indicates that two-way coupled simulation reduces RMSE and increases correlation, offering also improvements in standard deviation (Figure 5.16e).

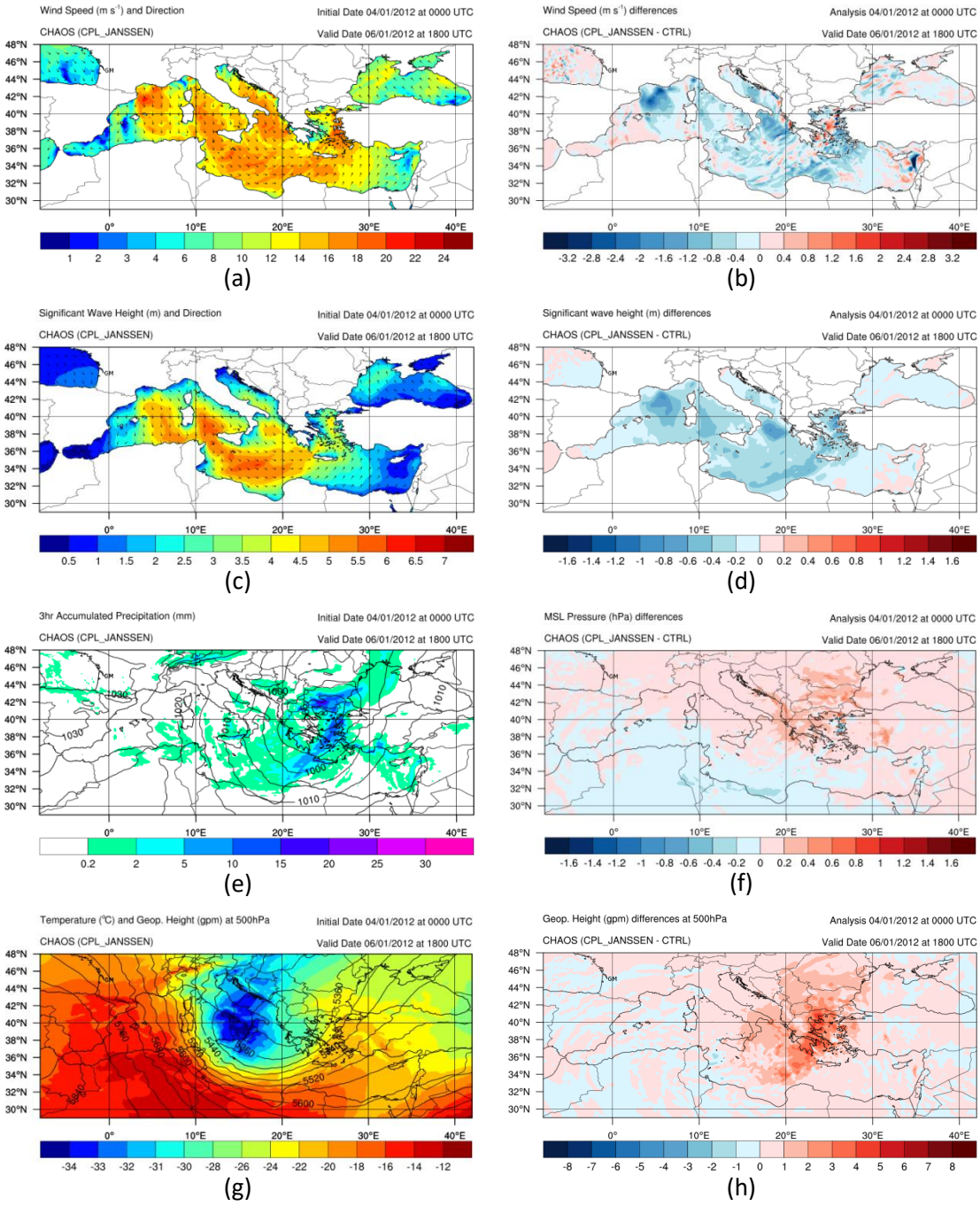

Figure 5.15: Horizontal distribution of (a) CPL wind speed (m s^{-1}) and direction, (b) wind speed (m s^{-1}) differences between CPL and CTRL, (c) CPL significant wave height (m) and direction, (d) significant wave height (m) differences between CPL and CTRL, (e) CPL MSLP (hPa) and 3hr accumulated precipitation, (f) MSLP (hPa) differences between CPL and CTRL, (g) CPL geopotential height (gpm) and temperature (°C) at 500 hPa and (h) geopotential height (gpm) differences between CPL and CTRL. Figures (a-h) refer to 6 January 2012 at 18:00 UTC.

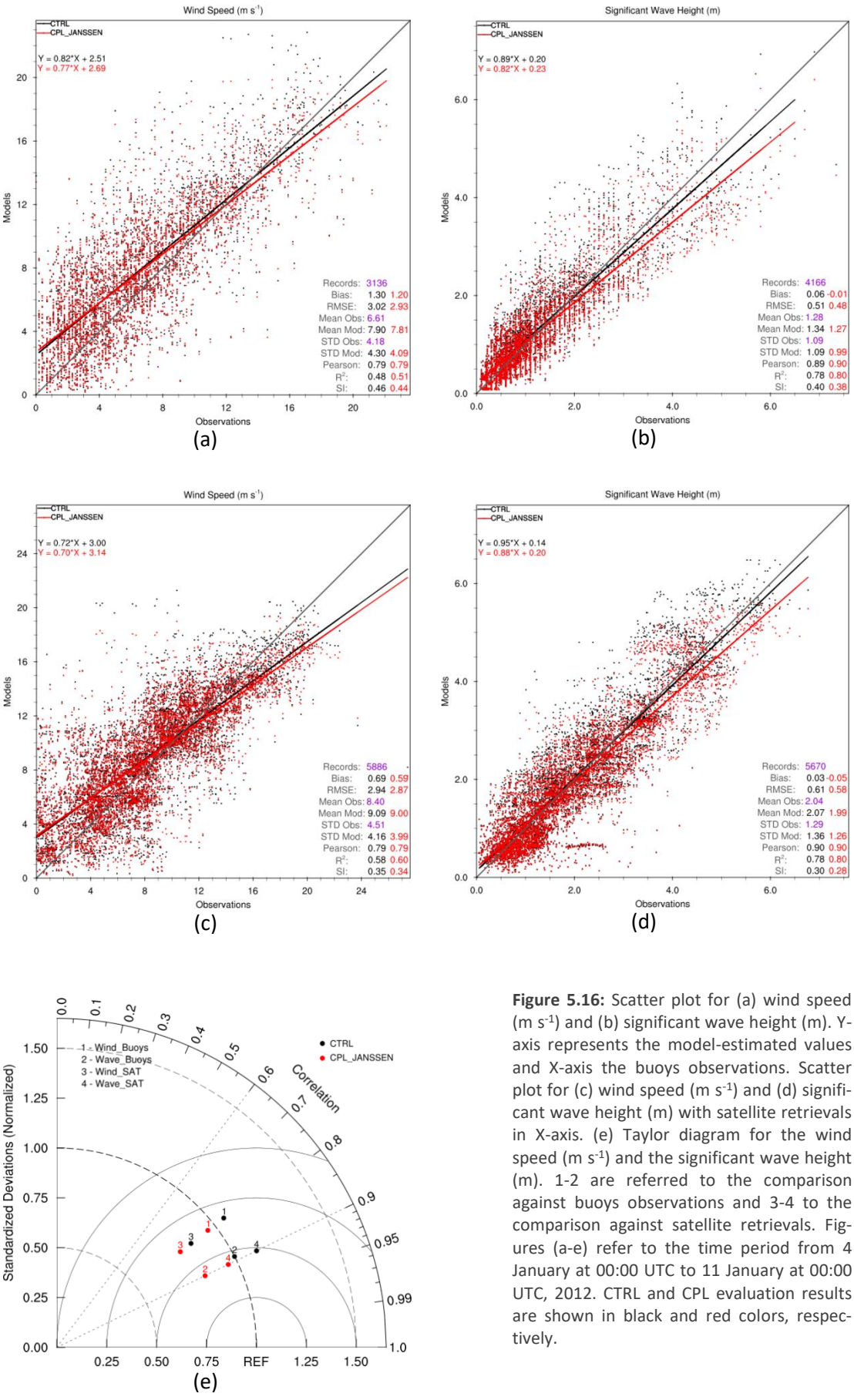

Figure 5.16: Scatter plot for (a) wind speed (m s^{-1}) and (b) significant wave height (m). Y-axis represents the model-estimated values and X-axis the buoys observations. Scatter plot for (c) wind speed (m s^{-1}) and (d) significant wave height (m) with satellite retrievals in X-axis. (e) Taylor diagram for the wind speed (m s^{-1}) and the significant wave height (m). 1-2 are referred to the comparison against buoys observations and 3-4 to the comparison against satellite retrievals. Figures (a-e) refer to the time period from 4 January at 00:00 UTC to 11 January at 00:00 UTC, 2012. CTRL and CPL evaluation results are shown in black and red colors, respectively.

5.2.3. Case Study D: 9-13 December, 2010

On 9 December, 2010, a barometric low system accompanied by fronts passed over Italy (Figure 5.17a). Moving on to the next days, the system deepened and provoked gale force winds over the Adriatic Sea, the Aegean Sea and the Black Sea due to the meridional invasion of an upper-level trough from central Europe (Figure 5.17b-d).

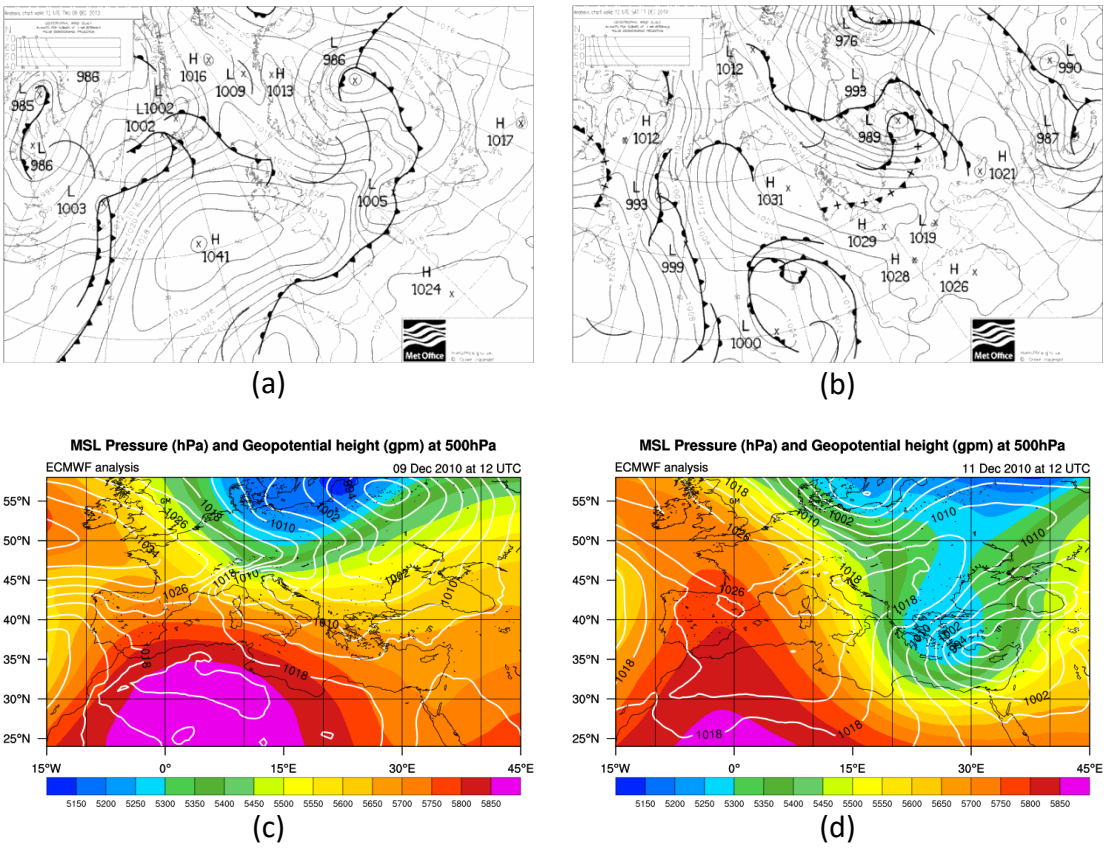

Figure 5.17: Surface pressure analysis map (hPa) for (a) 9 December at 12:00 UTC and (b) 11 December at 12:00 UTC, 2010. The maps derived from UK Met office surface analyses archive. Mean Sea Level Pressure (contours in hPa) and geopotential height at 500 hPa (colored shaded in gpm) for (c) 9 December at 12:00 UTC and (d) 11 December at 12:00 UTC, 2010. Data are based on ECMWF operational analyses.

The main characteristic of this case study is the spatial variability of wind and wave fields as the extreme phenomena were mainly located over a limited area (eastern Mediterranean Sea). The most remarkable observation to emerge from the Figure 5.18 (a-f) is that, CPL experiment decreases wind speed and SWH over the eastern Mediterranean and the Black Seas decaying the upper-level trough (~ 3-6 gpm) at 500 hPa.

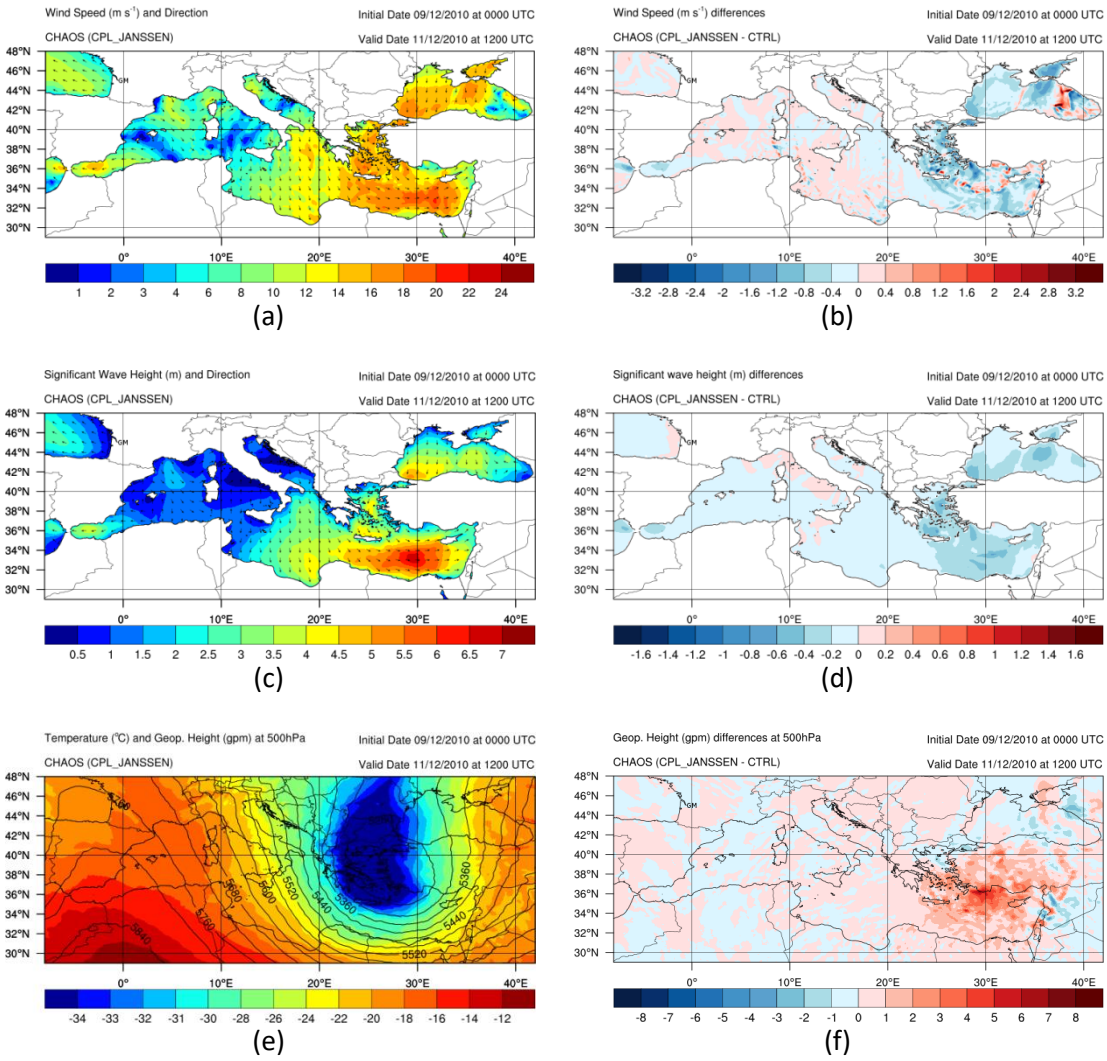

Figure 5.18: Horizontal distribution of (a) CPL wind speed (m s^{-1}) and direction, (b) wind speed (m s^{-1}) differences between CPL and CTRL, (c) CPL significant wave height (m) and direction, (d) significant wave height (m) differences between CPL and CTRL, (e) CPL geopotential height (gpm) and temperature (°C) at 500 hPa and (f) geopotential height (gpm) differences between CPL and CTRL. Figures (a-f) refer to 11 December 2010 at 12:00 UTC.

Compared against buoys observations, both simulation modes seem to overestimate the near surface wind speed. The overestimation is more prominent for wind speeds up to 15 m s^{-1} (Figure 5.19a). CPL run (with respect to the CTRL run) yields a reduction of the RMSE by approximately 2%. Additionally, CPL decreases the bias score and preserves the correlation improving R^2 and SI. The bias scores of the SWH indicate a slight overestimation for both simulations (Figure 5.19b). CPL offers an overall reduction of SWH bias and RMSE (~9%) improving Pearson, SI and R^2. Compared against remotely sensed data, CPL reduces the RMSE up to approximately 2% (Figure 5.19c).

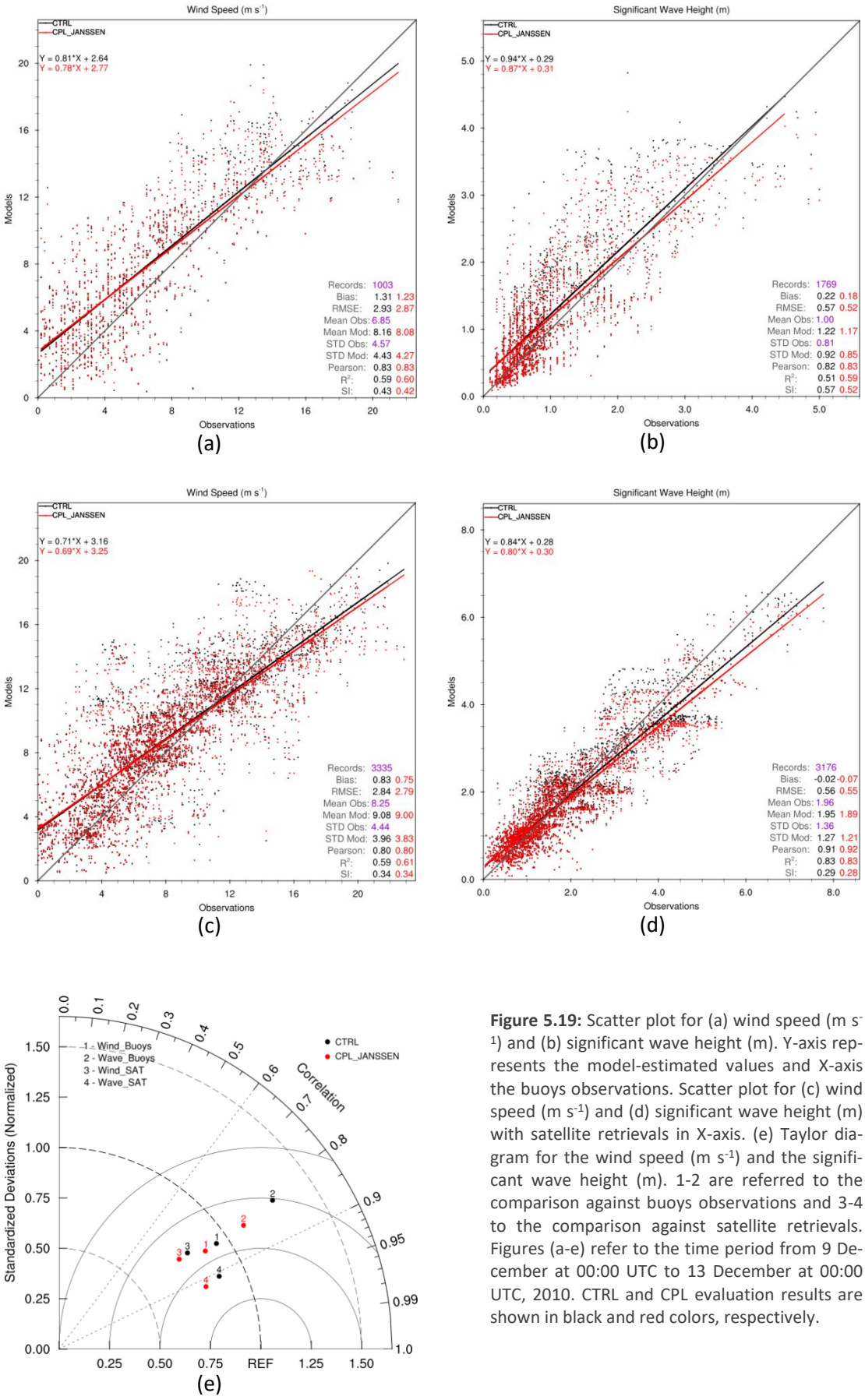

Figure 5.19: Scatter plot for (a) wind speed (m s^{-1}) and (b) significant wave height (m). Y-axis represents the model-estimated values and X-axis the buoys observations. Scatter plot for (c) wind speed (m s^{-1}) and (d) significant wave height (m) with satellite retrievals in X-axis. (e) Taylor diagram for the wind speed (m s^{-1}) and the significant wave height (m). 1-2 are referred to the comparison against buoys observations and 3-4 to the comparison against satellite retrievals. Figures (a-e) refer to the time period from 9 December at 00:00 UTC to 13 December at 00:00 UTC, 2010. CTRL and CPL evaluation results are shown in black and red colors, respectively.

Additionally, CPL decreases bias error as well as improves R^2 (~3%). The bias scores of the SWH indicate a slight underestimation for both simulations (Figure 5.19d). CTRL offers slightly better bias error than CPL. This may be attributed to the isolation of cyclonic evolution over the eastern Mediterranean Sea. The rest of the evaluation areas are characterized by low and moderate sea state conditions. Under these conditions two-way coupling do not offer many improvements (Wahle et al., 2017). However, CPL reduces RMSE (~2%) improving Pearson (~1%) and SI (~3%). The results are characterized by high confidence level (>95%). Moreover, Taylor diagram shows that two-way coupling offers smaller improvements than the other case studies (Figure 5.19e).

5.3. Long-term Study: 1 December 2013 - 1 December 2014

5.3.1. Simulation Configuration

In order to investigate the overall long-term performance of CHAOS over Mediterranean and Black Seas, continuous simulations for one-year period were conducted (Figure 5.20). The period from 1 December 2013 to 1 December 2014 was selected due to the adequate availability of buoys observations and satellite retrieval to support the statistical evaluation over sea. The simulation period begins on 1 December 2013 in order to evaluate the seasonality of the processes occur on the air-sea interface.

The execution of the continuous simulations was designed using an operational approach, based on the methodology proposed by Papadopoulos et al. (2011) as depicted on Figure 5.20. CHAOS was configured to a 30-h forecasting mode and 366 simulations were conducted to cover the one-year period (1 simulation was utilized as a warm-up for the wave spectrum + 365 simulations for each day of the one-year period). The first simulation was initialized on 30 November 00 UTC using ECMWF analyses for the atmospheric parameters (as atmospheric initial conditions; AIC) and the SST field. “Cold start” method was selected for the generation of wave spectrum (as wave initial conditions; WIC). For the next days, each simulation is initialized at 00 UTC based on ECMWF analyses while the ocean wave component was initialized on “hot start” mode based on the previous cycle wave spectrum estimation. This configuration implies that there is a 6-hour overlapping between the simulations of two consecutive daily cycles. However, the first 6-hour period of each simulation is actually considered as the spin-up time of the models. As a result, the data produced during this period are considered of lower quality and, therefore, discarded as proposed by various studies (e.g. Lo et al., 2008;

Thompson et al., 2016). Consequently, the model outputs that are actually considered in the final dataset of atmospheric and ocean wave parameters of the study are in the forecast window between the 6th and the 30th hour of each simulation.

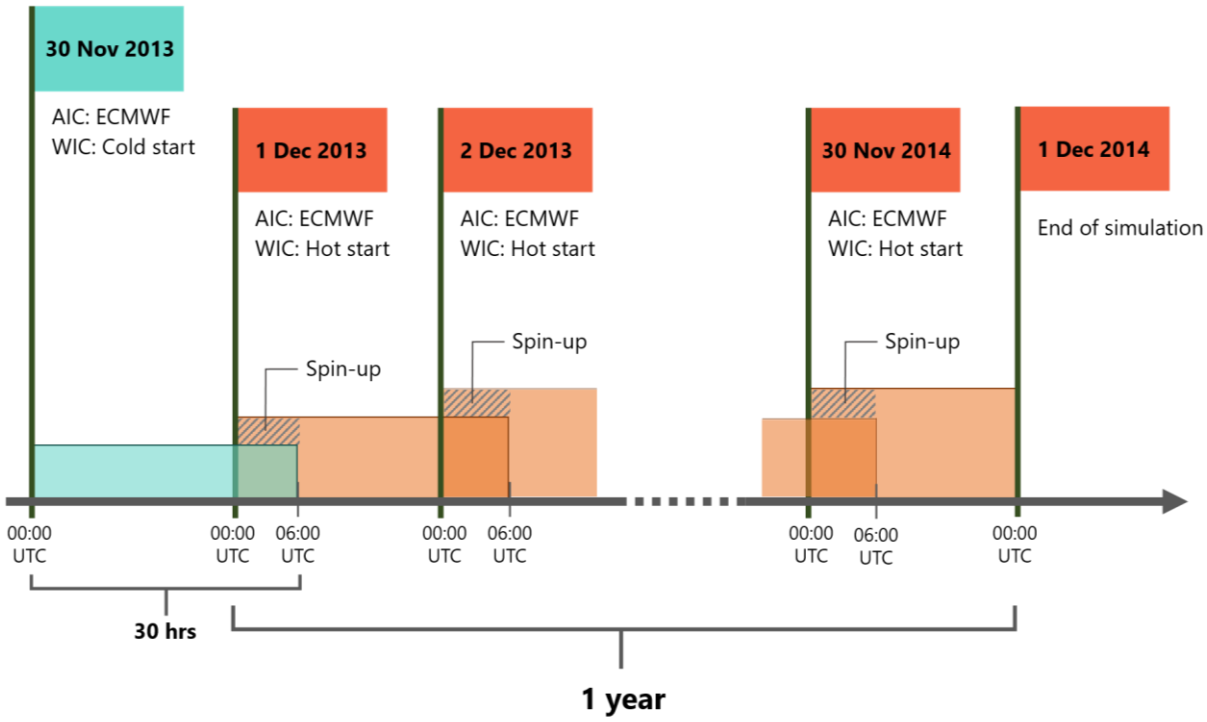

Figure 5.20: Long-term simulation timeline. Each simulation is initialized at 00:00 UTC and lasts 30 hours starting from 30 November 2013 until 1 December 2014. The crosshatched area represents the spin-up time (00:00-06:00 UTC) of each simulation. The atmospheric initial conditions (AIC) are based on ECMWF analyses while for wave initial conditions (WIC) "cold start" was applied for the 1st day and "hot start" for the rest of days.

5.3.2. Statistical Evaluation

In this section, the overall assessment of the CHAOS to perform simulations over a one-year period is discussed. The integration of the statistical scores over a large period usually hides the variations and the peaks of the forecast skill. It is noteworthy that better statistical scores are observed in some buoys during periods characterized by extreme weather events. For instance, in case of buoy 61196 at the Balearic Sea (Figure 5.21a) two-way coupling mode offers larger improvements under high wind and sea state conditions in comparison to its overall performance. In specific, for a 4-day period from 21 to 25 October 2014, which was characterized by gale-force winds and high waves over the Balearic Sea, two-way coupling offers wind speed and SWH improvements up to 12% and 34%, respectively.

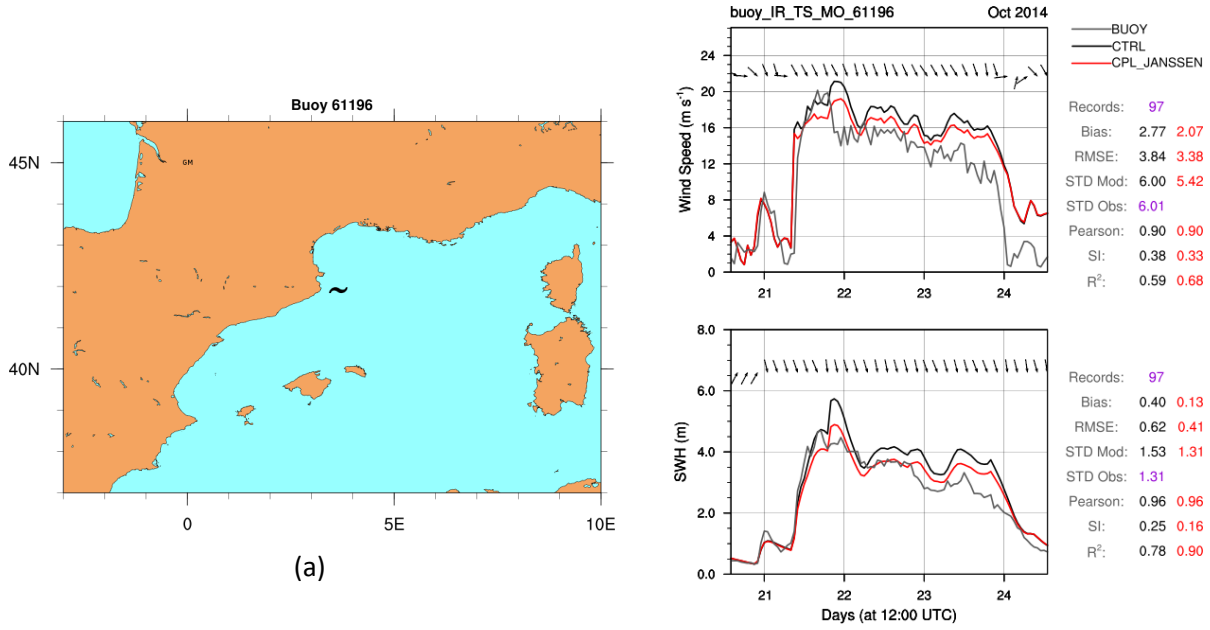

Figure 5.21: (a) Location of Mediterranean buoy 61196. Time series of wind speed (m s^{-1}) and SWH (m) based on the observations of Mediterranean buoy 61196 (gray), CTRL (black) and CPL (red) simulations. On the right, the results of statistical evaluation through the calculation of statistical indices are illustrated. Time period (b) from 21 October at 00:00 UTC to 25 October at 00:00 UTC, 2014. The black arrows represent wind and SWH directions, measured by the buoy. (c) Time period from 1 December at 00:00 UTC, 2013 to 1 December at 00:00 UTC, 2014.

On the other hand, the 1-year improvements for wind speed and SWH are up to 2% and 10%, respectively (Figure 5.21c). Despite the fact that these improvements are larger than the overall 1-year performance of two-way coupling, they are smaller than the improvements dur-

ing high wind and sea state conditions. Thus, two-way coupling massively reduces the forecast error mainly in cases of high wind and SWH conditions when one-way coupling is characterized by increased overestimation. This is attributed to the dependence of the two-way coupling contribution on wind and wave intensity (e.g. Desjardins et al., 2000; Katsafados et al., 2016a; Wahle et al., 2017).

Overall, compared against buoys observations a systematic overestimation of the wind speed is evidenced for both simulations. The positive biases are speculated to be mainly due to inaccuracies of the PBL and surface layer schemes in WRF (Katsafados et al., 2011; Shimada and Ohsawa, 2011; Jimenez et al., 2012). However, the results of CPL run yield a reduction of RMSE (~1%) improving the R^2 (~4%) and the SI (~2%) [Figure 5.22a]. The overall improvement in the wind speed has positive effect in SWH. Thus, CPL reduces bias error and RMSE (~6%) while improving R^2 (~4%) and SI (5%) [Figure 5.22b]. Moreover, CPL contributes to equivalent correlation coefficient as CTRL run. The results are characterized by high confidence level (>95%).

The systematic overestimation of the wind speed and the SWH exists also in the evaluation against satellite retrievals. Similar performance was also demonstrated by the A-D case studies statistical scores. This may be attributed to the fact that buoys of the Mediterranean Sea are near shore located where the simulation errors are mainly exaggerated due to the inadequate representation of the complex coastlines and the inaccurate resolve of the shallow water wave reflection. On the other hand, satellite retrievals refer to offshore areas and fit better with the model gridded values than the buoys measurements since they represent area-averaged values (see Figure 4.7 and Figure 4.8). Additionally, remotely sensed data are characterized by a systematic overestimation compared to buoys observations (Ardhuin et al., 2007; Zieger et al., 2009; Abdalla et al., 2010; Durrant et al., 2010). For that reason, CHAOS presents lower overestimation against remotely sensed data than against buoys measurements. Figure 5.22c indicates that the overestimation is more prominent for lower wind speeds and CPL presents an overall improvement up to 0.5-2.4% in the wind speed. The SWH is underestimated by both experiments with slightly better bias error for CTRL mode (Figure 5.22d). Moreover, CPL offers statistical improvements up to 2.7% for the majority of statistical indices.

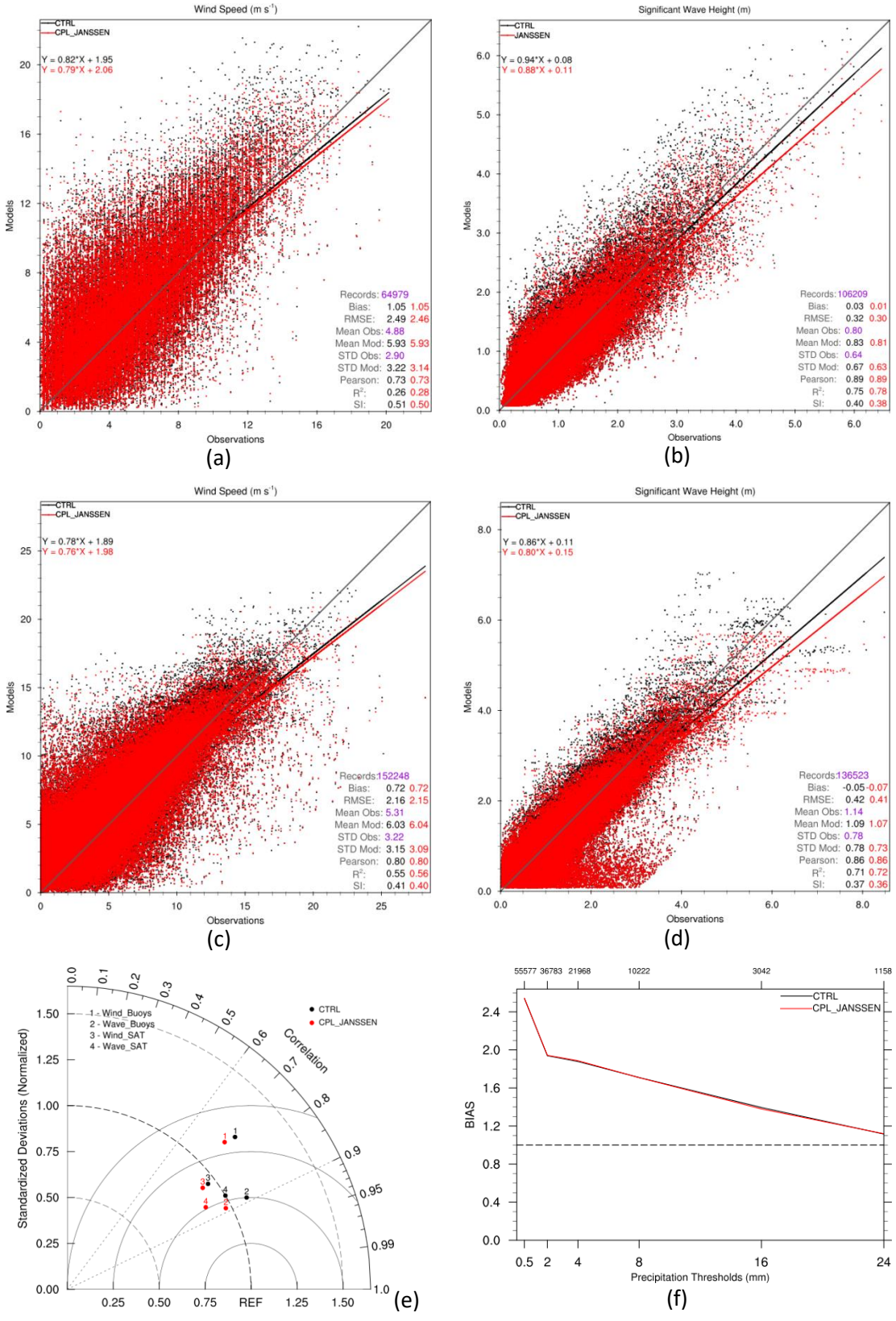

Figure 5.22: Scatter plot for (a) wind speed (m s^{-1}) and (b) significant wave height (m). Y-axis represents the model-estimated values and X-axis the buoys observations. Scatter plot for (c) wind speed (m s^{-1}) and (d) significant wave height (m) with satellite retrievals in X-axis. (e) Taylor diagram for the wind speed (m s^{-1}) and the significant wave height (m). 1-2 are referred to the comparison against buoys observations and 3-4 to the comparison against satellite retrievals. (f) BIAS for specific 6-hour precipitation (mm) thresholds. The numbers above each tick mark denote the sample for the corresponding threshold value. Figures (a-f) refer to the time period from 1 December at 00:00 UTC, 2013 to 1 December at 00:00 UTC, 2014. CTRL and CPL evaluation results are shown in black and red colors, respectively.

The Taylor diagram (Figure 5.22e) confirms the improved overall performance of CPL. The positions of dots 1 and 3 indicates that the CPL simulated wind speed is characterized by lower standard deviation than the CTRL run. Additionally, the diagram shows that CPL offers better RMSE and correlation. The locations of dots 2 and 4 demonstrate that CPL improves RMSE, STD and correlation for the SWH.

The statistical scores and the scatter plot for wind speed, MSLP, temperature and precipitation over the land are almost undistinguishable for both CTRL and CPL. Both simulations underestimate temperature and MSLP and overestimate wind speed. The statistical results agree with previous studies for the WRF model performance (e.g. Katsafados et al., 2011). Additionally, both simulations yield an overestimation of precipitation which gradually decreases for moderate and high thresholds (Figure 5.22f).

5.4. Summary of Statistical Evaluation Results

This section summarizes the CHAOS performance for the 4 case studies and the long-term operational approach analyzed in this chapter. The statistical scores of wind speed and SWH over the sea produced by one-way (CTRL) and two-way (CPL) coupling modes against buoys observations and satellite retrievals are summarized in Tables 5.1 – 5.4. It is obvious that two-way coupling concentrates its improvements in cases characterized by intense wind and sea state conditions, as also observed by Katsafados et al. (2016a) and Wahle et al. (2017). In case studies A-D, two-way coupling reduces the RMSE up to 5% and 20% for wind speed and SWH, respectively. The long-term RMSE reduction reaches 1.2% and 6.3% for wind speed and SWH, respectively. This is attributed to the fact that low and moderate wind and wave conditions are dominant in a long-term operational approach reducing the improvements of the forecast skill attributed to higher intensities. Additionally, two-way coupling improvements are evidenced especially over open sea. This may be attributed to the fact that wave spectrum intensity is dependent to wind-generated waves and, consequently, to near surface wind speed and fetch (Janssen, 2004). Over open-sea long-fetch areas, the surface layer of two-way coupled simulation incorporates rougher sea surface information in comparison to the one-way coupling mode. This causes reduction of wind speed and intense attenuation of wind-generated waves decreasing the overestimation of SWH. This reduction mechanism is more prominent over open sea than over short-fetch areas near the shore. Moreover, SWH is sensitive on near surface wind speed

and, thus, a small decrease of wind speed can cause a more intense decrease of SWH (e.g. de León and Soares, 2008).

Furthermore, two-way coupling slightly improves the forecast skill over the land. All the simulations overestimate wind speed and underestimate temperature and MSLP. The statistical scores reflect the intrinsic forecast skill of WRF and they are in agreement with previous studies regarding WRF model performance (e.g. Katsafados et al., 2011; Shimada and Ohsawa, 2011). However, two-way coupling mode of CHAOS offers up to ~1% RMSE reduction over the land which may be attributed to the impact of ocean waves on the tropospheric processes. The impact of two-way coupling over the sea is characterized by teleconnection effects on atmospheric flow and stability up to mid- to upper-tropospheric levels, modifying the dynamical and thermodynamic mechanisms of PBL and cloud microphysics even over the land.

Table 5.1: Summary of CHAOS wind speed statistical scores against buoys observations for the 4 case studies and the long-term study in one-way (CTRL) and two-way (CPL) modes.

	Case A			Case B			Case C			Case D			Long-term		
	CTRL	CPL	%	CTRL	CPL	%	CTRL	CPL	%	CTRL	CPL	%	CTRL	CPL	%
Bias	0.89	**0.81**	9	1.14	**1.08**	5.3	1.30	**1.20**	7.7	1.31	**1.23**	6.1	1.06	1.06	0
RMSE	3.05	**2.95**	3.3	2.93	**2.85**	2.7	3.02	**2.93**	3	2.93	**2.87**	2	2.48	**2.45**	1.2
Pearson	0.80	**0.81**	1.3	**0.74**	0.73	1.4	0.79	0.79	0	0.83	0.83	0	**0.74**	0.73	1.4
R^2	0.55	**0.58**	5.5	0.26	**0.30**	15	0.48	**0.51**	6.3	0.59	**0.60**	1.7	0.27	**0.28**	3.7
SI	0.43	**0.42**	2.3	0.46	**0.44**	4.3	0.46	**0.44**	4.3	0.43	**0.42**	2.3	0.51	**0.50**	2

Table 5.2: Summary of CHAOS wind speed statistical scores against satellite retrievals for the 4 case studies and the long-term study in one-way (CTRL) and two-way (CPL) coupling modes.

	Case A			Case B			Case C			Case D			Long-term		
	CTRL	CPL	%	CTRL	CPL	%	CTRL	CPL	%	CTRL	CPL	%	CTRL	CPL	%
Bias	0.96	**0.77**	9.4	1.20	**1.08**	10	0.69	**0.59**	14	0.83	**0.75**	9.6	0.72	0.72	**0**
RMSE	2.54	**2.42**	4.7	2.97	**2.82**	5	2.94	**2.87**	2.4	2.84	**2.79**	1.8	2.16	**2.15**	0.5
Pearson	0.86	0.86	0	0.79	**0.80**	1.3	0.79	0.79	0	0.80	0.80	0	0.80	0.80	0
R^2	0.68	**0.71**	4.4	0.44	**0.49**	11	0.58	**0.60**	3.4	0.59	**0.61**	3.4	0.55	**0.56**	1.8
SI	0.31	**0.29**	6.5	0.40	**0.38**	5	0.35	**0.34**	2.9	0.34	0.34	0	0.41	**0.40**	2.4

Table 5.3: Summary of CHAOS significant wave height (SWH) statistical scores against buoys observations for the 4 case studies and the long-term study in one-way (CTRL) and two-way (CPL) coupling modes.

	Case A			Case B			Case C			Case D			Long-term		
	CTRL	CPL	%	CTRL	CPL	%	CTRL	CPL	%	CTRL	CPL	%	CTRL	CPL	%
Bias	0.31	**0.20**	36	0.21	**0.14**	33	0.06	**-0.01**	83	0.22	**0.18**	18	0.03	**0.01**	67
RMSE	0.68	**0.64**	5.9	0.52	**0.46**	12	0.51	**0.48**	5.9	0.57	**0.52**	8.8	0.32	**0.30**	6.3
Pear-son	0.90	0.90	0	0.88	0.88	0	0.89	**0.90**	1.1	0.82	**0.83**	1.2	0.89	0.89	0
R^2	0.75	**0.78**	4	0.64	**0.72**	13	0.78	**0.80**	2.6	0.51	**0.59**	16	0.75	**0.78**	4
SI	0.44	**0.42**	4.5	0.44	**0.39**	11	0.40	**0.38**	5	0.57	**0.52**	8.8	0.40	**0.38**	5

Table 5.4: Summary of CHAOS significant wave height (SWH) statistical scores against satellite retrievals for the 4 case studies and the long-term study in one-way (CTRL) and two-way (CPL) coupling modes.

	Case A			Case B			Case C			Case D			Long-term		
	CTRL	CPL	%	CTRL	CPL	%	CTRL	CPL	%	CTRL	CPL	%	CTRL	CPL	%
Bias	0.20	**0.08**	60	0.19	**0.12**	37	**0.03**	-0.05	67	**-0.02**	-0.07	250	**-0.05**	-0.07	40
RMSE	0.59	**0.47**	20	0.60	**0.54**	10	0.61	**0.58**	4.9	0.56	**0.55**	1.8	0.42	**0.41**	2.4
Pear-son	0.92	0.92	0	0.91	0.91	0	0.90	0.90	0	0.91	**0.92**	1.1	0.86	0.86	0
R^2	0.73	**0.83**	14	0.71	**0.77**	8.5	0.78	**0.80**	2.6	0.83	0.83	0	0.71	**0.72**	1.4
SI	0.32	**0.26**	19	0.37	**0.33**	11	0.30	**0.28**	6.7	0.29	**0.28**	3.4	0.37	**0.36**	2.7

Chapter 6

Implementation and Impact of Nesting Techniques

6.1. Configuring Nesting in CHAOS

The nesting capabilities of WRF have been employed configuring CHAOS accordingly. The nesting capabilities in WAM were not investigated and, thus, WAM is configured to run in one high-resolution domain. As far as WRF is concerned, the implementation of a uniformly high resolution over a large domain requires an excessive amount of computational resources. Nesting enables simulations at finer resolution over a sub-domain of interest avoiding this problem (Bhaskar Rao et al., 2009). A nest is a finer-resolution model run which may be embedded simultaneously within a coarser-resolution (parent) model run. The nest covers a portion of the parent domain and is driven along its lateral boundaries by the parent domain. CHAOS arrangement of nested grid domain permits use of fine resolution to resolve the air-sea processes embedded in the larger parent domain. Thus, the atmospheric component is configured to run on a parent domain covering the Mediterranean Sea and the Black Sea while using a nested sub-domain including the central and eastern Mediterranean and a large part of the Black Sea as shown in Figure 6.1. In this context, the use of nesting offers reduces computing time in comparison to the use of one large domain with very high resolution for the entire area of parent domain. Nesting in WRF resolves additional frequencies at the tail of the atmospheric spectrum modifying the momentum and heat fluxes over the air-sea interface. Additionally, the advantage of such approach is that WAM is driven by finer resolution wind fields produced by the nested domain of WRF, returning more detailed roughness information to both domains of WRF.

This alternative configuration of the system required several modifications to its native procedures. Due to the fact that the single domain of WAM should exchange information with both the parent and the nested domains of WRF, the number of variables exchanged between the atmospheric and wave components was doubled. Moreover, the capability to select the wind source for WAM from the parent or the nested domain of WRF was incorporated in CHAOS. The number of grid, mask and restart files utilized by the system was doubled and, consequently, additional auxiliary files for both parent and nested domains were needed. The methodology used for the regridding and the exchange of information between WAM and the nested domain of WRF through the OASIS coupler is similar to that used for parent domain as described at Chapter 4. It is noteworthy that, the definition of the LAG value (see more in Appendix) was a critical decision of the implementation of nesting in CHAOS. For the synchroniza-

tion among the components and domains, LAG should be equal to the time step of the nested domain of WRF.

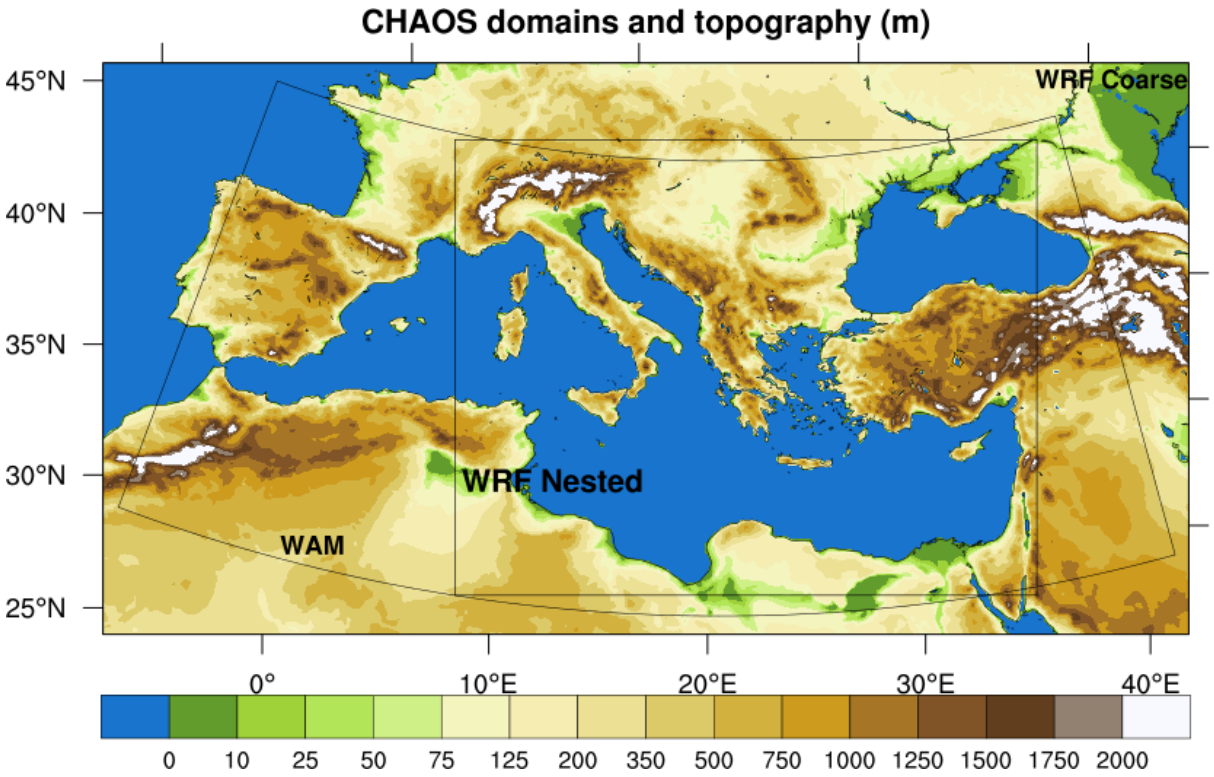

Figure 6.1: Parent or coarse and nested (black line) domain configurations of WRF and WAM (black line) models of CHAOS and topography (m) distribution used by WRF are depicted.

Several tests were performed using nesting in WRF in various horizontal resolutions. Despite the fact that the system supports multiple domains, the use of two domains for WRF proved to be efficient. As abovementioned WAM utilized one high-resolution domain in all the tests, without the investigation of its nesting capabilities. Finally, the parent domain of WRF covers the Mediterranean Sea and the Black Sea in horizontal resolution of 9km x 9km with 550x290 C-grid points and the nested domain (black line) covers the eastern Mediterranean and the Black Seas in horizontal resolution of 3km x 3km with 883x691 C-grid points. It is noteworthy that the parent domain of this configuration is different from the single domain of 10km x 10km configuration (Section 4.2). Due to higher resolution of the nested domain, the description of topography is much more detailed (Figure 6.2). The finer resolution of the nested domain improves the representation of the complex landscape characteristics and land-sea dis-

continuities that generate local circulations and finally affect the air-sea interaction processes. Time steps of 60 sec and 20 sec are used for the integration of the numerical procedures for the parent and the nested domain, respectively. The grid of WAM for the Mediterranean and Black Seas covers the geographical area 8° W - 42° E and 29° N - 48° N as shown in Figure 6.1 (black line) using high resolution of 0.05°x0.05° (higher than the 10km x 10km configuration; Section 4.2) with 1001x381 regular lat-lon points. WAM has a propagation time step of 37.5 sec and source time step 300 sec (5 min). The coupling procedure exchanges data on the source time step of WAM model, every 300s. Moreover, the MPI topology of the system was configured according to scalability tests in supercomputer ARIS (Section II). The tests showed similar computing behavior with the 10 km x 10 km configuration (Section 4.2) increasing the CPUs. Finally, the MPI topology (in supercomputer ARIS) using 140 and 20 CPUs for atmospheric and ocean wave components respectively was found to be the most efficient. The rest of the characteristics and the parameterization schemes are equivalent to those used in 10 km x 10 km configuration (Section 4.2).

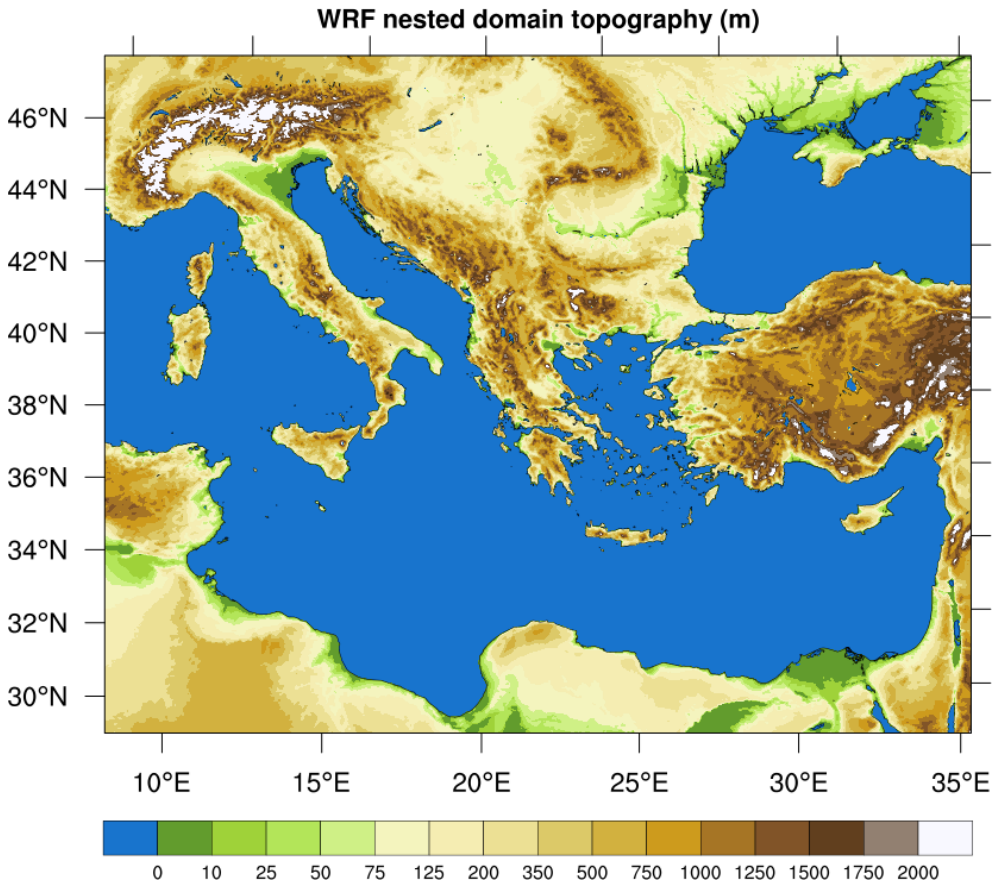

Figure 6.2: CHAOS nested domain topography (m).

Table 6.1: Configuration of CHAOS with nesting

CHAOS	Atmospheric Component	Ocean Wave Component
Model	WRF-ARW, WRF-Chem V3.8 and WRF-Hydro V3.0	WAM Version 4.5.4
Coupler	OASIS3-MCT Version 3.0	
Integration Domain	Mediterranean Sea, Europe, Black Sea	
Grid	Arakawa semi-staggered C-grid	Spherical latitude-longitude grid
Horizontal grid Increment	9km x 9km with nested 3km x 3km	0.05°x0.05°
Spectral resolution	–	24 directional bins (15° directional resolution), 25 frequency bins (ranging from 0.042 to 0.411 Hz)
Vertical coordinate	Terrain-following hydrostatic pressure η coordinate	–
Vertical levels	38	–
Time steps	Parent domain: 60 s and nested: 20 s	Propagation time step: 37.5 s Source time step: 300 s
Initial & boundary Conditions	ECMWF, 0.5°x0.5° 17 isobaric levels 6h update of boundary conditions	Hot start
SST	ECMWF SST update every 6 hours	–
Exchange rate	300 s	
Surface layer	Revised Monin-Obukhov	–
PBL	YSU	–
Microphysics	Thompson	–
Cumulus	Kain-Fritsch	–
Land surface	Unified NOAH	–
Radiation	RRTM and Dudhia schemes	–
Chemistry options	Disabled	–
Coupled to WRF-Hydro	Disabled	–
Topography	30-arc-second USGS GMTED2010	–
Vegetation	MODIS FPAR	–
Land-use	21-class IGBP MODIS	–
Bathymetry	–	ETOPO1
Water approximation	–	Shallow water approximation with depth refraction and wave breaking due to depth change near shore
MPI topology	140 CPUs	20 CPUs

6.2. Sensitivity Tests and Statistical Impact of Nesting

This section is dedicated to the results of the sensitivity tests and the statistical evaluation of CHAOS using nesting (more information at Chapter 6.1) for a selected case study. Case study C (4-11 January 2012) was chosen for this purpose due to the moderate performance of the two-way coupling and the rapid cyclogenesis of the system characterized by small spatiotemporal scale processes. In order to assess the performance of two-way coupling mode using wind fields from the nested WRF domain in WAM, two simulations were designed:

- WAM_coarse_wind: WAM uses wind fields produced by the parent (coarse) domain of WRF.
- WAM_nest_wind: WAM uses wind fields produced by the nested domain of WRF. However, the wind fields produced by the nested domain of WRF do not cover the entire domain of WAM and, thus, wind field values produced by the parent domain of WRF are additionally used for the areas out of nested domain. A 1-2-1 smoothing filter (e.g. Katsafados et al., 2016a) is applied over the transition zone of nested and parent wind fields in order to reduce the wind discontinuities.

Hence, the difference between the two simulations is the origin of the wind fields that are used as input to WAM. Both simulations are two-way coupled using the Janssen parameterization while two domains of WRF and one domain of WAM are exchanging the parameters described in Section 4.1.1. The results of both simulations for wind speed used by WAM and SWH have been statistically evaluated against buoys observations, satellite retrievals and land surface measurements enclosed in the WRF nested domain area. A summary of the most important statistical scores is available in Table 6.2 at the end of the section.

The horizontal distribution of the wind speed and direction for the WAM_coarse_wind experiment on 6 January 2012 at 12:00 UTC, is depicted in Figure 6.3a. Additionally, the differences between WAM_nest_wind and WAM_coarse_wind experiments for wind speed are illustrated in Figure 6.3b. WAM_coarse_wind wind speed ranges from 14 m s^{-1} to 20 m s^{-1} over a widespread area of the Mediterranean Sea. WAM_nest_wind experiment mainly increases wind speed with local differences exceeding 3 m s^{-1} more prominent over the areas with the maximum wind speeds. As expected, the differences are located mainly over the nested domain area. A percentage of these differences is artificial due to the scales resolved by the domains. The differences are mainly raised from the additional mesoscale frequencies of the at-

mospheric spectrum that are resolved by the nested domain as also described by Mass et al. (2002). As shown in Figure 6.3c, SWH follows the distribution of wind speed, presenting local values exceeding 5 m. WAM_nest_wind experiment reveals a systematic increase of SWH exceeding 0.4 m mainly over nested domain (Figure 6.3d). The increase of SWH is attributed to the mesoscale and local scale features that are resolved by nesting offering additional energy to the atmospheric flow and, consequently, to the wind-wave generation (Mass et al., 2002; Janssen, 2004). Nested domain involves rapidly-varying winds and short-wavelength atmospheric processes near sea surface which support an additional growth of young wind-waves. This affects sea surface roughness, surface layer processes and even the MABL and tropospheric properties. The mechanisms of wind-generated waves and their impact to sea state and atmospheric conditions are also analyzed in Sections 2.2 and 5.1.2.

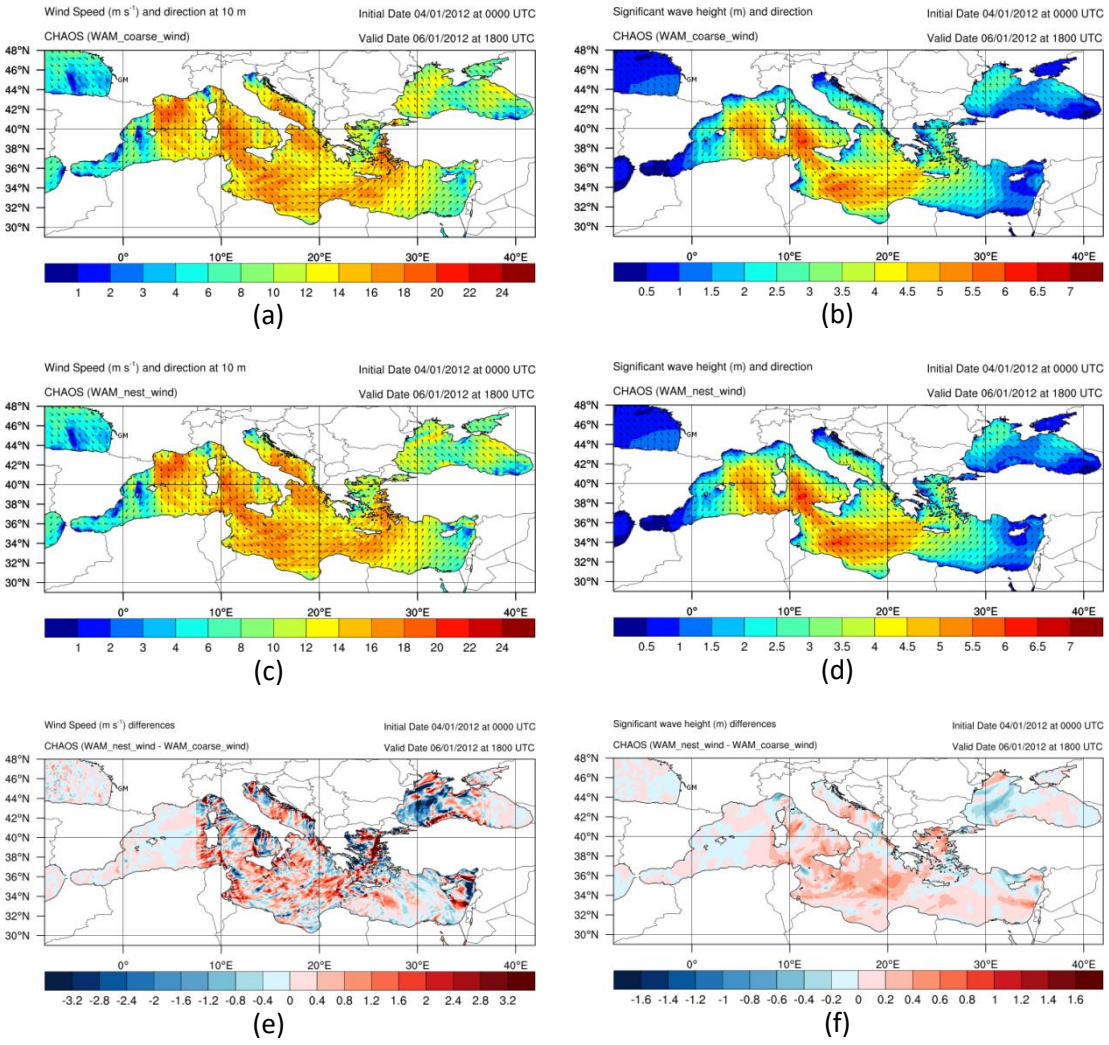

Figure 6.3: Horizontal distribution of WAM_coarse_wind (a) wind speed (m s^{-1}) and direction and (b) significant wave height (m) and direction. Horizontal distribution of WAM_nest_wind (c) wind speed (m s^{-1}) and direction and (d) significant wave height (m) and direction. Horizontal distribution of (e) wind speed (m s^{-1}) and (f) significant wave height (m) differences between WAM_nest_wind and WAM_coarse_wind experiments. Figures (a-f) refer to 6 January 2012 at 18:00 UTC.

The two simulations are statistically assessed against buoys observations, remotely sensed data and land surface measurements only over the nested domain area. It is noteworthy that, WAM_nest_wind presents local effects on the overestimation of wind speed and underestimation of SWH improving RMSE. In the case of buoy Cetraro over the Tyrrhenian Sea (Figure 6.4a) the RMSE reduction reaches 11% and 16% for wind speed and SWH, respectively (Figure 6.4b).

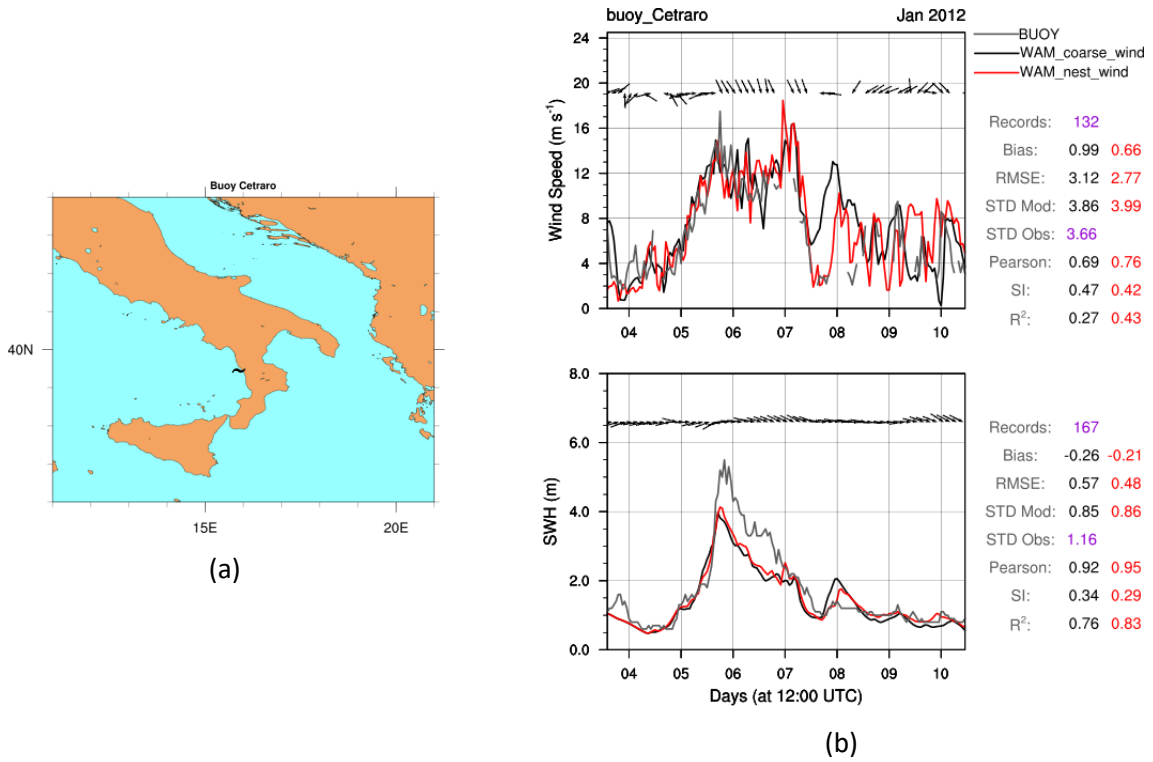

Figure 6.4: (a) Location of Mediterranean buoy Cetraro. (b) Time series of wind speed (m s^{-1}) and SWH (m) based on the observations of Mediterranean buoy Cetraro (gray), WAM_coarse_wind (black) and WAM_nest_wind (red) simulations. The black arrows represent wind and SWH directions, measured by the buoy. On the right, the results of statistical evaluation through the calculation of statistical indices are illustrated. Time period from 4 January at 00:00 UTC to 11 January at 00:00 UTC, 2012.

Overall, both simulations present a systematic overestimation of wind speed against buoys observations (Figure 6.5a). The overestimation is more prominent for low and moderate intensities. WAM_nest_wind (with respect to the WAM_coarse_wind simulation) reduces the RMSE (~4%) improving the R^2 (~9%), the Pearson coefficient (~4%) and the SI (~2%). The results are characterized by high confidence level (>95%). Additionally, WAM_nest_wind decreases the bias error. As far as SWH is concerned, WAM_nest_wind reduces the RMSE (~8%) improving the R^2 (~4%), the Pearson coefficient (~1%) and the SI (~8%) [Figure 6.5b]. Compared against satellite retrievals, WAM_nest_wind presents worse bias error, RMSE (~1%) and R^2 (~1%) for the wind speed (Figure 6.5c). The SWH is underestimated by both runs (Figure 6.5d).

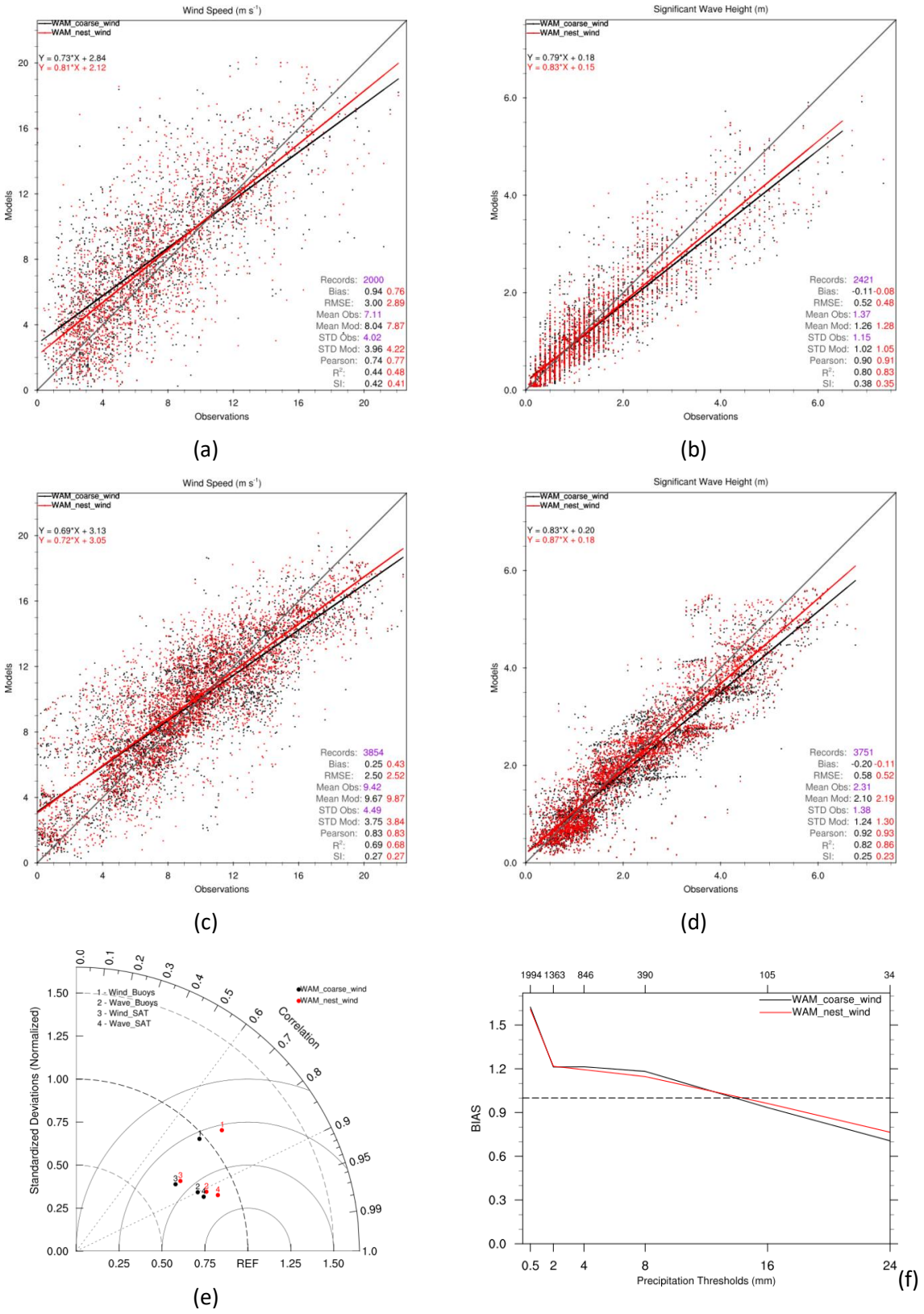

Figure 6.5: Scatter plot for (a) wind speed (m s^{-1}) and (b) significant wave height (m). Y-axis represents the model-estimated values and X-axis the buoys observations. Scatter plot for (c) wind speed (m s^{-1}) and (d) significant wave height (m) with satellite retrievals in X-axis. (e) Taylor diagram for the wind speed (m s^{-1}) and the significant wave height (m). 1-2 are referred to the comparison against buoys observations and 3-4 to the comparison against satellite retrievals. (f) BIAS for specific 6-hour precipitation (mm) thresholds. The precipitation data refer to the nested domain of atmospheric component. The numbers above each tick mark denote the sample for the corresponding threshold value. Figures (a-f) refer to time period from 4 January at 00:00 UTC to 11 January at 00:00 UTC, 2012. WAM_coarse_wind and WAM_nest_wind evaluation results are shown in black and red colors, respectively. Buoys observations, remotely sensed data and land surface measurements only over the nested domain area are used in the statistical assessment.

WAM_nest_wind reduces the RMSE (~10%) improving the R^2 (~5%), the Pearson coefficient (~1%) and the SI (~8%). Overall, as shown by the Taylor diagram of Figure 6.5e, WAM_nest_wind improves the ratio between the modeled STD and the STD of observations mainly for SWH. This may be attributed to the resolve of mesoscale processes which can increase wind speed variations offering more wind-generated waves. Additionally, the diagram shows that the two simulations have almost similar correlations and RMSEs.

The results of the two simulations produced by the nested domain of WRF are statistically evaluated against land surface measurements. Negligible differences are observed for wind speed, MSLP and temperature. As far as precipitation is concerned, both runs yield an overestimation for low thresholds and an underestimation for high thresholds (Figure 6.5f). WAM_nest_wind offers slightly better BIAS score (nearest to the value 1) for medium and high thresholds. The response over the land is attributed to sea waves reflection on atmospheric conditions which determine the distribution and intensity of precipitation as analyzed in Section 5.1.2.

The statistical scores of the wind speed and SWH values as produced by WAM_coarse_wind and WAM_nest_wind experiments against buoys observations and satellite retrievals are summarized in Table 6.2. The results unveil an interesting finding. Wind fields produced by the nested domain of WRF incorporate more detailed information for the near surface atmospheric conditions in WAM. These also include the synergistic effects of a larger range of processes improving wind-wave generation. This is statistically reflected to the overall RMSE reduction of SWH up to 10%. The improved wave growth has, consequently, positive feedback to surface layer processes near the shore yielding RMSE reduction up to 3.7%.

Table 6.2: Summary of CHAOS wind speed and significant wave height (SWH) statistical scores against buoys observations and satellite retrievals for the two simulation modes WAM_coarse_wind (or COARSE) and WAM_nest_wind (or NEST). The scores refer to case study C, from 4 January at 00:00 UTC to 11 January at 00:00 UTC, 2012. Buoys observations and remotely sensed data only over the nested domain area are used in the statistical assessment.

	Wind Buoys			**Wind SAT**			**Wave Buoys**			**Wave SAT**		
	COARSE	NEST	%	COARSE	NEST	%	COARSE	NEST	%	COARSE	NEST	%
Bias	0.94	**0.76**	19	**0.25**	0.43	72	-0.11	**-0.08**	27	-0.20	**-0.11**	45
RMSE	3.00	**2.89**	3.7	2.50	**2.52**	0.8	0.52	**0.48**	7.7	0.58	**0.52**	10
Pearson	0.74	**0.77**	4	0.83	0.83	0	0.90	**0.91**	1.1	0.92	**0.93**	1.1
R^2	0.44	**0.48**	9	**0.69**	0.68	1.4	0.80	**0.83**	3.8	0.82	**0.86**	4.9
SI	0.42	**0.41**	2.4	0.27	0.27	0	0.38	**0.35**	7.9	0.25	**0.23**	8

Chapter 7

Modeling Atmosphere – Ocean Wave Interactions during Hurricane Sandy (2012)

Following the sensitivity tests for extreme weather events over the Mediterranean Sea, CHAOS can now be employed to resolve atmosphere-ocean wave interactions during hurricane-force conditions. It is well-known that hurricanes are characterized by extremely high winds, intense ocean wave growth and heavy rainfall. Hence, the representation of wave age, wind-induced wave breaking accompanied by sea spray production and rain-wave interactions, as described at Chapter 2, is crucial for a more realistic simulation of atmosphere-ocean wave interactions. In this context, alternative parameterizations are employed in the hurricane sensitivity tests (see Section 4.1.2). For the sensitivity tests, hurricane Sandy (2012) is selected due to the severity of sustained phenomena and its exceptional trajectory (Varlas et al., 2017c). Sandy was characterized as "Superstorm" or "Frankestorm" because it was a freakish confluence of a tropical hurricane and a winter (Halverson and Rabenhorst, 2013).

Hurricane Sandy was formed on the 22nd of October 2012 as a result of the transformation of a wave disturbance to a tropical depression over southern Caribbean. The system slowly moved northeastward and begun to deepen 2 days later. At first, Sandy affected the Greater Antilles area, the Bahamas and Bermuda. Sandy was upgraded to a hurricane Category 2 and temporarily to Category 3 on the Saffir-Simpson hurricane wind scale (Simpson and Saffir, 1974), when it reached the eastern coast of Cuba, with wind gusts exceeding 50 m s^{-1} and a minimum pressure of 954 hPa (Blake et al. 2013). On 29 October, Sandy transitioned to an extratropical cyclone and on 30 October at 22:24 UTC made landfall in New Jersey at Northeastern United States coast (Blake et al. 2013). The minimum central pressure during landfall was recorded at 945.5 hPa, based on the National Ocean Service (NOS) station ACYN4 at the Atlantic City of New Jersey. The overall minimum central pressure of Sandy is estimated to be 940 hPa, which occurred on 29 October around 18:00 UTC, a few hours before its landfall.

Sandy mainly affected the eastern coast of the United States, due to significant storm surges, causing coastal inundation along the entire east coast from Florida to Maine. Torrential rain, inland flooding and strong winds caused electricity blackouts and extensive damage over the Mid-Atlantic States (New York, Connecticut, Maryland, Delaware and New Jersey). In total, hurricane-related fatalities reached 233, with at least 147 of them being direct fatalities. 72 of them occurred in the Mid-Atlantic and Northeastern United States (Blake et al., 2013; Diakakis et al., 2015). This is the biggest number of eastern United States direct fatalities related to a tropical cyclone since hurricane Agnes in 1972. As far as the economic damage is concerned, Sandy was the second costliest hurricane to have ever hit the United States. The economic

losses amounted to $71.4 billion (USD) for the United States and $75 billion (USD) in total (Apsan, 2013).

In the following section, the synoptic characteristics of the atmospheric circulation that affected the life cycle of the hurricane Sandy are analyzed. In particular, synoptic-scale factors, such as the interaction of the system with prevailing upper air conditions are examined. Afterwards, sensitivity tests on the impact of ocean waves on Sandy evolution and are presented. Wind-induced wave breaking, wave age parameterizations and rainfall impact on wave generation and its feedback to the atmospheric properties are investigated. Additionally, the results are statistically evaluated and discussed.

7.1. Synoptic Analysis of Hurricane Sandy

Hurricane Sandy was formed on the 22nd of October (2012) as a tropical depression system over the Caribbean Sea, where the SST exceeded 28.5°C (Figure 7.1a), almost 1°C warmer than normal (Figure 7.1b) [Varlas et al., 2017c]. Such conditions provided the necessary energy source for deepening the cyclonic circulation and forcing Sandy to follow a north-northeastern track over areas with positive SST anomalies where it continued to strengthen. On the 24th of October, the system moved northeastern due to the existence of a widespread ridge at 500 hPa (Figure 7.1c). Sandy's forward movement accelerated in advance of a middle- to upper-level trough over the northwestern Caribbean Sea and Gulf of Mexico. Early on the 25th of October, Sandy made landfall in Eastern Cuba as nearly a category 3 hurricane and then slightly weakened to category 1 status.

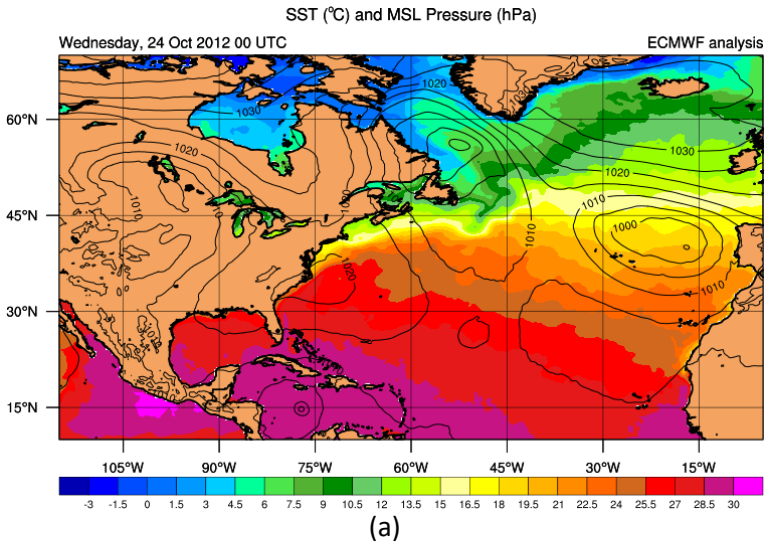

(a)

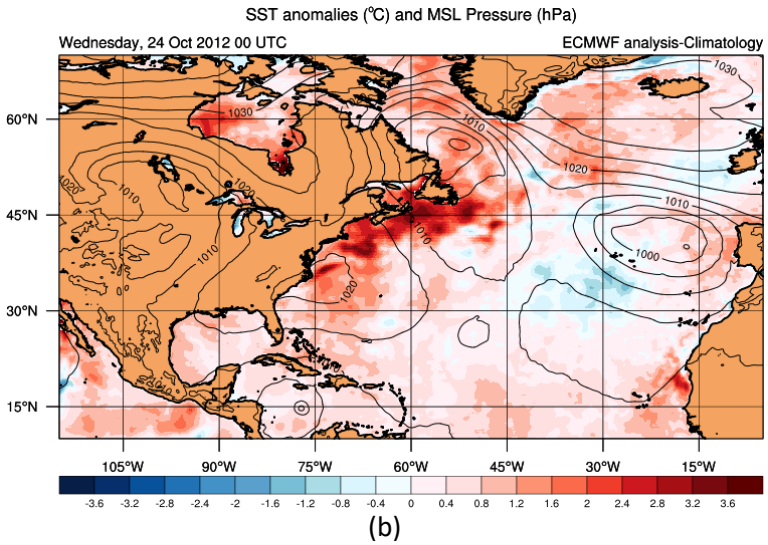

(b)

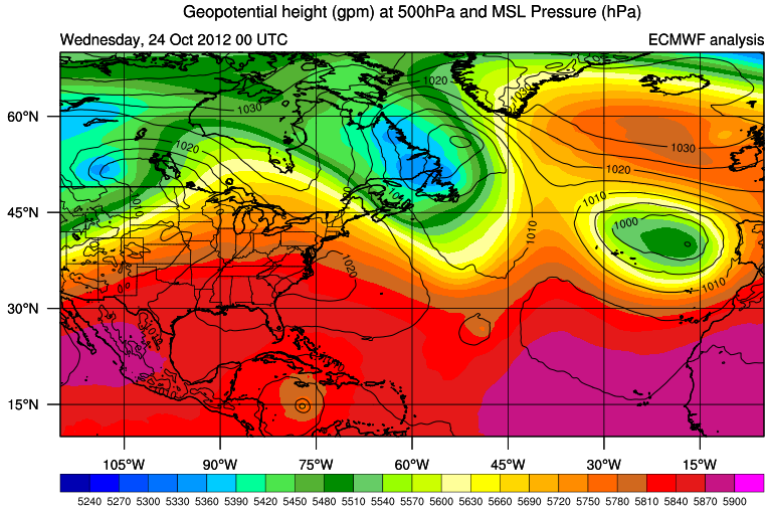

(c)

Figure 7.1: (a) Initial mean sea level (MSL) pressure (hPa) and sea surface temperature (SST; degrees Celsius), (b) initial MSL pressure (hPa) and SST anomalies and (c) geopotential height at 500 hPa (gpm) and MSL pressure (hPa) for 24 October at 00:00 UTC. Data are based on ECMWF analyses with horizontal resolution 0.25°×0.25° and NCEP/NOAA climatology (1981-2010) with horizontal resolution 0.083°×0.083° (Saha et al. 2010).

However, after passing over Cuba, Sandy continued to move over areas with slightly cooler SSTs than in Caribbean but still warmer than normal. From 26 to 29 October, the hurricane was being gradually affected by a polar jet stream at the northwest and a subtropical jet stream at the east (Figure 7.2a). This synoptic interaction played an important role in enhancing divergence and in establishing a strong temperature gradient in the upper-levels of the storm (Varlas et al., 2013, 2017c). The existence of the upper-level divergence enhanced the instability and intensified the hurricane. On early 29th of October, the displacement of the polar jet stream to the southeast amplified the large upper-level low (trough), which covered a vast area

from the Northeastern, to the Southeastern United States (Figure 7.2b, Figure 7.3a). The trough remained roughly stagnant over Canada and North United States for hours. Many areas of Canada, North and Central United States suffered from cold air outbreak and low temperatures.

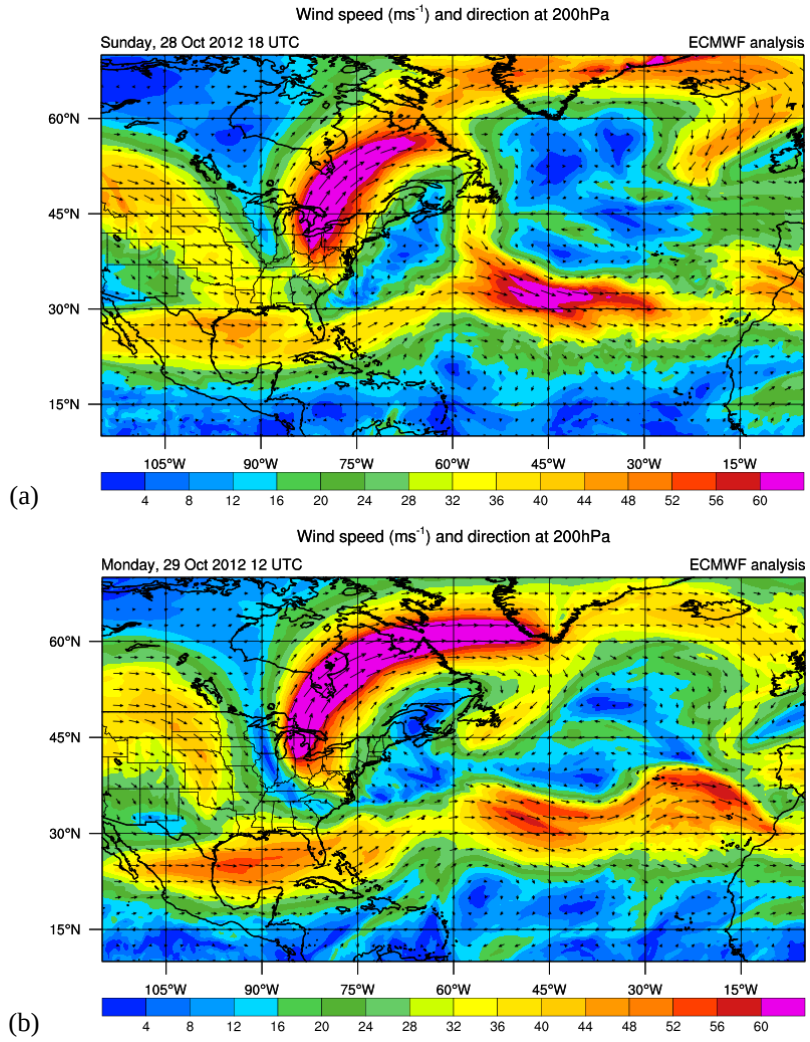

Figure 7.2: Wind speed (m s^{-1}) and direction at 200 hPa for (a) 28 October at 18:00 UTC and (b) 29 October at 12:00 UTC. Data are based on ECMWF analyses.

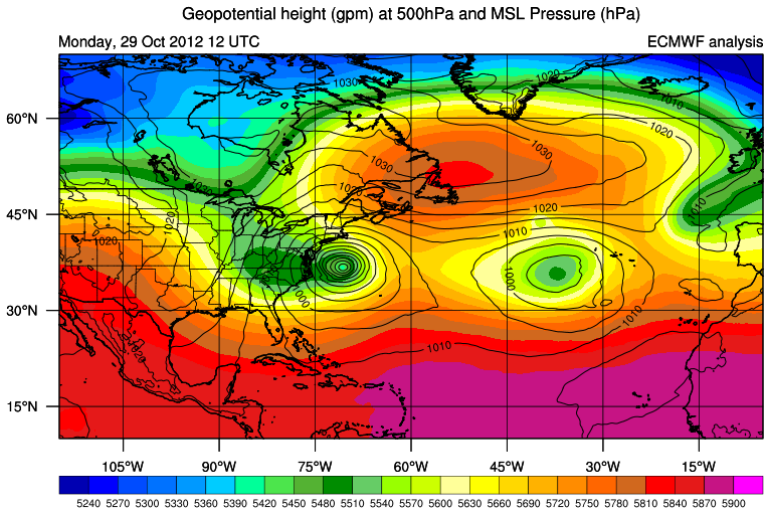

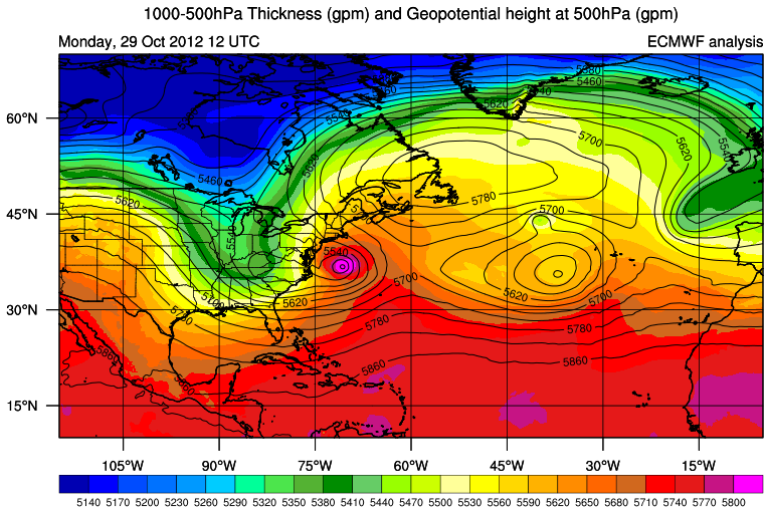

(b)

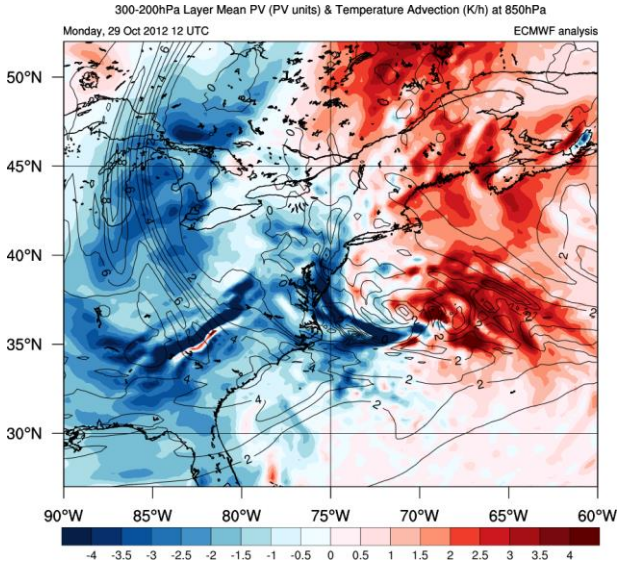

(c)

Figure 7.3: (a) Geopotential height at 500 hPa (gpm) and MSL pressure (hPa), (b) 1000-500hPa Thickness (gpm) and Geopotential height at 500 hPa (gpm), (c) 300-200 hPa layer mean potential vorticity (PV units; 1.0 PV unit = 10-6 m2 s-1 K kg-1) and temperature advection (K h-1) for 29 October at 12:00 UTC. Data are based on ECMWF analysis.

The interaction of the near surface warm and humid air masses with the cold air of the upper-level trough caused a warm seclusion development in Sandy's inner core few days before its landfall in the East Coast of the US. During the warm seclusion phase, Sandy intensified from a weak category-1 hurricane (27 October) to a category-2 hurricane (29 October) [Galarneau et al., 2013]. Moreover as shown in Figure 7.3a, Sandy covered almost 1000 km of ocean and preserved its strength for many hours before landfall. Meanwhile, the upper-level trough has been dynamically intensified as it is indicated by the negative 1000-500 hPa thickness advection from the northwest (Figure 7.3b) [Varlas et al., 2017c]. At the same time, the anticyclone over North Atlantic Ocean blocked a possible Sandy's northeastern movement. The upper-level trough was characterized by increased potential vorticity (PV) which is an indication of enhanced barocli-

nicity existence on the northwest side of Sandy (Figure 7.3c). Hence, the synergistic effect of the upper-level trough with the blocking anticyclone over North Atlantic Ocean steered Sandy northwestward toward the New Jersey shoreline. Additionally, as shown in Figure 7.3c, cold air advection (CAA) occurred when the surge of cold continental air cyclonically encircled Sandy's warm core prior to landfall, marking the beginning of Sandy's extratropical transition and producing a structure similar to the extratropical warm seclusion, originally described in Shapiro and Keyser (1990).

7.2. Configuration of CHAOS for Hurricane Sandy

CHAOS has been configured on a domain covering a widespread part of western Atlantic Ocean and the Caribbean Sea, in order to carry out the sensitivity tests under extreme wind and sea state conditions during hurricane Sandy (Figure 7.4). The atmospheric component has a horizontal resolution of 10km x 10km with 820x540 C-grid points, time step of 30 sec and 38 vertical levels stretching from surface to 50 mb. Gridded analysis data from the European Centre for Medium-Range Weather Forecasts (ECMWF) in horizontal resolution of 0.5^{o}x0.5^{o} and time increment of 6 hours were used for the creation of initial and boundary conditions of the atmospheric component. Moreover, ECMWF Sea Surface Temperature (SST) analyses were used for SST update every 6 hours during the simulations. The Global Multi-resolution Terrain Elevation Data (30-arc-sec USGS GMTED 2010; Danielson and Gesch, 2011), the vegetation data MODIS FPAR (Myneni et al., 2002) and the land-use data 21-class IGBP MODIS (Friedl et al., 2011) were used as static input data in the preprocessing stage of WRF model.

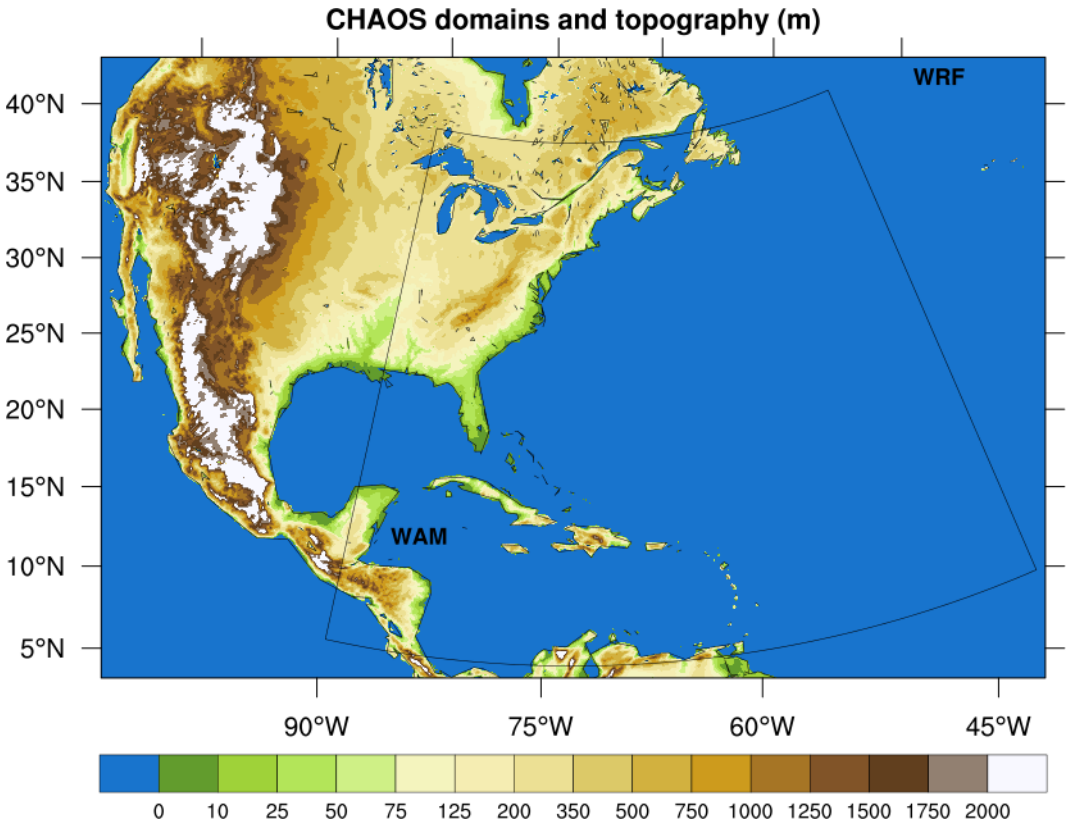

Figure 7.4: Domain configurations of WRF and WAM (black line) models of CHAOS and topography (m) distribution used by WRF are depicted.

The grid of the wave model for the western Atlantic Ocean and the Caribbean Sea covers the geographical area 90° W - 40° W and 10° N - 50° N as shown in Figure 7.4 (black line) using a resolution of 0.1°x0.1° with 501x401 regular lat-lon points. WAM has propagation time step of 75 sec and source time step 600 sec (10 min). Moreover, WAM uses 24 directional bins (15° directional resolution) and 25 frequency bins (ranging from 0.042 to 0.411 Hz) to represent the wave spectra distribution. The initialization of WAM is based on the "hot start" approach in order to obtain a realistic initial wave spectrum. The initial wave spectrum has been computed based on a prior CHAOS simulation (initialized with "cold start") of a one-day time period. The bathymetric map has been constructed from Etopo1 data (Amante and Eakins, 2009; 1 min Gridded Global Relief Data) using bi-linear interpolation and some degree of smoothing (Figure 7.5). In shallow areas, local corrections were introduced. Due to the complex bathymetry of the western Atlantic Ocean and the Caribbean Sea, the shallow water approximation with depth refraction and depth induced wave breaking was employed (Battjes and Janssen, 1978). Furthermore, the domain boundaries are closed in order to conserve the wave energy.

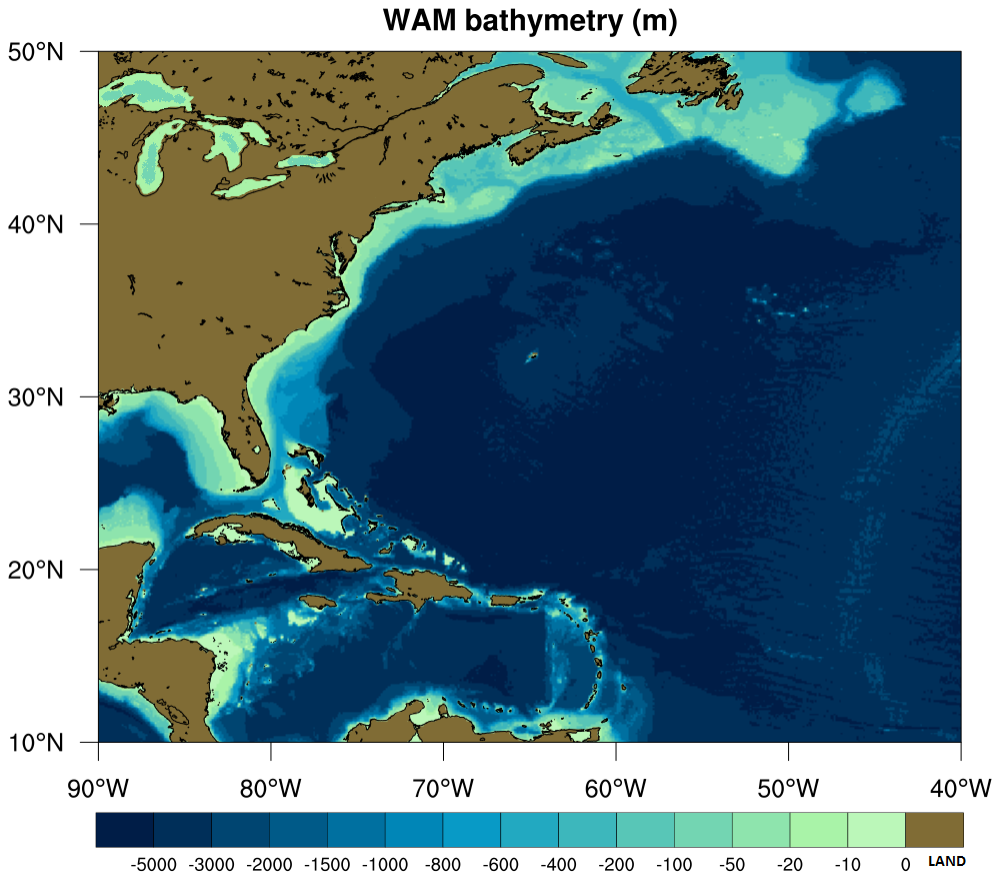

Figure 7.5: Bathymetry (m) distribution used by WAM model is illustrated. The bathymetric map has been constructed from Etopo1 data (Amante and Eakins, 2009; 1 min Gridded Global Relief Data (Etopo1); National Geophysical Data Center, NOAA - National Oceanic and Atmospheric Administration)

As far as the parameterizations of atmosphere-ocean wave interaction processes are concerned, the parameterization schemes described in Section 4.1.2 were integrated. Four simulation modes have been configured to simulate hurricane Sandy:

- Two-way coupling (CPL_JANSSEN): Both the atmospheric and ocean-wave component use information produced by the other model employing Janssen's parameterization for Charnock parameter as described in Section 4.1.2.
- Two-way coupling (CPL_SMITH): Both the atmospheric and ocean wave component use information produced by the other model employing Smith's parameterization scheme as described in Section 4.1.2. This parameterization is based on wave age calculated by WAM model. Wave age values ranging from 1 to 48 are acceptable in this test. The wave age limits are appropriately set so as the parameter $a_S = \frac{0.48}{z_a}$ to be within Janssen's Charnock parameter $a_J = \frac{0.01}{\sqrt{1-\frac{\tau_w}{\tau}}}$ limits (Sections 2.3 and 4.1.2).
- Two-way coupling (CPL_LIU): Both the atmospheric and ocean-wave component use information produced by the other model employing Liu's parameterization scheme as described

in Section 4.1.2. This parameterization is wave age and wind-induced wave breaking dependent.

- One-way coupling (control, CTRL): Only the ocean-wave component uses information produced by the atmospheric component. The Charnock parameter in the atmospheric component remains constant and equal to 0.0185 throughout the simulation (Sections 2.3 and 4.1.2). The results of this simulation mode are going to be used as a reference for the sensitivity tests and the statistical evaluation of the two-way coupled simulations.

The coupling procedure exchanges data on the source time step of WAM model, every 600 sec. As the time step of the atmospheric model was set 30 sec, the exchange took place every 20 time steps of the atmospheric model. Moreover, an MPI topology (in supercomputer ARIS) using 150 and 10 CPUs for atmospheric and ocean wave components respectively was found to be the most efficient. The configuration of the system and the main parameterization schemes used are summarized in Table 7.1.

Table 7.1: Configuration of CHAOS

CHAOS	Atmospheric Component	Ocean Wave Component
Model	WRF-ARW, WRF-Chem V3.8 and WRF-Hydro V3.0	WAM Version 4.5.4
Coupler	OASIS3-MCT Version 3.0	
Integration Domain	Western Atlantic Ocean, Caribbean Sea, United States	
Grid	Arakawa semi-staggered C-grid	Spherical latitude-longitude grid
Horizontal grid Increment	10km x 10km	0.1°x0.1°
Spectral resolution	–	24 directional bins (15° directional resolution), 25 frequency bins (ranging from 0.042 to 0.411 Hz)
Vertical coordinate	Terrain-following hydrostatic pressure η coordinate	–
Vertical levels	38	–
Time steps	30 s	Propagation time step: 75 s Source time step: 600 s
Initial & boundary Conditions	ECMWF, 0.5°x0.5° 17 isobaric levels 6h update of boundary conditions	Hot start

SST	ECMWF SST update every 6 hours	–
Exchange rate	600 s	
Surface layer	Revised Monin-Obukhov	–
PBL	YSU	–
Microphysics	Thompson	–
Cumulus	Kain-Fritsch	–
Land surface	Unified NOAH	–
Radiation	RRTM and Dudhia schemes	–
Chemistry options	Disabled	–
Coupled to WRF-Hydro	Disabled	–
Topography	30-arc-second USGS GMTED2010	–
Vegetation	MODIS FPAR	–
Land-use	21-class IGBP MODIS	–
Bathymetry	–	ETOPO1
Water approximation	–	Shallow water approximation with depth refraction and wave breaking due to depth change near shore
MPI topology	150 CPUs	10 CPUs

7.3. Methodology of Statistical Evaluation

The methodology of statistical evaluation of CHAOS simulating hurricane Sandy is similar as described in Section 4.3. The outputs from simulations have been statistically evaluated based on the point-to-point hourly comparison between model-generated variables and the available buoy measurements. Moreover, the results have been statistically evaluated against satellite retrievals and land surface measurements. The meteorological variables considered in the evaluation exercise are: the near surface wind speed, the significant wave height, the near surface temperature, the mean sea level pressure (MSLP) and the accumulated precipitation. The performance of CHAOS at the case study of hurricane Sandy has been assessed using the network of 23 available buoys in the western Atlantic Ocean and the Caribbean Sea as depicted on Figure 7.6.

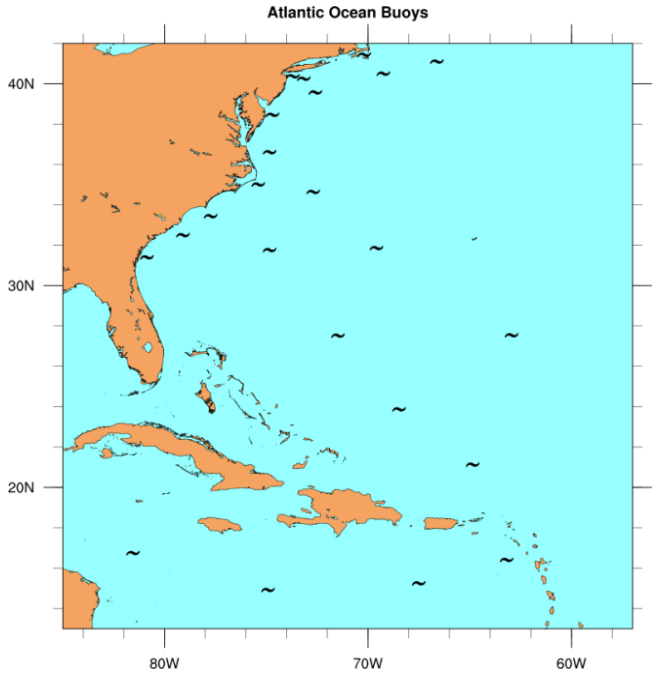

Figure 7.6: Spatial distribution of buoys applied for the evaluation of the system. Data were made available by National Data Buoy Center (NDBC) of National Oceanic and Atmospheric Administration (NOAA) of United States.

The system was also evaluated against remotely sensed data retrieved from satellites Jason 1 and Jason 2 (Figure 7.7). The sensitivity of the system was also assessed over the land at the positions of 113 surface meteorological stations across eastern United States and Caribbean Islands (Figure 7.8).

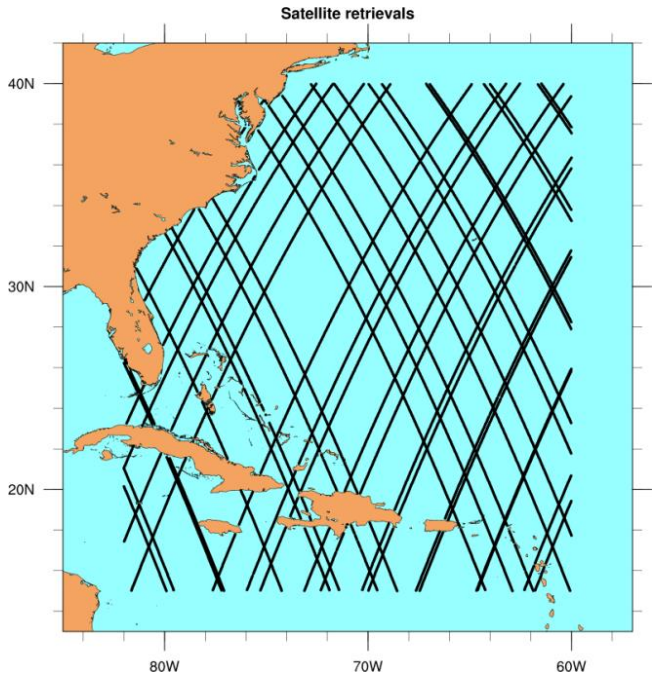

Figure 7.7: Trajectories of satellite retrievals used for the evaluation of the system. The altimeter data (Jason-1, 2) were produced and distributed by Aviso (http://www.aviso.altimetry.fr/), as part of the Ssalto ground processing segment.

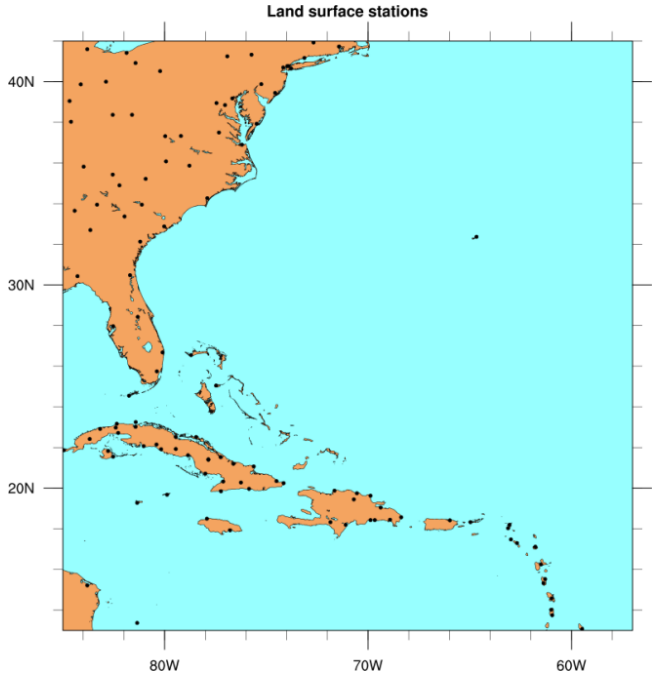

Figure 7.8: Spatial distribution of the land surface stations applied for the evaluation of the system. Data source: ECMWF-GTS network.

7.4. Wave Age, Wave Breaking and Sea Spray effects

Sea surface roughness is mainly determined by the existence of young waves at the medium to high frequencies of the spectrum (Smith, 1988; Janssen, 1991; Donelan et al., 1993). These waves tend to break especially under high wind conditions and affect the bubble mechanism, producing sea spray droplets as well as modifying surface fluxes (Andreas and Monahan, 2000; de Leeuw et al., 2011; Shi et al., 2016). Makin (2005) observed that at a wind speed of about 33 m s^{-1}, the drag coefficient starts levelling off, implying that the sea spray droplets begin to influence the dynamics of the atmospheric flow. Powell et al. (2003) assumed that increased foam coverage resulting from intensively breaking waves could progressively form a “slip” surface at the air-sea interface that leads to the reduction of the sea drag at wind speeds above 40 m s^{-1}. Moreover, during wave breaking, the “rain” of spray droplets back onto the sea surface creates a mass flux with a magnitude that has been shown to damp the short waves that sustain most of the atmospheric drag on the sea surface (Andreas, 2004). Therefore, spray may play a key role in a negative feedback loop that limits air-sea momentum transfer.

The impact of the above described mechanisms on the thermodynamic characteristics of hurricane Sandy has been studied in a set of simulations employing alternative parameterizations based on wave age and wind-induced wave breaking (see more in Sections 2.3, 4.1.2 and 7.2). Hurricane conditions multiply the response of the wind speed and the SWH on different parameterizations, as it might be expected. Indeed, Figure 7.9 (a-d) and Figure 7.10 (a-d) show that the four experiments are characterized by large differences in wind speed and SWH up to 30% and 50%, respectively. CPL_SMITH presents the smallest differences compared against CTRL while CPL_JANSSEN yields the largest differences.

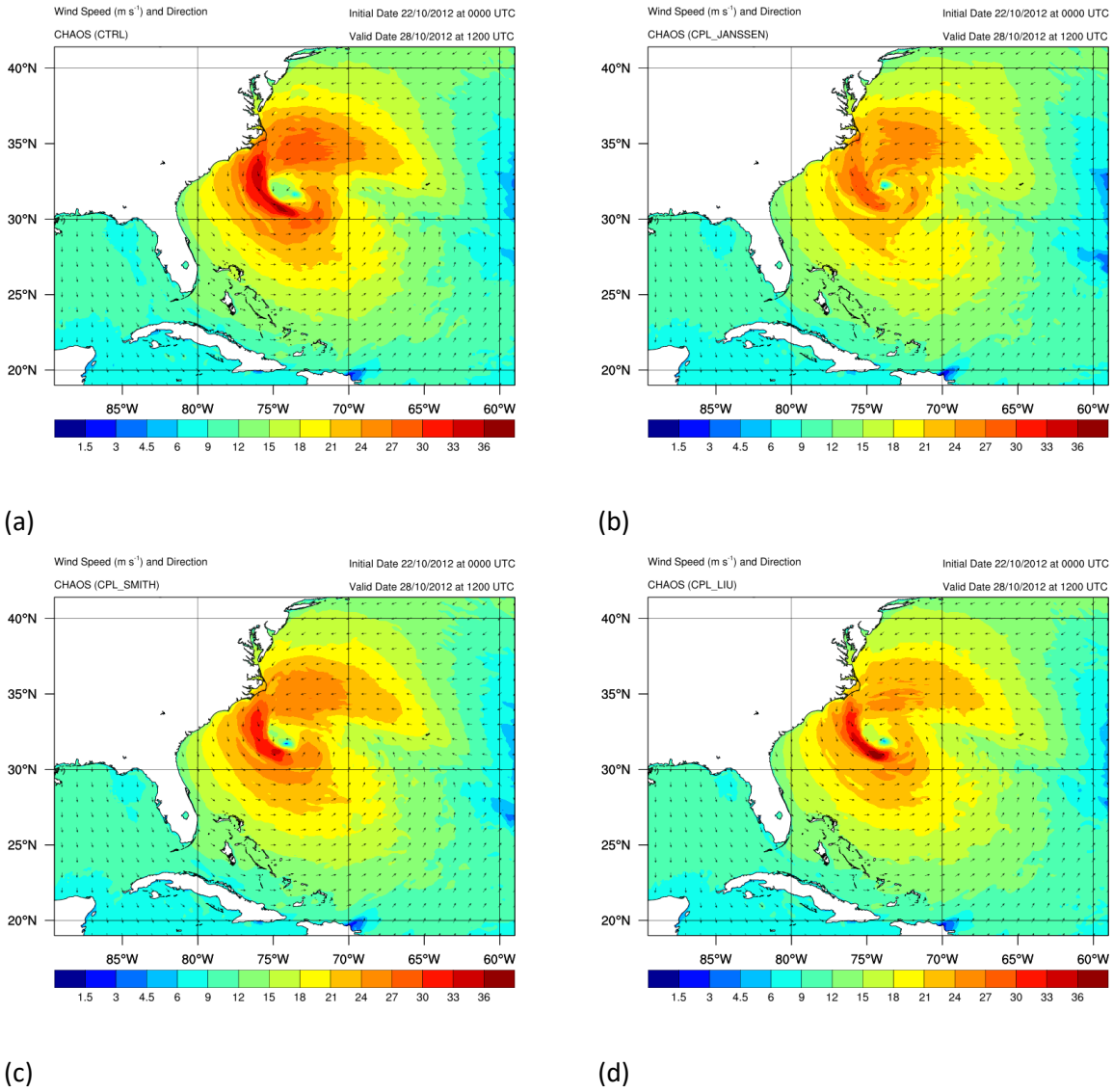

Figure 7.9: Horizontal distribution of wind speed (m s^{-1}) and direction from (a) CTRL, (b) CPL_JANSSEN, (c) CPL_SMITH and (d) CPL_LIU experiments. Figures (a-d) refer to 28 October 2012 at 12:00 UTC.

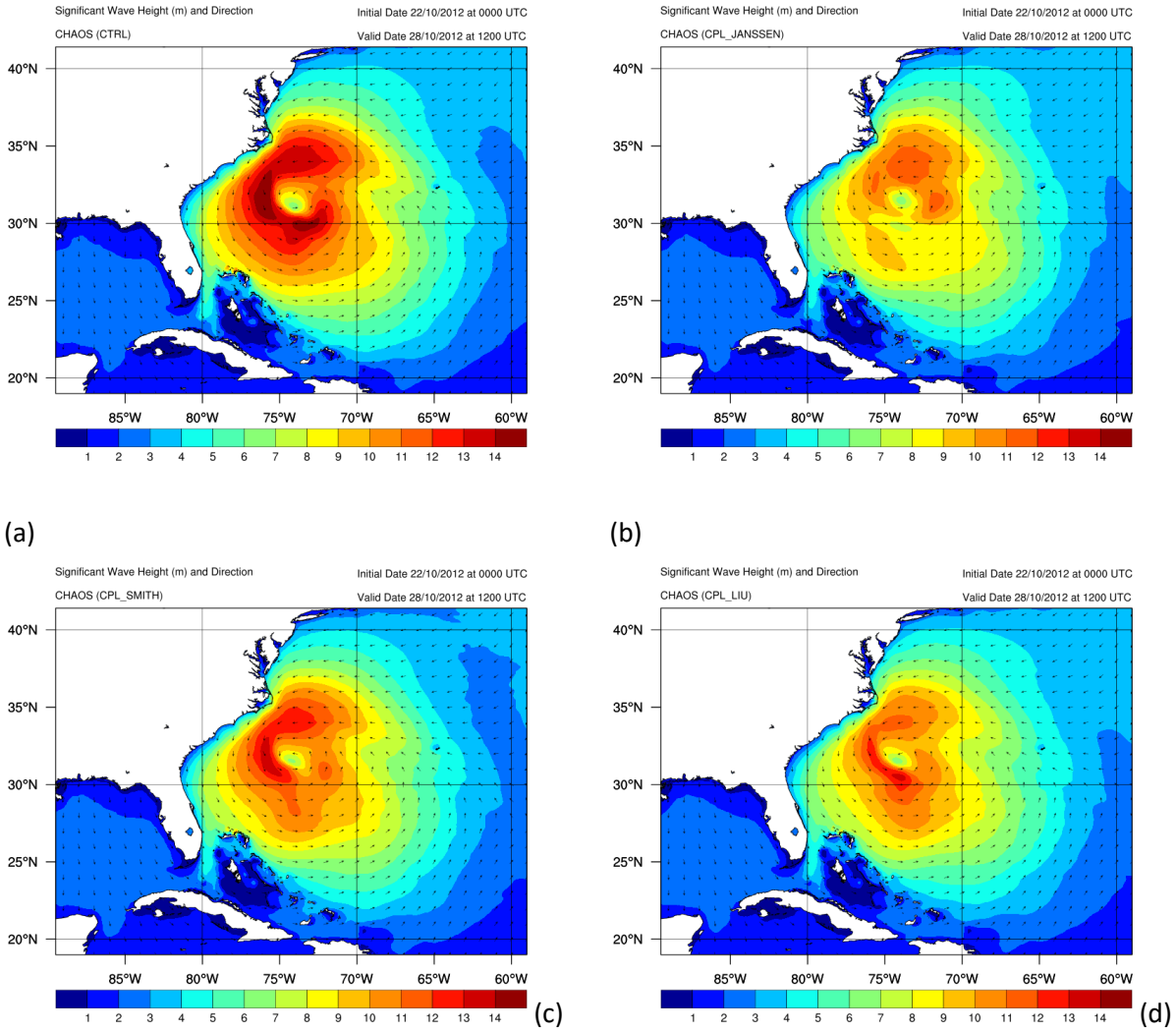

Figure 7.10: Horizontal distribution of SWH (m) and direction from (a) CTRL, (b) CPL_JANSSEN, (c) CPL_SMITH and (d) CPL_LIU experiments. Figures (a-d) refer to 28 October 2012 at 12:00 UTC.

The responses on the wind flow and sea state among the experiments are mainly raised by the different approaches in Charnock parameter estimation among the four schemes (see more in Sections 2.3, 4.1.2 and 7.2). As also analyzed at Chapter 5, Janssen's approach takes into consideration the increase of wave-induced stress under young wave conditions. As far as CPL_SMITH is concerned, the parameterization of Charnock parameter is directly proportional to inverse wave age (ratio between friction velocity and wave phase velocity at the peak of the spectrum; see more in Section 2.3). Janssen (2004) proposed that the wave stress is determined by medium to high-frequency gravity waves and it is approximately proportional to inverse wave age. Wave stress mostly increases for the inverse wave age ranging from 0.1 to 1 or wave age from 10 to 1. In order to represent older waves, the maximum wave age limit is set to 48, as described in Section 7.2. Concerning CPL_LIU, the parameterization of Charnock is based on

wave age ranging from 1 to 35 and wind-induced wave breaking accompanied by sea spray production for friction velocities exceeding 1.6 m s^{-1}.

The dependence of roughness length on friction velocity for the entire set of experiments are shown in Figure 7.11a. Similarly to the results of Chapter 5, two-way coupling decreases the wind speed and SWH as a response to the increased roughness length. All the schemes increase roughness length with the friction velocity except CPL_LIU which decreases roughness length for friction velocities exceeding ~1.6 m s^{-1}. Such behavior of CPL_LIU is attributed to the incorporation of wind-induced wave breaking and sea spray mechanisms. Under high winds, wave breaking and wind tearing wave crests disrupt the air-sea interface and generate sea spray causing a positive forcing to the atmospheric flow and, consequently to ocean wave growth (Andreas, 2004; Donelan et al., 2004; Makin, 2005; Liu et al., 2011). The first physical mechanism partaking in this phenomenon is the partial momentum transfer from atmosphere to sea spray (Andreas, 2004). The decrease of atmosphere-wave momentum flux decays the growth of young waves decreasing sea surface roughness. The second physical mechanism is the damping of short waves by sea spray droplets (Andreas, 2004). Since sea spray droplets have substantial mass, they eventually plunge back into the ocean, delivering their momentum to the surface, attenuating short-waves and, consequently, decreasing sea surface roughness.

Indeed, CPL_LIU estimates higher wind speed (Figure 7.9d) and SWH (Figure 7.10d) than CPL_JANSSEN, with local maxima over the southwestern area of the hurricane. Roughness length decrease due to wind-induced wave breaking is more prominent under young wave conditions characterized by wave age up to 7 (Figure 7.11b). In CPL_JANSSEN Charnock parameter tends to be saturated under high friction velocities (i.e. 2 m s^{-1}) as it is shown in Figure 7.11c and discussed earlier in experiments at the Mediterranean Sea (Chapter 5). However, this saturation does not have critical effect on roughness length as in CPL_LIU experiment. This explains why CPL_JANSSEN is characterized by large decrease of atmospheric flow and wave growth. On the other hand, Figure 7.11d demonstrates that roughness length in CPL_SMITH experiment is reduced for old waves and even for low to moderate wave age (values from 10 to 20). It is only for young waves (wave age from 1 to 10) that CPL_SMITH presents a sharp increase of roughness length. This distribution explains why CPL_SMITH is characterized by a marginal decrease of wind speed and SWH compared to CTRL. Despite the fact that Liu's and Smith's schemes employ wave age to represent sea state, they present differences. These are

attributed to both the different empirical formulation and the integration of wave breaking by CPL_LIU.

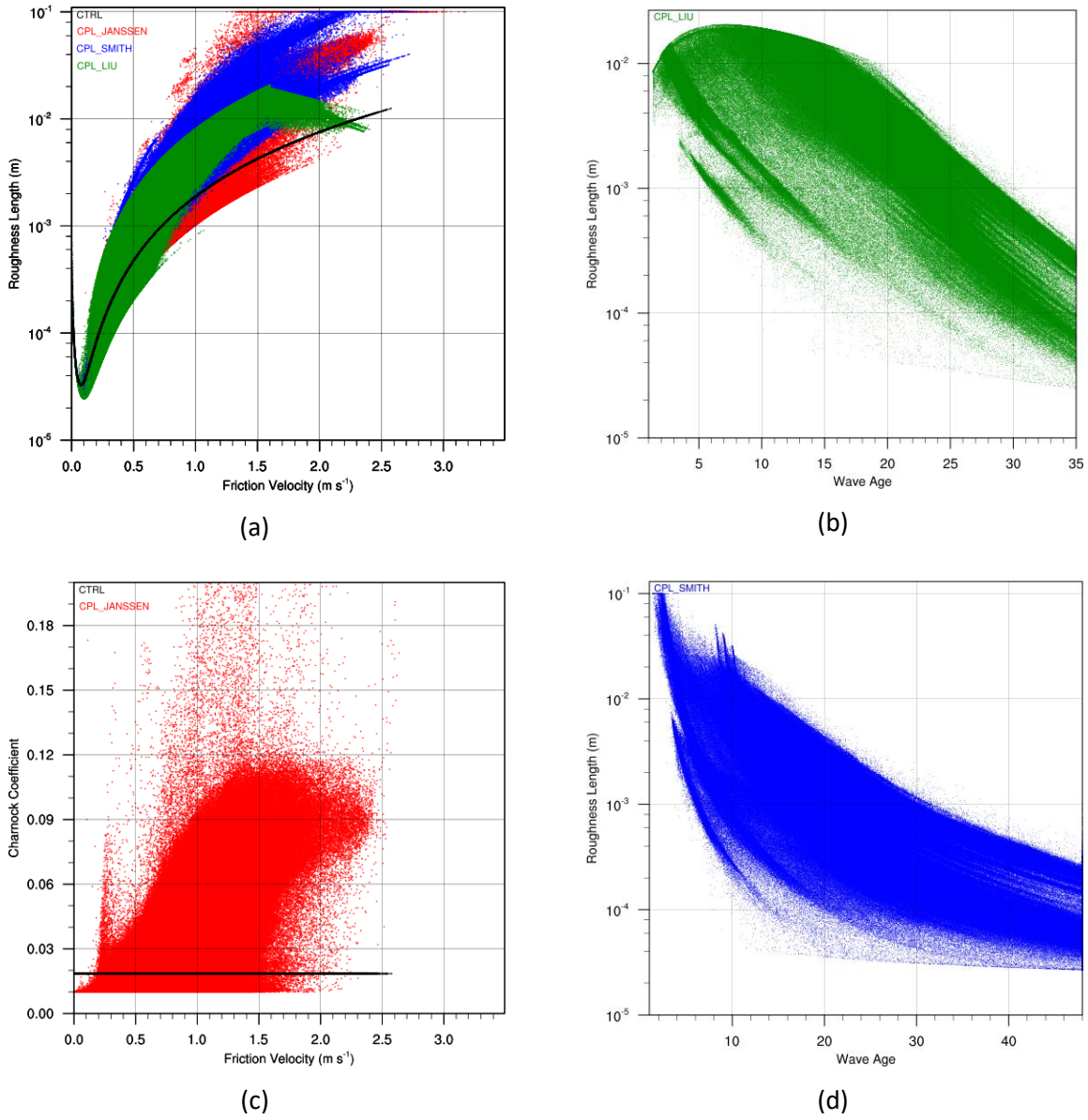

Figure 7.11: (a) Roughness length (m) dependence on the friction velocity (m s^{-1}). (b) CPL_LIU roughness length dependence on the wave age. (c) CPL_JANSSEN Charnock parameter dependence on the wind speed (m s^{-1}) The black line stands for the constant Charnock (0.0185) in CPL simulation. (d) CPL_SMITH roughness length dependence on the wave age. Figures (a-d) refer to the time period from 22 October at 00:00 UTC to 31 October at 00:00 UTC, 2012. CTRL, CPL_JANSSEN, CPL_SMITH and CPL_LIU results are shown in black, red, blue and green colors, respectively.

Figure 7.12 (a-d) demonstrates the dependence of surface momentum, enthalpy and moisture fluxes as well as C_k/C_d ratio on wind speed at 10 m. CPL_SMITH and CPL_LIU are characterized by weaker increase of momentum, enthalpy and moisture fluxes in contrast to CPL_JANSSEN. Moreover, C_k/C_d ratio values are consistent with measurements during other hurricanes (Black et al., 2007; Drennan et al. 2007; French et al. 2007; Zhang et al., 2008; An-

dreas, 2011; Bell et al., 2012). Two-way coupling yields atmospheric momentum and kinetic energy loss while increasing surface enthalpy and moisture fluxes feeding the atmosphere with thermal energy and water vapor. These findings corroborate the experiments for the cyclonic conditions over the Mediterranean Sea analyzed earlier (Section 5.1.2). The decrease of ratio in moderate and high wind speeds in two-way coupled simulations indicates that the energy loss due to sea surface stress exceeds the enthalpy gain. C_k/C_d ratio is an indicator of the energy equilibrium that determines the structure and intensity of the hurricane (Ooyama, 1969; Rosenthal, 1971; Emanuel, 1995).

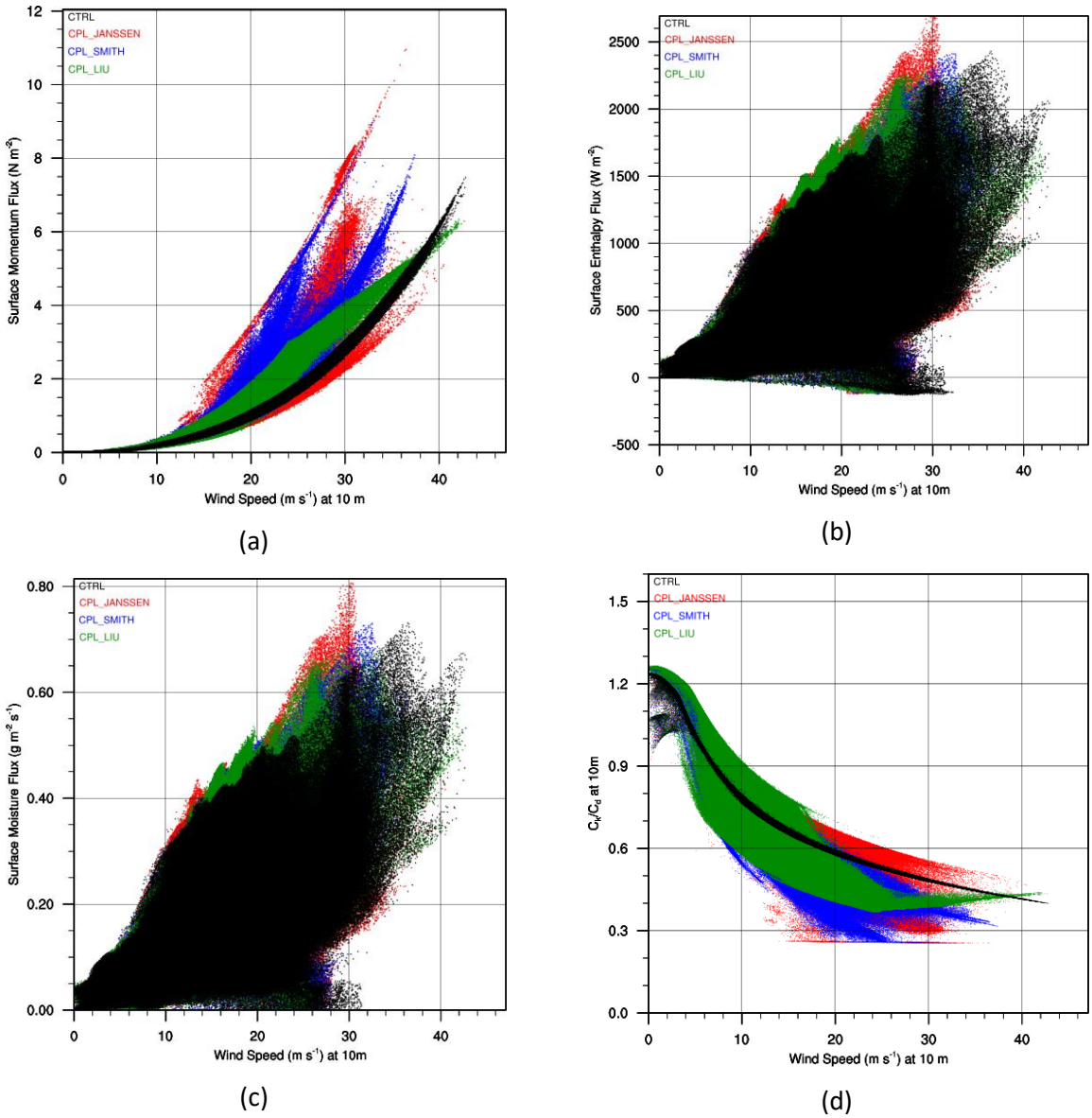

Figure 7.12: Surface (a) momentum flux (N m^{-2}), (b) enthalpy flux (W m^{-2}) and (c) moisture flux (g m^{-2} s^{-1}) dependence on the wind speed (m s^{-1}) at 10 m. (d) Dependence of ratio between the dimensionless bulk transfer coefficients for enthalpy (C_k) and momentum (C_d) to the wind speed (m s^{-1}) at 10 m. Figures (a-h) refer to the time period from 22 October at 00:00 UTC to 31 October at 00:00 UTC, 2012. CTRL, CPL_JANSSEN, CPL_SMITH and CPL_LIU results are shown in black, red, blue and green colors, respectively.

It is interesting that wind-induced wave breaking (CPL_LIU) decreases momentum transfer from atmospheric flow to waves even at lower values than CTRL experiment when wind speed exceeds 40 m s^{-1}. This is attributed to the disruption of air-sea interface during wave breaking which has positive effect on flow, as described previously. Furthermore, CPL_LIU presents an increase of C_k/C_d over 25 m s^{-1} which indicates that the positive effect on flow is accompanied by intensification of the hurricane in contrast to CPL_JANSSEN and CPL_SMITH.

Similarly to the cyclonic conditions over the Mediterranean Sea (Chapter 5), two-way coupling affects MSLP, MABL and upper-level conditions modifying Sandy's track. Figure 7.13 demonstrates that CPL_JANSSEN (compared to CTRL) causes a reduction of SWH as well as of cloud formation and water content during the landfall at 00:00 UTC on 30 October 2012. This is attributed to the lower energy equilibrium in the two-way coupling mode which results to a more rapid attenuation of Sandy's dynamical and thermodynamic structure. Figure 7.14 illustrates the simulated track of hurricane Sandy by the 4 experiments as well as the observed track based on best track analysis data retrieved from the National Hurricane Center (NHC) of United States (http://www.nhc.noaa.gov/data/). Two-way coupling affects hurricane track and MSLP having positive and negative effects. In more details, the impact of two-way coupling on track is quite variable with ocean wave feedback resulting in changes ranging from 3 hPa deeper to 5 hPa shallower comparing to CTRL run. The larger positive and negative differences are more prominent for CPL_JANSSEN experiment. This may be attributed to the higher dispersion that characterizes ocean feedback using Janssen's parameterization. The above findings are consistent with the results of previous studies (Bao et al., 2000; Desjardins et al., 2000; Doyle et al., 2002; Wahle et al., 2017). Moreover, CPL_LIU is characterized by the best estimation of Sandy's minimum central pressure, evidenced by the smallest variations from the observed values. This may attributed to the incorporation of many air-wave effects such as wave breaking and sea spray. Although the spatial differences among the simulated tracks are slight, it is shown that CTRL track is closer to observed track. This may be attributed to the long simulation period which introduces larger errors in two-way coupled simulations stemming from the atmospheric and ocean wave representations. Another explanation is the calculation of total roughness length considering only wave, turbulent and viscous stresses, neglecting rain impact, which is important under hurricane-force conditions. The effect of rainfall on waves and its feedback to the atmosphere will be investigated in the following section (Section 7.5).

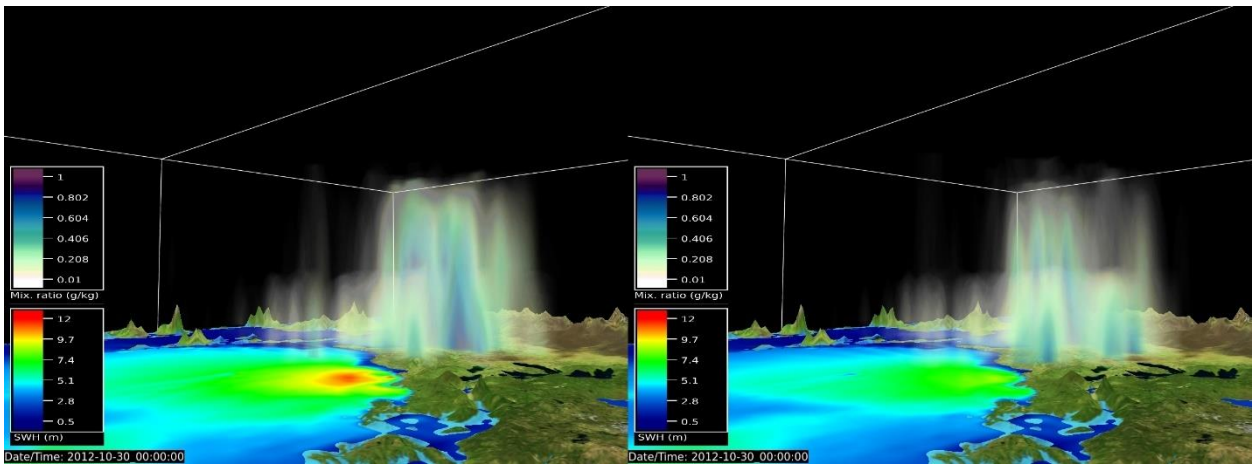

Figure 7.13: 3D distribution of water content (cloud, rain, ice, snow and graupel in g kg^{-1} and horizontal distribution of SWH (m) at 00:00 UTC (approximately the time of landfall of Sandy at eastern United States) on 30 October 2012, based on CTRL (left) and CPL_JANSSEN (right) results.

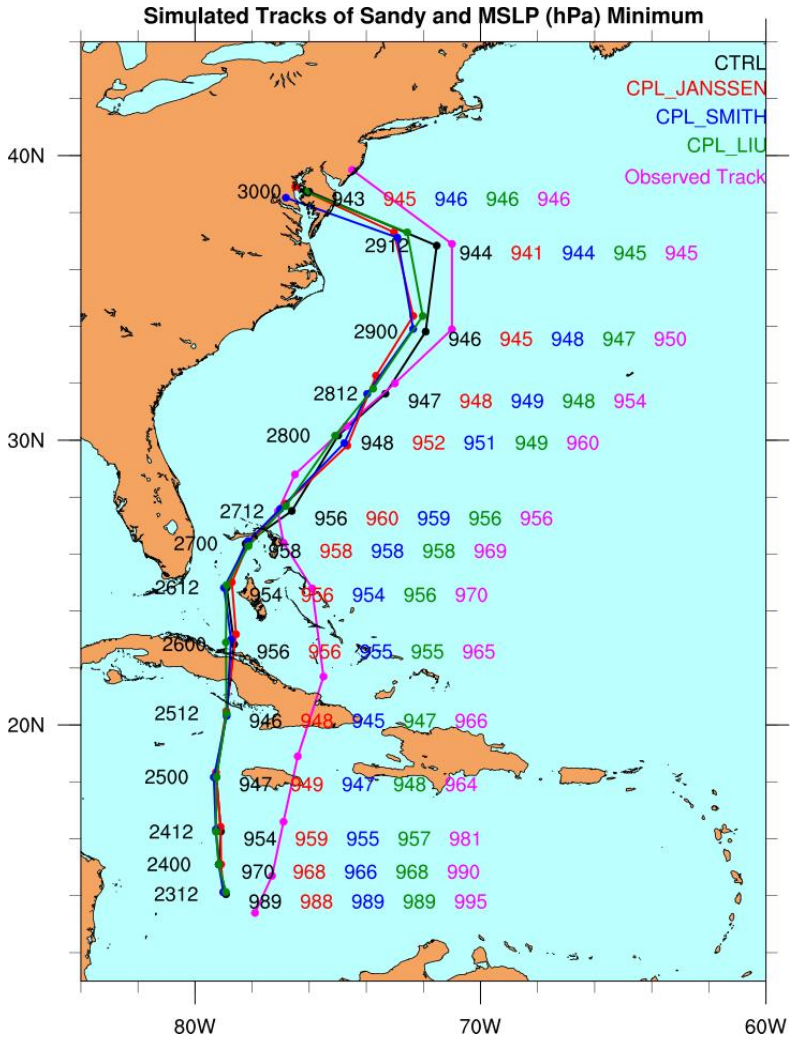

Figure 7.14: Track of the hurricane Sandy based on best track analysis data (magenta line), CTRL (black line), CPL_JANSSEN (red line), CPL_SMITH (blue line) and CPL_LIU (green line) simulations. Figure refers to time period from 23 October at 12:00 UTC to 30 October 00:00 UTC, 2012. Best track analysis data are retrieved from the National Hurricane Center (NHC) of United States (http://www.nhc.noaa.gov/data/).

As far as the comparison against the buoys 41001 and 41002 over the Atlantic Ocean (Figure 7.15a, b) is concerned, the RMSE reduction reaches 32% and 42% for wind speed and SWH, respectively (Figure 7.15c, d). CPL_JANSSEN and CPL_LIU present the most remarkable reduction, especially during high wind and sea state conditions, decreasing the bias error.

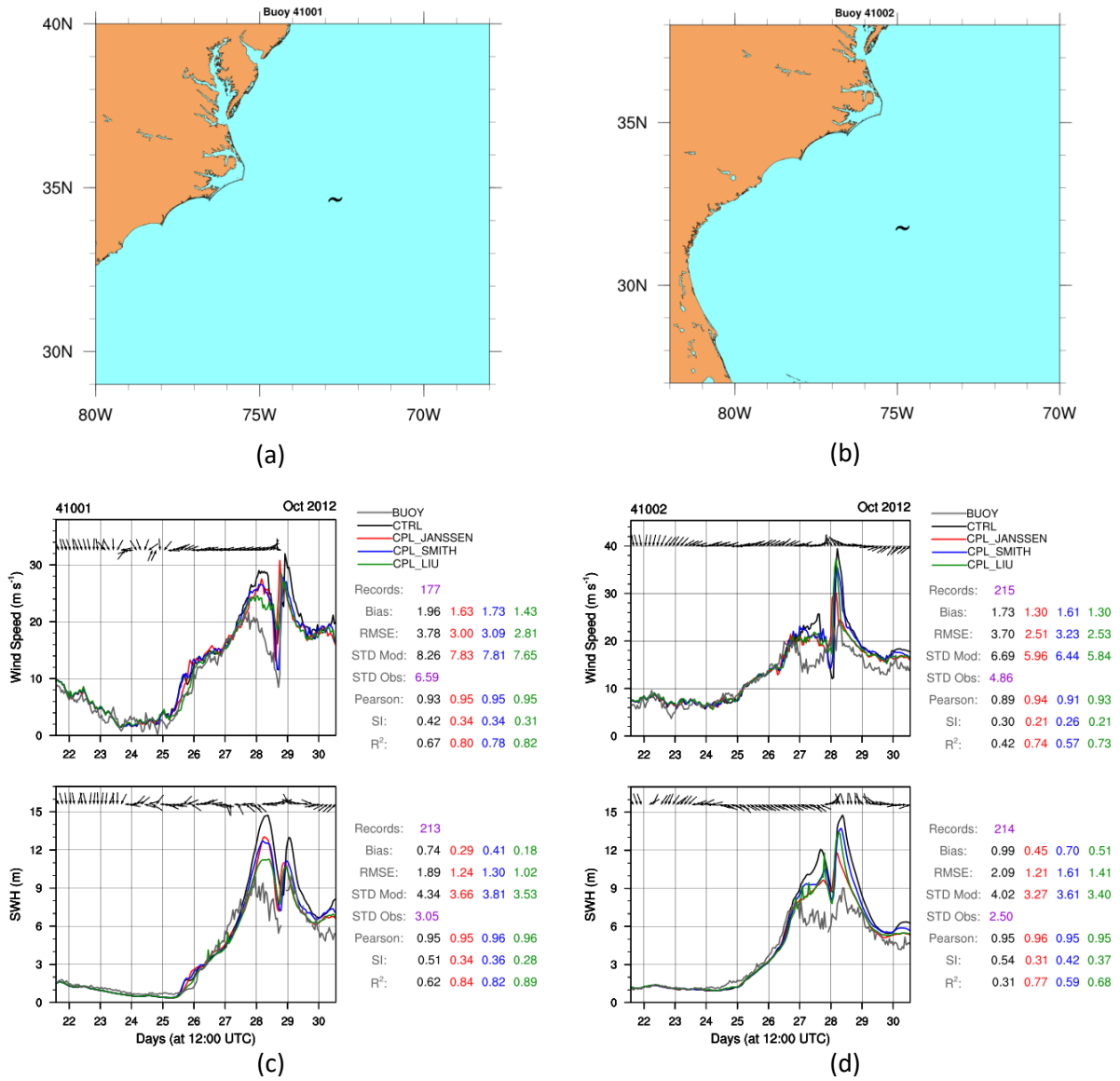

Figure 7.15: Location of buoy (a) 41001 and (b) 41002. Time series of wind speed (m s^{-1}) and SWH (m) based on the observations of buoy (c) 41001 (gray), (d) 41002 (gray), CTRL (black) CPL_JANSSEN (red), CPL_SMITH (blue) and CPL_LIU (green) simulations. The black arrows represent wind and SWH directions, measured by the buoy. On the right, the results of statistical evaluation through the calculation of statistical indices are illustrated. Time period from 22 October at 00:00 UTC to 31 October at 00:00 UTC, 2012.

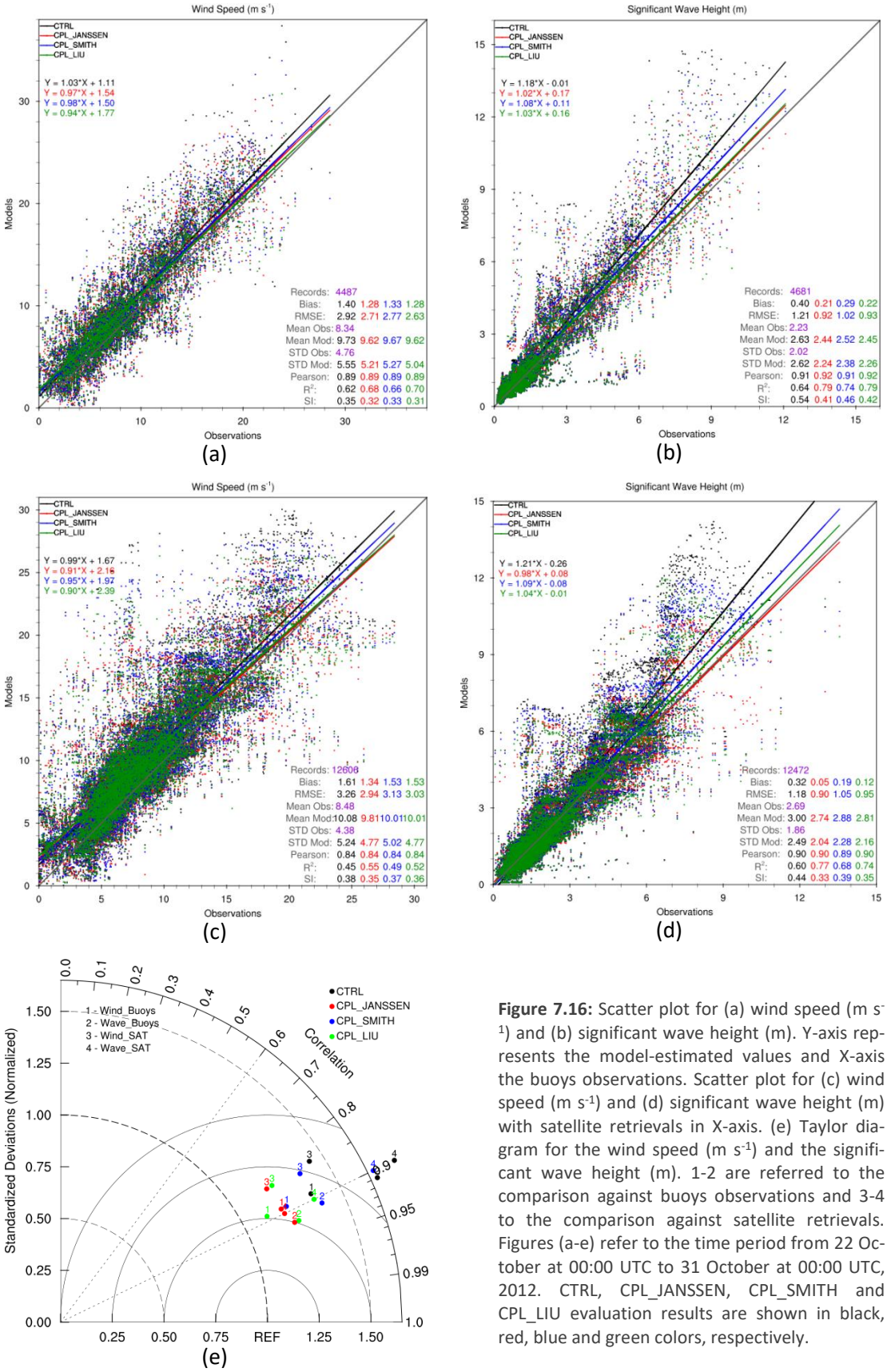

Figure 7.16: Scatter plot for (a) wind speed (m s^{-1}) and (b) significant wave height (m). Y-axis represents the model-estimated values and X-axis the buoys observations. Scatter plot for (c) wind speed (m s^{-1}) and (d) significant wave height (m) with satellite retrievals in X-axis. (e) Taylor diagram for the wind speed (m s^{-1}) and the significant wave height (m). 1-2 are referred to the comparison against buoys observations and 3-4 to the comparison against satellite retrievals. Figures (a-e) refer to the time period from 22 October at 00:00 UTC to 31 October at 00:00 UTC, 2012. CTRL, CPL_JANSSEN, CPL_SMITH and CPL_LIU evaluation results are shown in black, red, blue and green colors, respectively.

Overall, the impact of two-way coupling is reflected to the forecast skill (Figure 7.16a-d) shows that the two-way coupled simulations (with respect to the one-way coupled simulation) improve statistical scores reducing the overestimation of wind speed over the sea and SWH

comparing against buoys observations and satellite retrievals. It is interesting that, Taylor diagram indicates that two-way coupled simulations reduce RMSE and increase correlation (Figure 7.16e). The highest RMSE reduction for wind speed over the sea and SWH reaches 10% and 24%, respectively. Other statistical indices such as R^2 and SI present even larger improvements (up to 22%). It is noteworthy that, Janssen's scheme presents the best forecast skill. The results are characterized by high confidence level (>95%).

The statistical evaluation over the land yields improvements for wind speed and precipitation while, on the other hand, the behavior for temperature and MSLP is the opposite (Figure 7.17). These inaccuracies for temperature and MSLP may be attributed to the long simulation period and the differences in Sandy's track. Overall, CPL_JANSSEN presents the best performance followed by CPL_LIU and CPL_SMITH which offer smaller improvements to the forecast skill. CPL_JANSSEN reduces the RMSE of precipitation over the land up to 5%.

It is obvious that, the representation of sea surface roughness only considering wave age, results to partial description of physical mechanisms. The introduction of wind-induced wave breaking accompanied by sea spray production enriches the representation of atmosphere-ocean wave interaction. Nevertheless, CPL_JANSSEN which includes information only for the ratio between wave-induced stress and total stress (see more in Section 2.3) neglecting sea spray effects, offers better overall forecast skill. Summarizing, the lack of forecast skill presented by CPL_LIU but especially by CPL_SMITH may be attributed to the deficient configuration of parameterizations through empirical methods and data (see more in Section 2.3 and at Smith et al., 1992 and Liu et al., 2011). A future upgrade of Janssen's scheme in order to incorporate wind-induced wave breaking and sea spray effects might be an interesting approach.

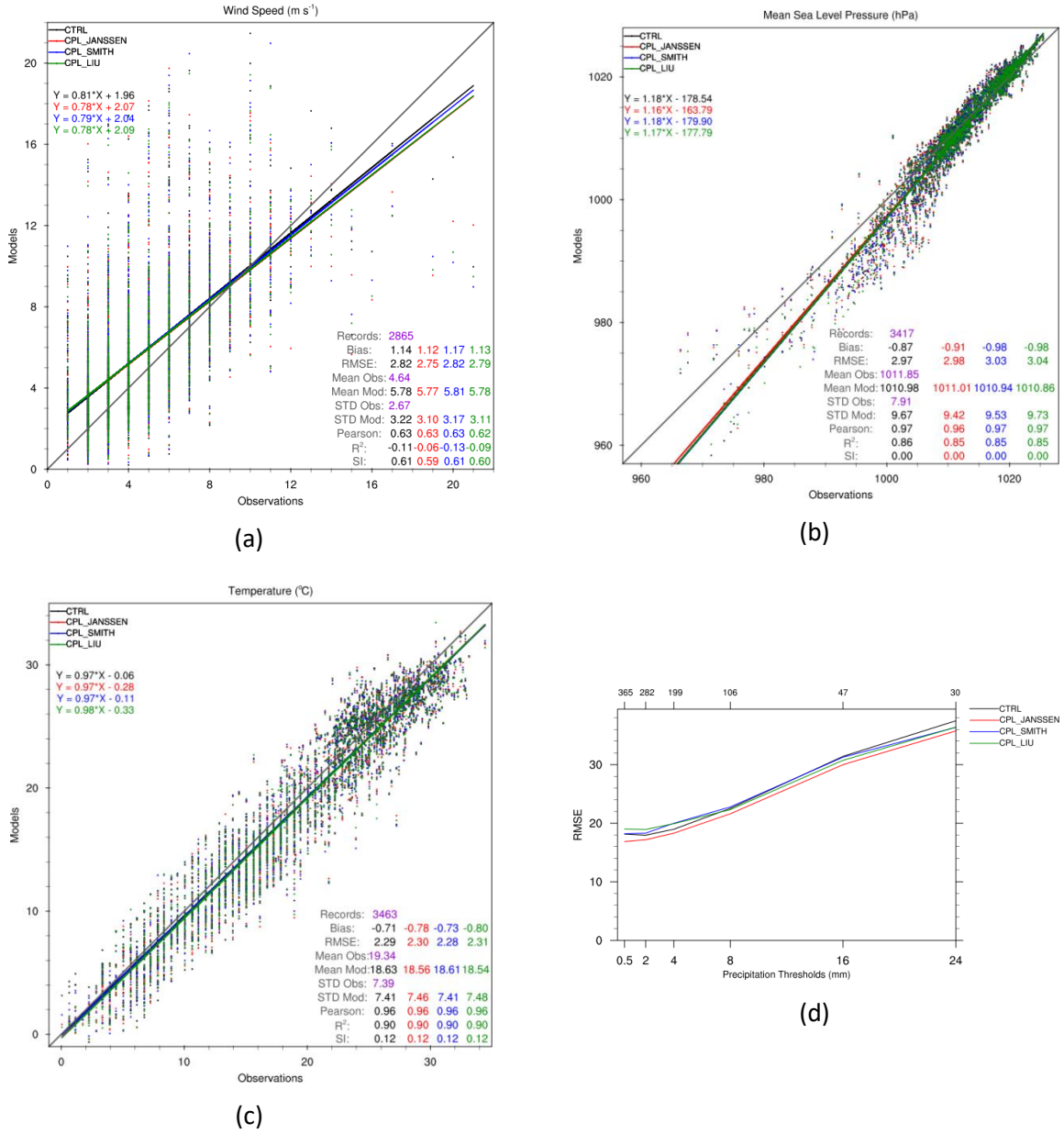

Figure 7.17: Scatter plot for (a) wind speed (m s^{-1}), (b) MSLP (hPa) and (c) temperature (°C) over the land. Y-axis represents the model-estimated values and X-axis the buoys observations. (d) RMSE for specific 6-hour precipitation (mm) thresholds. The numbers above each tick mark denote the sample for the corresponding threshold value. Figures (a-f) refer to the time period from 22 October at 00:00 UTC to 31 October at 00:00 UTC, 2012. CTRL, CPL_JANSSEN, CPL_SMITH and CPL_LIU evaluation results are shown in black, red, blue and green colors, respectively.

7.5. The Impact of Rain on Wave Evolution and its Feedback to the Atmosphere

A rather unknown percentage of shear stress at ocean surface is caused by the impact of descending raindrops and their interactions with the sea state. As proposed Cavaleri et al. (2015), rain primarily damps high-frequency young waves modifying sea surface roughness and near surface wind. Nevertheless, this mechanism is nonlinear, as sea surface roughness is deter-

mined by the codependent viscous, turbulent, wave and rain-induced stresses. Rain generally increases sea surface roughness and, subsequently, can affect wind and wave conditions near air-sea interface (Kumar et al., 2009). Poon et al. (1992) quantified the ratio of rain-induced stress and wind stress at sea surface to be in the order of 7-25% based on an experimental study in a circulating wind-wave tank. The damping of high-frequency waves may locally increase wind and, consequently, wind-generated waves. On the other hand, sea surface is rougher where raindrops strike despite the fact that rain-induced ripple waves can be considered as isotropic low-interaction waves (Cavaleri et al., 2015). Exceptionally, the rain-induced isotropic waves would not affect other waves in the case of mature sea or of calm conditions. However, there are increased rain-wave and wave-wave interactions under high-intensity rainfall conditions. These interactions can increase sea surface roughness decreasing wind and wind-wave growth. Nevertheless, the decrease of whitecapping by the raindrops striking is an opposing factor that can determine a more slip sea surface (Cavaleri et al., 2015).

All abovementioned interactions constitute a complex dynamical equilibrium involving several factors such sea state, wind, air and water viscosities, whitecaps, duration and intensity of rainfall, raindrops distribution, diameter, terminal velocity, angle that raindrops intact sea surface, ocean mixing layer as well as the direct interaction between wind and raindrops (Reynolds, 1900; van Dorn, 1953; Malkus, 1962; Roll, 1965; Caldwell and Elliott, 1971, 1972; Kitaigorodskii, 1973; Manton, 1973; Houk and Green, 1976; Tsimplis and Thorpe, 1989; Le Mehaute and Khangaonkar, 1990; Tsimplis, 1992; Poon et al., 1992; Yang et al., 1997; Kumar et al., 2009; Peirson et al., 2013; Cavaleri et al., 2015). For more details, see also at Chapter 1. CHAOS offers a unique capability to incorporate the most of these factors and exchange them after major developments in both atmosphere and ocean wave components (Varlas et al., 2017b).

Kumar formulation (see Section 4.1.3) is employed in CHAOS surface layer parameterization scheme in order to resolve the representation of complex nonlinear rain-wave processes. It assumes that rain directly affects the sea surface roughness length and it accordingly modifies the wind flow and consequently the wave height. Thus, an additional term, the rain-induced roughness length, is also included in the wave-induced and viscous-induced ones for the estimation of the total roughness length over sea surface. Kumar parameterization incorporates only a few of the abovementioned terms such as the rain intensity and the raindrop diameter with its terminal velocity. Therefore, it provides a rough estimation of the rain impact on ocean wave spectrum because it ignores a number of important factors.

Two simulation modes have been configured to investigate the rain-wave interactions for the case study of hurricane Sandy:

- Two-way coupling without rain-wave effects (NO_RAIN): Both the atmospheric and ocean-wave component use information produced by the other model employing Janssen's parameterization for Charnock parameter as described in Section 4.1.2.
- Two-way coupling involving rain-wave effects (RAIN): The same as NO_RAIN with the addition of Kumar's scheme introducing the rain-induced roughness length as described in Section 4.1.2. For convective rainfall, terminal velocity of raindrop and raindrop diameter are set equal to 5 m s^{-1} and 1 mm respectively whereas for stratiform rainfall the corresponding values are 3 m s^{-1} and 0.5 mm (Salles and Creutin, 2003; Tokay et al., 2008; Niu et al., 2010).

Rain increases total roughness length and, subsequently, decreases wave growth by the enhanced friction of the atmospheric flow at the air-sea interface. The wave-induced roughness length is therefore decreased over SWH maxima having negative effect on the total roughness length and a positive feedback to the atmospheric flow. This mechanism is more prominent mostly over rainfall maxima. An interesting finding is that RAIN changes rainfall distribution and intensity (Figure 7.18a, b). This is attributed to the feedback of rain-wave evolution interaction to the atmospheric conditions which will be analyzed in following paragraphs. Roughness length is generally characterized by higher values in NO_RAIN experiment while RAIN increases roughness length in a wider area, following the rainfall distribution (Figure 7.18c, d). Nevertheless, rain-induced roughness length has positive effect on total roughness length over calm sea. Hence, rain decreases roughness length maxima while yielding an overall increase over a widespread area, following rainfall distribution. Kumar et al. (2009) presented similar responses of wind and wave on raindrops striking at the sea surface.

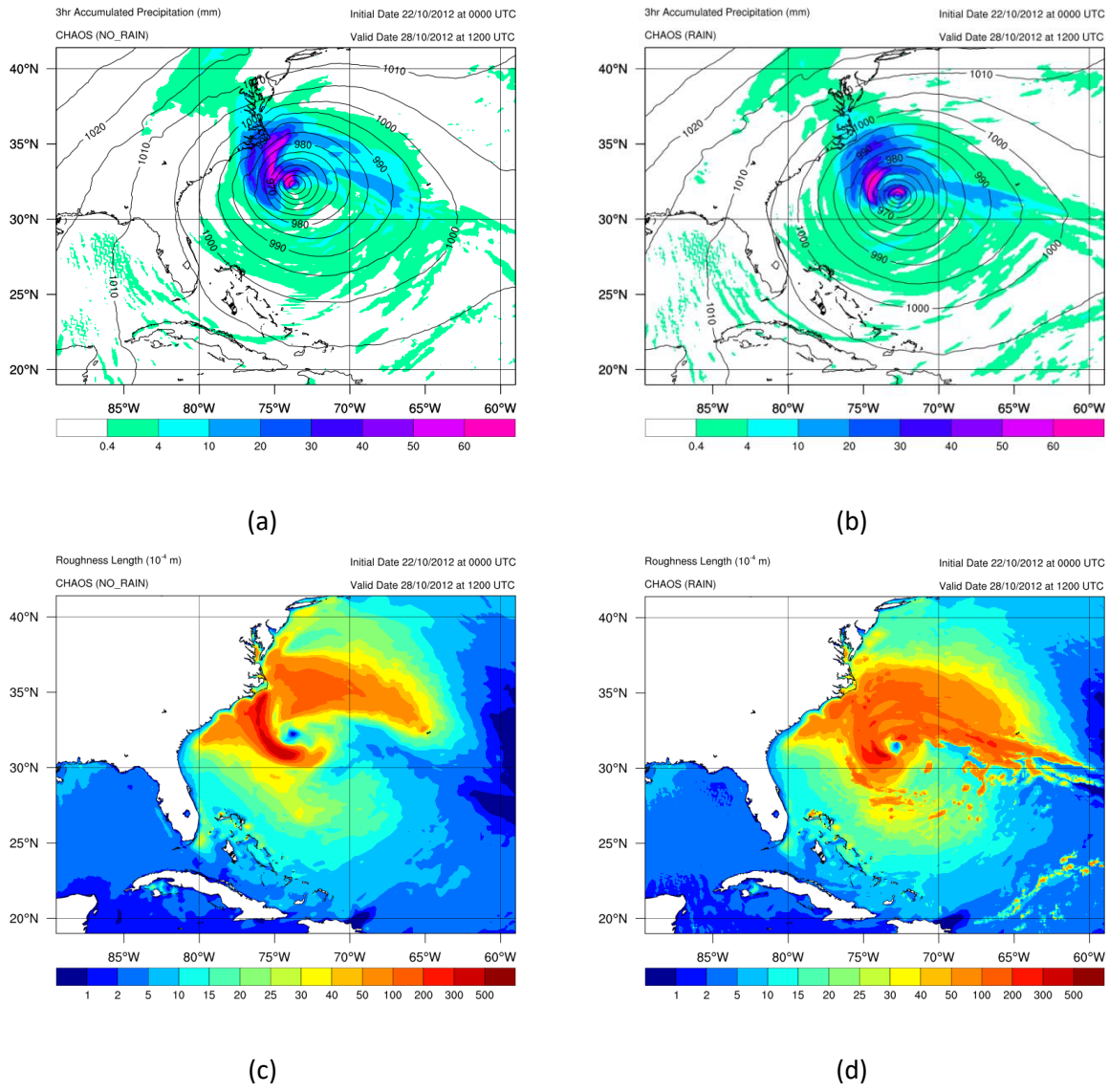

Figure 7.18: Horizontal distribution of 3hr precipitation (mm) and MSLP (hPa) from (a) NO_RAIN and (b) RAIN experiments. Horizontal distribution of roughness length (m) from (c) NO_RAIN and (d) RAIN experiments. Figures (a-d) refer to 28 October 2012 at 12:00 UTC.

In Figure 7.19 differences of wind speed and SWH up to 30% are depicted. They are mainly attributed to the modification of sea surface roughness primarily by the rain-induced stress and indirectly by the wave-induced stress variations. The relative equilibrium of rain-induced and wave-induced stresses is dependent on wind, wave and rain intensity and distribution.

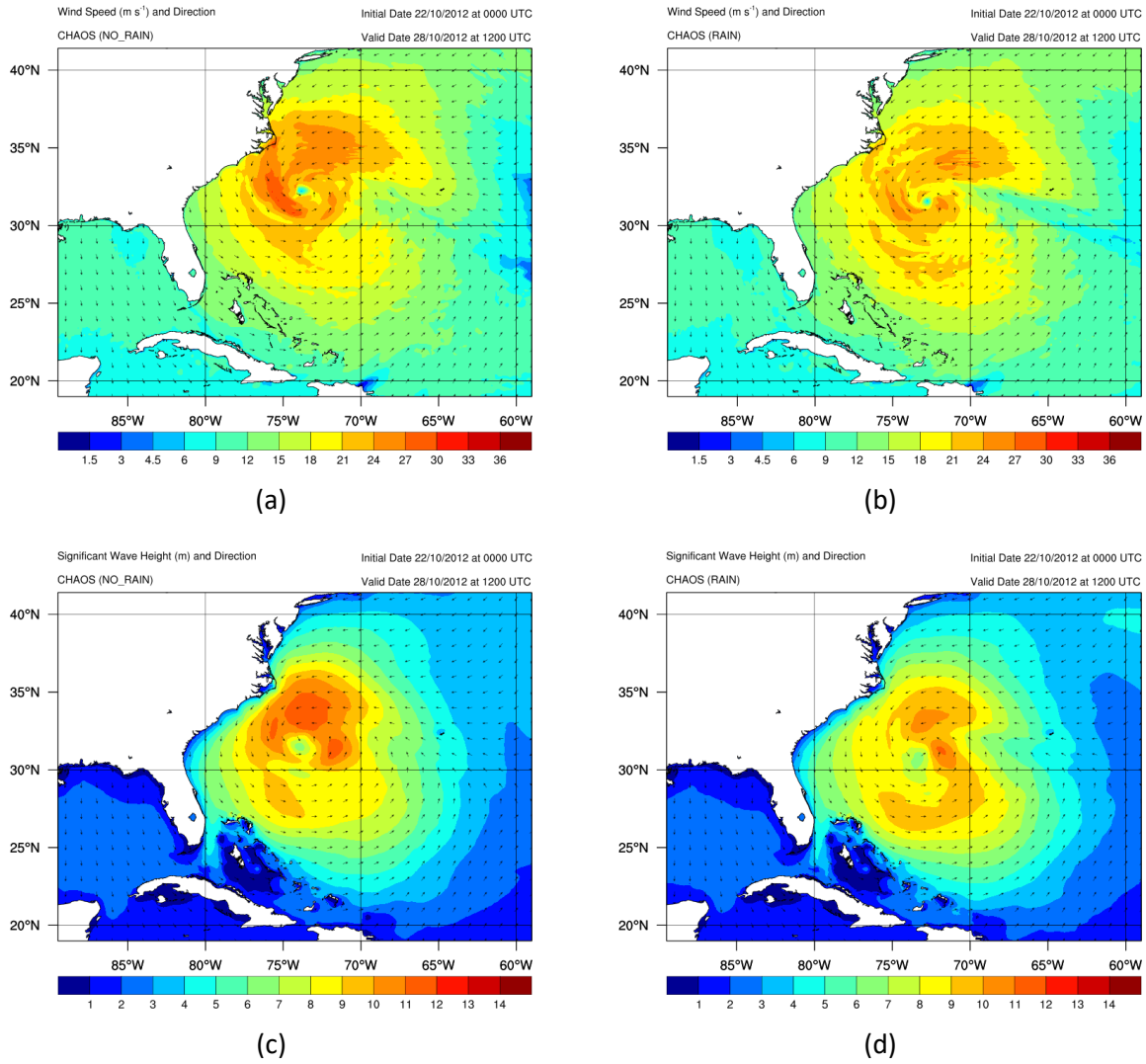

Figure 7.19: Horizontal distribution of wind speed (m s^{-1}) and direction from (a) NO_RAIN and (b) RAIN experiments and SWH (m) from (c) NO_RAIN and (d) RAIN. Figures (a-d) refer to 28 October 2012 at 12:00 UTC.

Roughness length response on rain-wave forcing is illustrated in Figure 7.20a. The dependence of roughness length on friction velocity indicates that the representation of rain impact on wave yields interesting results. Rain increases roughness reducing the atmospheric flow and, subsequently, the wave growth. This wave damping implies a slight decrease of roughness length which has positive effect on wind. The overall result of the above opposing factors is the wind and wave decay due to rainfall which is accompanied by a decrease of C_k/C_d ratio (Figure 7.20b). This finding is more prominent mainly under moderate wind conditions. This behavior may be attributed to the fact that intense rainbands are distributed over areas characterized by moderate winds. As far as surface layer is concerned, the increase of the kinetic energy loss is more significant than the thermal energy gain.

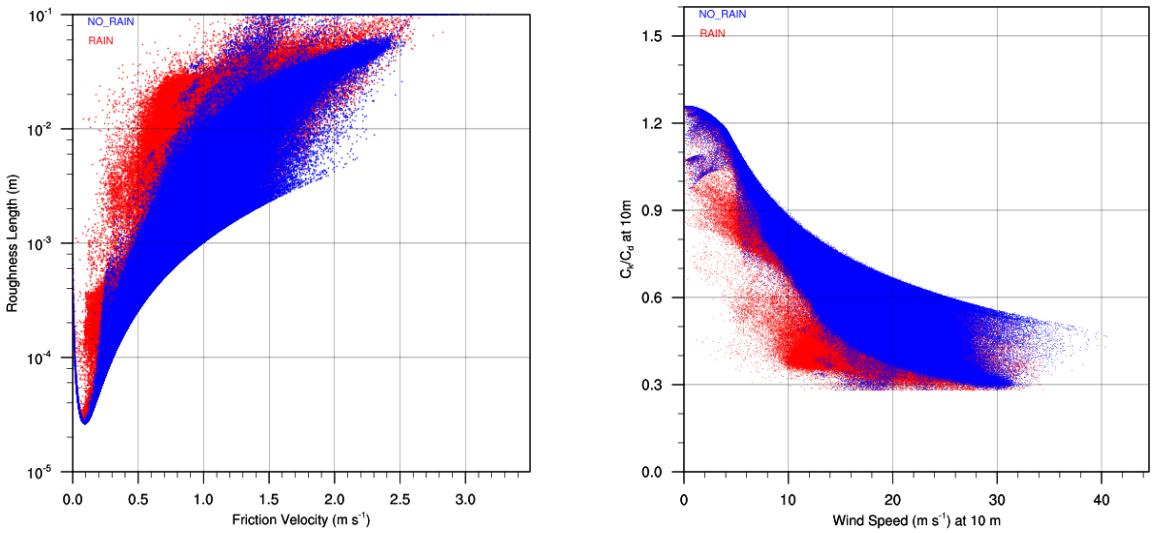

Figure 7.20: Roughness length (m) dependence on friction velocity (m s^{-1}). (b) Dependence of ratio between the dimensionless bulk transfer coefficients for enthalpy (C_k) and momentum (C_d) on the wind speed (m s^{-1}) at 10 m. Figures (a-b) refer to the time period from 22 October at 00:00 UTC to 31 October at 00:00 UTC, 2012. NO_RAIN and RAIN results are shown in blue and red colors, respectively.

The energy equilibrium determines the structure and intensity of the hurricane adjusting upper-level atmospheric conditions and its track (Figure 7.21). RAIN simulation improves the track of the cyclone mainly during the intensification stage (28-30 October) before landfall. The forecast skill of the coupling simulation is substantially improved considering the rain effect on sea state. Thus, RAIN simulation yields multi-response on minimum MSLP ranging from 10 hPa deeper to 4 hPa shallower. Such differences are larger than those between two-way and one-way coupling modes studied in the previous section. These findings are resulted from the large variations of the rain-induced roughness length as a response on precipitation intensity and type (convective or stratiform). Space-time variability of roughness length can modulate the dynamical and thermodynamic structure of the hurricane as already described at previous chapters. The heterogeneity of roughness length modifies Sandy's asymmetry, affects its central pressure and finally determines the track of the system towards the observed one (Varlas et al., 2017c and references therein).

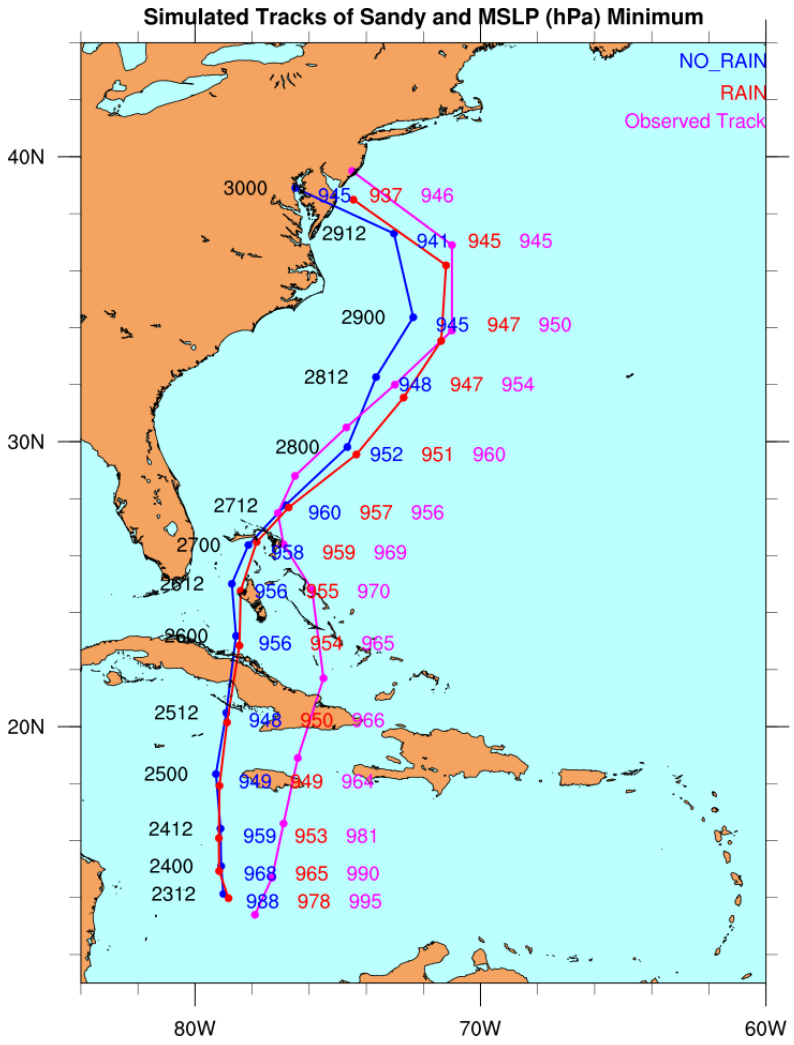

Figure 7.21: Track of the hurricane Sandy based on best track analysis data (magenta line), NO_RAIN (blue line) and RAIN (red line) simulations. Figure refers to time period from 23 October at 12:00 UTC to 30 October 00:00 UTC, 2012. Best track analysis data are retrieved from the National Hurricane Center (NHC) of United States (http://www.nhc.noaa.gov/data/).

In the case of buoys 41002 and 44025 over the Atlantic Ocean (Figure 7.22a, b) the RMSE reduction by RAIN reaches 15% and 44% for wind speed and SWH, respectively (Figure 7.22c, d). RAIN decreases the overestimation while improving the hurricane phase-shift presented by NO_RAIN simulation. This is primarily attributed to the fact that RAIN simulates a more realistic thermodynamic structure of Sandy.

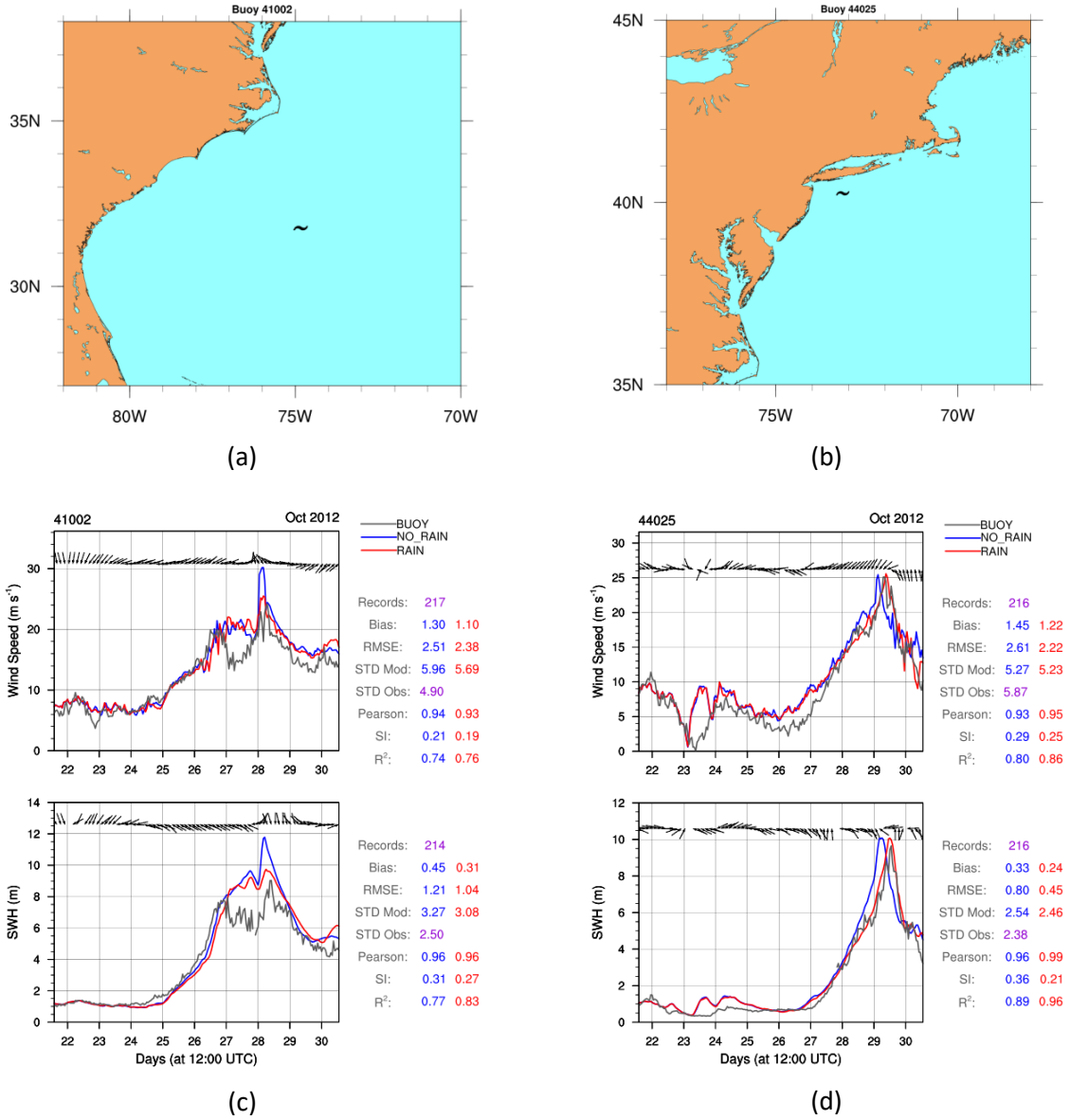

Figure 7.22: Location of buoy (a) 41002 and (b) 44025. Time series of wind speed (m s^{-1}) and SWH (m) based on the observations of buoy (c) 41002 (gray), (d) 44025 (gray), NO_RAIN (blue) and RAIN (red) simulations. The black arrows represent wind and SWH directions, measured by the buoy. On the right, the results of statistical evaluation through the calculation of statistical indices are illustrated. Time period from 22 October at 00:00 UTC to 31 October at 00:00 UTC, 2012.

Figure 7.23 (a-e) shows that the representation of the rain impact on waves yields improvements on the forecast skill decreasing the overestimation of wind speed over the sea and SWH, comparing against buoys observations and satellite retrievals.

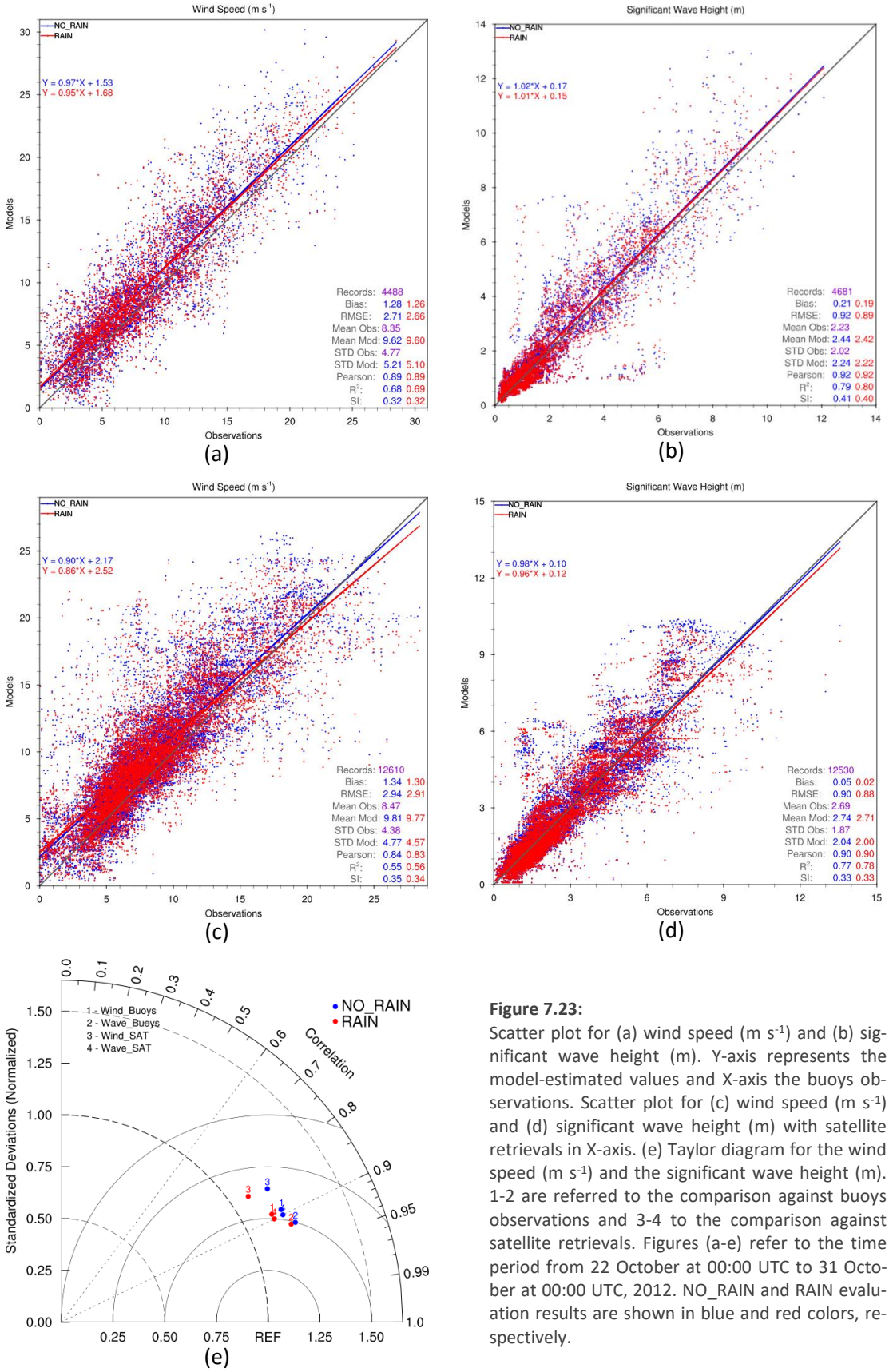

Figure 7.23:
Scatter plot for (a) wind speed (m s^{-1}) and (b) significant wave height (m). Y-axis represents the model-estimated values and X-axis the buoys observations. Scatter plot for (c) wind speed (m s^{-1}) and (d) significant wave height (m) with satellite retrievals in X-axis. (e) Taylor diagram for the wind speed (m s^{-1}) and the significant wave height (m). 1-2 are referred to the comparison against buoys observations and 3-4 to the comparison against satellite retrievals. Figures (a-e) refer to the time period from 22 October at 00:00 UTC to 31 October at 00:00 UTC, 2012. NO_RAIN and RAIN evaluation results are shown in blue and red colors, respectively.

It is noteworthy that, Taylor diagram indicates that RAIN decreases RMSE and increases correlation, offering also improvements in standard deviation (Figure 7.23e). The highest RMSE reduction for wind speed over the sea and SWH reach 2% and 3%, respectively. The improve-

ments over land are up to 3.6% despite the fact of the negligible impact for the two-way coupling mentioned in Section 5.1.2 (Figure 7.24). The results are characterized by high confidence level (>95%). The response of the forecast skill is mainly amplified from the different thermodynamic structure of Sandy at the time of landfall as it was simulated by RAIN. RAIN improves MSLP and precipitation as well. These improvements are attributed to the better simulation of Sandy's track and structure by RAIN.

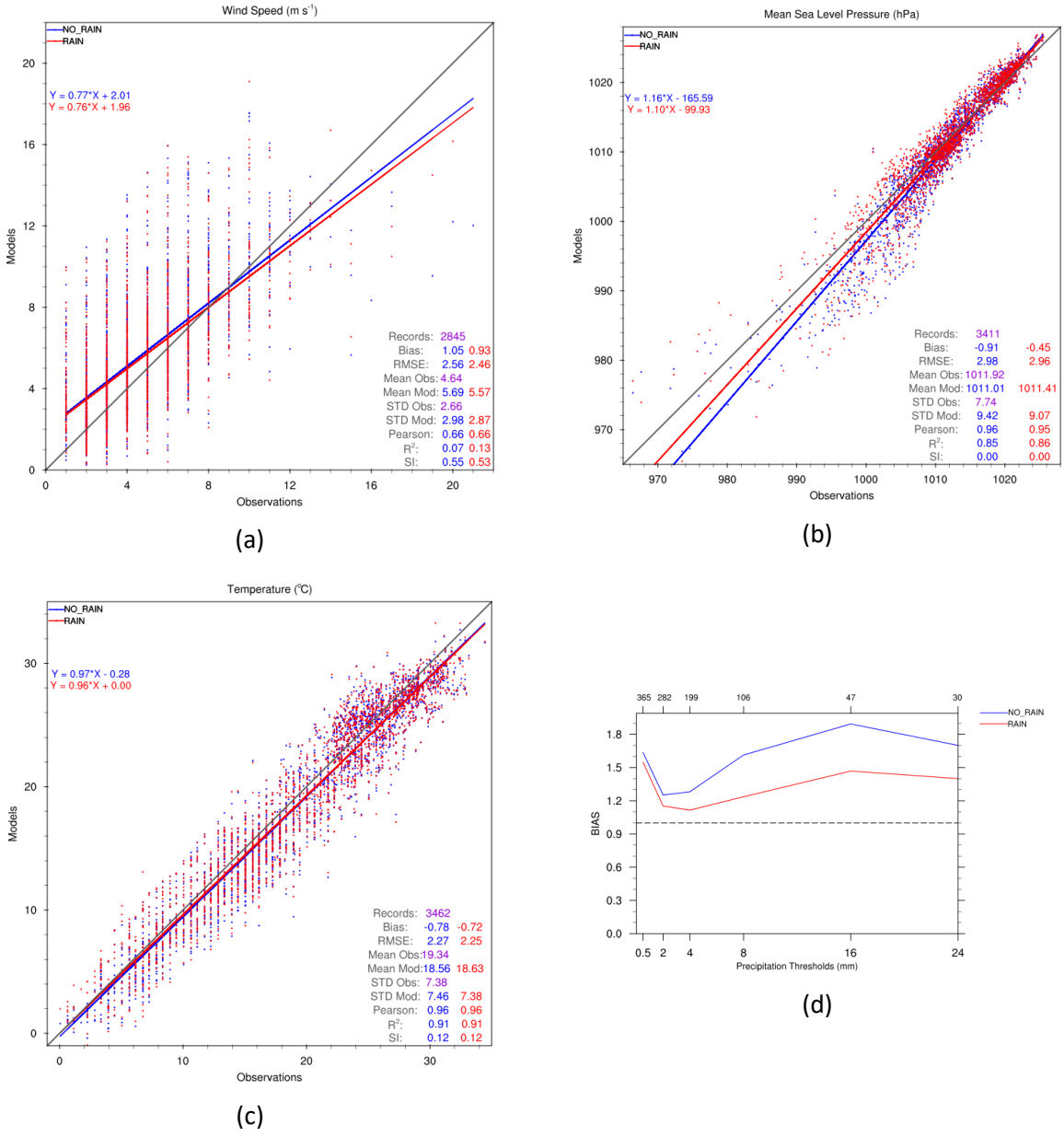

Figure 7.24: Scatter plot for (a) wind speed (m s^{-1}), (b) MSLP (hPa) and (c) temperature (°C) over the land. Y-axis represents the model-estimated values and X-axis the buoys observations. (d) BIAS for specific 6-hour precipitation (mm) thresholds. The numbers above each tick mark denote the sample for the corresponding threshold value. Figures (a-f) refer to the time period from 22 October at 00:00 UTC to 31 October at 00:00 UTC, 2012. NO_RAIN and RAIN evaluation results are shown in blue and red colors, respectively.

Chapter 8

Conclusions and Future Plans

8.1. Goals accomplishment and concluding remarks

In conclusion, the research goals of this thesis to simulate and analyze air-ocean wave interaction were achieved through the implementation of CHAOS, a two-way coupled atmosphere-ocean wave modeling system. The results and the statistical scores of CHAOS simulations confirm the significance of atmosphere-ocean wave interactions adding substantially to our understanding of these important physical mechanisms.

8.1.1. Technical Achievements

The main stages of the effort that led to the implementation CHAOS and the execution of the appropriate simulations are the following:

1. Compilation of OASIS3-MCT coupler which produced the respective libraries and object files. WRF and WAM models were compiled including the libraries and object files of OASIS3-MCT. Implementation of interface between WAM and OASIS3-MCT. Integration of ocean wave parameters calculation and various software adjustments to perform two-way coupled simulations with WRF through OASIS3-MCT. Extensive modifications in the existing interface between WRF and OASIS3-MCT. Preparation of WRF registry and framework modules for coupling with WAM through OASIS3-MCT.
2. Generation of grid, mask and restart files required by OASIS3-MCT. Appropriate tuning of parameters which control the synchronization and the exchange of information between the components. Scalability tests on CHAOS computing performance.
3. Implementation of an integrated surface layer in order to encapsulate various parameters of atmosphere-ocean wave interactions such as rapidly-varying near surface wind speed, Charnock parameter, wave age, wind-induced wave breaking accompanied by sea spray production and rain-wave interactions.
4. Design of statistical evaluation methodology of CHAOS. Configuration of CHAOS for simulations of extreme weather events over the Mediterranean Sea. Employment of nesting techniques in CHAOS and appropriate design and configuration for long-term simulations. CHAOS configuration to simulate tropical cyclones such as hurricane Sandy over the Atlantic Ocean. In that manner CHAOS can be configured in any area even in global scale.

8.1.2. Main findings

The most remarkable research findings that emerged from the utilization of CHAOS to simulate and analyze the atmosphere-ocean wave interaction are summarized below:

1. The atmosphere-ocean wave interactions are characterized by nonlinear mechanisms, various spatiotemporal scales and complex feedbacks that are described only by the employment of an atmosphere-ocean wave fully coupled system. The physical and dynamical processes in surface layer over ocean bodies are totally sea state dependent. The physical and dynamical processes in surface layer over ocean bodies are totally sea state dependent. The integrated wind-wave parameterization schemes in surface layer of CHAOS offer a more realistic representation of the aerodynamic roughness especially over rough sea surfaces. Young wind-generated ocean waves are dominant on the modulation of momentum, mass, enthalpy and moisture fluxes in the atmospheric surface layer. These fluxes primarily modify the atmospheric flow and the ocean wave growth. An important concluding remark is that two-way coupling change the equilibrium of air-sea enthalpy and momentum. Atmosphere dynamically loses momentum and energy by ocean waves but it thermodynamically gains more enthalpy. Two-way coupling balances lower the energy equilibrium attenuating atmospheric flow and, consequently ocean wave growth. This implies that two-way coupling simulates a more turbulent and deeper MABL having a weakening effect on the cyclonic systems as well. The energy imbalance delays the cyclone evolution and produces an average increase of the minimum MSLP. Two-way coupling simulates Mediterranean cyclones up to 2 hPa shallower than one-way coupling mode. The impact on the hurricane Sandy over the Atlantic Ocean is more intense with up to 5 hPa shallowing or 3 hPa deepening. The minimum central MSLP of the hurricanes is determined by complex nonlinear processes unveiling heterogeneities of two-way coupling performance in shallowing or deepening the system. The troposphere also responds on the perturbations that come from the sea surface fluxes. Differences in water vapor mixing ratio and relative humidity are detectable up to 7 km alongside with the wind speed, the vertical velocity and the temperature up to the tropopause. The lower energy equilibrium in the two-way coupling mode results to attenuation of dynamical and thermodynamic structure as

well as of cloud formation. However, such feedbacks are still characterized by increased uncertainty as they are mainly modulated by complex and nonlinear processes. It is, thus, difficult to draw distinct conclusions regarding any systematic effect of the sea surface roughness on the dynamical and thermodynamic structure of the troposphere.

2. The simulation of atmosphere-ocean wave interactions improves the forecast skill. During extreme weather events, two-way coupling mode of CHAOS offers robust RMSE reduction up to 10% and 24% for wind speed and SWH over the sea, respectively, as well as up to 5% for wind speed, MSLP, temperature and precipitation over the land. Over the sea, the improvement percentage is approximately proportional but in a nonlinear way to the intensity of wind and sea state conditions. Moreover, two-way coupling mode also improves the long-term (1 December 2013 - 1 December 2014) operational performance of CHAOS by up to 3.7% and 6.3% for wind speed and SWH, respectively. The improvements in long-term approach are smaller than those in extreme weather events simulation because low and moderate wind and wave conditions are dominant reducing the improvements of the forecast skill in higher intensities. The improvement percentage is approximately proportional but in a nonlinear way to the intensity. Such response initiates from the explicit estimation of the Charnock parameter instead of the remained constant parameter (0.0185) throughout the one-way simulation. Space-time Charnock variability decreases the medium to high-frequency gravity waves as the roughness length and the friction velocity are also increased. The roughness reduces for low-frequency waves forming a more slip sea surface under swell conditions. Additionally, two-way coupling improvements are evidenced especially over open sea. This may be attributed to the fact that wave spectrum intensity is dependent to wind-generated waves and, consequently, to near surface wind speed and fetch (Janssen, 2004). Over open-sea long-fetch areas, the surface layer of two-way coupled simulation incorporates rougher sea surface information in comparison to the one-way coupling mode. This causes reduction of wind speed and intense attenuation of wind-generated waves decreasing the overestimation of SWH. This reduction mechanism is more prominent over open sea than over short-fetch areas near the shore. Moreover, SWH is sensitive on near surface wind speed and, thus, a small decrease of wind speed can cause a more intense decrease of SWH (e.g. de León and Soares, 2008).

3. The research findings employing nesting techniques in CHAOS have important implications for solving the problem of complex atmosphere-ocean wave interactions in small spatiotemporal scales. Nesting in WRF resolves additional frequencies at the tail of the atmospheric spectrum modifying the momentum and heat fluxes over the air-sea interface. This finding indicates that, the interactions between short sea surface disturbances with rapidly time- and spatial-varying winds contribute to high-frequency wave growth and, consequently, increase the SWH. Nesting techniques in CHAOS refine the simulations results in higher spatiotemporal resolutions with up to 10% statistical improvements for the SWH. The improvement in the representation of wave growth has a positive feedback to the resolve of sea surface roughness, which is statistically reflected to the wind speed especially near the shore with improvements up to 9% as well as to the estimation of precipitation over the land. However, nesting increases the wind speed overestimation over open sea resulting to a slight increase of wind speed RMSE.
4. CHAOS is able to simulate the wave breaking processes accompanied by sea spray production on the development of a hurricane over the Atlantic Ocean. The representation of sea surface aerodynamic roughness only considering wave age (Smith's scheme) resulted to partial description of physical mechanisms and up to 16% improvements. Involving wind-induced wave breaking accompanied by sea spray production (Liu's scheme) enriches the representation of atmosphere-ocean wave interaction with statistical improvements up to 23% and better estimation of central minimum pressure. This is attributed to the encapsulation of more physical mechanisms such as the reduction of atmospheric momentum loss during wave breaking. Janssen's scheme offered even better overall forecast skill with improvements reaching 24%. The differences between the schemes may be attributed to the deficient configuration of the parameterizations employing empirical methods and data. There is lack of universality in the air-sea parameterizations as proposed by Soloviev et al. (2014). Summarizing, a future upgrade of Janssen's scheme incorporating wind-induced wave breaking and sea spray effects might be an interesting approach.
5. The impact of rainfall on wave formation and evolution is also investigated by CHAOS after a major upgrade of the Janssen's scheme to incorporate the effect of the rain droplets on sea surface roughness length according to an approach by Kumar et al. (2009). The complex nonlinear rain-wave interactions modify sea surface roughness

having an overall negative contribution to the atmospheric flow and wave growth. They also led to an additional modification of energy equilibrium. The heterogeneity of roughness length variations modifies the asymmetry of a cyclonic system affecting its central pressure and track. Rainfall intensity and pattern distribution are also influenced. The incorporation of rain impact on waves during extreme weather conditions offers statistical improvements up to 3% and 3.6% over the sea and the land, respectively. The forecast skill improvements especially over the land are partially attributed to the estimation of a more accurate track. The improvements are smaller than those resulted by the comparison between the two-way and the one-way coupling modes. However, these are enough to unveil the important role of rain-wave interactions in the performance of foresting systems which even today do not incorporate them.

8.2. Future Plans

Reasonably, the accomplishment of research goals in the framework of this PhD thesis left some questions unanswered while new research issues born. The proposed issues which future research could focus can be summarized as follows:

- The investigation of rain-wave interactions including additional processes is in the near future plans of author. It is a controversial research issue due to its dependence on many nonlinear processes and feedbacks. Modifications on the existing parameterization scheme of CHAOS or the implementation of a more advanced one will offer substantial improvements on resolving rain-wave interactions. Other factors such as the air and water viscosities, the whitecaps, the sea spray due to raindrop striking, the raindrops downfall angle, the interaction between wind and raindrops as well as the direct mass and momentum transfer from raindrop to the sea surface will be also investigated.

- The impact of the ocean waves on atmospheric chemistry is an additional topic for advanced research. Ocean waves modulate sea spray production and, subsequently, sea salt nuclei which are major cloud condensation nuclei. CHAOS has the capability to concurrently simulate ocean wave, atmospheric, chemical and hydrological processes. Thus, it can simulate the modification of sea spray production due to sea state and the advection of sea spray droplets in the atmosphere accompanied by modified momentum, enthalpy and moisture fluxes. In this context, there is the necessity to implement the appropriate pa-

rameterization schemes for sea salt emissions through both atmospheric flow and sea state information.

More details see at https://www.espa.gr/.

- The impact of the ocean waves on hydrology is also an interesting research issue. Ocean waves determine both the aerodynamic roughness and sea salt particles distribution which can indirectly affect hydrological processes taking consideration the feedbacks of these mechanisms. For this purpose, it is essential to implement algorithms for the representation of wave-hydro-meteorological interaction processes and to calibrate the complex air-sea-land equilibriums.

Appendix

Technical Implementation of CHAOS

I. Design Decisions

The first step towards the coupling of WRF and WAM was to manage to execute the two models concurrently on multiple autonomous processors as a so-called "Multiple Programs Multiple Data" (MPMD) application. To that end, the `mpirun` (or `mpiexec`) instruction is employed as follows:

```
mpirun –np <nwrf> wrf.exe : -np <nwam> wam.exe
```

where `wrf.exe` and `wam.exe` are the executables of WRF and WAM and <`nwrf`> and <`nwam`> the number of parallel tasks for each model respectively. For example, let's assume a computer node with 20 central processing units (CPUs) and running the two models as an MPMD application allocating 12 tasks to `wrf.exe` and 8 tasks to `wam.exe`, as follows:

```
mpirun -np 12 wrf.exe : -np 8 wam.exe
```

In this case, both models start running as per allocated number of tasks. However, `MPI_COMM_WORLD` owns all 20 `(<nwrf> + <nwam>)` tasks. As the two models run using the same communicator, `MPI_COMM_WORLD`, a deadlock may occur since the sum of the tasks allocated for the execution of each model has to be equal to the total number of tasks of its communicator (Takayama et al., 2010).

In general, there are three ways to avoid this deadlock. The first solution is to unify the source code of the two models building one common executable. This approach, though, is in this case very demanding as the two models are characterized by different code architecture, grid structure, dynamics, physics, numerical schemes etc. Additionally, since it is a custom solution for the integration of these specific models, the resulting system would lack extensibility and interoperability with other models.

The second solution is to introduce a different communicator for each model (Gropp et al., 1999; Takayama et al., 2010). A first attempt was to build the coupled system employing solely MPI directives, as the parallelization of both models is developed based on MPI architecture (Snir et al., 1998). This approach, despite being proposed by previous studies (e.g. Katsafados et al., 2016a), was not chosen for the coupling of WRF and WAM models in the current work. WRF model already uses an advanced grouping methodology for many internal MPI processes while the communication between WRF and WAM tasks requires the introduction of in-

ter- and intra-communicators. In this context, it is very complex to enable the exchange of information between the models due to the extensive modifications in MPI architecture of both models that are required. The exchange of information between the tasks needs to be defined explicitly and, consequently, such a system is MPI topology dependent and it is characterized by limited scalability and extensibility.

The third solution is the use of a coupler in combination with MPI directives. Although in the past, couplers had limited capabilities in terms of portability, flexibility, scalability and efficient use of memory, nowadays there is great evolution in coupling techniques and capabilities. Hence, OASIS3-MCT coupler is the "state-of-the-art" of couplers and it has proven to be a powerful tool for climate and weather modeling (Valcke, 2015). Previous studies (Béranger et al., 2011; Masson et al., 2012; Colas et al., 2013; Samson et al., 2014) presenting the use of older versions of OASIS for the coupling of WRF with the ocean model NEMO (Madec, 2008) were a positive indication about the plausibility of exploiting OASIS3-MCT for the current coupling WRF-WAM. Taking also into consideration the advanced features of the current version of OASIS3-MCT presented in Section 3.3, the decision was to investigate the feasibility of WRF-WAM coupling using OASIS3-MCT along with MPI directives.

In this context, WRF and WAM models have been configured to run as parallel tasks on different processors exchanging information through OASIS3-MCT. The role of the coupler is to support the exchange of information between the two models as well as its spatial transformation required to overcome the different grid structure of the models.

II. Hardware and Software Infrastructure

The system was initially built on the computer cluster of Atmosphere and Climate Dynamics Group (ACDG) at Harokopio University of Athens (HUA). The cluster currently consists of 5 computational nodes with 4 Intel Xeon (3.3GHz) CPUs each. However, in order to prove the scalability of the system, the configuration was afterwards successfully transplanted to the High Performance Computer (HPC) ARIS consisting of 532 computational nodes of 20-40 cores with CPU frequency ranging from 2.4 to 2.8 GHz (http://doc.aris.grnet.gr/hardware/).

OASIS3-MCT, WRF and WAM were compiled using Intel Fortran and C compilers (serial and MPI). Additional libraries were also employed, such as:

- MPICH – enabling the MPI capabilities of the system
- NetCDF – required in order to manage netcdf files
- Zlib, libpng, JasPer – WRF-specific libraries

III. Implementation of WAM - OASIS3-MCT and WRF - OASIS3-MCT interfaces

To begin with, both WRF and WAM models have parallel structure in the sense that the performed computations are broken down to sub-processes which are executed simultaneously using multiple computing resources (processors). This architecture requires an overall control/coordination mechanism which is called *communicator*. The standard platform used by both WRF and WAM for message passing between their sub-processes is MPI and each model runs under the global MPI communicator, `MPI_COMM_WORLD` (Barker, 2015).

The standalone execution of WAM requires the MPI routines `MPI_Init()` in order to start the simulation and `MPI_Finalize()` in order to terminate the simulation. Moving forward with the creation of the interface of WAM with OASIS3-MCT, the above structure has to get encapsulated in the respective initialization and termination function of the coupler. This is achieved using OASIS3-MCT routines `oasis_init_comp()` and `oasis_terminate()` replacing `MPI_Init()` and `MPI_Finalize()` respectively:

```
MPI_Init()                          oasis_init_comp()
    ⋮                                   ⋮
MPI_Finalize()                      oasis_terminate()
```

Using `oasis_init_comp()`, OASIS3-MCT is appropriately configured in order to identify WAM as a component that it is coupled with. The global communicator `MPI_COMM_WORLD`, which is the default communicator for WAM and manages the total of `(<nwrf> + <nwam>)` tasks, is split into two communicators. Initially, the *local communicator*, which manages all `<nwam>` tasks, is created and then the *coupling communicator*, required by a subset of the `<nwam>` tasks for the communication between WAM and OASIS3-MCT is built. In order to implement this local communicator in the WAM-OASIS3-MCT interface, the OASIS3-MCT routine `oasis_get_localcomm()` was employed. Additionally, WAM was modified appropriately to

replace MPI_COMM_WORLD with the new local communicator in all MPI routines of the model. As far as the coupling communicator is concerned, another OASIS3-MCT routine was introduced for its implementation, oasis_create_couplcomm(). The number of tasks managed by the coupling communicator out of the total of <nwam> tasks is configurable and depends on the volume of data that need to be exchanged between WAM and OASIS3-MCT. The structure of the interface becomes thus:

```
oasis_init_comp()
      ⋮
      oasis_get_localcomm()
           ⋮
      oasis_create_couplcomm()
      ⋮
oasis_terminate()
```

Similar approach of a local and a coupling communicator is also applied to incorporate the already existing WRF-OASIS3-MCT interface in the system. The local communicator is created first managing all <nwrf> tasks. Afterwards, the coupling communicator is created handling the tasks used for WRF-OASIS3-MCT communication. However, in this case, OASIS3-MCT routine oasis_set_couplcomm() is employed instead of oasis_create_couplcomm() that was used for WAM, as the coupling communicator in WRF is already utilized. Additionally, the local communicator of WRF is internally split to sub-communicators. This is required in order to support the more complex computations and structure of WRF.

The split of MPI_COMM_WORLD to local and coupling communicators of WRF and WAM is illustrated in Figure 1.

It is noteworthy that each of the new communicators renumbers the tasks allocated to it. Thus, the deadlock described in Section I is avoided and the models can either run separately or concurrently through OASIS3-MCT even without exchanging information.

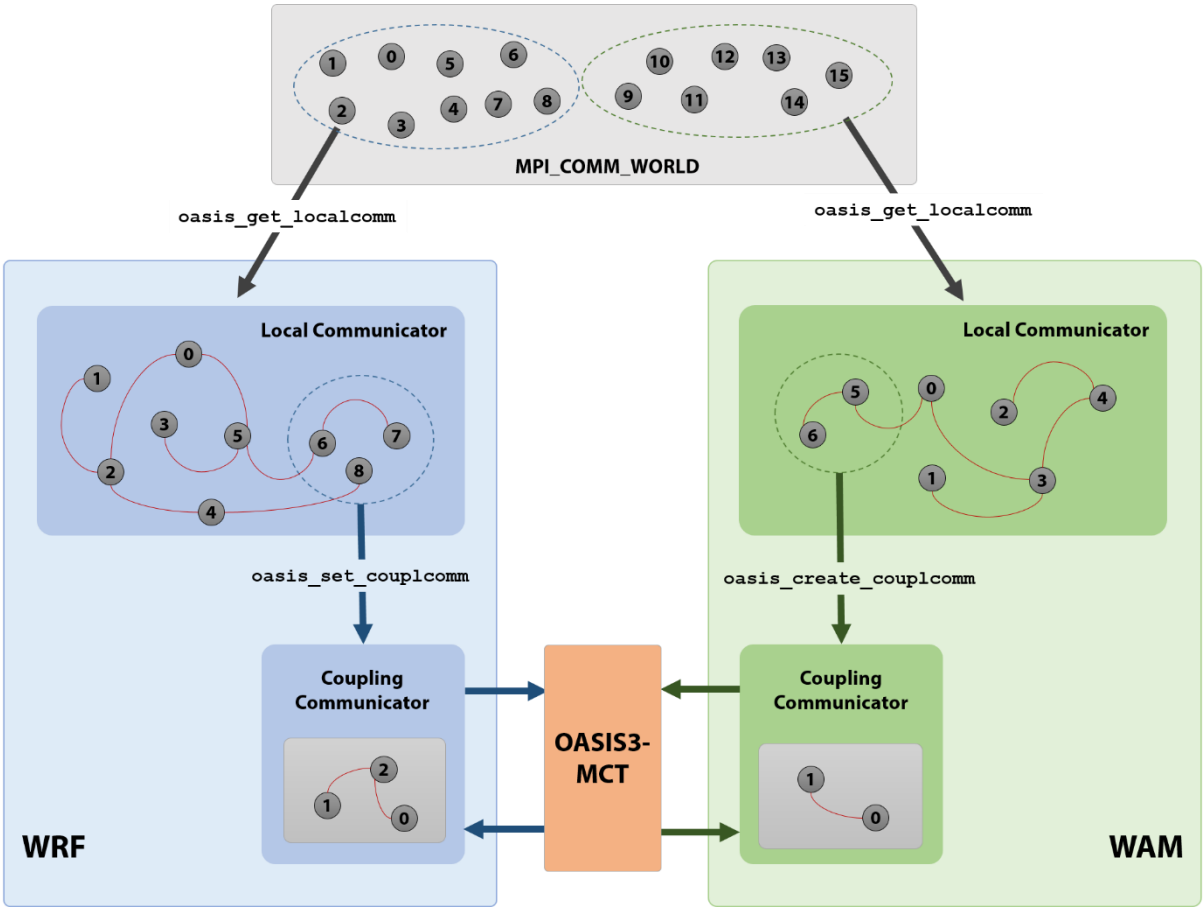

Figure 1: The split of MPI_COMM_WORLD communicator and the creation of local and coupling communicators in both models WRF and WAM through OASIS3-MCT routines.

In Figure 2, a multi-level flowchart of the parallel execution of the system and the data exchanges between WRF and WAM through OASIS3-MCT are depicted. In this example, a typical configuration of WRF and WAM is assumed with time step ratio 1/10 and 3 exchanged fields, the near surface wind components (u, v) calculated by WRF and the Charnock parameter produced by WAM. Additionally, the coupling time -the period of exchange of information between the models- is equal to the time step of WAM. For simplicity reasons, so far, only the exchange of the wind field and Charnock parameter between the two models is discussed. However, CHAOS system has been configured in order to also facilitate the exchange of a number of other variables during its execution.

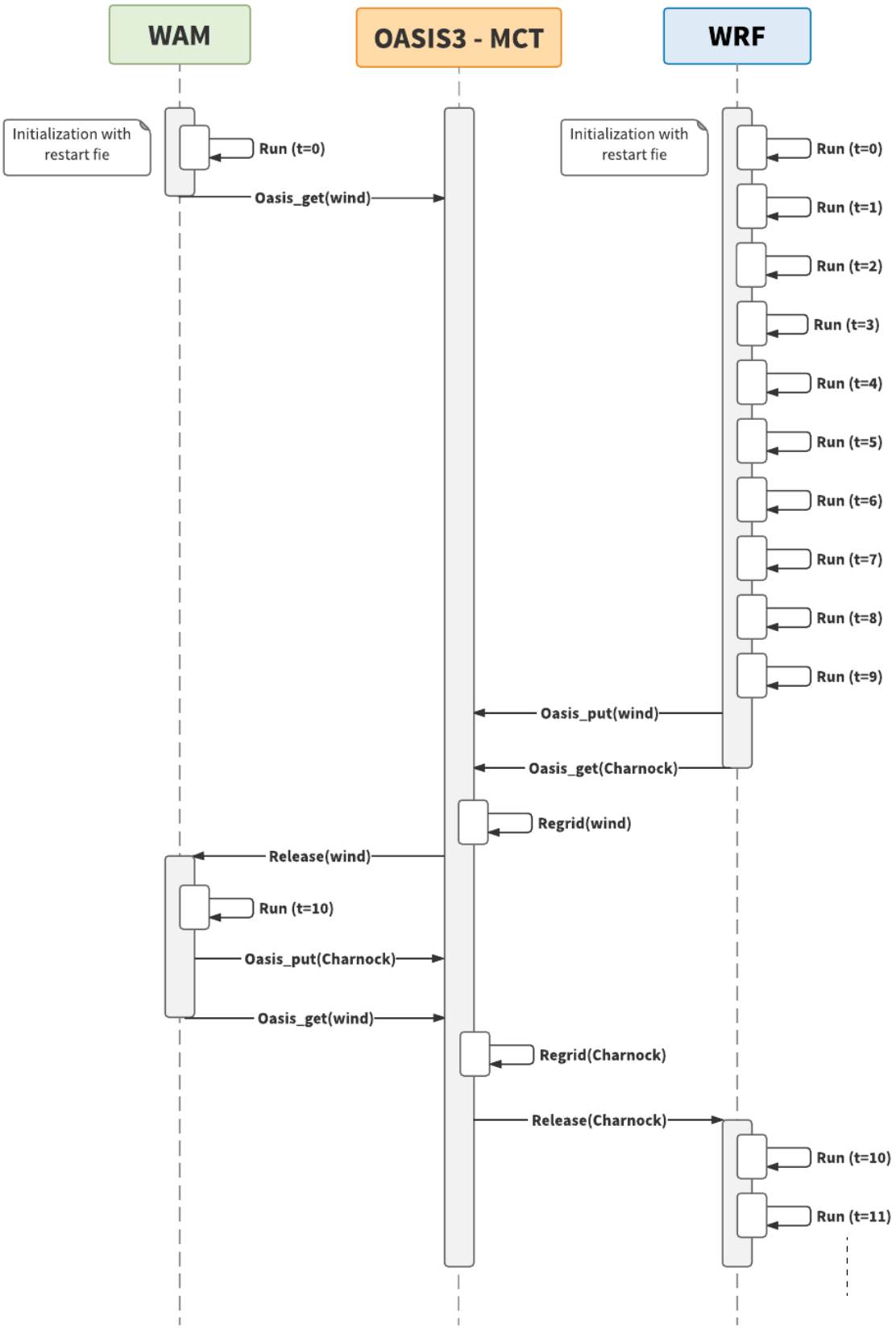

Figure 2: A multi-level flowchart of the parallel execution of the system where the data exchanges between WRF and WAM through OASIS3-MCT are depicted. The time step ratio between WRF and WAM is 1/10.

To begin with, three OASIS3-MCT routines are employed in order to define essential configuration parameters of each interface. `oasis_def_partition()` routine is firstly utilized as the processes that exchange coupling data must define their local partition in the global grid indexing space. Afterwards, `oasis_def_var()` is used so as to declare the fields sent or received during the simulation. Finally, `oasis_enddef()` is called to generate the regridding files from the previous steps, as well as to synchronize all processes before starting the data exchange. OASIS3-MCT uses these auxiliary data files for convenience, defining the grids and the masks of the models being coupled as well as the regridding weights and addresses. The regridding files are built during the first execution of the system and are only rebuilt in case the grids of the models have been modified to save execution time.

Moving on, `oasis_get()` and `oasis_put()` routines are used to support the exchange of the coupling fields. Each model calls `oasis_get()` in order to request and receive data from the other model through OASIS3-MCT while `oasis_put()` is used so as for the models to send data requested by the other model through OASIS3-MCT. `oasis_get()` routine is called at the beginning of the execution of each time step as each model has been configured in order to use information originating from the other model.

During the first time step (`coupling_time=0`), the values required by the models are retrieved from initialization (restart) files. However, for the next time steps each model receive the field that is actually produced by the other one. Since both models have reached the point of executing `oasis_get()` they will keep waiting until they receive the required fields, resulting to a deadlock. This issue can be resolved by introducing the “lag” concept. Setting a LAG value for one of the models results to shifting of the time at which the data is sent but not the time at which the data is received. In this case, a lag of 1 WRF time step for WRF is set. Using this configuration, after the initialization of the two models (`coupling_time=0`), WAM will execute its `oasis_get()` requesting the wind field for its next time step (`coupling_time = 1, WAM_timestep=1, WRF_timestep=10`) but it will receive the values that are produced by the simulation of WRF at `WRF_timestep=9`. Once WRF has completed the execution of `WRF_timestep=9` it broadcasts the wind field (`oasis_put()`) which is then propagated to WAM while it begins the execution of `WRF_timestep=10`. At this point, WRF will execute `oasis_get()` expecting the Charnock parameter field from WAM at that time step. Meanwhile, having received the wind field required to execute its next time step, WAM starts the execution of `WAM_timestep=1`, calculating the Charnock parameter field WRF is waiting for

and sends the respective data to it using `oasis_put()`. This way, WRF resumes its execution for `WRF_timestep=10` and so on. Consequently, WRF calls `oasis_get()` and `oasis_put()` at every time step but the fields are exchanged only when `WRF_time = coupling_time` for `oasis_get()` and `WRF_time=coupling_time-LAG` for `oasis_put()`. In contrast to WRF, in WAM model the fields are exchanged for both `oasis_get()` and `oasis_put()` when `WAM_time = coupling_time`.

On each data exchange, OASIS3-MCT transforms the data from the grid of the sender model to the grid of the receiver one as shown in Figure 2. Due to the fact that OASIS3-MCT internally uses MCT regridding procedures (see more at Valcke et al., 2015), there are several options with respect to the method of regridding. For the purposes of this thesis, bilinear regridding was chosen which performs interpolation based on local bilinear approximations. After each model receives the external data through its coupling communicator, the MPI routine `MPI_Bcast()` is called in order to broadcast the data from the coupling processes to local processes controlled by the local communicator.

To sum up, the interface of each model has the following structure:

```
oasis_init_comp()
      ⋮
      oasis_get_localcomm()
      ⋮
      oasis_create_couplcomm()
      ⋮
      oasis_def_partition()
      ⋮
      oasis_def_var()
      ⋮
      oasis_enddef()
      ⋮
      oasis_get()
      ⋮
      oasis_put()
      ⋮
oasis_terminate()
```

Publications in International Research Journals

1. Katsafados, P., Papadopoulos, A., **Varlas, G**., Papadopoulou, E., and Mavromatidis, E. (2014). Seasonal predictability of the 2010 Russian heat wave. *Natural Hazards and Earth System Sciences*, *14*(6), 1531.

2. Christakos, K., **Varlas, G**., Reuder, J., Katsafados, P., and Papadopoulos, A. (2014). Analysis of a low-level coastal jet off the western coast of Norway. *Energy Procedia*, *53*, 162-172.

3. Christakos, K., Cheliotis, I., **Varlas, G**., and Steeneveld, G. J. (2016). Offshore wind energy analysis of cyclone Xaver over North Europe. *Energy Procedia*, *94*, 37-44.

4. Katsafados, P., Papadopoulos, A., Korres, G., and **Varlas, G**. (2016). A fully coupled atmosphere-ocean wave modeling system for the Mediterranean Sea: interactions and sensitivity to the resolved scales and mechanisms. *Geoscientific Model Development*, *9*(1), 161-173.

5. Katsafados, P., **Varlas, G**., Papadopoulos, A., and Korres, G. (2017). Implementation of a Hybrid Surface Layer Parameterization Scheme for the Coupled Atmosphere-Ocean Wave System WEW. *Perspectives on Atmospheric Sciences*, Springer International Publishing, 159-165.

6. **Varlas, G**., Katsafados, P., and Papadopoulos, A. (2017). Temperature Seasonal Predictability of the WRF Model. *Perspectives on Atmospheric Sciences*, Springer International Publishing, 75-80.

7. Cheliotis, I., **Varlas, G**., and Christakos, K. (2017). The Impact of Cyclone Xaver on Hydropower Potential in Norway. *Perspectives on Atmospheric Sciences,* Springer International Publishing, 175-181.

8. **Varlas, G**., Papadopoulos, A., and Katsafados, P. (2017). An Analysis of the Synoptic and Dynamical Characteristics of Hurricane Sandy (2012). *Meteorology and Atmospheric Physics Journal (under review).*

9. **Varlas, G**., Katsafados, P., Papadopoulos, A., and Korres, G. (2017). Implementation of a two-way coupled atmosphere-ocean wave modeling system for assessing air-sea interaction over the Mediterranean Sea. *Atmospheric Research Journal (accepted with minor revisions).*

10. **Varlas, G**., Christakos, K., Cheliotis, I., Papadopoulos, A., and Steeneveld, G. J. (2017). Spatiotemporal variability of marine renewable energy resources in Norway. *Energy Procedia (in press).*

11. **Varlas, G**., Katsafados, P., Papadopoulos, A., and Korres, G. (2017). The integration of Argo temperature measurements in numerical weather prediction. *Mediterranean Marine Science Journal (in preparation).*

12. **Varlas, G**., Katsafados, P., Papadopoulos, A., and Korres, G. (2017). The impact of rain on wave evolution and its feedback to the atmosphere. *(drafted).*

Publications/Presentations in International and National Conferences

1. **Varlas, G**., Papadopoulos, A., and Katsafados, P. (2013). A long-term spatio-temporal illustration of precipitation in Greece. 1st Conference of Spatial Analysis, May 17-18 2013, Athens, Greece.

2. **Varlas, G**., Katsafados, P., and Papadopoulos, A. (2013). The synoptic and dynamical characteristics of the hurricane Sandy. 13th CEST 5-7 September 2013, Athens, Greece.

3. Christakos, K., **Varlas, G**., Reuder, J., Katsafados, P., and Papadopoulos, A. (2014). Metocean analysis of a low-level coastal jet off the Norwegian coast. 11th Deep Sea Offshore Wind R&D Conference 22-24 January 2014, Trondheim, Norway.

4. Katsafados, P., Papadopoulos, A., **Varlas, G**., and Korres, G. (2014). The coupled atmosphere-ocean wave modeling system WEW. 12th International Conference on Meteorology, Climatology and Atmospheric Physics (COMECAP 2014), University of Crete, Heraklion, Crete, Greece, 28-31 May 2014.

5. **Varlas, G**., Papadopoulos A., Korres G., and Katsafados P. (2014). Modeling the air-sea wave interaction processes in an explosive cyclone over the Mediterranean Sea. 12th International Conference on Meteorology, Climatology and Atmospheric Physics (COMECAP 2014), University of Crete, Heraklion, Crete, Greece, 28-31 May 2014.

6. Katsafados, P., Papadopoulos, A., **Varlas, G**., and Korres, G. (2015). A hybrid surface layer parameterization scheme for the two-way fully coupled ocean-wave system WEW. European Geosciences Union General Assembly 2015, Vienna, Austria, 12-17 April 2015.

7. **Varlas, G**., and Katsafados, P. (2015). Statistical approaches and evaluation of seasonal weather forecasting. 28th Panhellenic Conference on Statistics, Harokopio Univesity of Athens, Athens, Greece, 15-18 April 2015.

8. **Varlas, G**.,Papadopoulos, A., Korres G., and Katsafados, P. (2015). Evaluation of a fully coupled atmosphere - ocean waves system (WEW) under high impact wind-wave conditions. 11th Panhellenic Symposium of Oceanography & Fisheries, University of the Aegean, Mytilini, Lesvos, Greece, 13-17 May 2015.

9. **Varlas, G**., and Katsafados, P. (2015). Computational improvements in seasonal weather forecasting. FOSSCOMM 2015, Technological Educational Institute of Athens, Athens, Greece, 7-8 November 2015.

10. Christakos, K.., Cheliotis, I., **Varlas, G**., Steeneveld, G.J. (2016). Analysis of cyclone Xaver (2013) for offshore wind energy. 13th Deep Sea Offshore Wind R&D Conference 20-22 January 2016, Trondheim, Norway.

11. Cheliotis, I., **Varlas, G**., and Christakos, K. (2016). The impact of Cyclone Xaver on Hydropower Potential in Norway. 13th International Conference on Meteorology, Climatology and Atmospheric Physics (COMECAP 2016), Aristotle University of Thessaloniki, Thessaloniki, Greece, 19-21 September 2016.

12. Katsafados, P., **Varlas, G**., Papadopoulos A., and Korres G. (2016). Implementation of a hybrid surface layer parameterization scheme for the coupled atmosphere-ocean wave system WEW. 13th International Conference on Meteorology, Climatology and Atmospheric Physics (COMECAP 2016), Aristotle University of Thessaloniki, Thessaloniki, Greece, 19-21 September 2016.

13. **Varlas, G**., Katsafados, P., and Papadopoulos A. (2016). Seasonal predictability of the WRF model. 13th International Conference on Meteorology, Climatology and Atmospheric Physics (COMECAP 2016), Aristotle University of Thessaloniki, Thessaloniki, Greece, 19-21 September 2016.

14. Christakos, K., **Varlas, G**., Cheliotis, I., Aalstad, K., Papadopoulos, A., Katsafados, P., and Steeneveld, G.J. (2017). Quantitative variability of renewable energy resources in Norway. European Geosciences Union (EGU) General Assembly 2017, Vienna, Austria, 23-28 April 2017.

15. Nomikou, V.M., **Varlas, G**., Theofanidi, S., Karymbalis, E., Papadopoulos, A., and Katsafados, P. (2017). A study on the dynamic interaction of the atmospheric and hydrologic environment in the drainage basin of Sperchios River, Greece. European Geosciences Union (EGU) General Assembly 2017, Vienna, Austria, 23-28 April 2017.

16. **Varlas, G**., Katsafados, P., Papadopoulos, A., and Korres, G. (2017). The impact of rain on wave evolution and its feedback to the atmosphere. European Geosciences Union (EGU) General Assembly 2017, Vienna, Austria, 23-28 April 2017.

Bibliography

Abdalla, S., Janssen, P. A., and Bidlot, J. R. (2010). Jason-2 OGDR wind and wave products: Monitoring, validation and assimilation. *Marine Geodesy*, *33*(S1), 239-255.

Aijaz, S., Ghantous, M., Babanin, A. V., Ginis, I., Thomas, B., and Wake, G. (2017). Nonbreaking wave-induced mixing in upper ocean during tropical cyclones using coupled hurricane-ocean-wave modeling. *Journal of Geophysical Research: Oceans*.

Alari, V., Staneva, J., Breivik, Ø., Bidlot, J. R., Mogensen, K., and Janssen, P. (2016). Surface wave effects on water temperature in the Baltic Sea: simulations with the coupled NEMO-WAM model. *Ocean Dynamics*, 1-14.

Amante, C., and Eakins, B. W. (2009). *ETOPO1 1 arc-minute global relief model: procedures, data sources and analysis* (p. 19). Colorado: US Department of Commerce, National Oceanic and Atmospheric Administration, National Environmental Satellite, Data, and Information Service, National Geophysical Data Center, Marine Geology and Geophysics Division.

Andreas, E. L. (2004). Spray stress revisited. *Journal of Physical Oceanography*, *34*(6), 1429-1440.

Andreas, E. L. (2011). Fallacies of the enthalpy transfer coefficient over the ocean in high winds. *Journal of the Atmospheric Sciences*, *68*(7), 1435-1445.

Andreas, E. L., Decosmo, J. (2002). The signature of sea spray in the HEXOS turbulent heat flux data. *Boundary-layer meteorology*, *103*(2), 303-333.

Andreas, E. L., Mahrt, L., and Vickers, D. (2015). An improved bulk air-sea surface flux algorithm, including spray-mediated transfer. *Quarterly Journal of the Royal Meteorological Society*, *141*(687), 642-654.

Andreas, E. L., and Monahan, E. C. (2000). The role of whitecap bubbles in air–sea heat and moisture exchange. *Journal of physical oceanography*, *30*(2), 433-442.

Andrews, T., Gregory, J. M., Webb, M. J., and Taylor, K. E. (2012). Forcing, feedbacks and climate sensitivity in CMIP5 coupled atmosphere-ocean climate models. *Geophysical Research Letters*, 39(9).

Ardhuin, F., Bertotti, L., Bidlot, J. R., Cavaleri, L., Filipetto, V., Lefevre, J. M., and Wittmann, P. (2007). Comparison of wind and wave measurements and models in the Western Mediterranean Sea. *Ocean Engineering*, *34*(3), 526-541.

Arya, S. P. (1988). Introduction to Micrometeorology. Academic Press, San Diego, United States, 307 pp.

Bao, J. W., Fairall, C. W., Michelson, S. A., and Bianco, L. (2011). Parameterizations of sea-spray impact on the air–sea momentum and heat fluxes. *Monthly Weather Review*, *139*(12), 3781-3797.

Bao, J.W., Wilczak, J.M., Choi, J.K., and Kantha, L.H. (2000). Numerical simulations of air-sea interaction under high wind conditions using a coupled model: a study of hurricane development. *Mon. Wea. Rev.*, 128, 2190–2210.

Barker, B. (2015, January). Message passing interface (mpi). In *Workshop: High Performance Computing on Stampede*.

Battisti, D. S. (1988). Dynamics and thermodynamics of a warming event in a coupled tropical atmosphere-ocean model. *Journal of the Atmospheric Sciences*, *45*(20), 2889-2919.

Battjes, J. A., and Janssen, J. P. F. M. (1978). Energy loss and set-up due to breaking of random waves. In *Coastal Engineering* 1978 (pp. 569-587).

Beljaars, A. (1995). The parametrization of surface fluxes in large-scale models under free convection. *Quarterly Journal of the Royal Meteorological Society*, 121(522), 255-270.

Beljaars, A. C. M., and Holtslag, A. A. M. (1991). Flux parameterization over land surfaces for atmospheric models. *Journal of Applied Meteorology*, 30(3), 327-341.

Bell, M. M., Montgomery, M. T., and Emanuel, K. A. (2012). Air–sea enthalpy and momentum exchange at major hurricane wind speeds observed during CBLAST. *Journal of the Atmospheric Sciences*, *69*(11), 3197-3222.

Bender, M. A., Ginis, I., Tuleya, R., Thomas, B., and Marchok, T. (2007). The operational GFDL coupled hurricane–ocean prediction system and a summary of its performance. *Monthly Weather Review*, *135*(12), 3965-3989.

Béranger, K., Lebeaupin-Brossier, C., Drobinski, P., Bastin, S., Mailler, S., Samson, G., ... and Maisonnave, É. (2011, October). HyMeX-The regional coupled system WRF-NEMO over the Mediterranean (MORCE plateform): impacts of mesoscale coupled processes on the water budget estimation. In *WCRP Open Science Conference* (p. TH225).

Bhaskar Rao, D. V., Hari Prasad, D., and Srinivas, D. (2009). Impact of horizontal resolution and the advantages of the nested domains approach in the prediction of tropical cyclone intensification and movement. *Journal of Geophysical Research: Atmospheres*, *114*(D11).

Bidlot, J. R. (2012). Present status of wave forecasting at ECMWF. Proceeding from the ECMWF Workshop on Ocean Waves. 25-27 June 2012, Reading, UK. (Online: http://www.ecmwf.int/sites/default/files/elibrary/2012/8234-present-status-wave-forecasting-ecmwf.pdf, accessed 08.05.2017)

Bidlot, J., Janssen, P., Abdalla, S. (2007). A revised formulation of ocean wave dissipation and its model impact. Tech. Rep. Memorandum 509, ECMWF, Reading, UK. (Online: http://www.ecmwf.int/sites/default/files/elibrary/2007/8228-revised-formulation-ocean-wave-dissipation-and-its-model-impact.pdf, accessed 08.05.2017)

Black, P. G., D'Asaro, E. A., Sanford, T. B., Drennan, W. M., Zhang, J. A., French, J. R., ... and Walsh, E. J. (2007). Air–sea exchange in hurricanes: synthesis of observations from the coupled boundary layer air–sea transfer experiment. *Bulletin of the American Meteorological Society*, *88*(3), 357-374.

Bolanos, R., Larsen, X. G., Petersen, O. S., Nielsen, J. R., Kelly, M., Kofoed-Hansen, H., ... and Badger, M. (2014). Coupling atmosphere and waves for coastal wind turbine. *Coastal Engineering Proceedings*, *1*(34), 33.

Breivik, Ø., Mogensen, K., Bidlot, J. R., Balmaseda, M. A., and Janssen, P. A. (2015). Surface wave effects in the NEMO ocean model: Forced and coupled experiments. *Journal of Geophysical Research: Oceans*, *120*(4), 2973-2992.

Bruneau, N., and Toumi, R. (2016). A fully-coupled atmosphere-ocean-wave model of the Caspian Sea. *Ocean Modelling*.

Boumediene, Y., and Valcke, S. (2015, April). Les Performances Des Coupleurs OASIS3-MCT et OpenPALM Pour. *Rapport technique*.

Burgers, G., Janssen, P. A. E. M., and Anderson, D. L. T. (1995). Impact of sea-state dependent fluxes on the tropical ocean circulation. *WORLD METEOROLOGICAL ORGANIZATION-PUBLICATIONS-WMO TD*, 643-646.

Businger, J. A. (1973). A note on free convection. *Boundary-Layer Meteorology*, 4(1-4), 323-326.

Butterfield, S., Musial, W., Jonkman, J., Sclavounos, P., and Wayman, L. (2005, October). Engineering challenges for floating offshore wind turbines. In *Copenhagen Offshore Wind Conference, Copenhagen, Denmark* (pp. 377-382).

Cai, Y., Wen, Y., Wu, L., Zhou, C., and Zhang, F. (2017). Impact of wave breaking on upper-ocean turbulence. *J. Geophys. Res. Oceans*, 122, doi:10.1002/2016JC012654.

Caldwell, D. R., and Elliott, W. P. (1971). Surface stresses produced by rainfall. *Journal of Physical Oceanography*, *1*(2), 145-148.

Caldwell, D. R., and Elliott, W. P. (1972). The effect of rainfall on the wind in the surface layer. *Boundary-Layer Meteorology*, *3*(2), 146-151.

Carniel, S., Benetazzo, A., Bonaldo, D., Falcieri, F. M., Miglietta, M. M., Ricchi, A., and Sclavo, M. (2016). Scratching beneath the surface while coupling atmosphere, ocean and waves: Analysis of a dense water formation event. *Ocean Modelling*, 101, 101-112.

Cavaleri, L., Bertotti, L., and Bidlot, J. R. (2015). Waving in the rain. *Journal of Geophysical Research: Oceans*, *120*(5), 3248-3260.

Cavaleri, L., Fox-Kemper, B., and Hemer, M. (2012a). Wind waves in the coupled climate system. *Bulletin of the American Meteorological Society*,*93*(11), 1651-1661.

Cavaleri, L., Roland, A., Dutour Sikiric, M., Bertotti, L., and Torrisi, L. (2012b). On the coupling of COSMO to WAM. In *Proceedings of the ECMWF Workshop on Ocean-Waves*.

Charnock, H. (1955). Wind stress on a water surface. *Q. J. Royal Meteorol. Soc*., 81, 639-640.

Chen, S. S., Zhao, W., Donelan, M. A., and Tolman, H. L. (2013). Directional wind-wave coupling in fully coupled atmosphere-wave-ocean models: Results from CBLAST-Hurricane. *Journal of the Atmospheric Sciences*,*70*(10), 3198-3215.

Chen, S. S., Zhao, W., Donelan, M. A., Price, J. F., and Walsh, E. J. (2007). The CBLAST-Hurricane Program and the Next-Generation Fully Coupled Atmosphere-Wave-Ocean Models for Hurricane Research and Prediction. *Bulletin of the American Meteorological Society*, *88*(3), 311-317.

Christakos, K., Cheliotis, I., Varlas, G., and Steeneveld, G. J. (2016). Offshore wind energy analysis of cyclone Xaver over North Europe. *Energy Procedia*, 94, 37-44.

Christakos, K., Varlas, G., Reuder, J., Katsafados, P., and Papadopoulos, A. (2014). Analysis of a low-level coastal jet off the western coast of Norway. *Energy Procedia*, *53*, 162-172.

Clementi, E., Oddo, P., Korres, G., Drudi, M., and Pinardi, N. (2013). Coupled wave-ocean modelling system in the Mediterranean Sea. In *13th international workshop on wave hindcasting and 4th coastal hazards symposium,* Alberta, Canadas.

Colas, F., Berthet, S., Masson, S., Echevin, V., and Oerder, V. (2013, December). A new coupled tropical channel WRF-OASIS-NEMO: Sensitivity to the horizontal resolution. In *AGU Fall Meeting Abstracts* (Vol. 1, p. 02).

Colle, B. A., Mass, C. F., and Westrick, K. J. (2000). MM5 Precipitation Verification over the Pacific Northwest during the 1997-99 Cool Seasons*. *Weather and Forecasting*, *15*(6), 730-744.

Csanady, G. T. (2001). Air-sea interaction: laws and mechanisms. *Cambridge University Press*, London, United Kingdom.

D'Asaro, E. A., Thomson, J., Shcherbina, A. Y., Harcourt, R. R., Cronin, M. F., Hemer, M. A., and Fox-Kemper, B. (2014). Quantifying upper ocean turbulence driven by surface waves. *Geophysical Research Letters*, 41(1), 102-107.

Danielson, J. J., Gesch, D. B. (2011). Global multi-resolution terrain elevation data 2010 (GMTED2010) (No. 2011-1073). US Geological Survey. (Online: https://pubs.er.usgs.gov/publication/ofr20111073, accessed 08.05.2017)

Davis, C., Wang, W., Chen, S. S., Chen, Y., Corbosiero, K., DeMaria, M., ... and Reeves, H. (2008). Prediction of landfalling hurricanes with the Advanced Hurricane WRF model. *Monthly weather review*, 136(6), 1990-2005.

Deane, G. B., and Stokes, M. D. (2002). Scale dependence of bubble creation mechanisms in breaking waves. *Nature*, 418(6900), 839-844.

de Leeuw, G., Andreas, E.L., Anguelova, M.D., Fairall, C.W., Lewis, E.R., O'Dowd, C., Schulz, M. and Schwartz, S.E. (2011). Production flux of sea spray aerosol. Reviews of Geophysics, 49(2).

de León, S. P., and Soares, C. G. (2008). Sensitivity of wave model predictions to wind fields in the Western Mediterranean sea. *Coastal Engineering*, *55*(11), 920-929.

Desjardins, S., Mailhot, J., and Lalbeharry, R. (2000). Examination of the impact of a coupled atmospheric and ocean wave system. Part I: Atmospheric aspects. *Journal of physical oceanography*, *30*(2), 385-401.

Dietrich, J. C., Zijlema, M., Westerink, J. J., Holthuijsen, L. H., Dawson, C., Luettich, R. A., ... and Stone, G. W. (2011). Modeling hurricane waves and storm surge using integrally-coupled, scalable computations. *Coastal Engineering*, 58(1), 45-65.

Dobson, F., Hasse, L., and Davis, R. (2012). *Air-sea interaction: instruments and methods*. Springer Science and Business Media.

Donelan, M. A. (1990). Air-sea interaction. The sea, 9(Part A), 239-292.

Donelan, M. A., Dobson, F. W., Smith, S. D., and Anderson, R. J. (1993). On the dependence of sea surface roughness on wave development. *Journal of Physical Oceanography*, *23*(9), 2143-2149.

Donelan, M. A., Haus, B. K., Reul, N., Plant, W. J., Stiassnie, M., Graber, H. C., ... and Saltzman, E. S. (2004). On the limiting aerodynamic roughness of the ocean in very strong winds. *Geophysical Research Letters*, *31*(18).

Dorrestein, R. (1960). Simplified method of determining refraction coefficients for sea waves. *Journal of Geophysical Research*, *65*(2), 637-642.

Doyle, J. D. (1995). Coupled ocean wave/atmosphere mesoscale model simulations of cyclogenesis. *Tellus A*, *47*(5), 766-778.

Doyle, J. D. (2002). Coupled atmosphere-ocean wave simulations under high wind conditions. *Monthly weather review*, *130*(12), 3087-3099.

Drennan, W. M., Graber, H. C., Hauser, D., and Quentin, C. (2003). On the wave age dependence of wind stress over pure wind seas. *Journal of Geophysical Research: Oceans*, 108(C3).

Drennan, W. M., Taylor, P. K., and Yelland, M. J. (2005). Parameterizing the sea surface roughness. *Journal of physical oceanography*, 35(5), 835-848.

Drennan, W. M., Zhang, J. A., French, J. R., McCormick, C., and Black, P. G. (2007). Turbulent fluxes in the hurricane boundary layer. Part II: Latent heat flux. *Journal of the atmospheric sciences*, *64*(4), 1103-1115.

Dudhia, J. (1989). Numerical study of convection observed during the winter monsoon experiment using a mesoscale two-dimensional model. *Journal of the Atmospheric Sciences*, *46*(20), 3077-3107.

Durrant, T. H., Greenslade, D. J., and Simmonds, I. (2009). Validation of Jason-1 and Envisat remotely sensed wave heights. *Journal of Atmospheric and Oceanic Technology*, *26*(1), 123-134.

Edson, J. B., Jampana, V., Weller, R. A., Bigorre, S. P., Plueddemann, A. J., Fairall, C. W., ... and Hersbach, H. (2013). On the exchange of momentum over the open ocean. Journal of Physical Oceanography, 43(8), 1589-1610.

Emanuel, K. A. (1995). Sensitivity of tropical cyclones to surface exchange coefficients and a revised steady-state model incorporating eye dynamics. *Journal of the Atmospheric Sciences*, *52*(22), 3969-3976.

Emanuel, K. (2005). Increasing destructiveness of tropical cyclones over the past 30 years. *Nature*, *436*(7051), 686-688.

Fairall, C. W., Bradley, E. F., Hare, J. E., Grachev, A. A., and Edson, J. B. (2003). Bulk parameterization of air-sea fluxes: Updates and verification for the COARE algorithm. Journal of climate, 16(4), 571-591.

Fairall, C. W., Bradley, E. F., Rogers, D. P., Edson, J. B., and Young, G. S. (1996). Bulk parameterization of air-sea fluxes for tropical ocean-global atmosphere coupled-ocean atmosphere response experiment. *Journal of Geophysical Research: Oceans*, *101*(C2), 3747-3764.

Fan, Y., and Griffies, S. M. (2014). Impacts of parameterized Langmuir turbulence and nonbreaking wave mixing in global climate simulations. *Journal of Climate*, *27*(12), 4752-4775.

French, J. R., Drennan, W. M., Zhang, J. A., and Black, P. G. (2007). Turbulent fluxes in the hurricane boundary layer. Part I: Momentum flux. *Journal of the atmospheric sciences*, *64*(4), 1089-1102.

Friedl, M. A., Sulla-Menashe, D., Tan, B., Schneider, A., Ramankutty, N., Sibley, A., and Huang, X. (2010). MODIS Collection 5 global land cover: Algorithm refinements and characterization of new datasets. *Remote sensing of Environment*, *114*(1), 168-182.

Garratt, J. R. (1977). Review of drag coefficients over oceans and continents. Monthly weather review, 105(7), 915-929.

Geernaert, G. L., Katsaros, K. B., and Richter, K. (1986). Variation of the drag coefficient and its dependence on sea state. Journal of Geophysical Research: Oceans, 91(C6), 7667-7679.

Gochis, D. J., Yu, W., Yates, D. N., 2015. The WRF-Hydro model technical description and user's guide, version 3.0. NCAR Technical Document, Boulder, Colorado, USA. (Online: https://ral.ucar.edu/sites/default/files/public/images/project/WRF_Hydro_User_Guide_v3.0.pdf, accessed 08.05.2017)

Gopalakrishnan, S. G., Liu, Q., Marchok, T., Sheinin, D., Surgi, N., Tuleya, R., Yablonsky, R., Zhang, X., 2010. Hurricane Weather Research and Forecasting (HWRF) model scientific documentation. NOAA Earth System Research Laboratory, Boulder, Colorado, USA. (Online: http://photino.cwb.gov.tw/rdcweb/lib/brief/2011/201106-27-28__HWRF/HWRF_final_2-2_cm.pdf, accessed 08.05.2017)

Green, B. W., and Zhang, F. (2013). Impacts of air-sea flux parameterizations on the intensity and structure of tropical cyclones. *Monthly Weather Review*, *141*(7), 2308-2324.

Grell, G. A., Peckham, S. E., Schmitz, R., McKeen, S. A., Frost, G., Skamarock, W. C., and Eder, B. (2005). Fully coupled "online" chemistry within the WRF model. *Atmospheric Environment*, *39*(37), 6957-6975.

Gropp, W., Lusk, E., and Skjellum, A. (1999). Using MPI: portable parallel programming with the message-passing interface (Vol. 1). MIT press.

Groves, G. W., and Melcer, J. (1961). On the propagation of ocean waves on a sphere. *Geof. Int*, *8*, 77-93.

Gunther, H., Hasselmann, S., and Janssen, P. A. (1992). *The WAM model cycle 4* (No. DKRZ-TR--4 (REV. ED.)). Deutsches Klimarechenzentrum (DKRZ).

Hara, T., and Belcher, S. E. (2004). Wind profile and drag coefficient over mature ocean surface wave spectra. *Journal of physical oceanography*, *34*(11), 2345-2358.

Hari Prasad, K. B. R. R., Venkata Srinivas, C., Venkateswara Naidu, C., Baskaran, R., and Venkatraman, B. (2016). Assessment of surface layer parameterizations in ARW using micro-meteorological observations from a tropical station. Meteorological Applications, 23(2), 191-208.

Hasselmann, K. (1961). On the non-linear energy transfer in a gravity-wave spectrum. Part 1. General theory. *J. Fluid Mech*., 12, 481–500.

Heimann, M., and Reichstein, M. (2008). Terrestrial ecosystem carbon dynamics and climate feedbacks. *Nature*, *451*(7176), 289.

Hersbach, H., and Janssen, P. A. E. M. (1999). Improvement of the short-fetch behavior in the Wave Ocean Model (WAM). *Journal of Atmospheric and Oceanic Technology*, *16*(7), 884-892.

Hodur, R. M. (1997). The Naval Research Laboratory's coupled ocean/atmosphere mesoscale prediction system (COAMPS). *Monthly Weather Review*, *125*(7), 1414-1430.

Holthuijsen, L. H., Powell, M. D., and Pietrzak, J. D. (2012). Wind and waves in extreme hurricanes. *Journal of Geophysical Research: Oceans*, *117*(C9).

Hong, S. Y., Dudhia, J., and Chen, S. H. (2004). A revised approach to ice microphysical processes for the bulk parameterization of clouds and precipitation. *Monthly Weather Review*, *132*(1), 103-120.

Hong, S. Y., Noh, Y., and Dudhia, J. (2006). A new vertical diffusion package with an explicit treatment of entrainment processes. *Monthly Weather Review*, *134*(9), 2318-2341.

Houk, D., and Green, T. (1976). A note on surface waves due to rain. *Journal of Geophysical Research*, 81(24), 4482-4484.

Hristov, T., Miller, S., and Friehe, C. (2003). Dynamical coupling of wind and ocean waves through waveinduced air flow. *Nature*, 422, 55-58.

Hurrell, J., Meehl, G. A., Bader, D., Delworth, T. L., Kirtman, B., and Wielicki, B. (2009). A unified modeling approach to climate system prediction. *Bulletin of the American Meteorological Society*, *90*(12), 1819.

IFS Documentation, Part VII, 2013. ECMWF wave model (Online: http://www.ecmwf.int/sites/default/files/elibrary/2014/9207-part-vii-ecmwf-wave-model.pdf, accessed 08.05.2017)

Janssen, P.A.E.M. (1989). Wave-induced stress and the drag of air flow over sea waves. *J. Phys. Oceanogr*., 19, 745-754.

Janssen, P.A.E.M. (1991). The Quasi-linear theory of wind wave generation applied to wave forecasting. *J. Phys. Oceanogr*., 21, 1631–1642.

Janssen, P. (2004). *The interaction of ocean waves and wind*. Cambridge University Press, London, United Kingdom.

Janssen, P. A. E. M., Doyle, J. D., Bidlot, J., Hansen, B., Isaksen, L., and Viterbo, P. (2002). Impact and feedback of ocean waves on the atmosphere. *Advances in Fluid Mechanics*, *33*, 155-198.

Janssen, P. A., and Komen, G. J. (1985). Effect of atmospheric stability on the growth of surface gravity waves. Boundary-layer meteorology, 32(1), 85-96.

Janssen, P. A., Komen, G. J., and De Voogt, W. J. (1984). An operational coupled hybrid wave prediction model. Journal of Geophysical Research: Oceans, 89(C3), 3635-3654.

Janssen, P. A., Saetra, O., Wettre, C., Hersbach, H., and Bidlot, J. (2004). Impact of the sea state on the atmosphere and ocean. In *Annales hydrographiques* (Vol. 3, No. 772, pp. 3-1). Service hydrographique et océanographique de la marine.

Janssen, P. A., and Viterbo, P. (1996). Ocean waves and the atmospheric climate. *Journal of climate*, *9*(6), 1269-1287.

Jarosz, E., Mitchell, D. A., Wang, D. W., and Teague, W. J. (2007). Bottom-up determination of air-sea momentum exchange under a major tropical cyclone. *Science*, *315*(5819), 1707-1709.

Jenkins, A. D., Paskyabi, M. B., Fer, I., Gupta, A., and Adakudlu, M. (2012). Modelling the effect of ocean waves on the atmospheric and ocean boundary layers. *Energy Procedia*, *24*, 166-175.

Jiménez, P. A., and Dudhia, J. (2014). On the wind stress formulation over shallow waters in atmospheric models. Geoscientific Model Development Discussions, 7(6), 9063-9077.

Jiménez, P. A., Dudhia, J., González-Rouco, J. F., Navarro, J., Montávez, J. P., and García-Bustamante, E. (2012). A revised scheme for the WRF surface layer formulation. Monthly Weather Review, 140(3), 898-918.

Jones, I. S., and Toba, Y. (2001). *Wind stress over the ocean*. Cambridge University Press.

Kain, J. S. (2004). The Kain-Fritsch convective parameterization: An update. *J. Appl. Meteor.*, 43, 170–181.

Kallos, G., Nickovic, S., Papadopoulos, A., et al. (1997). The regional weather forecasting system SKIRON: An overview, in: *Proceedings of the Symposium on Regional Weather Prediction on Parallel Computer Environments*, Athens, Greece, 15–17 October 1997, 109-122.

Karl, T. R., and Trenberth, K. E. (2003). Modern global climate change. *science*, *302*(5651), 1719-1723.

Katsafados, P., Papadopoulos, A., Korres, G., and Varlas, G. (2016a). A fully coupled atmosphere–ocean wave modeling system for the Mediterranean Sea: interactions and sensitivity to the resolved scales and mechanisms. *Geoscientific Model Development*, *9*(1), 161-173.

Katsafados, P., Papadopoulos, A., Mavromatidis, E., and Gikas, N. (2011). Quantitative verification statistics of WRF predictions over the Mediterranean region. *12th Annual WRF Users' Event*, 20-24.

Katsafados, P., Papadopoulos, A., Varlas, G., and Korres, G. (2015). A hybrid surface layer parameterization scheme for the two-way fully coupled ocean-wave system WEW. European Geosciences Union General Assembly 2015, Vienna, Austria, 12 – 17 April 2015.

Katsafados, P., Papadopoulos, A., Varlas, G., and Korres, G. (2014). The coupled atmosphere-ocean wave modeling system WEW. *12th International Conference on Meteorology, Climatology and Atmospheric Physics (COMECAP 2014)*, University of Crete, Heraklion, Crete, Greece, 28-31 May 2014.

Katsafados, P., Varlas, G., Papadopoulos A., and Korres G. (2016b). Implementation of a hybrid surface layer parameterization scheme for the coupled atmosphere-ocean wave system WEW. *13th International Conference on Meteorology, Climatology and Atmospheric Physics (COMECAP 2016)*, Aristotle University of Thessaloniki, Thessaloniki, Greece, 19-21 September 2016.

Katsafados, P., Varlas, G., Papadopoulos, A., and Korres, G. (2017). Implementation of a Hybrid Surface Layer Parameterization Scheme for the Coupled Atmosphere-Ocean Wave System WEW. *Perspectives on Atmospheric Sciences*, Vol I, Eds. Springer, ISBN 978-3-319-35094-3.

Kerbiriou, M. A., Prevosto, M., Maisondieu, C., Clément, A., and Babarit, A. (2007, September). Influence of sea-states description on wave energy production assessment. In *Proceedings of the Seventh European Wave and Tidal Energy Conference,* Porto, Portugal.

Kim, H. S., Lozano, C., Tallapragada, V., Iredell, D., Sheinin, D., Tolman, H. L., ... and Sims, J. (2014). Performance of ocean simulations in the coupled HWRF-HYCOM model. Journal of Atmospheric and Oceanic Technology, 31(2), 545-559.

Kitaigorodskii, S. A., Kuznetsov, O. A., and Panin, G. N. (1973). Coefficients of drag, sensible heat, and evaporation in the atmosphere over the surface of the sea. Izv. Acad. Sci. USSR, Atmos. Ocean. Phys, 9, 644-647.

Kitaigorodskii, S. A., and Volkov, Y. A. (1965). On the roughness parameter of the sea surface and the calculation of momentum flux in the near-water layer of the atmosphere. Izv. Atmos. Oceanic Phys, 1, 973-988.

Knutti, R., and Hegerl, G. C. (2008). The equilibrium sensitivity of the Earth's temperature to radiation changes. Nature Geoscience, 1(11), 735-743.

Koesterke, L., Huang, L., and Vienne, J. (2016, November). A Comparative Study of Application Performance and Scalability on the Intel Knights Landing Processor. In *High Performance Computing: ISC High Performance 2016 International Workshops, ExaComm, E-MuCoCoS, HPC-IODC, IXPUG, IWOPH, P3MA, VHPC, Frankfurt, Germany, June 19–23, 2016, Revised Selected Papers* (Vol. 9945, p. 307). Springer.

Komen, G. J., Cavaleri, L., Donelan, M., Hasselmann, K., Hasselmann, S., Janssen, P. A. E. M., 1994. Dynamics and modeling of ocean waves. Cambridge university press, Cambridge, UK.

Korres, G., Nittis, K., Perivoliotis, L., Tsiaras, K., Papadopoulos, A., Triantafyllou, G., Hoteit, I., and Abdullah, K. (2010). Forecasting the Aegean Sea hydrodynamics within the POSEIDON-II operational system. *Journal of Operational Oceanography*, 3(1), 37-49.

Korres, G., Papadopoulos, A., Katsafados, P., Ballas, D., Perivoliotis, L., and Nittis, K. (2011). A 2-year intercomparison of the WAM-Cycle4 and the WAVEWATCH-III wave models implemented within the Mediterranean Sea. *Mediterranean Marine Science*, 12(1), 129-152.

Kudryavtsev, V. N. (2006). On the effect of sea drops on the atmospheric boundary layer. *Journal of Geophysical Research: Oceans*, *111*(C7).

Kudryavtsev, V. N., Makin, V. K., and Chapron, B. (1999). Coupled sea surface-atmosphere model: 2. Spectrum of short wind waves. *Journal of Geophysical Research: Oceans*, *104*(C4), 7625-7639.

Kudryavtsev, V. N., and Makin, V. K. (2001). The impact of air-flow separation on the drag of the sea surface. *Boundary-layer meteorology*, *98*(1), 155-171.

Kudryavtsev, V. N., and Makin, V. K. (2002). Coupled dynamics of short waves and the airflow over long surface waves. *Journal of Geophysical Research: Oceans*, *107*(C12).

Kudryavtsev, V., Makin, V., and Zilitinkevich, S. (2012). *On the sea-surface drag and heat/mass transfer at strong winds*. Technical Report, Royal Netherlands Meteorological Institute, De Bilt, Nederlands.

Kumar, R. R., Kumar, B. P., and Subrahamanyam, D. B. (2009). Parameterization of rain induced surface roughness and its validation study using a third generation wave model. *Ocean Science Journal*, *44*(3), 125-143.

Lau, W. K. M., and Waliser, D. E. (2011). *Intraseasonal variability in the atmosphere-ocean climate system*. Springer Science and Business Media.

Le Méhauté, B., and Khangaonkar, T. (1990). Dynamic interaction of intense rain with water waves. *Journal of physical oceanography*, *20*(12), 1805-1812.

Lee, C. Y., and Chen, S. S. (2012). Symmetric and asymmetric structures of hurricane boundary layer in coupled atmosphere-wave-ocean models and observations. *Journal of the Atmospheric Sciences*, *69*(12), 3576-3594.

Ličer, M., Smerkol, P., Fettich, A., Ravdas, M., Papapostolou, A., Mantziafou, A., ... and Petan, S. (2016). Modeling the ocean and atmosphere during an extreme bora event in northern Adriatic using one-way and two-way atmosphere–ocean coupling. *Ocean Science*, *12*(1), 71-86.

Lionello, P., Martucci, G., and Zampieri, M. (2003). Implementation of a coupled atmosphere-wave-ocean model in the Mediterranean Sea: Sensitivity of the short time scale evolution to the air-sea coupling mechanisms, *Global Atmos. Ocean Syst.*, 9, 65 – 95.

Liss, P. S., and Duce, R. A. (2005). *The sea surface and global change*. Cambridge University Press.

Liu, B., Guan, C., and Xie, L. (2012). The wave state and sea spray related parameterization of wind stress applicable from low to extreme winds. *Journal of Geophysical Research: Oceans*, *117*(C11).

Liu, B., Liu, H., Xie, L., Guan, C., and Zhao, D. (2011). A coupled atmosphere-wave-ocean modeling system: Simulation of the intensity of an idealized tropical cyclone. *Monthly Weather Review*, *139*(1), 132-152.

Lo, J. C. F., Yang, Z. L., and Pielke, R. A. (2008). Assessment of three dynamical climate downscaling methods using the Weather Research and Forecasting (WRF) model. *Journal of Geophysical Research: Atmospheres*, *113*(D9).

Madec, G. (2008). NEMO reference manual, ocean dynamic component: NEMO-OPA. *Preliminary version. Note du Pole de modélisation, Institut Pierre-Simon Laplace (IPSL), France*, (27), 1288-161.

Mahrt, L. T., and Sun, J. (1995). The subgrid velocity scale in the bulk aerodynamic relationship for spatially averaged scalar fluxes. Monthly weather review, 123(10), 3032-3041.

Makin, K. (2005). A note on the drag of the sea surface at hurricane winds. *Bound. Lay. Meteor*. 115.1: 169-176.

Makin, V. K., and Kudryavtsev, V. N. (1999). Coupled sea surface-atmosphere model: 1. Wind over waves coupling. *Journal of Geophysical Research: Oceans*, *104*(C4), 7613-7623.

Malkus, J. S. (1962). Large Scale Interactions. In: Hill MN (ed) The Sea, Vol-I. Interscience Publishers, New York, pp 88-294.

Manton, M. J. (1973). On the attenuation of sea waves by rain. *Geophysical and Astrophysical Fluid Dynamics*, *5*(1), 249-260.

Mass, C. F., Ovens, D., Westrick, K. J., and Colle, B. A. (2002). Does increasing horizontal resolution produce more skillful forecasts? *B. Am. Meteorol. Soc*., 83, 407-430.

Masson, S., Hourdin, C., Benshila, R., Maisonnave, E., Meurdesoif, Y., Mazauric, C., ... and Valcke, S. (2012). Tropical Channel NEMO-OASIS-WRF Coupled simulations at very high resolution. In *13th WRF Users' Workshop–25-29 June*.

Mastenbroek, C., Burgers, G., and Janssen, P. A. E. M. (1993). The dynamical coupling of a wave model and a storm surge model through the atmospheric boundary layer. *Journal of Physical Oceanography*, *23*(8), 1856-1866.

Melville, W. K., and Matusov, P. (2002). Distribution of breaking waves at the ocean surface. Nature, 417(6884), 58-63.

Mesinger, F. (1996). Improvements in quantitative precipitation forecasts with the Eta regional model at the National Centers for Environmental Prediction: The 48-km upgrade. *B. Am. Meteorol. Soc*., 77, 2637–2649.

Mesinger, F., Janjic, Z.I., Nickovic, S., Gavrilov, D., and Deaven, D.G. (1988). The step-mountain coordinate: Model description and performance for cases of Alpine lee cyclogenesis and for a case of an Appalachian redevelopment. *Mon. Wea. Rev*., 116, 1493-1518.

Michalakes, J., Hacker, J., Loft, R., McCracken, M. O., Snavely, A., Wright, N. J., Spelce, T., Gorda, B., Walkup, R., 2008. WRF nature run. J. of Phys.: Conf. Ser. IOP Publishing. Vol. 125, No. 1, pp. 012-022.

(Online: http://iopscience.iop.org/article/10.1088/1742-6596/125/1/012022/meta, accessed 08.05.2017)

Mlawer, E. J., Taubman, S. J., Brown, P. D., Iacono, M. J., and Clough, S. A. (1997). Radiative transfer for inhomogeneous atmospheres: RRTM, a validated correlated-k model for the longwave. *Journal of Geophysical Research: Atmospheres*, *102*(D14), 16663-16682.

Miles, J.W. (1957). On the generation of surface waves by shear flows. *J. Fluid Mech*, 3, 185-204.

Monbaliu, J., Padilla-Hernandez, R., Hargreaves, J. C., Albiach, J. C. C., Luo, W., Sclavo, M., and Guenther, H. (2000). The spectral wave model, WAM, adapted for applications with high spatial resolution. *Coastal engineering*, *41*(1), 41-62.

Monin, A. S., and Obukhov, A. M. F. (1954). Basic laws of turbulent mixing in the surface layer of the atmosphere. Contrib. Geophys. Inst. Acad. Sci. USSR, 151(163), e187.

Moon, I. J., Hara, T., Ginis, I., Belcher, S. E., and Tolman, H. L. (2004a). Effect of surface waves on air-sea momentum exchange. Part I: Effect of mature and growing seas. *Journal of the atmospheric sciences*, *61*(19), 2321-2333.

Moon, I. J., Ginis, I., and Hara, T. (2004b). Effect of surface waves on air-sea momentum exchange. Part II: Behavior of drag coefficient under tropical cyclones. *Journal of the atmospheric sciences*, *61*(19), 2334-2348.

Moon, I. J., Ginis, I., and Hara, T. (2004c). Effect of surface waves on Charnock coefficient under tropical cyclones. *Geophysical Research Letters*, *31*(20).

Moon, I. J., Ginis, I., Hara, T., and Thomas, B. (2007). A physics-based parameterization of air-sea momentum flux at high wind speeds and its impact on hurricane intensity predictions. *Monthly weather review*, *135*(8), 2869-2878.

Myneni, R. B., Hoffman, S., Knyazikhin, Y., Privette, J. L., Glassy, J., Tian, Y., ... and Lotsch, A. (2002). Global products of vegetation leaf area and fraction absorbed PAR from year one of MODIS data. *Remote sensing of environment*, *83*(1), 214-231.

NCL - The NCAR Command Language (Version 6.3.0) [Software]. (2016). Boulder, Colorado: UCAR/NCAR/CISL/TDD. http://dx.doi.org/10.5065/D6WD3XH5.

Niu, S., Jia, X., Sang, J., Liu, X., Lu, C., and Liu, Y. (2010). Distributions of raindrop sizes and fall velocities in a semiarid plateau climate: Convective versus stratiform rains. *Journal of Applied Meteorology and Climatology*, *49*(4), 632-645.

Obukhov, A. M. (1946). Turbulence in the atmosphere with inhomogeneous temperature. Trudy geofiz. inst. AN SSSR, 1.

Olabarrieta, M., Warner, J. C., Armstrong, B., Zambon, J. B., and He, R. (2012). Ocean–atmosphere dynamics during Hurricane Ida and Nor'Ida: an application of the coupled ocean–atmosphere–wave–sediment transport (COAWST) modeling system. *Ocean Modelling*, *43*, 112-137.

Oost, W. A., Komen, G. J., Jacobs, C. M. J., and Van Oort, C. (2002). New evidence for a relation between wind stress and wave age from measurements during ASGAMAGE. Boundary-Layer Meteorology, 103(3), 409-438.

Oost, W. A., and Oost, E. M. (2004). An alternative approach to the parameterization the momentum flux over the sea. *Boundary-layer meteorology*, *113*(3), 411-426.

Ooyama, K. (1969). Numerical simulation of the life cycle of tropical cyclones. *Journal of the Atmospheric Sciences*, *26*(1), 3-40.

Panofsky, H. A. (1963). Determination of stress from wind and temperature measurements. Quarterly Journal of the Royal Meteorological Society, 89(379), 85-94.

Papadopoulos, A., Chronis, T. G., and Anagnostou, E. N. (2005). Improving convective precipitation forecasting through assimilation of regional lightning measurements in a mesoscale model. *Monthly weather review*, *133*(7), 1961-1977.

Papadopoulos, A., and Katsafados, P. (2009). Verification of operational weather forecasts from the POSEIDON system across Eastern Mediterranean. *Nat. Haz. Eart. Sys. Sci*., 9(4), 1299-1306.

Papadopoulos, A., Korres, G., Katsafados, P., Ballas, D., Perivoliotis, L., and Nittis, K. (2011). Dynamic downscaling of the ERA-40 data using a mesoscale meteorological model. *Mediterranean Marine Science*, *12*(1), 183-198.

Partanen, A. I., Dunne, E. M., Bergman, T., Laakso, A., Kokkola, H., Ovadnevaite, J., ... and O'Dowd, C. (2014). Global modelling of direct and indirect effects of sea spray aerosol using a source function encapsulating wave state. *Atmospheric Chemistry and Physics*, *14*(21), 11731-11752.

Peduzzi, P., Chatenoux, B., Dao, H., De Bono, A., Herold, C., Kossin, J., ... and Nordbeck, O. (2012). Global trends in tropical cyclone risk. *Nature climate change*, *2*(4), 289-294.

Philander, S. G. H., Pacanowski, R. C., Lau, N. C., and Nath, M. J. (1992). Simulation of ENSO with a global atmospheric GCM coupled to a high-resolution, tropical Pacific Ocean GCM. *Journal of Climate*, *5*(4), 308-329.

Phillips, O. M. (1957). On the generation of waves by turbulent wind. J. Fluid Mech, 2(5), 417-445.

Phillips, O. M. (1960). On the dynamics of unsteady gravity waves of finite amplitude Part 1. The elementary interactions. Journal of Fluid Mechanics, 9(02), 193-217.

Pielke, R. (2002). Mesoscale Meteorological Modelling. Academic Press. San Diego, CA. 676 pp.

Peirson, W. L., Beyá, J. F., Banner, M. L., Peral, J. S., and Azarmsa, S. A. (2013). Rain-induced attenuation of deep-water waves. *Journal of Fluid Mechanics*, *724*, 5-35.

Poon, Y. K., Tang, S., and Wu, J. (1992). Interactions between rain and wind waves. *Journal of Physical Oceanography*, *22*(9), 976-987.

Potter, H., Graber, H. C., Williams, N. J., Collins III, C. O., Ramos, R. J., and Drennan, W. M. (2015). In situ measurements of momentum fluxes in typhoons. *Journal of the Atmospheric Sciences*, *72*(1), 104-118.

Powell, M. D., Vickery, P. J., and Reinhold, T. A. (2003). Reduced drag coefficient for high wind speeds in tropical cyclones. *Nature*, *422*(6929), 279-283.

Powers, J. G., and Stoelinga, M. T. (2000). A coupled air-sea mesoscale model: Experiments in atmospheric sensitivity to marine roughness. *Monthly weather review*, *128*(1), 208-228.

Renault, L., Chiggiato, J., Warner, J. C., Gomez, M., Vizoso, G., and Tintore, J. (2012). Coupled atmosphere-ocean-wave simulations of a storm event over the Gulf of Lion and Balearic Sea. *Journal of Geophysical Research: Oceans*, *117*(C9).

Reynolds, O. (1900). Papers on Mechanical and Physical Subjects. Vol. I, 86, Cambridge Univ. Press.

Ricchi, A., Miglietta, M. M., Falco, P. P., Benetazzo, A., Bonaldo, D., Bergamasco, A., ... and Carniel, S. (2016). On the use of a coupled ocean-atmosphere-wave model during an extreme cold air outbreak over the Adriatic Sea. *Atmospheric Research*, *172*, 48-65.

Roberts, W. H., and Battisti, D. S. (2011). A new tool for evaluating the physics of coupled atmosphere–ocean variability in nature and in general circulation models. *Climate dynamics*, *36*(5-6), 907-923.

Roll, H. U. (1965). Physics of the Marine Atmosphere. Academic Press, New York, 434 p.

Rosenthal, S. L. (1971). The response of a tropical cyclone model to variations in boundary layer parameters, initial conditions, lateral boundary conditions, and domain size. *Mon. Wea. Rev*, *99*(10), 767-777.

Rutgersson, A., Nilsson, E. O., and Kumar, R. (2012). Introducing surface waves in a coupled wave-atmosphere regional climate model: Impact on atmospheric mixing length. *Journal of Geophysical Research: Oceans*, *117*(C11).

Rutgersson, A., Sætra, Ø., Semedo, A., Carlsson, B., and Kumar, R. (2010). Impact of surface waves in a regional climate model. *Meteorologische Zeitschrift*, *19*(3), 247-257.

Sahlée, E., Drennan, W. M., Potter, H., and Rebozo, M. A. (2012). Waves and air-sea fluxes from a drifting ASIS buoy during the Southern Ocean Gas Exchange experiment. *Journal of Geophysical Research: Oceans*, *117*(C8).

Salles, C., and Creutin, J. D. (2003). Instrumental uncertainties in Z-R relationships and raindrop fall velocities. *Journal of Applied Meteorology*, *42*(2), 279-290.

Samson, G., Masson, S., Lengaigne, M., Keerthi, M. G., Vialard, J., Pous, S., ... and Marchesiello, P. (2014). The NOW regional coupled model: Application to the tropical Indian Ocean climate and tropical cyclone activity. *Journal of Advances in Modeling Earth Systems*, *6*(3), 700-722.

Sathe, A., and Bierbooms, W. (2007). Influence of different wind profiles due to varying atmospheric stability on the fatigue life of wind turbines. In *Journal of Physics: Conference Series* (Vol. 75, No. 1, p. 012056). IOP Publishing.

Sharqawy, M. H., Lienhard, J. H., and Zubair, S. M. (2010). Thermophysical properties of seawater: a review of existing correlations and data. *Desalination and Water Treatment*, *16*(1-3), 354-380.

Shi, J., Zhong, Z., Li, X., Jiang, G., Zeng, W., and Li, Y. (2016). The Influence of wave state and sea spray on drag coefficient from low to high wind speeds. *Journal of Ocean University of China*, *15*(1), 41-49.

Shimada, S., and Ohsawa, T. (2011). Accuracy and characteristics of offshore wind speeds simulated by WRF. *Sola*, *7*, 21-24.

Sikirić, M. D., Roland, A., Janeković, I., Tomažić, I., and Kuzmić, M. (2013). Coupling of the Regional Ocean Modeling System (ROMS) and Wind Wave Model. *Ocean Modelling*, *72*, 59-73.

Skamarock, W. C., Klemp, J. B., Dudhia, J., Gill, D. O., Barker, D. M., Dudha, M. G., Huang, X., Wang, W., Powers, Y., 2008. A description of the advanced research WRF Ver. 3.0. NCAR Technical Note, Boulder, Colorado, USA. (Online: http://www2.mmm.ucar.edu/wrf/users/docs/arw_v3.pdf, accessed 08.05.2017)

Smith, S. D. (1988). Coefficients for sea surface wind stress, heat flux, and wind profiles as a function of wind speed and temperature. Journal of Geophysical Research: Oceans, 93(C12), 15467-15472.

Smith, S. D., Anderson, R. J., Oost, W. A., Kraan, C., Maat, N., De Cosmo, J., ... and Chadwick, H. M. (1992). Sea surface wind stress and drag coefficients: The HEXOS results. Boundary-Layer Meteorology, 60(1-2), 109-142.

Snir, M. (1998). *MPI--the Complete Reference: The MPI core* (Vol. 1). MIT press.

Soden, B. J., and Held, I. M. (2006). An assessment of climate feedbacks in coupled ocean-atmosphere models. *Journal of Climate*, *19*(14), 3354-3360.

Soloviev, A. V., Lukas, R., Donelan, M. A., Haus, B. K., and Ginis, I. (2014). The air-sea interface and surface stress under tropical cyclones. *Scientific reports*, *4*.

Sorensen, R. M. (2005). Basic coastal engineering (Vol. 10). Springer Science and Business Media.

Staneva, J., Wahle, K., Günther, H., and Stanev, E. (2016). Coupling of wave and circulation models in coastal-ocean predicting systems: a case study for the German Bight. *Ocean Science*, *12*(3), 797-806.

Stewart, R. W. (1974). The air-sea momentum exchange. Boundary-Layer Meteorology, 6(1-2), 151-167.

Stewart, R. H. (2008). *Introduction to physical oceanography* (pp. 133-147). Texas: Texas A and M University.

Stull, R. B. (1988). An Introduction to Boundary Layer Meteorology. Kluwer Academic, 666 pp.

Sullivan, P. P., Edson, J. B., Hristov, T., and McWilliams, J. C. (2008). Large-eddy simulations and observations of atmospheric marine boundary layers above nonequilibrium surface waves. *Journal of the Atmospheric Sciences*, *65*(4), 1225-1245.

Sullivan, P., and Williams, J. Mc (2010). Dynamics of winds and currents coupled to surface waves. Annu. Rev. Fluid Mech., 42, 19–42.

Takayama, A., Shimizu, K., Tomita, Y., and Takizuka, T. (2010). A new framework for integrated simulation model using MPMD approach. *J. Plasma Fusion Res. SERIES*, *9*, 604.

Taylor, K. E. (2001). Summarizing multiple aspects of model performance in a single diagram. *Journal of Geophysical Research: Atmospheres*, *106*(D7), 7183-7192.

Taylor, P. K., and Yelland, M. J. (2001). The dependence of sea surface roughness on the height and steepness of the waves. Journal of physical oceanography, 31(2), 572-590.

Tewari, M., Chen, F., Wang, W., Dudhia, J., LeMone, M. A., Mitchell, K., Gayno, G., Wegiel, J., and Cuenca, R. H. (2004). Implementation and verification of the unified NOAH land surface model in the WRF model. Proc. of 20th Conf. on Weather Anal. and Forecast./16th Conf. on Numer. Weather Predict. 12-16 January 2004, Seattle, USA, pp. 2165-2170. (Online: https://ams.confex.com/ams/84Annual/techprogram/paper_69061.htm, accessed 08.05.2017)

Thompson, G., Field, P. R., Rasmussen, R. M., and Hall, W. D. (2008). Explicit forecasts of winter precipitation using an improved bulk microphysics scheme. Part II: Implementation of a new snow parameterization. *Monthly Weather Review*, *136*(12), 5095-5115.

Thompson, G., Tewari, M., Ikeda, K., Tessendorf, S., Weeks, C., Otkin, J., and Kong, F. (2016). Explicitly-coupled cloud physics and radiation parameterizations and subsequent evaluation in WRF high-resolution convective forecasts. *Atmospheric Research*, *168*, 92-104.

Tokay, A., Bashor, P. G., Habib, E., and Kasparis, T. (2008). Raindrop size distribution measurements in tropical cyclones. *Monthly Weather Review*, *136*(5), 1669-1685.

Torrisi L., Cavaleri L., Korres G., Papadopoulos A., Varlas G., and Katsafados P.: Report on Wave Coupling, My Wave EU funded project, D-1.4, 63 pp., 2014.

Tsimplis, M. N. (1992). The effect of rain in calming the sea. *Journal of Physical Oceanography*, *22*(4), 404-412.

Tsimplis, M., and Thorpe, S. A. (1989). Wave damping by rain. *Nature*, *342*(6252), 893-895.

Tucker, M. J., and Pitt, E. G. (2001). *Waves in ocean engineering* (No. Volume 5).

Turuncoglu, U. U., Giuliani, G., Elguindi, N., and Giorgi, F. (2013). Modelling the Caspian Sea and its catchment area using a coupled regional atmosphere-ocean model (RegCM4-ROMS): model design and preliminary results. *Geoscientific Model Development*, 6(2), 283-299.

Valcke, S. (2013). The OASIS3 coupler: a European climate modelling community software. *Geoscientific Model Development*, *6*(2), 373-388.

Valcke, S., Craig, T., Coquart, L., 2015. OASIS3-MCT_3.0 coupler User Guide. CERFACS/CNRS, Toulouse, France. (Online: http://www.cerfacs.fr/oa4web/oasis3-mct_3.0/oasis3mct_UserGuide.pdf, accessed 08.05.2017)

van Dorn, W. (1953). Wind tides on an artificial pond. *J. Mar. Res*, *12*, 249.

van Nes, E. H., Scheffer, M., Brovkin, V., Lenton, T. M., Ye, H., Deyle, E., and Sugihara, G. (2015). Causal feedbacks in climate change. *Nature Climate Change*, 5(5), 445-448.

Varlas, G., Katsafados, P., Papadopoulos, A., and Korres, G. (2017a). Implementation of a two-way coupled atmosphere-ocean wave modeling system for assessing air-sea interaction over the Mediterranean Sea. (*Sumbitted to the Atmospheric Research Journal*).

Varlas, G., Katsafados, P., Papadopoulos, A., and Korres, G. (2017b). Implementation of a rain-ocean wave parameterization scheme in the two-way coupled system CHAOS. *European Geosciences Union (EGU) General Assembly 2017*, Vienna, Austria, 23-28 April 2017.

Varlas, G., Papadopoulos A., and Katsafados P. (2017c). An Analysis of the Synoptic and Dynamic Characteristics of Hurricane Sandy (2012). (*Submitted to the Meteorology and Atmospheric Physics Journal*).

Varlas, G., Katsafados, P., and Papadopoulos, A. (2013). The synoptic and dynamical characteristics of the hurricane Sandy. *13th CEST*, Athens, Greece, 5-7 September 2013.

Varlas, G., Papadopoulos A., Korres G., and Katsafados P. (2014). Modeling the air-sea wave interaction processes in an explosive cyclone over the Mediterranean Sea. *12th International Conference on Meteorology, Climatology and Atmospheric Physics (COMECAP 2014)*, University of Crete, Heraklion, Crete, Greece, 28-31 May 2014.

Varlas, G.,Papadopoulos, A., Korres G., and Katsafados, P. (2015). Evaluation of a fully coupled atmosphere - ocean waves system (WEW) under high impact wind-wave conditions. *11th Panhellenic Symposium of Oceanography and Fisheries*, University of the Aegean, Mytilini, Lesvos, Greece, 13-17 May 2015.

Veiga, J. A. P., and Queiroz, M. R. (2015). Impact of the Waves on the Sea Surface Roughness under Uniform Wind Conditions: Idealized Cases for Uniform Winds (Part I). *Atmospheric and Climate Sciences*, *5*(03), 317.

Voldoire, A., Sanchez-Gomez, E., y Mélia, D. S., Decharme, B., Cassou, C., Sénési, S., ... and Déqué, M. (2013). The CNRM-CM5. 1 global climate model: description and basic evaluation. *Climate Dynamics*, *40*(9-10), 2091-2121.

Von Schuckmann, K., Palmer, M. D., Trenberth, K. E., Cazenave, A., Chambers, D., Champollion, N., Hansen, J., Josey, S. A., Loeb, N., Mathieu, P. P. and Meyssignac, B. (2016). An imperative to monitor Earth's energy imbalance. *Nature Climate Change*, *6*(2), 138-144.

Voorrips, A. C., Makin, V. K., and Komen, G. J. (1995). The influence of atmospheric stratification on the growth of water waves. *Boundary-Layer Meteorology*, *72(3)*, 287-303.

Wahle, K., Staneva, J., Koch, W., Fenoglio-Marc, L., Ho-Hagemann, H., and Stanev, E. V. (2017). An atmosphere–wave regional coupled model: improving predictions of wave heights and surface winds in the southern North Sea. *Ocean Science*, *13*(2), 289-301.

WAMDI group: Hasselmann, S., Hasselmann, K., Bauer, E., Janssen, P.A.E.M., Komen, G.J., Bertotti, L., Lionello, P., Guillaume, A., Cardone, V.C., Greenwood, J.A., Reistad, M., Zambresky, L., and Ewing, J.A. (1988). The WAM model - a third generation ocean wave prediction model. *J. Phys. Oceanogr.*, 18, 1775-1810.

Warner, J. C., Armstrong, B., He, R., and Zambon, J. B. (2010). Development of a coupled ocean-atmosphere-wave-sediment transport (COAWST) modeling system. *Ocean modelling*, 35(3), 230-244.

Webster, P. J., Holland, G. J., Curry, J. A., and Chang, H. R. (2005). Changes in tropical cyclone number, duration, and intensity in a warming environment. *Science*, *309*(5742), 1844-1846.

Webster, P. J., Moore, A. M., Loschnigg, J. P., and Leben, R. R. (1999). Coupled ocean–atmosphere dynamics in the Indian Ocean during 1997-98. *Nature*, *401*(6751), 356-360.

Wilks, D. S. (2011). *Statistical methods in the atmospheric sciences* (Vol. 100). Academic press.

Williams, R.S., Jr., and Ferrigno, J.G., eds. (2012). State of the Earth's cryosphere at the beginning of the 21st century–Glaciers, global snow cover, floating ice, and permafrost and periglacial environments. U.S. Geological Survey Professional Paper 1386-A, 546 p. (Available at http://pubs.usgs.gov/pp/p1386a, accessed 22.05.2017)

Wu, J. (1982). Wind-stress coefficients over sea surface from breeze to hurricane. Journal of Geophysical Research: Oceans, 87(C12), 9704-9706.

Wu, L., Rutgersson, A., and Sahlée, E. (2015). Upper-ocean mixing due to surface gravity waves. *Journal of Geophysical Research: Oceans*, *120*(12), 8210-8228.

Yablonsky, R. M., Ginis, I., Thomas, B., Tallapragada, V., Sheinin, D., and Bernardet, L. (2015). Description and analysis of the ocean component of NOAA's Operational Hurricane Weather Research and Forecasting Model (HWRF). Journal of Atmospheric and Oceanic Technology, 32(1), 144-163.

Yang, Z., Tang, S., and Wu, J. (1997). An experimental study of rain effects on fine structures of wind waves. *Journal of Physical Oceanography*, *27*(3), 419-430.

Zambon, J. B., He, R., and Warner, J. C. (2014). Investigation of hurricane Ivan using the coupled ocean–atmosphere–wave–sediment transport (COAWST) model. Ocean Dynamics, 64(11), 1535-1554.

Zhang, J. A., Black, P. G., French, J. R., and Drennan, W. M. (2008). First direct measurements of enthalpy flux in the hurricane boundary layer: The CBLAST results. *Geophysical Research Letters*, *35*(14).

Zhang, M. Y., and Li, Y. S. (1996). The synchronous coupling of a third-generation wave model and a two-dimensional storm surge model. Ocean Engineering, 23(6), 533-543.

Zhao, D., and Toba, Y. (2001). Dependence of whitecap coverage on wind and wind-wave properties. *Journal of oceanography*, *57*(5), 603-616.

Zieger, S., Vinoth, J., and Young, I. R. (2009). Joint calibration of multiplatform altimeter measurements of wind speed and wave height over the past 20 years. *Journal of Atmospheric and Oceanic Technology*, *26*(12), 2549-2564.